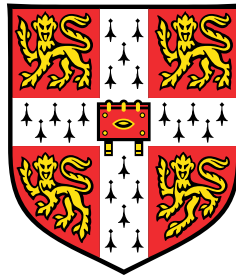


Emerging Bioelectronic Devices and Methods for Neuromodulation



Shao-Tuan Chen

Department of Engineering
University of Cambridge

This dissertation is submitted for the degree of
Doctor of Philosophy

This thesis is dedicated to my parents Shih-Chih, Jui-Yu, my brother Shao-Yung, and my loving partner Yung-Fang for their unyielding love, support, and encouragement.

Declaration

I confirm that this thesis contains fewer than 65,000 words including appendices, bibliography, footnotes, tables and equations and has fewer than 150 figures. All the work presented in this thesis has been carried out by me under the supervision of Prof. George Malliaras, Dr. Chris Proctor, and Dr. Damiano Barone at the University of Cambridge; with the exception of the following:

- Chapter 3: Synthesis and characterization of ionic liquids (performed by Dr. Liliana C. Tomé from University of the Basque Country UPV/EHU).
- Chapter 3: ELISA analysis for drug leakage characterization (performed by Megan Renny from University of Colorado, Boulder).
- Chapter 5: Tissue phantom and spinal cord stimulator fabrication for *in vitro* validation (performed by lab-mate Ben Woodington from Bioelectronics Laboratory, University of Cambridge).

I hereby declare the contents of this thesis are original and have not been submitted in whole or in part for consideration for any other degree or qualification.

Shao-Tuan Chen
December 2020

Acknowledgements

I remain ever grateful to my supervisor, Prof. George Malliaras, for broadening my perspective for scientific work and his encouragement throughout my PhD. I am grateful for having been a member of his research group in Cambridge.

I am indebted to all members in the bioelectronics laboratory. They helped me a great deal, particularly when I was first starting out, and trained me how to be an independent researcher.

I would also like to thank all the wonderful people outside of work who have helped make my time in Cambridge so enjoyable.

Finally, I am ever grateful to my parents, Shih-Chih and Jui-Yu, for their continued belief and support, and, of course, my partner, Yung-Fang. Without her love and support, none of this would have been possible.

Abstract

Demands for healthcare tools providing better detections, diagnoses, and treatments are at an all-time high as we gradually transitioning into an aging society. To tackle this challenge, bioelectronic devices made of conformable, soft and biocompatible materials ranging from sensors, actuators, drug delivery devices, to individual computing units were developed to help push forward the healthcare technology. Various translational researches and experimental works have brought forth breakthroughs and innovations from laboratories into clinics, benefitting the quality of life for countless patients. However, the level of understanding in how these devices interact with biology are lacking. As the complexities and types of bioelectronic devices increase, this gap of knowledge makes subsequent device design and improvement difficult, inefficient, and often times sub-optimal.

Computational models are ideal candidates to provide insights and guidelines for researchers to design bioelectronic devices and better understand their working principles. A proper model not only captures the important components of a system, providing a clear direction for experimental efforts, but also allows the possibility to perform large quantities of *in silico* studies in a relatively short amount of time. These advantages can reveal a clear relationship of how different components and their properties affect the overall device performance and how bioelectronics interact with biology.

In this thesis, two types of neuromodulation devices - the electrophoretic drug delivery device and the spinal cord stimulator were investigated. The working principle of these devices were identified and represented as governing equations. Subsequently, strategies to optimize the performance of existing neuromodulation devices for different applications, and/or new device operation modalities to overcome current limitations due to device architectures were presented. Finally, the theoretical predictions and numerical calculations in this work were validated with experimental measurements. The findings from this work can help design next-generation neuromodulation devices with better efficiency, higher reliability, and greater level of safety for the patients.

Publication

Journal manuscripts

- Shao-Tuan Chen, Christopher M. Proctor, and George G. Malliaras. "Materials and Device Considerations in Electrophoretic Drug Delivery Devices." *Scientific Reports* 10.1 (2020): 1-7.
- Shao-Tuan Chen, Megan N. Renny, Liliana C. Tomé, Jorge L. Olmedo-Martínez, Esther Udabe, Elise P.W. Jenkins, David Mecerreyes, George G. Malliaras, Robert R. McLeod and Christopher M. Proctor. "Reducing Passive Drug Diffusion from Electrophoretic Drug Delivery Devices through Co-ion Engineering." *Under review*.
- Shao-Tuan Chen, Elise P. W. Jenkins, Shunsuke Yamamoto and George G. Malliaras. "Enhancing Electrophoretic Delivery rate via Split Electrode Design and Optimal Switching Scheme." *In preparation*.
- Shao-Tuan Chen, Ben Woodington, Damiano G. Barone and George G. Malliaras. "Steerable and Localized Spinal Cord Stimulation via Temporal Interference Fields." *In preparation*.

Conference proceedings

- Shao-Tuan Chen, Christopher M. Proctor, and George G. Malliaras (Dec 2019) "Device Physics and Transient Behavior of Microfluidic Ion Pumps" *Materials Research Society Fall Meeting* (Boston, United States).
- Shao-Tuan Chen, Christopher M. Proctor and George G. Malliaras (Jul 2019) "Device Optimization of Microfluidic Ion Pumps with Numerical Simulation" *Biomedical Engineering Conference* (London, United Kingdom)
- Shao-Tuan Chen, Christopher M. Proctor, and George G. Malliaras (Mar 2019) "Device Models of Electrophoretic Drug Delivery Devices" *International Winter-school on Bioelectronics* (Kirchberg in Tirol, Austria)

Table of contents

List of figures	vii
List of tables	xi
Nomenclature	xiii
1 Background overview	1
1.1 Thesis motivation and objective	1
1.2 Computational modeling - Finite Element Method	3
1.3 Chemical neuromodulation	7
1.4 Ion exchange membrane	8
1.4.1 Charge selectivity - Donnan potential	8
1.4.2 Diffusion in electrolyte - Diffusiophoresis	13
1.4.3 Diffusion in IEM - Manning's condensation theory	15
1.5 Electrodes for electrophoretic delivery devices	21
1.5.1 Equivalent circuit model for ion pumps- RC circuit and τ	23
1.5.2 Electrical double layer formation - diffuse charge dynamics	24
1.5.3 Conducting polymer coatings to increase τ	25
1.5.4 Electrode design to increase active delivery time	27
1.6 Electrical neuromodulation	27
1.7 Spinal cord stimulation	28

1.7.1	Applications in pain management and motor control	31
1.7.2	Working principle of spinal cord stimulation	31
1.7.3	Common stimulation waveforms for spinal cord stimulation	33
1.7.4	Limitations of existing spinal cord stimulation technologies	33
1.8	Thesis chapter overview	36
2	Materials and device considerations in electrophoretic drug delivery devices	37
2.1	Introduction	38
2.2	Computational model for the electrophoretic delivery device	39
2.3	Transient behavior of an electrophoretic drug delivery device	41
2.4	Performance indices for electrophoretic drug delivery devices	44
2.5	Device performance optimization	52
2.6	Discussion	53
2.7	Conclusion	54
3	Reducing passive drug diffusion from electrophoretic drug delivery devices through co-ion engineering	55
3.1	Introduction	56
3.2	Mass transport in an electrophoretic drug delivery device	57
3.3	Diffusion experiments of acetylcholine paired with different co-ions	59
3.4	Computational modeling of drug diffusion through ion exchange membranes	63
3.5	Device active performance when paired with different co-ions	67
3.6	Discussion	69
3.7	Conclusion	70
3.8	Experimental setup and procedures	71
3.9	Theory for drug diffusion mechanisms	73

4	Enhancing electrophoretic delivery rate via split electrode design and optimal switching scheme	75
4.1	Introduction	76
4.2	Split electrode design validation with electrophoretic delivery experiment . .	78
4.3	Equivalent circuit model for split electrode design	80
4.4	Optimal switching scheme	84
4.5	Extending the applicability of split electrode design to n electrodes	88
4.6	Conclusion	91
4.7	Experimental section	92
5	Steerable and localized neuromodulation via temporal interference field	95
5.1	Introduction	96
5.2	Working principle of temporal interfering stimulation	101
5.3	Computational models for spinal cord stimulation	105
5.4	Localized spinal cord stimulation via temporal interfering fields	117
5.5	Parameters affecting the performance of temporal interfering stimulation . . .	130
5.6	Discussion	137
5.7	Conclusion	138
6	Conclusion and future work	139
6.1	Summary of key findings	139
6.2	Future work	142
	References	143
	Appendix A Synthetic procedure of co-ions used in Chapter 3	163
A.1	Synthetic Procedures	163
A.1.1	Synthesis of ACh Carboxylate Ionic Liquids	163
A.1.2	Synthesis of poly(sulfopropyl acrylate ACh)	164

Appendix B	Axon model parameters and circuit models for Chapter 5	169
B.1	Axon parameters and equivalent circuits	169
B.1.1	Sensory axon parameters	169
B.1.2	Motor axon parameters	170
B.1.3	Simulink model for sensory and motor axon based on MRG model . .	172
B.2	Matlab scripts for temporal interfering stimulation	174
B.2.1	Calculate the angle between two electric field	174
B.2.2	Extract amplitude modulated stimulation from experimental data . . .	175
B.2.3	Extract modulation index from experimental data	175
B.2.4	Animations of recruitment areas with varying stimulation intensities .	176
B.3	Axon activation maps for different base frequencies f	178
B.3.1	$f = 1500$ Hz	178
B.3.2	$f = 2500$ Hz	179
Appendix C	Publication list	181

List of figures

1.1	Work flow of constructing a FEM model	4
1.2	Donnan potential as a function of concentration ratio C_{IM}/C_D	10
1.3	Ion concentration profile in an IEM	11
1.4	Electric potential profile in an IEM	11
1.5	Co-ion concentration in IEM C_{co}^m with different C_{IM}	12
1.6	Co-ion concentration in IEM C_{co}^m with different C_D	13
1.7	Schematic for diffusiophoresis	15
1.8	Schematic for ion diffusion in an IEM	16
1.9	Schematics for counter-ion condensation	18
1.10	Faradaic versus capacitive electrodes and respective cyclic voltammograms	21
1.11	Schematic of the electrical double layer	23
1.12	Schematic and equivalent circuit of an electrophoretic delivery device	24
1.13	EDL formation	25
1.14	Commercial electrical neuromodulation systems	29
1.15	SCS device implant location	30
1.16	SCS placement and common stimulation waveforms	32
1.17	SCS placement and activation threshold contour	34
2.1	Computational domain of an electrophoretic drug delivery device	39
2.2	Concentration and potential profile of an ion pump during active state	43

2.3	Amount of drug transported Q with different C_D	45
2.4	Amount of drug transported Q with different C_{IM}	45
2.5	Amount of drug transport Q between ON and OFF states.	47
2.6	Transient ON/OFF ratio following results in Fig 2.5	47
2.7	Contour plot of amount of drug transported Q as a function of C_{IM} and C_D	49
2.8	Contour plot of pumping efficiency η as a function of C_{IM} and C_D	50
2.9	Contour plot of ON/OFF ratio as a function of C_{IM} and C_D	51
2.10	Q as a function of C_{IM} between ON and OFF state	52
3.1	Drug diffusion mechanisms through an ion exchange membrane	57
3.2	Acetylcholine:Carboxylate salt diffusion profile	60
3.3	Photo of the custom-made test cell for drug diffusion experiment	61
3.4	SPA ACh monomer and polymer diffusion profile	62
3.5	Numerical simulation results of diffusion profiles as a function of D_{co}	64
3.6	Diffusion profiles as functions of D_{co} and D_{drug}	65
3.7	Steady-state leakage rate contour as functions of D_{co} and D_{drug}	66
3.8	Device performance during active state with different co-ions	67
3.9	Active performance contour as both functions of D_{co} and D_{drug}	68
4.1	Experimental setup for electrode design validation	78
4.2	Conductivity measurement for electrode design validation	79
4.3	Equivalent circuit model for an electrophoretic delivery device	80
4.4	Electric potential and ionic current in an electrophoretic delivery device	81
4.5	Transported charge comparison for split electrode design	83
4.6	Timing diagram for optimal switching scheme	84
4.7	Ionic current for 3-split electrode design with optimal switching scheme.	85
4.8	Transported charge comparison between single and 3-split electrode design	86
4.9	Electric potential and field lines in an electrophoretic delivery device	88

4.10	Crosstalk current in an electrophoretic delivery device	89
4.11	Numerical simulations of delivery rate and relative power consumption	90
4.12	Numerical simulations of power efficiency and source-target current	90
5.1	Components and X-ray image of commercial spinal cord stimulators	97
5.2	Common electrical stimulation waveforms for spinal cord stimulators	98
5.3	Temporal interfering fields illustration	102
5.4	Equivalent circuit model for sensory and motor axons	107
5.5	Sensory axon activation map as functions of $ \vec{E}_1 $ and $ \vec{E}_2 $	111
5.6	Frequency-dependent impedance between an RC circuit and a neuron	113
5.7	Cross-sectional view of SCS computational domain	116
5.8	Workflow of obtaining an axon recruitment map	119
5.9	In vitro validation with 2-8 working electrode configuration	121
5.10	In vitro validation with 4-10 working electrode configuration	122
5.12	Recruitment area comparison for anterior corticospinal tract	124
5.11	Recruitment area comparison for dorsal column stimulation	125
5.13	Stimulation hotspot steerability with temporal interfering stimulation	128
5.14	TIS Recruited area with different base frequency f	131
5.15	Cont'd, TIS Recruited area with different base frequency f	132
5.16	Effect of ground electrode configurations on localization of TIS waveforms	134
5.17	Effect of electrode size on localization of TIS waveforms	135
A.1	NMR data for ACh carboxylate ionic liquids	164
A.2	NMR data for ACh 3-sulfopropyl acrylate	165
A.3	Synthetic pathways for co-ions in the study	166
A.4	^1H – NMR spectra of ACh SPA monomer and respective polyanions	167
B.1	Equivalent circuit for mammalian sensory axon	172

B.2	Fast Na ion channel	173
B.3	Persistent Na ion channel	173
B.4	Fast K ion channel	173
B.5	Slow K ion channel	174
B.6	Axon activation map where $f_1 = 1500$ Hz and $f_2 = 1510$ Hz	178
B.7	Axon activation map where $f_1 = 2500$ Hz and $f_2 = 2510$ Hz	179

List of tables

2.1	List of variables used in this study	41
4.1	Relative charging time and delivery rate for a n -split electrode setup	87
5.1	Tissue conductivity values used in the computational model.	117

Nomenclature

Roman Symbols

α	First rate constant for ion channel gating variable x
β	Second rate constant for ion channel gating variable x
ϵ_0	Vacuum permittivity
η	Ion pump pumping efficiency
γ	Activity coefficient
λ_b	Bjerrum number
μ	Ion mobility
ϕ_w	Membrane water volume fraction
τ	RC time constant
θ	Intersecting angle between two Electric fields
φ	Electrolyte potential
ξ	Manning parameter for counter-ion condensation
a	Ion activity
C	Concentration
D	Diffusion coefficient
E	Electric field

F	Faraday's constant
f_n	Neural oscillation frequency
g	Nonlinear ion channel conductance
K	Membrane conductivity
L	Device length
Q	Amount of drugs transported
Q_{Co}	Ions transported in a charging phase
R	Gas constant
R_s	Membrane resistance
T	Temperature
T_{Co}	Electrode charging phase
V	Electric potential
X	$\phi_w \frac{C_{IM}}{C_{co}^m}$
x	Gating variable for ion channel
z	Charge number

Superscripts

m	membrane phase
s	solution phase

Subscripts

AM	Amplitude modulated signal
co	co-ion
$counter$	counter-ion
$crit$	Critical state

<i>D</i>	Drug in the source reservoir
<i>IM</i>	Fixed charge polymers in the membrane
<i>net</i>	Combined electric field
<i>s</i>	coupled ion

Acronyms / Abbreviations

AC	Alternating Current
ACh	Acetylcholine
AEM	Anion Exchange Membrane
AID	Associated Ion Diffusion
AM	Amplitude Modulation
But	Butyrate
CAD	Computer Aided Design
CEM	Cation Exchange Membrane
CSF	Cerebrospinal Fluid
DBS	Deep Brain Stimulation
EDL	Electrical Double Layer
FEM	Finite Element Method
FFT	Fast Fourier Transform
Hex	Hexanoate
IE	Ion Exchange
IEM	Ion Exchange Membrane
IPG	Implantable Pulse Generator
LU	Lower-Upper factorization

MRG McIntyre-Richardson-Grill double-cable axon model

MW Molecular Weight

But Octanoate

OEIP Organic Electronic Ion Pump

PEDOT:PSS poly(3,4ethylenedioxythiophene):poly(styrenesulfonate)

SCS Spinal Cord Stimulation

SPA Sulfopropyl acrylate

TIF Temporal Interfering Field

TIS Temporal Interfering Stimulation

Chapter 1

Background overview

1.1 Thesis motivation and objective

The field of bioelectronics can trace its origin back to the 1780s, when Luigi Galvani first performed a series of work identifying the electrical signal transmission in biological tissues such as nerves and muscles [Cajavilca et al. (2009)]. Today, active research in the field of bioelectronics are being carried out all over the world. Innovations in material development, device design, and new clinical applications all contributed to this rapidly growing research community [Berggren and Richter-Dahlfors (2007); Liao et al. (2015); Someya et al. (2016)].

Bioelectronic devices constitute a wide spectrum of applications; from measuring and detecting various analyte and biomarkers with organic electrochemical transistors (OECTs) [Simon et al. (2016); White et al. (1984)], using conjugated-polymer coated neural probes to record electrophysiological signals [Kozai et al. (2012); Lacour et al. (2016)], building neuromorphic devices to mimic biological computing [Gkoupidenis et al. (2017); Jo et al. (2010)], to implanting organic electronic ion pumps (OEIPs) to electrophoretically deliver charged drug particles to targeted biological tissues [Isaksson et al. (2007); Simon et al. (2009)]. Of these bioelectronic applications from sensing, computing, to recording, the use of bioelectronic devices for treatments and intervention for various neurological diseases- a field termed '*Neuromodulation*', has also seen tremendous development in recent years.

Based on the modality, neuromodulation can be broadly categorized into two types - chemical neuromodulation and electrical modulation [Jastrzebska-Perfect et al. (2020)], with both types of neuromodulation devices undergoing immense refinements and progresses. As research in developing next-generation neuromodulation devices with more effective stimulation

strategies continues, fundamental understanding of the interactions between the device and the interfacing biological systems becomes ever more important.

In the case of electrophoretic drug delivery devices, the key factor dictating the device performance is the transport mechanism of charged species subjecting to applied electric field. In order to deliver drug particles with minimal power consumption while maintaining long-term device reliability and safety, the ion exchange membrane in the delivery device must possess high charge selectivity and low counter-ion resistance simultaneously. For electrical neuromodulation devices such as the spinal cord stimulator, the key factor in achieving better neuromodulation efficacy is the proper mechanistic understanding between the applied electrical stimulation and the evoked neural responses.

As we gradually transitioning into an aging society, the demand for healthcare tools capable of providing better understanding, diagnosis, and treatment of diseases and symptoms has skyrocketed. Translational research have successfully brought forward various experimental discoveries to the clinic and benefited the quality of lives for various patients. However, as the complexities and types of applications for these tools and devices grow, a fundamental understanding of how these devices operate and how they interact with the biology are lacking. This discrepancy between scientific understanding and clinical application often times leave the engineers having to design new devices to interact with a largely undetermined system. Any further device optimization are often sub-optimal and inefficient, as multiple facets of the entire system is not verified and well-understood.

In light of these challenges, this thesis focuses on developing computational models to provide device level understandings for emerging neuromodulation devices. Two types of neuromodulation devices- the electrophoretic drug delivery device and the spinal cord stimulator are studied. The ability to perform large quantities of *in silico* studies makes computational modeling a suitable platform to investigate how different components in the device and their properties affect the overall device performance and how the device interact with biology. By representing the entire system, including the devices together with the interfacing tissues, as a series of governing equations with appropriate boundary and initial conditions, the process of developing a computational model reveals the depth of current understanding for a specific system. These understandings can further direct experimental efforts and help develop next-generation bioelectronic devices. Below are brief introductions of theoretical background for developing a computational model for neuromodulation devices, and the physical principles of important components in neuromodulation devices.

1.2 Computational modeling - Finite Element Method

Computational models for bioelectronics devices, such as models for electrophoretic drug delivery device or the spinal cord stimulator, allow complex analysis and design optimizations through *in silico* studies. These models give experimentalists insights into the working principles of such devices and how they interact with biology. The computational models developed in this thesis are based on Finite Element Method (FEM). In this section, a brief overview of FEM including the process of developing a computational model is given. The section will also cover the process from defining, solving, to validating the modeling result based on the iterative nature of FEM.

One of the main reasons to use computational models is that for most real-world problems, analytical solutions often can not be obtained. To address this challenge, different numerical methods have been developed [Allaire and Allaire (2007); Cook and Jensen (2002); Grossmann et al. (2007)]. These numerical methods produce approximate results, allowing researchers to gradually increase the complexity of the models through iterative studies while gaining useful insights from these numerical models through the process. Finite Element Method - FEM, is one of the common numerical methods used to solve engineering and mathematical physics problems involving complex material properties, geometries, initial and boundary conditions. It was first developed by the aerospace industries to calculate the compound stresses and strains airplanes experience when subjecting to turbulence [Gupta and Meek (1996)]. With the drastic growth of computing powers in personal computers, FEM has reached almost all fields of engineering and science for engineers and researchers to develop realistic models with high complexities and study how different components interact with each other, with the environment, and with external applied forces.

The term *Finite Element* highlights the working principle of this type of numerical model: the algorithms in FEM softwares discretize the entire domain into much smaller, *finite*-sized *elements*. When obtaining the solution for a given FEM problem, instead of solving the entire model together, solutions are calculated individually in each of the small elements. From a high-level perspective, there are three phases involved when solving a particular problem using FEM: Pre-processing, solution, and post-processing. The following sections will use ion transport in a microfluidic ion pump as an example to illustrate the processes involved from defining the problem description to obtaining numerical solution using FEM. An illustrative work flow is shown in Figure 1.1.

Define the computational domain

The first step is to properly define the model in terms of geometries, necessary material properties, boundary conditions, and suitable governing equations. For the problem of calculating the amount of drug transport by a microfluidic ion pump subjected to external voltage, this step involves specifying the length scales of the microfluidic ion pump. The types of ionic species in each of the source, ion exchange membrane, and target reservoir in terms of diffusion coefficients and charge also need to be specified. The governing equation for ion transport due to electrochemical gradient is the Nernst-Planck equation (known as the drift-diffusion equation in semiconductor physics). To solve the Nernst-Planck equation, the initial condition at $t = 0$, and boundary conditions at electrode-electrolyte and electrolyte-IEM interfaces for concentration and electric potential boundary condition also need to be properly defined. Properly defining a FEM model is the most time-consuming and critical step. Often times, this process involves approximations and simplifications, since the geometry of the problem can be overly complicated, or the material properties involved are anisotropic, etc. As a result, having proper prior knowledge of the device physics or reliable experimental benchmarks to compare against are very beneficial for the validity and the accuracy of the numerical solutions.

Generate mesh for computation

Next step is to divide the entire geometry into small elements. In FEM softwares, this step is called creating a 'mesh' for the model. In general, mesh are repeated elements with primitive geometric shapes such as cubes, tetrahedrons, prisms or pyramids. The FEM softwares can use these primitive geometric elements to represent the original complicated computational domain. For converged results, the denser and finer the mesh elements are, the more accurate the FEM results are going to be, at the cost of more computation resources and runtime. The user can also specify the size and shape of the mesh, so that at critical interfaces (i.e., electrolyte-IEM interface for ion pump problem) the mesh are much denser than the bulk (i.e., the electrolyte). To ensure the accuracy of the FEM result, mesh convergence study is often employed, which is an iterative process of refining the mesh size and re-compute and compare the result to ensure the numerical result converge to a stable value.

Specify solver and types of solution

Once the pre-processing phase of specifying the computational domain and assigning proper mesh elements are performed, following step is to select an appropriate solver to obtain the desirable numerical results. Depending on the complexity and nonlinearity of the problem description, in general there are several direct (using Gauss elimination or LU decomposition) or iterative (iteration to minimize error) solvers to choose from in a given FEM software. For each problem, two types of solutions, i.e., steady-state and transient solution can be obtained. As described in the domain definition section, each problem is described by a set of governing equations, which are represented in the form of partial differential equations. The solutions for these partial differential equations can either be categorized as steady-state (time-independent) or transient (time-dependent). For the case of ion transport in a microfluidic ion pump, the steady-state solution will give the concentration distribution where the electrochemical gradient is zero, i.e., concentration distribution when no electric potential or concentration gradient is present in the system. Whereas transient solution will give the temporal evolution of the concentration distribution from $t = 0$ to the assigned time point. In practice, since transient simulations are harder to reach convergence and much more computationally intensive, user can often use the solution from steady-state simulations as the initial conditions for transient-studies to obtain time-dependent results more efficiently.

Post-processing to obtain simulation results

After sending the user-defined model to the FEM solver, the FEM software will then attempt to solve the model with a series of software-constrained criteria. Depending on the complexity of the model, the duration of the simulation can vary from a few seconds to several hours. If the model is ill-defined (e.g. unrealistic boundary condition or material properties), the solver will not reach convergence and the computation is aborted after a number of iterations. With a properly defined model, the error (residue) will decrease after each iteration, and when the error is below a threshold, the solver considered the problem converged and returned the simulation results. The user can then extract all the necessary simulation data from the FEM model. For the case of calculating drug transport in microfluidic ion pump, once the model converges, the time-dependent drug flux f_{drug} from the IEM-target interface can be obtained, and further changes of parameters (i.e., change the applied voltage V , change the drug reservoir concentration C_D or fixed charge concentration C_{IM}) can be performed to study the device performance.

1.3 Chemical neuromodulation

Currently, most common treatment and intervention method for neuromodulation is through medication, as in chemically modulating the neural activities. For chemical neuromodulation, medications are being delivered into the targeted tissues to produce desirable pharmacologic responses. Traditionally, medications are being administered orally. However, drugs administered orally can be metabolized extensively before reaching systemic circulation [Pollay (1993)], and for drugs targeting the central nervous system such as the brain or spinal cord, multiple neuroimmune barriers such as the blood-brain barrier would further restricting drugs from being delivered to the target [Pardridge (2007)]. To combat this, implantable drug delivery device such as the convection-enhanced delivery devices have been developed [Wesemann et al. (2014)]. These small, battery-powered implantable drug delivery devices can provide localized, on-demand drug delivery, and substantially improve the efficacy of the pharmacologic therapies for patients.

Out of these implantable drug delivery devices, organic electronic ion pumps (OEIPs) have shown great promises to provide precise dosage control and high spatial-temporal resolution of drug delivery. Since the drug are being electrophoretically drive from the device into the targeted tissue, OEIPs do not suffer drawbacks which limit pressure-drive drug delivery methods such as edema, back flow, or disruption of adjacent neural networks [Isaksson et al. (2007)]. An OEIP, or an electrophoretic drug delivery device, mainly consists of three components: the drug reservoir, the ion exchange membrane, and the electrodes. **Chapter 2** will introduce a computational model to study the time-dependent characteristics of a microfluidic organic electronic ion pump. The computational model is then used to provide guidelines in how to design such devices for different disease applications. Subsequently, **Chapter 3** will present a method to prolong the device lifetime and reliability for electrophoretic drug delivery devices. **Chapter 4** will introduce a new electrode design and operation switching scheme for electrophoretic delivery devices with aim to increase the instantaneous electrophoretic delivery rate. Below are the working principles of each component in an electrophoretic drug delivery device.

1.4 Ion exchange membrane

The most important component in an electrophoretic drug delivery device is the ion exchange membrane (IEM). The membrane separates the drug reservoir from the biological tissue, and the charge selectivity of the IEM allows the device to have high drug delivery efficiency (i.e., high pumping efficiency η) in active state and low drug leakage rate during idle state.

Ion exchange membranes (IEMs) are a class of semipermeable membranes which can selectively allow or block charged particles to pass through based on the electric charge of the particles. Due to their high ionic conductivity and selectivity, IEMs have been used in applications such as electro dialysis, fuel cells and water desalination [Li et al. (2008); Li and Zou (2011); Tanaka et al. (2003); Yanagi and Fukuta (2008); Zuo et al. (2008)]. In the context of bioelectronics applications, the charge selectivity of IEMs allow researchers to design drug delivery devices which can be driven by external applied electric field. By choosing the charge of the molecules according to the types of the IEM, precise delivery of drugs or analyte can be achieved while limiting unwanted ion transport. This section will give an overview of the working principle of IEMs including the ion permselectivity and ion transport in the context of drug delivery applications.

1.4.1 Charge selectivity - Donnan potential

IEMs are made of cross-linked charged polymers; the ones consisting negatively charged polymers would allow positively charged particles to pass through while blocking negatively charged ions, and vice versa. As a result, based on the electric charge of the polymers, IEMs can be classified into Cation Exchange Membranes (CEMs) and Anion Exchange Membranes (AEMs). For simplicity, for both CEMs and AEMs, in the electrolyte in contact with the membrane, ions with the opposite charge as the charged polymer are referred to as '*counter-ions*', and ions with the same charge as the polymer are referred to as '*co-ions*'.

In the IEM, in order to maintain electro-neutrality, the concentration of counter-ion $C_{counter}^m$ is higher than the co-ion concentration C_{co}^m when the membrane is in contact with electrolyte [Bard and Faulkner (2000)]. The relationship between $C_{counter}^m$ and C_{co}^m in the IEM can be described as:

$$z_{IM}C_{IM} + z_{counter}C_{counter}^m + z_{co}C_{co}^m = 0, \quad (1.1)$$

where z is the charge number, and C_{IM} represents the fixed charge concentration in the membrane. As seen from Equation 1.1, since the sign for $z_{counter}$ is the same as z_{IM} (both being negative for CEMs and positive for AEMs), and $C_{IM} > 0$ for a charged membrane, it follows that $C_{counter}^m > C_{co}^m$. This unequal amount of counter-ions and co-ions would result in an electric potential difference at the membrane/electrolyte interface, which is called the **Donnan potential**, φ_D . This Donnan potential φ_D further excludes co-ions from entering the membrane (i.e., phenomenon known as Donnan exclusion) and retains the counter-ions in the membrane.

Donnan potential can be described by the electrolyte potential difference in and out of the ion exchange membrane, and is given as [Donnan (1924)]:

$$\varphi_D = \varphi^m - \varphi^s, \quad (1.2)$$

$$= \frac{RT}{z_i F} \ln \frac{a_i^s}{a_i^m}, \quad (1.3)$$

$$\approx \frac{RT}{z_i F} \ln \frac{C_i^s}{C_i^m}, \quad (1.4)$$

where superscripts m and s denotes the membrane and solution phase, R is the universal gas constant, T is temperature and F is Faraday constant. z_i is the charge number, and a_i is the activity coefficient ($a_i = \gamma_i C_i$, for dilute solution, $\gamma_i \approx 1$) for the i^{th} species [Luo et al. (2018)]. For typical scenarios in electrodialysis or electrophoretic drug delivery applications, common concentration ratio is $C_i^s = 0.1 \times C_i^m$, therefore the Donnan potential φ_D based on Equation 1.4 ≈ -60 mV.

In order to verify that Donnan potential can accurately capture the potential difference due to fixed charge polymers and counter-ion co-ion mismatch the IEMs, the concentration and potential profile at an electrolyte/IEM interface were calculated with FEM-based numerical simulations [COMSOL (2018)]. In Figure 1.2, the potential difference in and out of the membrane is first calculated based on Equation 1.4 for different C_i^m/C_i^s ratio and compared against numerical simulation. As seen in Figure 1.2, the agreement between Equation 1.4 and electric potential obtained by numerical simulation shows the validity of thermodynamic equilibrium treatment in Donnan potential (Equation 1.4), which also shows the counter-ion concentration ratio in and out of the membrane is a crucial parameter in determining the Donnan potential of the membrane.

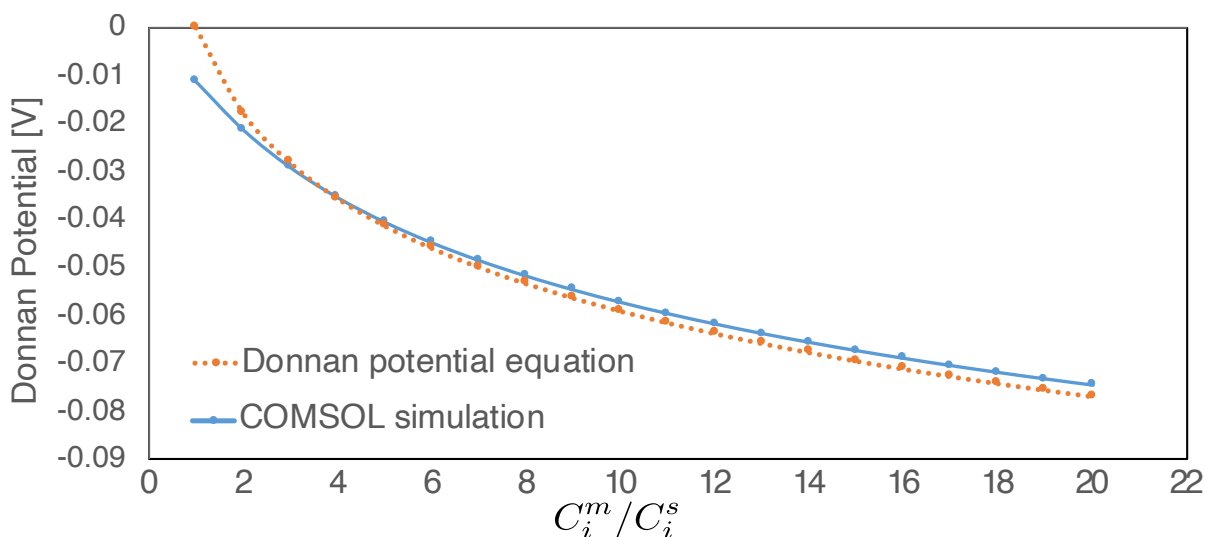


Fig. 1.2 Donnan potential calculation using Equation 1.4 and numerical simulation [COMSOL (2018)].

To further investigate the effect of change in IEM and electrolyte concentration have on co-ion exclusion and membrane permselectivity, consider the following example. In this case, the counter-ions and co-ions are chosen to be Na^+ and Cl^- , with the concentration for both ions C_D set to be 0.05 M in the electrolyte. The fixed charge concentration in the membrane C_{IM} is 0.5 M. Since the fixed charge concentration C_{IM} is substantially higher than the ion concentration in the electrolyte C_D , co-ion (Cl^-) concentration in the membrane is very low (≈ 5 mM in this case) (Figure 1.3). The calculated electrolyte potential ϕ_D (Figure 1.4) from the numerical simulation also fits well with the theoretical prediction for Donnan potential from Equation 1.4 ($\phi_D \approx -60$ mV for $C_{IM}/C_D = 10$).

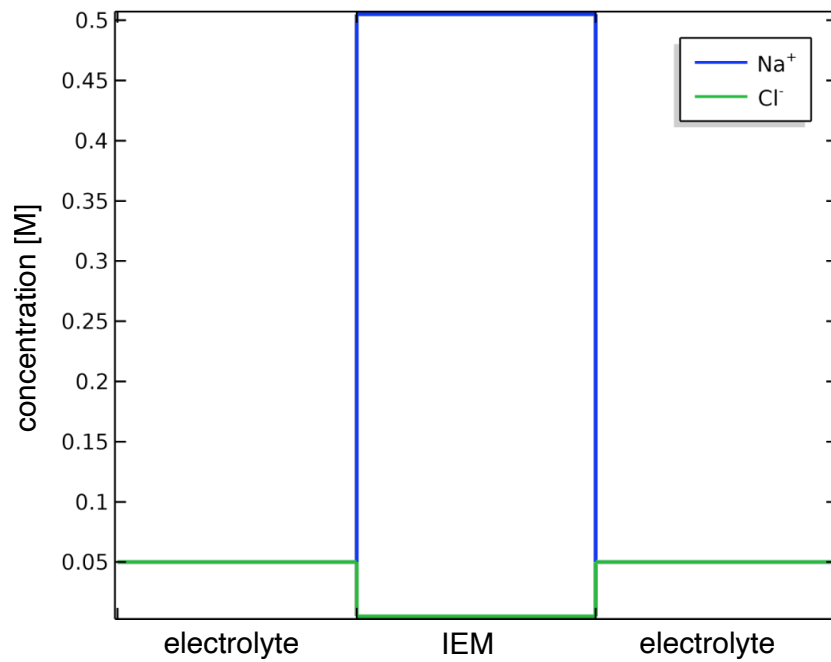


Fig. 1.3 Na⁺ and Cl⁻ concentration distribution at an electrolyte/IEM interface, where $C_{IM} = 0.5\text{ M}$ and $C_D = 0.05\text{ M}$.

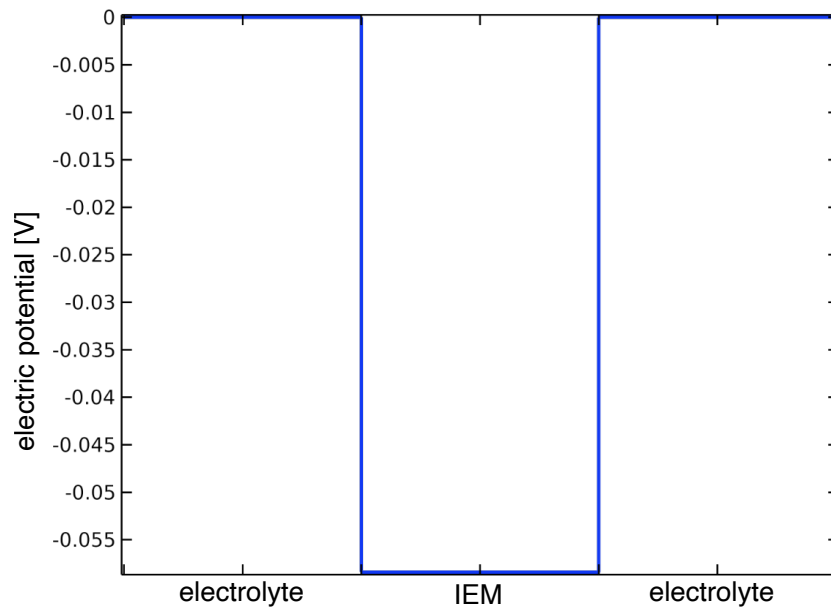


Fig. 1.4 Electric potential at an electrolyte/IEM interface, where the ratio of C_{IM}/C_D is 10.

As seen from Equation 1.1 and 1.4, higher fixed charge concentration C_{IM} would lead to higher counter-ion concentration $C_{counter}^m$ in the IEM. This increases the Donnan potential and further exclude the co-ions from entering the membrane. Also, if external electrolyte concentration (C_i^s) increases, φ_D in turn decreases in magnitude (less negative, reduce in magnitude). This would lead to less Donnan exclusion, and the co-ion concentration in the IEM C_{co}^m would therefore increase.

Figure 1.5 and Figure 1.6 illustrate the relative co-ion concentration in the IEM C_{co}^m with varying C_{IM} and C_D . As seen from Figure 1.5 and Figure 1.6, co-ions can be further excluded in the IEM by either increasing the fixed charge concentration C_{IM} or decreasing the drug concentration C_D . **Chapter 2** will present a complete computational model for an electrophoretic drug delivery device, and discuss how to optimize the device performance by changing concentration ratios between C_D and C_{IM} for different application scenarios.

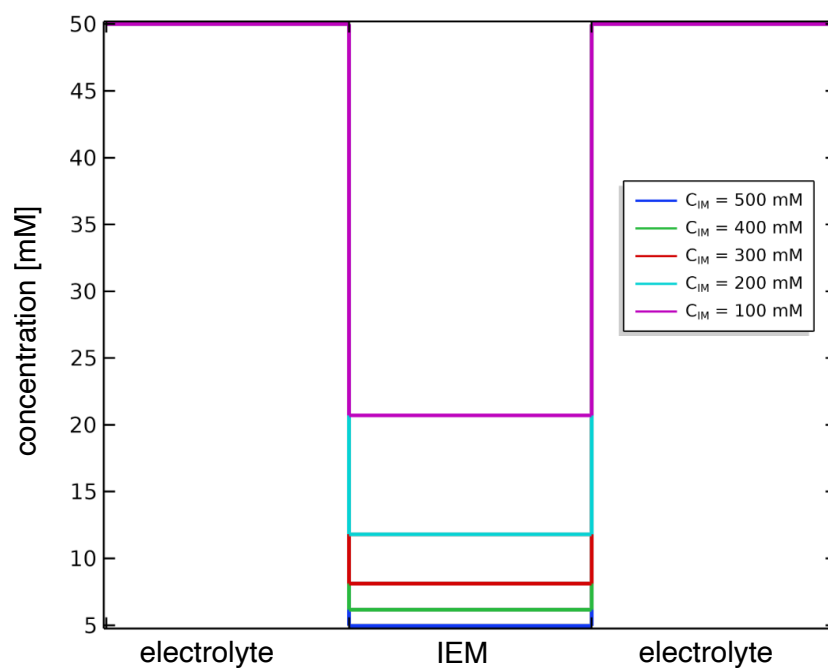


Fig. 1.5 Co-ion concentration in the IEM with different fixed charge concentrations C_{IM} .

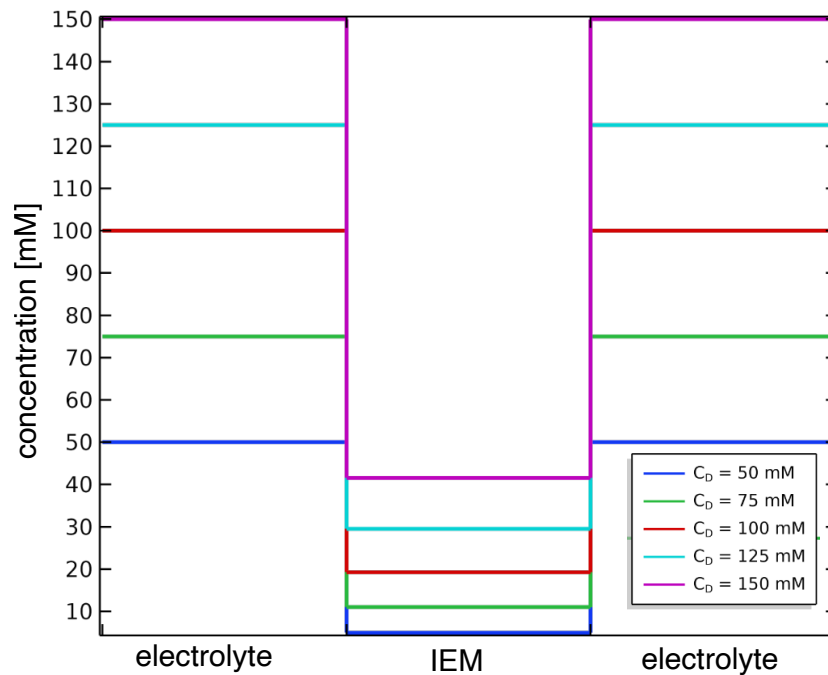


Fig. 1.6 Co-ion concentration in the IEM with different electrolyte concentrations C_D .

1.4.2 Diffusion in electrolyte - Diffusiophoresis

For an electrophoretic drug delivery device, the IEM separates the drug solution reservoir from the biological tissue. To achieve permselectivity and avoid drug leakage when the device is idle, the charge of the IEM should be the same as the drug (i.e, drug is the counter-ion in the electrolyte). In this context, when an external voltage is applied, the device can actively transport the counter-ions (drug) from the source reservoir through the IEM into the target (biological tissue). Also, due to the selectivity of the IEM, the co-ions from the target is blocked from entering the IEM when external voltage is applied.

However, IEMs are not perfectly selective, and co-ions can still diffuse across the membrane, given if the co-ions are coupled with the counter-ions. Also, when the device is idle, due to the high concentration gradient at the IEM-target interface, nontrivial amount of drug can still diffuse across the IEM. In this section, the ion transport mechanism of an electrophoretic device is analyzed, and a strategy to reduce the drug leakage rate of the electrophoretic device is presented in **Chapter 3**.

Ion transport in electrolyte and IEMs are driven by the change in electrochemical potential [Xu (2005)]. Electric potential differences caused by applied external voltage, or concentration

gradient in drug molecules in the source reservoir can both drive ion transport. The net ionic flux for ion i , J_i , is proportional to the electrochemical potential gradient multiplied by the diffusion coefficient. For one-dimensional transport phenomena, the system can be described by the Nernst-Planck equation [Strathmann (2004)] as:

$$J_i = -D_i \left(\frac{dC_i}{dx} + \frac{z_i F C_i}{RT} \frac{d\phi}{dx} \right), \quad (1.5)$$

where J_i is the ionic flux, D_i is diffusion coefficient, C_i is concentration, z_i is charge number, F is Faraday's constant, R is the gas constant, T is temperature and ϕ is the applied electric potential. As a result, both external applied voltage and drug concentration gradient can drive drug transport from the source reservoir through the IEM into the target reservoir.

For a 1:1 electrolyte in the source reservoir, the concentration of counter-ion and co-ion will be the same in order to maintain electro-neutrality [Bard and Faulkner (2000)]. As a result, in the absence of external electric potential, the difference in diffusion coefficient for counter-ions and co-ions would result in different diffusive fluxes as:

$$J_{counter} = -D_{counter} \nabla C_{counter}, \quad (1.6)$$

$$J_{co} = -D_{co} \nabla C_{co}, \quad (1.7)$$

where $\nabla C_{co} = \nabla C_{counter}$ in the electrolyte. The subscript *counter* and *co* here represent the diffusion coefficient and concentration values for counter-ion and the accompanying co-ion respectively [Prieve et al. (1984)].

Difference in diffusive flux between $J_{counter}$ and J_{co} will create an internal electric field. This electric field will slow down the faster ion and accelerate the slower ion [Hidalgo-Álvarez et al. (1996)]. The system reaches steady-state when the counter-ions and co-ions reach the same coupled drifting velocity $V_{coupled}$, and this phenomena is known as *diffusiophoresis* [Anderson and Prieve (1984)] (Figure 1.7).

The final coupled diffusion coefficient D_s considering the counter-ions and co-ions in the electrolyte depends on both $D_{counter}$ and D_{co} , and is given as [Crank and Park (1968)]:

$$D_s = \frac{D_{counter} D_{co}}{D_{counter} + D_{co}}, \quad (1.8)$$

which acts as the weighted average value between the counter-ion and co-ion diffusion coefficients $D_{counter}$ and D_{co} .

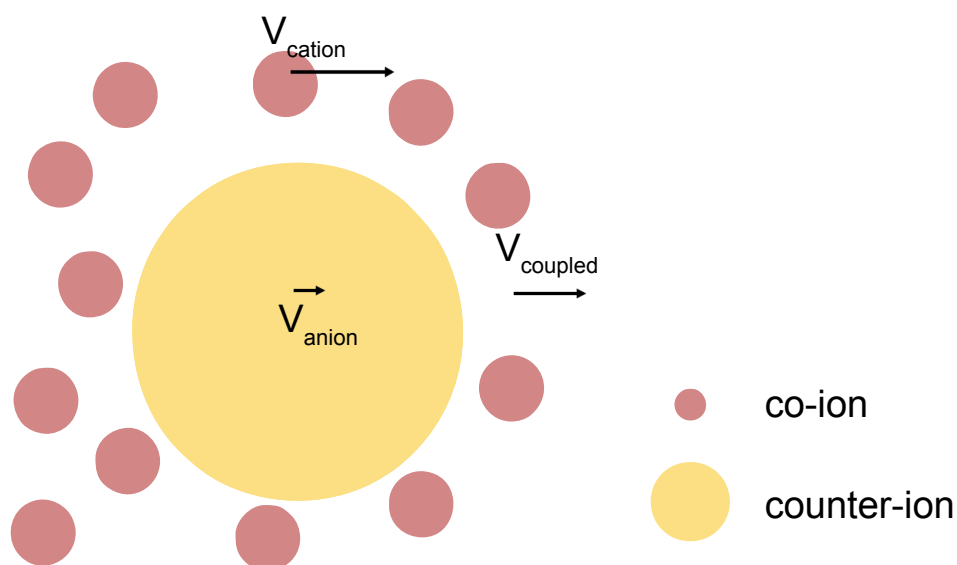


Fig. 1.7 Schematic for diffusiophoresis, showing concentration gradient driven diffusion for ions with different diffusion coefficients. At steady-state, both types of ions diffuse together, described by the coupled diffusion coefficient and coupled drifting velocity V_{coupled} .

As seen from Equation 1.8, the overall coupled diffusion coefficient D_s can be reduced by having a much smaller co-ion or counter-ion diffusion coefficient. Therefore, for drug delivery applications, leakage can be slowed down by designing a system with a low co-ion diffusion coefficient. **Chapter 3** will introduce a systematic approach of reducing drug leakage from electrophoretic drug delivery devices with a so-called 'co-ion engineering' approach.

1.4.3 Diffusion in IEM - Manning's condensation theory

Diffusion in electrolyte is mainly affected by the electrostatic interactions between ions, and the final coupled diffusion coefficient D_s of ions diffusing in electrolyte is described by Equation 1.8. However, when ions diffuse into the IEMs, apart from the electrostatic interactions between ions, they are also affected by the mechanical interactions with cross-linked polymer structures, along with the electrostatic interactions between ions and charged groups in the polymer structure (Figure 1.8). Several qualitative models have been developed to describe the ion diffusion coefficient for in IEMs [Geise et al. (2014); Yasuda et al. (1968)], some are quite inaccurate in lower concentration ranges, and others contain varying parameters, which need to be adjusted to fit to different membranes and different ions in the electrolyte.

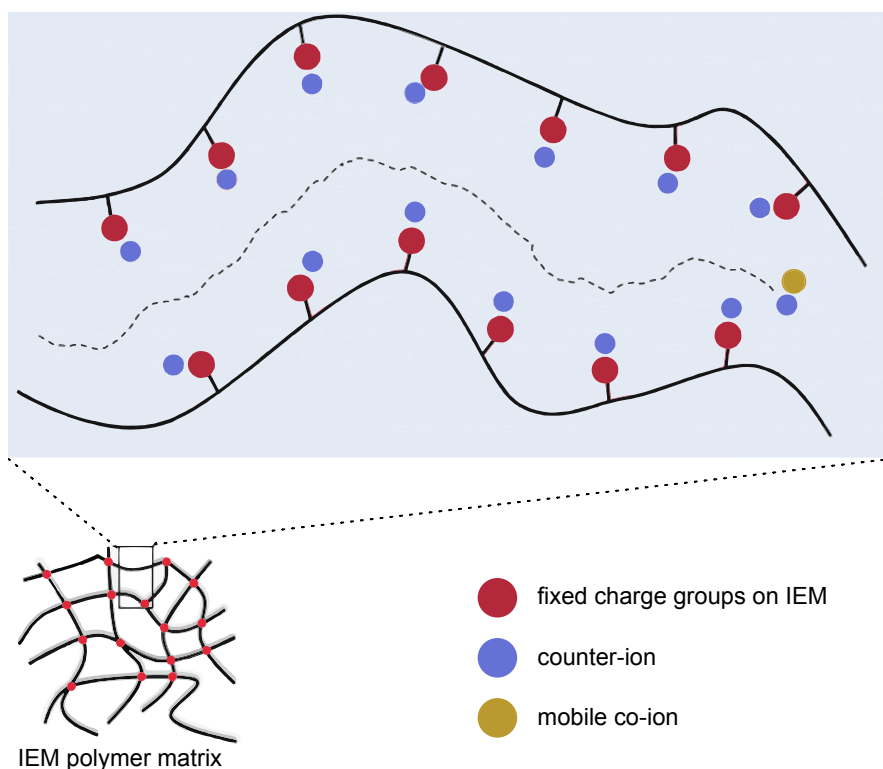


Fig. 1.8 Schematics for ion diffusion in an IEM. Both counter-ions and co-ions are affected by the mechanical interactions with the polymer matrix. Counter-ions can be electrostatically attracted by the fixed charge groups on the IEM. Mobile co-ions can diffuse through the IEM with a counter-ion to maintain electro-neutrality. Schematic adapted from [Kamcev et al. (2017c).]

Several seminal works combined have built up a comprehensive framework describing ion diffusion in IEMs [Kamcev et al. (2016, 2017b,c, 2018b)]. Starting from the classical solution-diffusion theory [Wijmans and Baker (1995)], the framework accounts for both the physical obstructions by the polymer network (tortuosity effect) with Mackie's model of ion diffusion in hydrated resin [Mackie et al. (1955)], and the electrostatic interactions between the ions and the fixed charge groups on the membrane with Manning's counter-ion condensation theory [Manning (1969)]. The following section will introduce the so-called 'slow-down factor' between the counter-ions and co-ions when diffusing from electrolyte into IEMs, as developed by Kamcev et al.

According to Manning's counter-ion condensation theory, electrostatic forces between the fixed charge on an IEM and mobile ions in the IEM are characterized by the dimensionless charge density number ξ , which is given as:

$$\xi = \frac{e^2}{4\pi\epsilon_0 k T b} = \frac{\lambda_b}{b}, \quad (1.9)$$

e is the elementary charge, ϵ_0 is the vacuum permittivity, k is Boltzmann's constant, T is temperature, λ_b is the Bjerrum number and b is the average distance between charges on the polymer chain [Manning (1969)]. The physical interpretation for ξ is the ratio between two length scales : λ_b , and b . The Bjerrum number λ_b represents the distance where electrostatic interaction is comparable to the thermal energy of that charge particle. On the other hand, b denotes the characteristic length between any two given neighboring fixed charges on the IEM. Manning's counter-ion condensation theory is based on the following hypothesis. If the distance b between a counter-ion to neighboring fixed charges on the polymer is smaller than the Bjerrum number λ_b , the counter-ion would not have sufficient thermal energy to diffuse away from the fixed charge groups on the IEM. In this case, the counter-ion is considered to be *condensed* on the IEM. For a 1:1 electrolyte, the critical value of ξ_{crit} for counter-ion condensation to occur, is $\xi_{crit} = 1$. Figure 1.9 shows the relative length scales for b and λ_b between a condensed and uncondensed scenario.

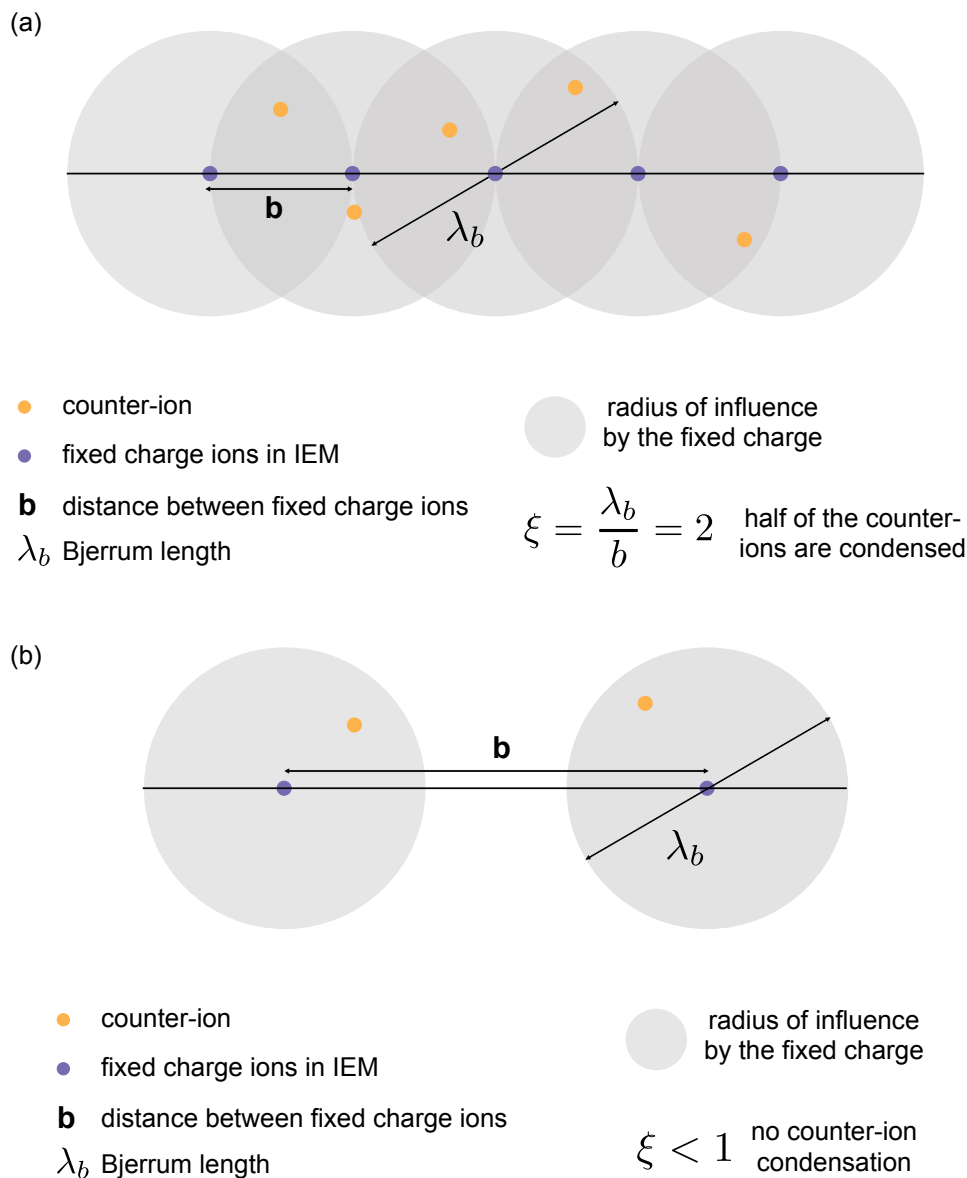


Fig. 1.9 Relative length scales between b and λ_b for (a) condensed (i.e., $\xi > \xi_{crit}$) and (b) uncondensed (i.e., $\xi < \xi_{crit}$) scenarios, where for a 1:1 electrolyte $\xi_{crit} = 1$. Schematic adapted from [Kamcev (2016).]

The ratio of condensed to uncondensed counter-ions is determined by the membrane properties, and source electrolyte concentration, which can be described by two parameters X and ξ [Manning (1969)] as :

$$\frac{C_{condensed}}{C_{uncondensed}} = \frac{1 - \xi^{-1}X}{X + 1}, \quad (1.10)$$

X here is a function the ratio between fixed charge concentration C_{IM} and co-ion concentration in the IEM (C_{co}^m) and the membrane water volume fraction ϕ_w as:

$$X = \phi_w \frac{C_{IM}}{C_{co}^m}, \quad (1.11)$$

For cases where $\xi > \xi_{crit}$, as counter-ions diffuse from the source electrolyte into the IEM, a portion of the counter-ions are condensed to the fixed charge groups on the IEM. The condensed counter-ions are electrostatically attracted by the IEM, resulting in an overall reduced diffusion coefficient for the counter-ions. To maintain electro-neutrality, the rest of the uncondensed counter-ions diffuse together with the mobile co-ions through the IEM, where the diffusion for both the uncondensed counter-ions and mobile co-ions are affected by the tortuosity effect due to prolonged diffusion length in the cross-linked polymer matrix.

Kamcev stated that for an IEM with high fixed charge concentration and high water volume fraction ϕ_w , counter-ion condensation would occur (i.e., $\xi > \xi_{crit}$) [Kamcev et al. (2017c, 2018b)]. Since condensation took place, the overall counter-ion diffusion coefficient $D_{counter}^m$ is determined by both the relative concentration of condensed and uncondensed counter-ions and their diffusion coefficients as:

$$D_{counter}^m = \frac{1 - \xi^{-1}X}{X + 1} D_{counter}^{condensed} + \frac{X/ + 1}{X + 1} D_{counter}^{uncondensed}, \quad (1.12)$$

where $D_{counter}^{condensed}$ is assumed to be zero (condensed counter-ions are electrostatically attracted by the fixed charge groups and assumed to be immobile). Finally, $D_{counter}^m$ and D_{co}^m , the ratio for counter-ion and co-ion diffusion coefficient within the IEM can be represented as a function of $D_{counter}$ and D_{co} values in the electrolyte as:

$$\frac{D_{counter}^m}{D_{counter}} = \left(\frac{X/\xi + 1}{X + 1} \right) \left(1 - \frac{1}{3} A \left(1; \frac{X}{\xi} \right) \right) \left(\frac{\phi_w}{2 - \phi_w} \right)^2, \quad (1.13)$$

$$\frac{D_{co}^m}{D_{co}} = \left(1 - \frac{1}{3} A \left(1; \frac{X}{\xi} \right) \right) \left(\frac{\phi_w}{2 - \phi_w} \right)^2, \quad (1.14)$$

where $A \left(1; \frac{X}{\xi} \right)$ is an infinite functional which can be approximated as:

$$A \left(1; \frac{X}{\xi} \right) \approx \frac{X}{2 + X \left(1 + \frac{\pi}{\xi} \right)}. \quad (1.15)$$

Equation 1.13 and 1.14 can be understood as the 'slow-down factor' for both counter-ions and co-ions when they enter the IEM from aqueous solution. Take a commonly used Nafion ion exchange membrane [Mauritz and Moore (2004)] as an example. The ξ value is 2.85. $X = 10$, and $\phi_w = 0.52$. In this case, the relative counter-ion and co-ion diffusion coefficient in the Nafion membrane compared to in electrolyte is:

$$\frac{D_{counter}^m}{D_{counter}} = 0.074, \quad (1.16)$$

$$\frac{D_{co}^m}{D_{co}} = 0.159. \quad (1.17)$$

This can be understood by the fact that since counter-ions are condensed to the fixed charge groups in the membrane, they are slowed down much more (7% of the original value in electrolyte) compared to co-ions (16% of the original value in electrolyte).

In **Chapter 3**, a strategy for limiting drug leakage with co-ion engineering approached was presented. Ion diffusion in the electrolyte and in the IEM were investigated in order to find out the relationship between both the drug and co-ion diffusion coefficient D_{drug} and D_{co} with the final drug leakage rate. In Chapter 3, the slow down factor for both the drug and co-ions are set to be 10%, consistent with previously reported values for electrophoretic drug delivery devices with PSS based membranes [Tanaka et al. (2003); Tybrandt (2017)]. However, as shown here, Manning's counter-ion condensation theory suggests that the fixed charge concentration C_{IM} and water volume fraction ϕ_w can have significant influence on the slow down factor for both the counter-ions and co-ions. Therefore, incorporating Manning's counter-ion condensation theory will be a potential future research direction on investigating how the IEM material properties can further influence drug leakage for electrophoretic drug delivery devices (in Chapter 6).

1.5 Electrodes for electrophoretic delivery devices

Besides the ion exchange membrane, the electrodes are also an important component of an electrophoretic drug delivery device. Based on the difference in charge transferring mechanism, electrodes used in bioelectronics applications can be classified into two types, non-polarizable and polarizable electrodes (Figure 1.10) [Berggren and Malliaras (2019)].

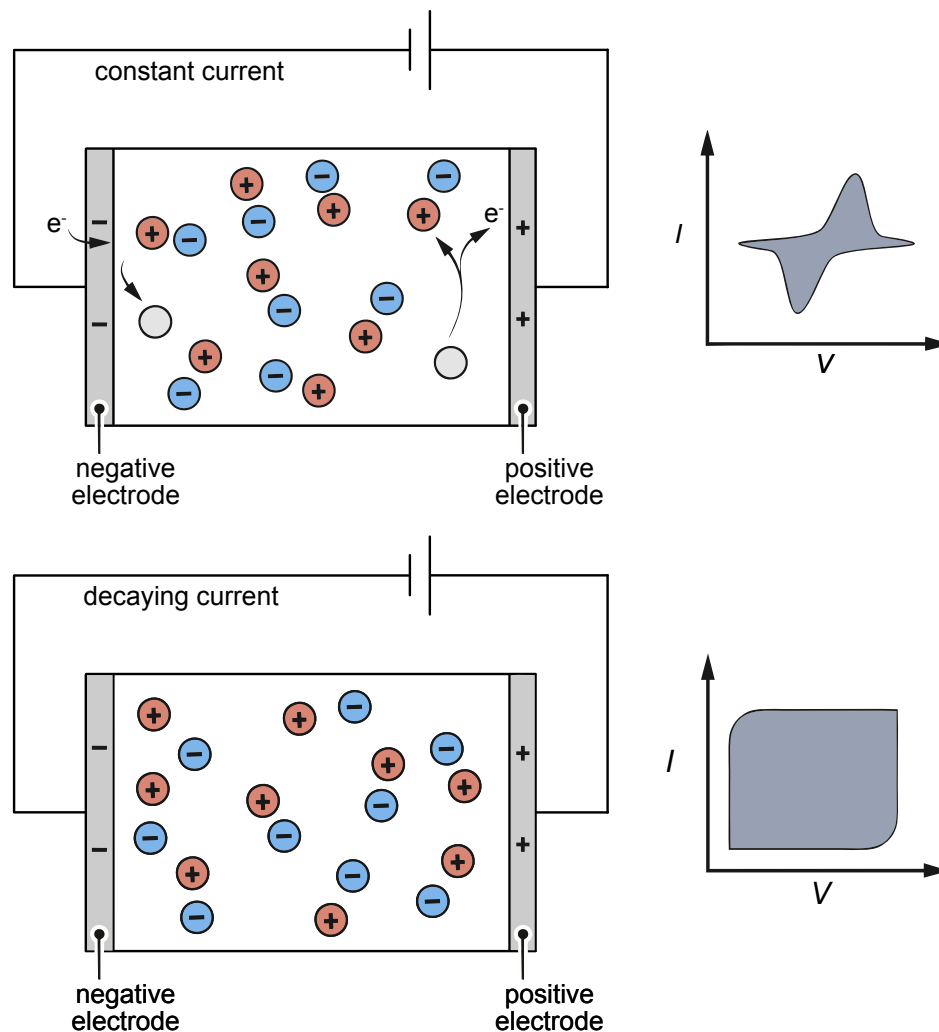
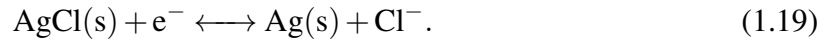


Fig. 1.10 Schematics for electrophoretic delivery devices with non-polarizable (top) VS polarizable (bottom) electrodes, with respective cyclic voltammograms on the right hand side. Faradaic reactions for the non-polarizable electrodes involve charge transfer across the electrode/electrolyte interface, and the corresponding cyclic voltammograms have distinct peaks. By contrast, electrical double layer forms at the surface of polarizable electrodes, and the corresponding cyclic voltammograms have box-shaped characteristics.

Non-polarizable electrodes such as Ag/AgCl electrodes can produce constant current, since the charge transfer mechanism for such electrodes involves redox reaction (Faradaic reactions), where the half reactions for the Ag/AgCl electrode can be written as:



As long as both silver ions and silver chloride are sufficient to sustain the redox reaction in Equation 1.19, the non-polarizable electrodes can continuously produce constant current. However, as seen from Equation 1.19, the production of gases and changes in pH due to Faradaic reactions can cause biocompatibility and safety concerns [Cogan (2008)]. Furthermore, the redox reaction degrades the electrode materials over time, and can lead to formation of metal-protein complexes [Rivnay et al. (2017)], which is detrimental to the longevity of the device. Therefore, non-polarizable electrodes are not a viable choice to be used in long-term implantable devices such as the microfluidic ion pump.

On the other hand, polarizable electrodes (e.g., Au or Pt electrodes) are more suitable to be used *in vivo*, as these electrodes do not involve electron transfer between the electrode and electrolyte when voltage is applied. Unwanted electrochemical reactions can be minimized by maintaining an applied potential below the charge-transfer redox threshold [Yanagi and Fukuta (2008)]. However, despite having better safety and longevity, one major limitation in using polarizable electrodes is the formation of electrical double layer (EDL) (Figure 1.11). The EDL is a structure forming at the electrode-electrolyte interface upon an electrical potential applied on the electrode. The first layer is termed the *compact layer*, and is consisted of a thin layer of ions (layer thickness is less than 10 nm for electrolyte with moderate concentration) absorbed onto the surface of the electrode. A second layer, termed the *diffuse layer* are ions in the adjacent region of the compact layer, which are also being electrostatically attracted to the surface of the electrode. Depending on the concentration of the electrolyte, the diffuse layer can extend to all the way to the bulk of the electrolyte. These two layers together form a capacitor at the electrode-electrolyte interface when an external voltage is applied, and can therefore screen out the applied electric potential.

Under DC voltage, unlike non-polarizable electrodes, polarizable electrodes produce an exponentially decaying current through reversible capacitive process as EDL builds up [Martin and Malliaras (2016)]. For electrophoretic delivery devices, the EDL acts as a capacitor which gradually screen out the externally applied voltage intended to transport charged species, thus limiting the delivery capacity of such devices [Cantrell et al. (2007); Grant and Lowery (2009)].

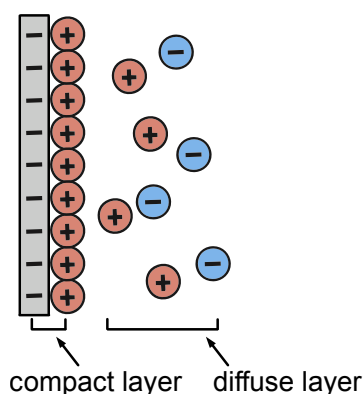


Fig. 1.11 Schematic of the electrical double layer around the charged surface of a polarizable electrode. The first layer is termed the compact layer, which consists of the ions absorbed to the surface of the electrode, and the second layer is termed the diffused layer, which consists of ions attracted by the surface charge of the electrode by electrostatic attraction.

1.5.1 Equivalent circuit model for ion pumps- RC circuit and τ

As mentioned in the previous section, the formation of electrical double layer (EDL) screens out the applied voltage, therefore understanding the time-dependent characteristics of EDL formation is important in order to maximize the delivery efficiency of electrophoretic delivery devices. To study how EDL forms upon the application of DC voltage, an equivalent circuit model for electrophoretic delivery devices with polarizable electrodes is developed (Figure 1.12). Figure 1.12 depicts the equivalent circuit model for an electrophoretic drug delivery device, where the ionic flux flowing across the device can be treated as the electric current in a circuit. This equivalent circuit model approach makes it possible to treat other components in an iontronic device as their electric circuit counterparts to provide conceptual images during analysis [Sjöström et al. (2018); Tybrandt et al. (2010)].

Previous works have demonstrated that the magnitude of the ionic current passing through an IEM is proportional to the external applied voltage, the same is also true for the ionic current in the electrolyte [Gabrielsson et al. (2012); Isaksson et al. (2007)]. Therefore, it is reasonable to treat the source and target reservoirs along with the IEM as resistors. The ionic resistances for the IEM and electrolyte in the source and target reservoirs are represented as resistors with difference resistance, R_1 , R_2 , and R_3 respectively (Figure 1.12). When applying a DC voltage to drive drugs through IEM, EDL forms at the electrode-electrolyte interface. The process of ions forming EDL can be considered as the charging process of the capacitors. As a result, in the equivalent circuit model, the polarizable electrodes as capacitors with capacitances C_1 and C_2 respectively.

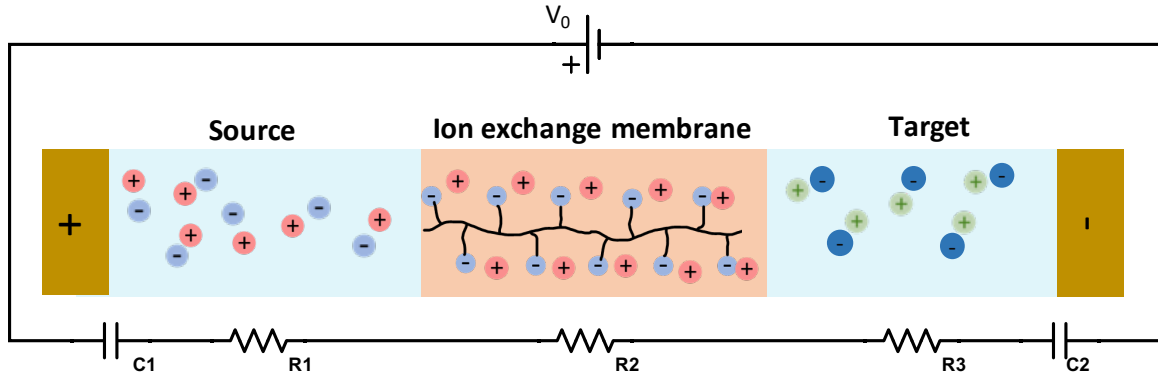


Fig. 1.12 Schematic and equivalent circuit of an electrophoretic delivery device. Components include: source and target reservoir, ion exchange membrane and capacitive electrodes. The equivalent circuit model treat the device as an RC circuit by representing each part of the electrophoretic delivery device with an electric component counterpart.

Follow the equivalent circuit model from Figure 1.12, the transient ionic current $I(t)$ in an electrophoretic delivery device upon applying a constant voltage V can be described as:

$$I(t) = \frac{1}{R_S} (V - V_{EDL}), \quad (1.20)$$

$$= \frac{1}{R_S} \left(V - V \left(1 - e^{-\frac{t}{\tau}} \right) \right), \quad (1.21)$$

$$= \frac{V}{R_S} e^{-\frac{t}{\tau}}, \quad (1.22)$$

where V_{EDL} is the charge stored in the electrical double layer, $R_S = R_1 + R_2 + R_3$ from Figure 1.12 τ is the time constant of the equivalent circuit in Figure 1.12, which depends on the ion concentration of the drug solution and the device geometry.

1.5.2 Electrical double layer formation - diffuse charge dynamics

The time constant τ in Equation 1.22 is a phenomenological term describing how fast EDL forms and relaxes when a DC voltage is applied to and disconnected from a polarizable electrode. The process of EDL formation/relaxation is called the diffuse-charge dynamics [Bazant et al. (2004)]. Diffuse-charge dynamics describes the screening process of EDL at the polarizable electrodes upon applying DC voltage (Figure 1.13). Decrease in electrolyte potential over time is caused by the process 'EDL relaxation', and this process is treated as the charging of a capacitor in a RC circuit. The characteristic time for the EDL relaxation is a combination

of varying fast and slow RC time constant, τ_D (proportional to λ_D^2), τ_C (proportional to $\lambda_D L$) and τ_L (proportional to L^2), where λ_D is the Debye length of the system, and L is the length of the device reservoir. During charging and discharging phase, the dominating behavior would depend on the initial ion concentration and degree of nonlinearity of the system [Biesheuvel and Bazant (2010)].

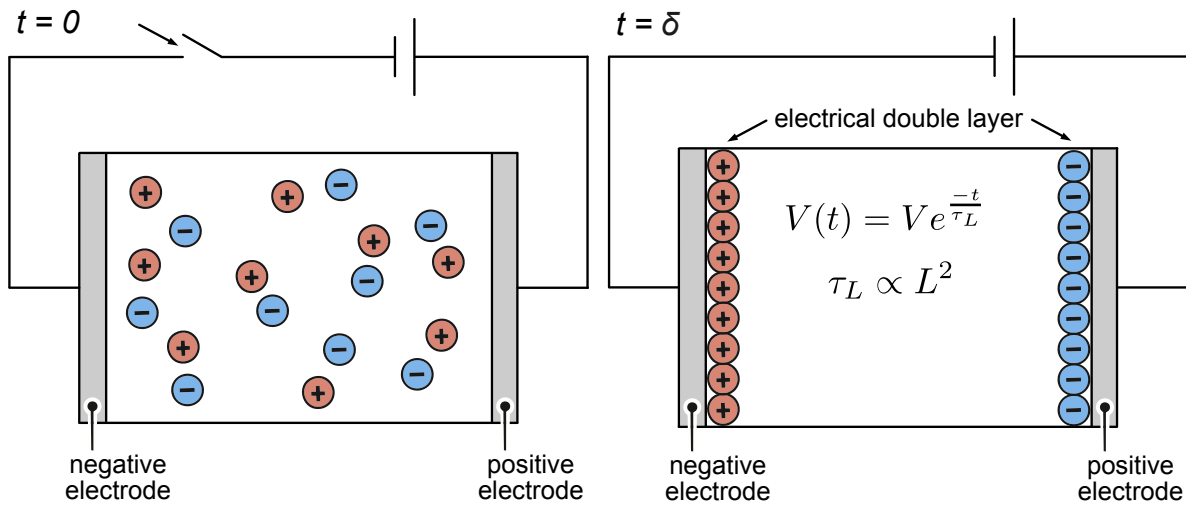


Fig. 1.13 Diffuse-charge dynamics describing how electrical double layer forms in an electrophoretic delivery device with polarizable electrode. Initially no potential difference is applied across the device, and a DC voltage is applied at $t = 0$ (top). At $t = \delta$, EDL is fully formed (bottom). The time-dependent voltage across the EDL is described by Equation 1.22, where τ can be determined experimentally.

1.5.3 Conducting polymer coatings to increase τ

To increase the electrode capacitance and the active delivering time (i.e., to increase τ), electrodes in ion pumps are usually coated with conducting polymers [Zeglio et al. (2019)]. Conducting polymers coatings have heterogeneous morphologies, consisting of conjugated polymer with molecular backbone surrounded by poly-electrolyte covalently bonded to the polymer chain [Martin and Malliaras (2016)]. For bioelectronics applications, increasing the capacitance of electrodes allows devices to reach smaller form factors and reduces invasiveness for implantation. Recent research regarding the molecular morphologies of conducting polymers [Volkov et al. (2017)] has revealed that for commonly used conducting polymer coating such as poly(3,4-ethylenedioxythiophene): polystyrene sulfonate (PEDOT:PSS), the

porous structure of the conducting polymer allows the electrode to form volumetric capacitance [Proctor et al. (2016)], or conversely, a significantly larger effective surface area when treating the electrical double layer as parallel-plate capacitors.

Within a PEDOT:PSS film, the positively charged PEDOT are electrostatically balanced by the negatively charged mobile PSS groups in the polyelectrolyte, and the spatial separation of charge carriers inside the conducting polymers create an EDL. The capacitance of such conducting polymers is found to vary linearly with the volume of the conducting polymer film, with no significant accumulation of ions at the electrode-electrolyte interface, thereby further verifying the volumetric characteristics of the capacitance in electrodes coated with conducted polymers. Researchers [Tybrandt et al. (2017)] recently have also developed a novel two-phase model to establish a theoretical framework for charge transport and volumetric capacitance characteristics of electrodes coated with conducting polymer.

Referring back to the equivalent circuit model for the electrophoretic delivery device in Figure 1.12, when applying an electric potential from the capacitive electrodes to drive charged species through the IEM, EDL forms within the entire volume of the porous conducting polymer film. The process of ions forming EDL within the polymer volume can be considered as the charging process of a parallel-plate capacitor with significantly larger surface area. This is because with conducting polymer coating such as PEDOT:PSS, EDL forms not only at the electrode-electrolyte interface, but also within the polymer matrix. As a result, the resulting volumetric capacitance is substantially larger than the parallel-plate capacitance of similar dimensions [Rivnay et al. (2015)], and the diffuse-charge dynamics for such system is suited for nonlinear analysis [Kilic et al. (2007)].

Following the analysis in [Bazant et al. (2004)], for systems with higher order of nonlinearity, such as ion absorption/desorption effects at the electrode and diffusion along with stronger concentration gradient in the bulk, the nonlinear time dependent charge dynamics response is best described by the longer relaxation time scale, τ_L . As a result, the electrolyte potential at the diffuse layer boundary of the electrode $V(t)$ from Equation 1.22 is an exponentially decaying function such that:

$$V(t) = \frac{V}{R_S} e^{-\frac{t}{\tau_L}}. \quad (1.23)$$

The RC time constant τ_L is governed by both the ion concentration in the source reservoir C_D and fixed charge concentration C_{IM} in the IEM, since higher ion concentration leads to higher

conductivity, and can be represented as:

$$\tau_L = f(C_D, C_{IM}) \quad (1.24)$$

Therefore, by changing the ion concentration in the source reservoir C_D and fixed charge concentration C_{IM} in the IEM, the active delivery time for the ion pump can be optimized. **Chapter 2** will discuss the relationship between C_D , C_{IM} and the time-dependent drug delivery Q with numerical simulations.

1.5.4 Electrode design to increase active delivery time

While the inclusion of PEDOT:PSS coatings on polarizable electrodes has shown to greatly increase the charge injection capability and electrode capacitance, the electrical double layer persists as the main limitation for electrophoresis protocols in long-term implantable drug delivery devices [Ferro and Melosh (2018)]. For applications where high delivery rate is required, pulsing stimulations are used to drive the electrophoretic delivery device [Proctor et al. (2018); Uguz et al. (2017)]. The duration of a single applied voltage pulse is based on the capacitance of the electrodes. The applied voltage is switched off when the electrical double layer on the electrode is fully charged. Switching off the applied voltage allows the ions in the double layer to diffuse away before another voltage pulse should be applied. The electrophoretic delivery rate by using pulsed stimulation is then limited by the time it takes for the electrical double layer on the electrode to be fully discharged. In **Chapter 4**, a new electrode design to overcome the limitation of electrical double layer formation is presented. By optimizing the pulse duration to timings relevant to the formation of the electrical double layer, combined with the electrode geometry, the new electrode design can improve the delivery rate of electrophoretic delivery devices while maintaining safe charge injection limit.

1.6 Electrical neuromodulation

Besides chemical neuromodulation and corresponding electrophoretic drug delivery devices for targeted chemical delivery, another common neuromodulation modality is electrical neuromodulation. Devices such as the cochlear implants, deep brain stimulators, or spinal cord stimulators all supply electrical stimulation to the nervous systems to either provide therapeutic benefits or aid impaired sensory-motor functions for patients. Figure 1.14 illustrate the components

of an electrical neuromodulation system, which involves: an implanted electrode to supply electrical stimulation to the interfacing tissue; an implantable pulse generator (IPG) to specify the stimulation duration, intensity, and waveform; a remote control for the patient to adjust the stimulation settings. In this thesis, a localized and steerable electrical neuromodulation device and method is developed and validated in the context of spinal cord stimulation. Below is a brief introduction of the working principle for the spinal cord stimulation. The therapeutic limitations of spinal cord stimulation due to existing device architecture and stimulation protocol is identified, and a combined computational and experimental work to validate the new spinal cord stimulation strategy is presented in **Chapter 5**.

1.7 Spinal cord stimulation

The gate control theory for pain, a framework of describing how electrical stimulations to the nerve fibers can block pain signals, was first published in 1965 [Melzack and Wall (1965)]. This theory posited that activating large-diameter sensory fibers can produce paresthesia (tingling, pins and needles sensations), thus blocking ('gating') pain transmission to the central nervous system. Two years later, the first clinical application of using electrical stimulations to control pain was performed in the context of spinal cord stimulation (SCS). The procedure involved surgically implanting an electrode array in the epidural space dorsal to the spinal cord column, and activating large-diameter ($A\beta$) sensory fibers with electrical stimulation [Shealy et al. (1967)]. Figure 1.15 illustrates the relative position of a SCS device when implanted in place.

Fueled by the growing prevalence of neuropathic pain and technology advancements, spinal cord stimulation therapy has seen drastic improvements since the first successful implant. Reduced invasiveness, higher device reliability, and better overall patient comfort and success rate have all further pushed forward such technology as the standard of care for a variety of diseases in the nervous system [Eldabe et al. (2016)]. Currently, spinal cord stimulation (SCS) is one of the most common electrical neuromodulation therapies, with around 50,000 patients receiving surgeries for implantations annually [Sdrulla et al. (2018)].

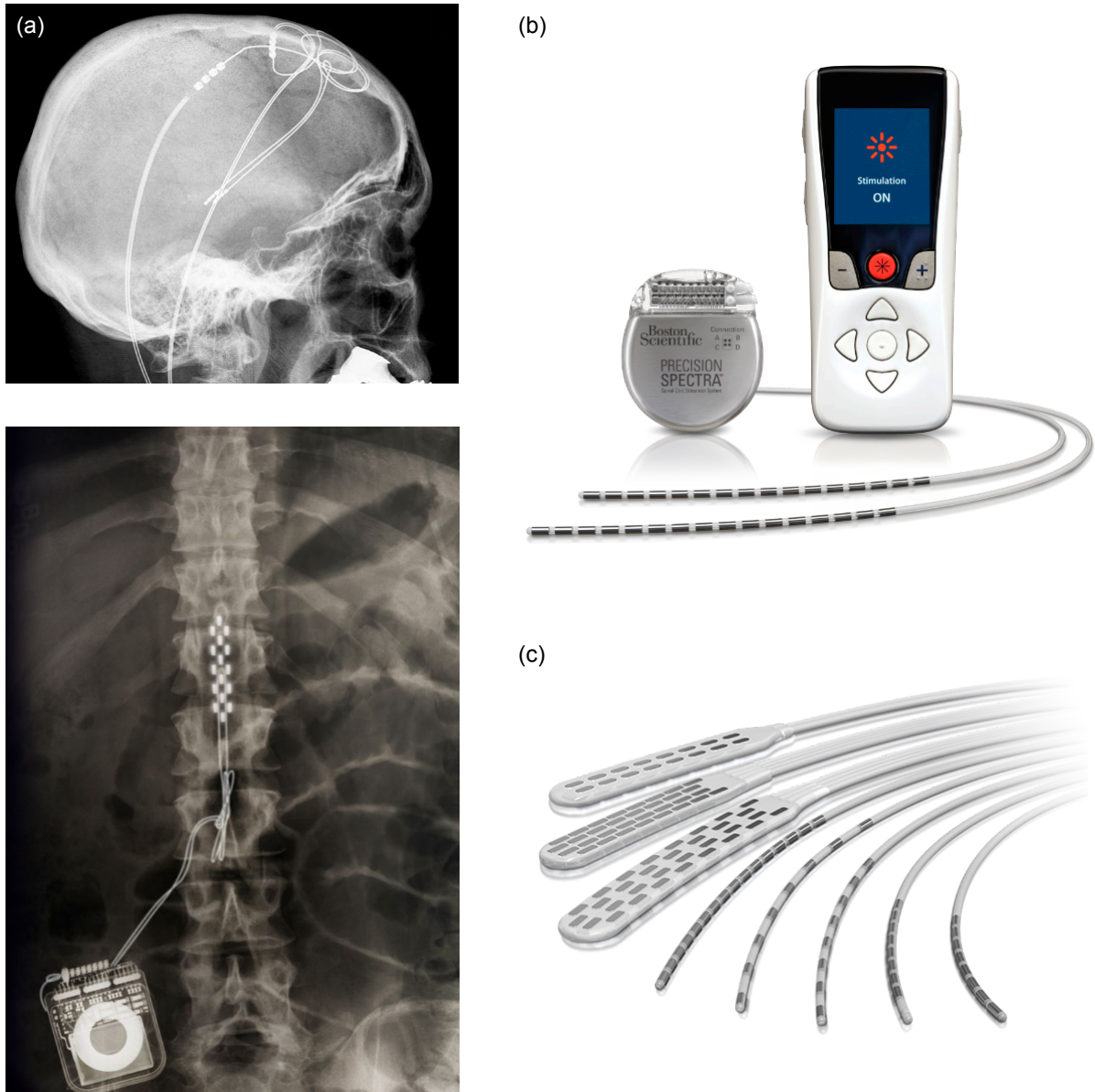


Fig. 1.14 A commercial electrical neuromodulation system, consisting of (a) a lead (top) or paddle type (bottom) implantable electrode (top is the electrode for deep brain stimulation and bottom is the electrode for spinal cord stimulation). (b) an IPG (left) connected to the lead, and a hand-held remote control for patients to adjust the device settings (right). (c) a close-up CAD rendering of different types of implantable electrodes. Image reproduced from [Adair (2017); Mconnell (2017); WadmanJun (2017); Whitehurst et al. (2005)].

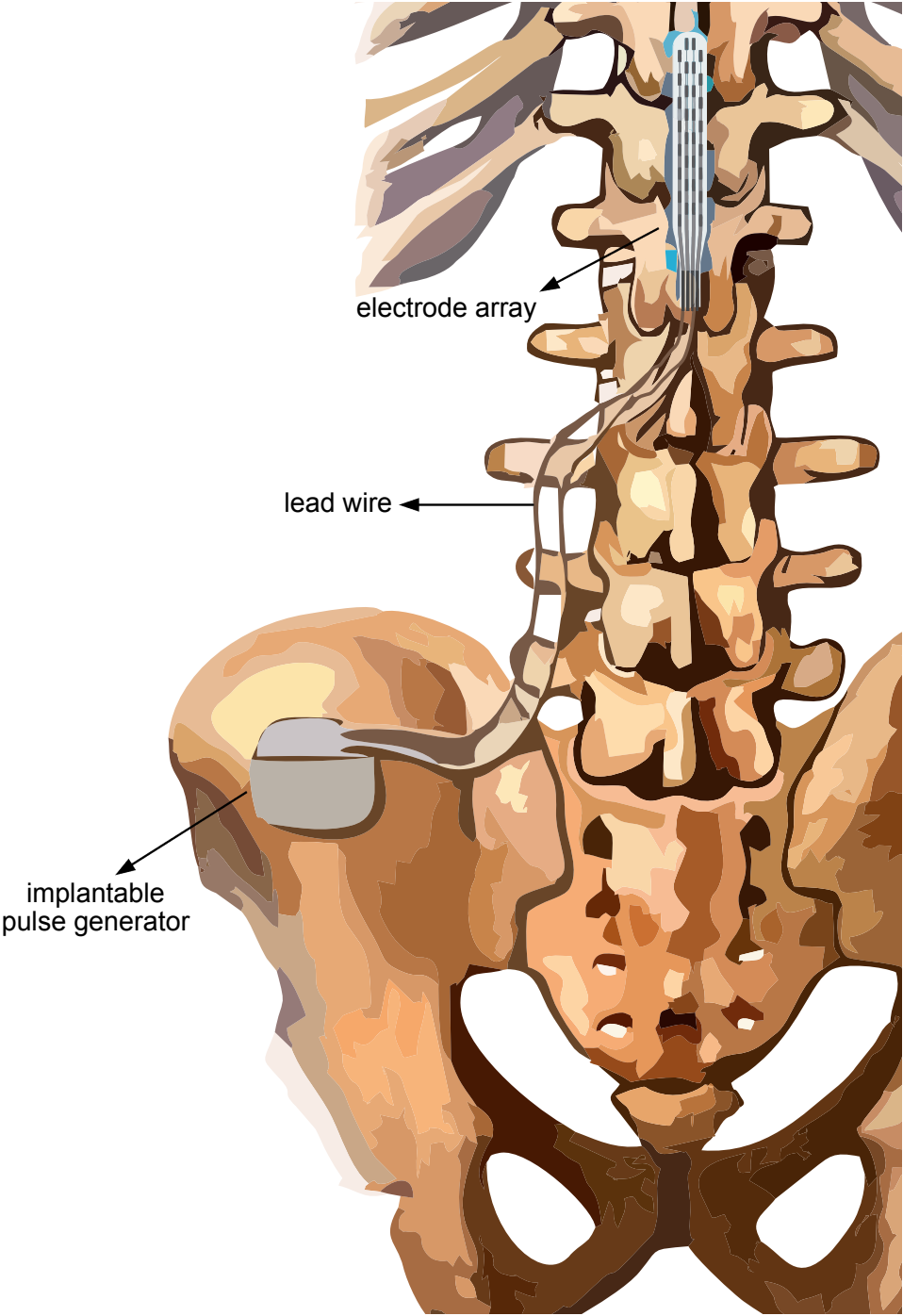


Fig. 1.15 An artistic rendering of a spinal cord stimulator implanted in the lower thoracic level. The complete device consists of an implantable pulse generator, generally located in the hip or back area, lead wires connecting the device, and a lead or paddle type electrode array interfacing with the spinal cord. Image adapted from [Nucleus (2018)].

1.7.1 Applications in pain management and motor control

For pain management applications, SCS is mainly used to manage neuropathic pains which are refractory to conventional treatments, such as failed back surgery syndrome or complex regional pain syndrome [Colloca et al. (2017); Kemler et al. (2000)]. But more recently, SCS devices have also been used to explore the possibility to improve motor control capabilities and treat movement disorders such as paralysis and freezing gait in Parkinson's patients [De Lima-Pardini et al. (2018); Samotus et al. (2018)]. Current state-of-the-art electrical stimulation techniques for improving motor control aim to stimulate the spinal cord dorsal column or afferent roots, when coupled with physiotherapy this approach has shown some promise in restoring motor function, especially in patients with paralysis below the waist [Courtine and Sofroniew (2019); Formento et al. (2018)].

1.7.2 Working principle of spinal cord stimulation

To modulate neural activities in the spinal cord, the electrode array would send out pulses of electrical currents, thus changing the electric potential in the epidural space near the implant. For both pain management and motor control, the paddle or lead shaped electrode array are placed near the physiological midline of the dorsal column (Except for the dorsal root ganglion stimulation where the lead is placed near the dorsal root ganglion [Deer et al. (2017)]). Figure 1.16(a) demonstrates the placement of a lead type electrode relative to the spinal cord dorsal column. As seen in Figure 1.16(a), when an electrical pulse is sent out by the lead, the membrane potential of adjacent excitable cells - such as axons in the dorsal column, can be perturbed by the applied electric potential. The change in axon membrane potential can therefore lead to action potential firing. As larger-diameter axons have lower activation threshold (lower external current necessary to elicit action potentials), larger axons such as the $A\beta$ sensory fibers can be preferentially activated with the applied pulse, therefore gating the pain transmission to the central nerve system.

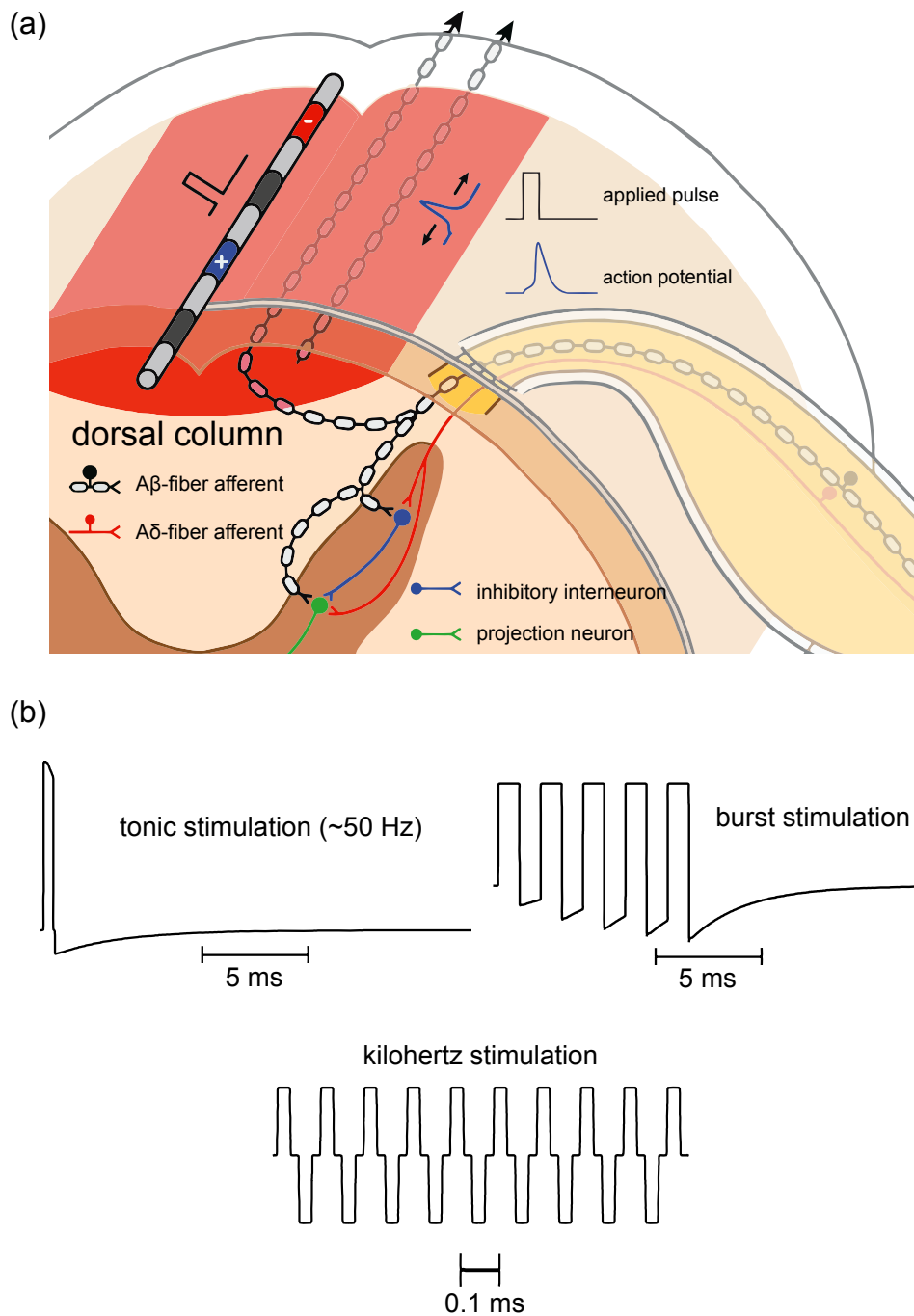


Fig. 1.16 (a) SCS placing at the midline of the dorsal column, eliciting action potentials propagating in the longitudinal direction of the spinal cord. (b) Common stimulation waveforms for spinal cord stimulations. Left: tonic stimulation, with $\approx 30 \mu\text{s}$ of pulses at a burst rate of 50-60 Hz. Right: burst stimulation, consisting of five-pulse train with 500 Hz of intra-burst frequency and burst rate of 40 Hz and bottom: kilohertz-frequency stimulation ($> 1 \text{ kHz}$). Schematics adapted from [Lempka and Patil (2018)].

1.7.3 Common stimulation waveforms for spinal cord stimulation

There are currently three common stimulation waveforms for SCS devices- tonic, burst, and kilohertz-frequency stimulation [Barchini et al. (2012); Crosby et al. (2015); Deer et al. (2018)] (Figure 1.16(b)). Tonic stimulation consists of short duration pulses ($\approx 30 \mu\text{s}$) firing at a relatively low-frequency (50-60 Hz) [Tang et al. (2014)]. Burst stimulation employs a pulse train of 5-6 pulses with duration of $\approx 2 \text{ ms}$ each, after the pulse train the current is switched off to allow passive recharge [Kapural et al. (2015)]. Kilohertz-frequency stimulation, as the name suggests, employs a high frequency AC current as the stimulation waveform ($f > 1 \text{ kHz}$).

Despite differences in stimulation patterns and mechanism of actions, the common limitations of these stimulation waveforms are the lack of specificity and spatial resolution. Based on previous computational studies, Figure 1.17 demonstrates the areas activated by the spinal cord stimulator with existing stimulation waveforms [Lempka et al. (2015); Zander et al. (2020)]. Since the spinal cord stimulator is implanted in the midline of the dorsal column (Figure 1.17(a), left), when supplying electrical stimulation, existing stimulation protocols continue to rely on dorsal column stimulation. The electric potential profile along the spinal cord cross-section when subjected to electrical stimulation is a layer-by-layer structure, as electric potential gradually decreases farther away from the electrode (Electric potential distribution shown in Figure 1.17(a), right).

For electrical neuromodulation such as the spinal cord stimulation, axons in the spinal cord are deemed activated, if the change in membrane potential due to electrical stimulation is large enough to elicit action potentials. As a result, when the spinal cord stimulator creates a layered electrical potential distribution, the area of axons being activated within the spinal cord follows this layer-by-layer distribution. Figure 1.17(b) and Figure 1.17(c) show the excitation current amplitude necessary to activate the axons in different layers for tonic and kilohertz-frequency stimulation, respectively. As seen from the axon-activation profile, existing stimulation waveforms are unable to localize the stimulated region. Moreover, if the targeted stimulation location lies in the deeper regions of the spinal cord, surface regions closer to the electrode would also be stimulated.

1.7.4 Limitations of existing spinal cord stimulation technologies

The lack of specificity and spatial resolution bring two main challenges to further improve the performance of spinal cord stimulation and the patient comfort. First is that for some patients

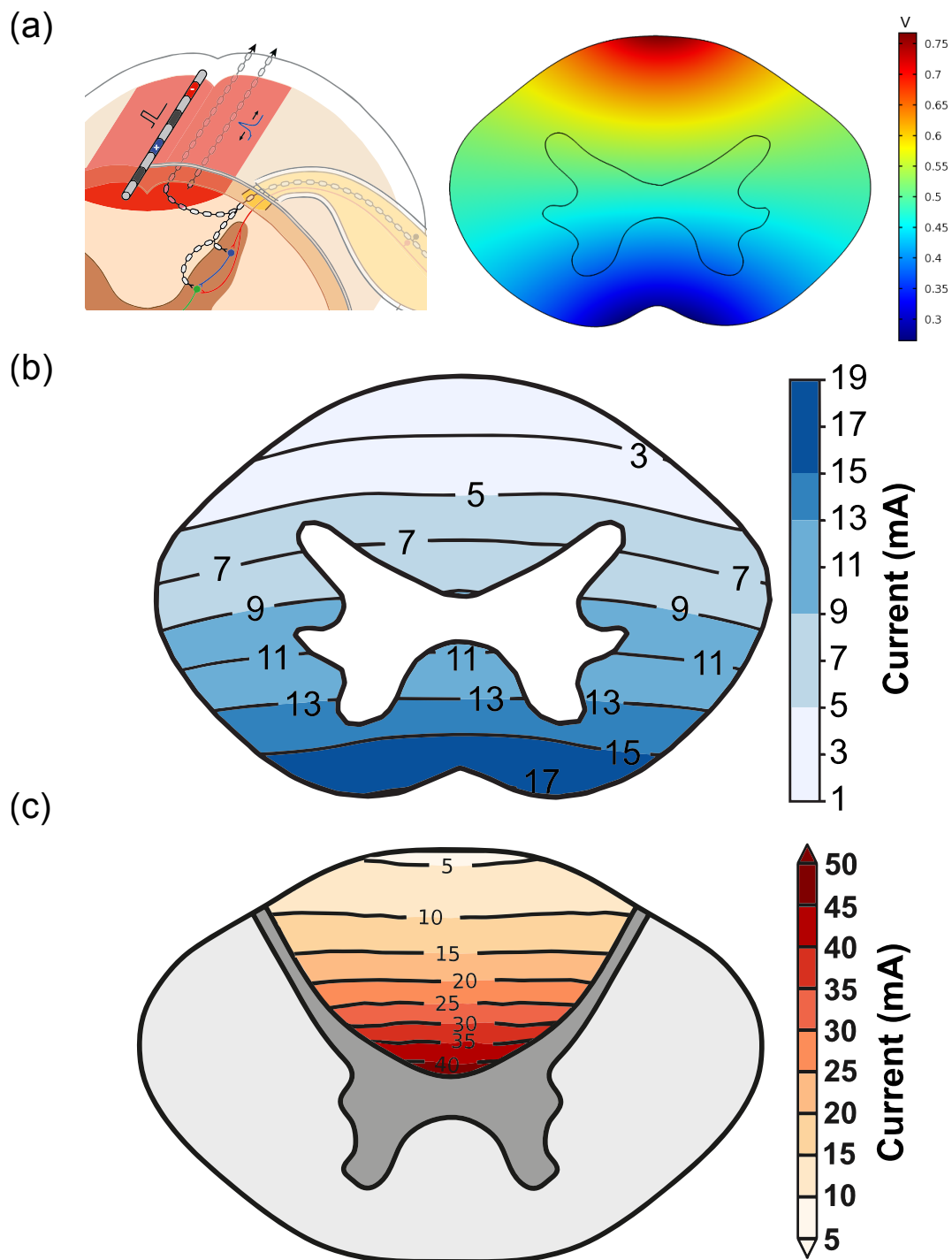


Fig. 1.17 (a) SCS placing at the midline of the dorsal column (left), and the relative isopotential contour in the spinal cord cross-section upon applying a 2V pulse (right). Computational studies of axon activation threshold, defined as the minimum current supplied by the SCS device necessary to elicit action potentials for (b) tonic stimulation and (c) kilo-hertz stimulation, both showing layered structure for dorsal column SCS placement. Figures adapted from (a) left: Lempka and Patil (2018), (b) Zander et al. (2020) and (c) Lempka et al. (2015).

where stronger stimulation intensity is needed, the non-localized stimulation can negatively affect the gait balance and proprioception of patients by accidentally triggering other regions of the spinal cord tracts [Rijken et al. (2013); Yozu et al. (2016)].

Furthermore, current spinal cord stimulation devices with paddle or lead-shape electrodes are unable to re-focus the stimulation hotspot once it is displaced [Mekhail et al. (2011)]. The most common complication for spinal cord stimulation surgery is lead migration, as a result of variation in intracranial pressure or external impact. Long-term lead displacement will result in reduction of electrical stimulation intensity to the intended regions [McGreevy et al. (2012)]. As a consequence, this will present a potential loss in effectiveness for long-term implanted spinal cord stimulators.

Currently, lead migration or unintended axon activation often requires surgical intervention, since the spinal cord stimulation device is unable to localize or re-focus its stimulation hotspot, given the device geometries and stimulation waveforms. Novel approaches such as using penetrating intraspinal electrodes can achieve sub-mm² hotspot, and also greatly reduce the risk of lead migration [Holinski et al. (2016); Moritz et al. (2007)]. However, this approach involves greater risks of infections and dural punctures [Barolat (1993)], and is therefore not being actively pursued for clinical applications.

In this thesis, a localized and steerable spinal cord stimulation is developed and validated with computational modeling and *in vitro* measurements. The challenge of localized neuromodulation is addressed by employing amplitude modulated (AM) signals as stimulation waveforms. Broadly utilized in telecommunication applications to transmit radio signals, the use of AM stimulations have recently been explored for sub-surface region neuromodulation such as deep brain stimulation. In **Chapter 5**, the working principle of amplitude modulated signals in neuromodulation is presented, and a coupled FEM-Neuron computational model is developed to reveal the nonlinear relationship between external electrical stimulation and spatial axonal response. Optimization of stimulation parameters were carried out to further improve the performance of the spinal cord stimulation method developed in this thesis.

1.8 Thesis chapter overview

The thesis focuses on using computational models to provide understanding of emerging neuromodulation devices. These understandings can be used to develop devices with better performance, higher reliability, and greater level of safety. The major contributions of each chapter are as follow:

- Chapter 2 introduces the computational model for an electrophoretic drug delivery device (microfluidic ion pump). The important performance indices are identified, and design guidelines for ion pumps used in different applications is presented based on the computational model.
- Chapter 3 introduces the concept of co-ion engineering to reduce drug leakage from an electrophoretic drug devices. Computational modeling and experimental work demonstrate how the choice of co-ion can reduce drug diffusion. The method developed is applicable to existing electrophoretic drug delivery applications, and more importantly, co-ion engineering does not affect the device active performance.
- Chapter 4 introduces a split electrode design and optimal switching scheme for electrophoretic drug delivery devices to increase the electrophoretic delivery rate. Theoretical predictions were compared with simulation and experimental work to provide practical limits of the electrode design method. Further improvements can be made with device geometry optimizations.
- Chapter 5 presents a localized and steerable spinal cord stimulation device and stimulation protocol using temporal interfering fields. The working principle of temporal interfering is introduced, and a coupled computational model combining FEM and neural circuits in the spinal cord is developed to reveal the nonlinear relationship between electrical stimulation and spinal cord stimulation. Parameter studies were carried out to further understand how to optimize the device performance and extend the use of temporal interfering stimulation to other electrical neuromodulation applications.
- Chapter 6 concludes the findings from this thesis, and provide directions for future work.

Chapter 2

Materials and device considerations in electrophoretic drug delivery devices

Abstract

Electrophoretic drug delivery devices are able to deliver drugs with exceptional temporal and spatial precision. This technology has emerged as a promising platform for treating pathologies ranging from neuropathic pain to epilepsy. As the range of applications continues to expand, there is an urgent need to understand the underlying physics and estimate materials and device parameters for optimal performance. In this chapter, the device physics of an electrophoretic drug delivery device is investigated with computational modeling. Three critical performance indices, namely, the amount of drug transported, the pumping efficiency and the ON/OFF ratio are investigated as a function of initial drug concentration in the device and fixed charge concentration in the ion exchange membrane. The results shown in this chapter is able to provide guidelines for future materials and device design with an eye towards tailoring device performance to match disease-specific demands. ¹

¹This chapter is based closely on previously published work: "Materials and Device Considerations in Electrophoretic Drug Delivery Devices," by Shao-Tuan Chen, Christopher M. Proctor, and George G. Malliaras in Scientific Reports 10.1 (2020) <https://doi.org/10.1038/s41598-020-64114-0>.

2.1 Introduction

Neurological disorders affect over 6% of the world population and cause major economic losses. Existing treatments for these disorders are often ineffective, as systemic drug administration to the central nervous system (CNS) is impeded by the blood-brain-barrier [Löscher and Potschka (2005)]. Localized drug delivery methods such as convection-enhanced delivery devices (CED) can bypass this physiological barrier by infusing drug solution directly to the targeted area under high pressure with a catheter [Bobo et al. (1994)]. However, CED causes pressure increase in the targeted areas, leading to edema and disruption of adjacent neural networks [Suzuki and Yoneyama (2003)]. Electrophoretic drug delivery devices have shown promise for a variety of eventual clinical applications in the treatment of neuropathic pain [Jonsson et al. (2015)] and epilepsy [Proctor et al. (2018)]. In these devices, drug ions are transported by electrophoresis from an internal source reservoir through an ion exchange membrane into the targeted treatment area. The device can be implanted in the targeted area, therefore bypassing the blood-brain barrier. Also, due to the ion exchange membrane, electrophoretic drug delivery devices offer the benefit of “dry” delivery as they transport only the drug without the solvent, avoiding the possibility of pressure buildup and edema in the targeted area. A key consideration for any localized drug delivery technology is the need to tailor performance to the targeted disease.

For instance, the treatment protocol for epilepsy might involve a chronic implantation for the delivery of small bursts of drugs before seizures, followed by extended periods of no drug delivery. However, for disease such as brain cancer, the treatment might involve a single dose delivered over a rather short period in an acute setting. Tailoring the performance of electrophoretic drug delivery devices to meet these varied demands however requires a deeper understanding of the device physics and trade-off between materials and device parameters. To date, our understanding of ion exchange membranes, the most critical component in an electrophoretic drug delivery device, is largely based on the research from water desalination and filtration communities [Tanaka (2015), Luo et al. (2018)]. However, there are significant differences in the operating voltage and ion concentration in the source reservoir between a typical water filtration plant and a drug delivery device. The dimensions of the source reservoir are also scaled down from meter-range for the industrialized filtration plant to micrometer-range for microfluidic-based drug delivery devices. This difference in scale accentuates physical phenomena at microscale, such as concentration polarization [Porter (1972)] and capacitive charging of electrodes [Bazant et al. (2004)]. The above reasons necessitate further investigation of ion exchange membranes in the context of electrophoretic drug delivery devices and biological interfacing.

In this chapter, a computational model is developed for electrophoretic drug delivery devices based on ion transport in a typical device geometry and using appropriate initial and boundary conditions. The computational model is further used to characterize these devices operating under different operating conditions. Three primary performance indices that describe the drug delivery process are investigated, namely, the amount of drug transported, the pumping efficiency, and the ON/OFF ratio. The results from this chapter provide insight into how membrane properties and initial drug concentration affect the delivery process and therefore inform future device design and materials development.

2.2 Computational model for the electrophoretic delivery device

The electrophoretic drug delivery device being investigated here consists of three main components: the source reservoir loaded with drug solution, an ion exchange membrane (IEM) and a target electrolyte (Figure 2.1). Metal electrodes in the source and target form the plates of a capacitor. The electrophoretic drug delivery device is represented with a one-dimensional model, and the corresponding governing equations were solved with finite-element based simulation software [COMSOL (2018)].

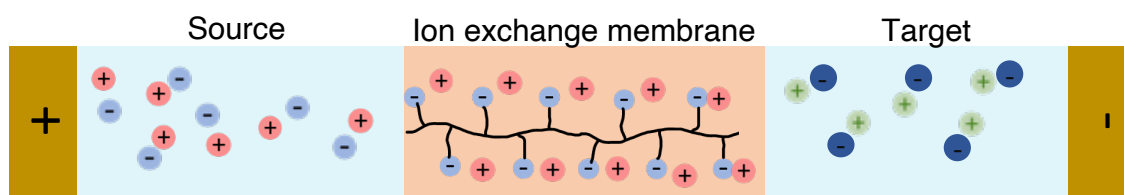


Fig. 2.1 A schematic showing the components of the computational model (not to scale): source and target solutions, ion exchange membrane and capacitive electrodes.

The motion of charged ions is described by the Nernst-Planck equation and combined with Poisson's equation, which relates the charge density to the external applied electric field, forms

the governing equations for the computational model of the device. The governing equations of the computational model is described as below:

Let subscript i represent the i^{th} ion in the system. The general form of the Nernst-Planck equation describing the concentration gradient of the i^{th} species is written as:

$$\frac{\partial c_i}{\partial t} = \nabla \cdot j_i, \quad (2.1)$$

where c is the concentration, t represents time and j is the magnitude of the ionic flux. The ionic flux j_i subjected to diffusion and electromigration can be also written as:

$$j_i = - \left[D_i \nabla c_i + \frac{D_i z_i e}{k_B T} c \nabla \phi \right], \quad (2.2)$$

where D represents the ionic diffusivity, z represents the valence of the ion, e is the elementary charge, k_B is the Boltzmann constant, T represents temperature, and ϕ is the voltage. The Poisson's equation relates the charge density ρ to the resulting electric field E by:

$$\nabla \cdot E = \frac{\rho}{\epsilon}, \quad (2.3)$$

where ϵ is the dielectric constant, and relationship between electric field E and potential ϕ is given by:

$$E = -\nabla \phi. \quad (2.4)$$

The computation domain consists of source and target solutions both of which have a length L of $100 \mu\text{m}$, separated by an IEM with width L_m of $10 \mu\text{m}$, consistent with experimentally reported values for the dimensions of a microfluidic ion pump [Jonsson et al. (2015), Proctor et al. (2018), Uguz et al. (2017)]. As for the boundary condition, the electrodes are considered to be blocking towards ions, while no additional restrictions on the flow of ions are imposed the source/IEM and IEM target interfaces. A list of variables used in this study can be found in Table 2.1.

Table 2.1 List of variables used in this study

Variables	Description
L	Channel length, $100\ \mu\text{m}$
L_m	Ion exchange membrane thickness, $10\ \mu\text{m}$
V_0	Applied voltage, $0.5\ \text{V}$
C_D	Initial drug concentration in the microfluidic ion pump, $1\text{-}1000\ \text{mM}$
C_{IM}	Fixed charge concentration in the ion exchange membrane, $0.01\text{-}10\ \text{M}$
μ_D	Ion mobility of drug, $5 \times 10^{-11}\ \text{m}^2/\text{s}$
η	Pumping efficiency
Q	Transported drugs, nmol

2.3 Transient behavior of an electrophoretic drug delivery device

At $t = 0$, the source reservoir is filled with cationic drugs and co-ions of the same initial concentration, i.e., $C_D = C_{Co}$. The immobilized charge groups in the IEM for this study are negatively charged, making the IEM a cation selective membrane. For different initial drug concentration C_D and different fixed charge concentration C_{IM} , the mobility μ for both the drug and co-ion in solution were set to be $\mu_D = \mu_{Co} = 5 \times 10^{-11}\ \text{m}^2/\text{s}$, consistent with previously reported values for common neurotransmitters [Tybrandt (2017)]. In the IEM, all fixed charge groups are initially compensated by the cationic drug at $t = 0$, i.e., the initial drug concentration in the membrane is equal to C_{IM} . The mobility of ions in the IEM is set to be 10% of their respective values compared to the mobility of these ions in solution, consistent with previously reported values [Tanaka (2015), Volkov et al. (2014)]. Finally, the target is taken to be a $160\ \text{mM}$ NaCl solution to mimic physiological conditions.

As a starting point, the computational model is employed to understand the spatial distribution of drug concentration and voltage in the device. Figure 2.2 shows drug concentration

and voltage profiles for an applied potential of 0.5 V with $C_D = 200$ mM and $C_{IM} = 2$ M at 20 s. The drug concentration in the source is observed to be stable for roughly half the length of the reservoir before decreasing closer to the IEM. This concentration gradient is caused by concentration polarization [Porter (1972)], as co-ions in the source reservoir are driven away from the IEM and counter ions (drug) follow the same concentration profile to maintain electroneutrality. The depletion zone describes the region adjacent to the IEM which is affected by concentration polarization. Within the depletion zone, the driving force for the drug from both applied potential and concentration gradient will drive the cationic drug towards the IEM. Concentration polarization also causes the influx of drug from the source to the IEM to be higher than the influx of drug from the IEM to the target, resulting in a drug concentration gradient opposite to the concentration gradient in the source. After the drug is delivered to the target, it moves away from the IEM, driven by both the concentration gradient and the applied potential.

The potential drop in the device shown in the bottom of Figure 2.2 is from a combination of ohmic drop due to electrolyte resistance and Donnan potential at solution/IEM interfaces [Donnan (1924)]. Between the electrodes, the potential drop is determined by ionic resistance, therefore the electrolyte potential gradually drops along the source to target direction. At the source/IEM and IEM/target interfaces, the potential drop is due to the Donnan potential [Donnan (1924)], which arises from ion concentration differences. The Donnan potential causes the negatively charged ions in the electrolyte to be electrostatically blocked from entering the IEM, known as the Donnan exclusion effect.

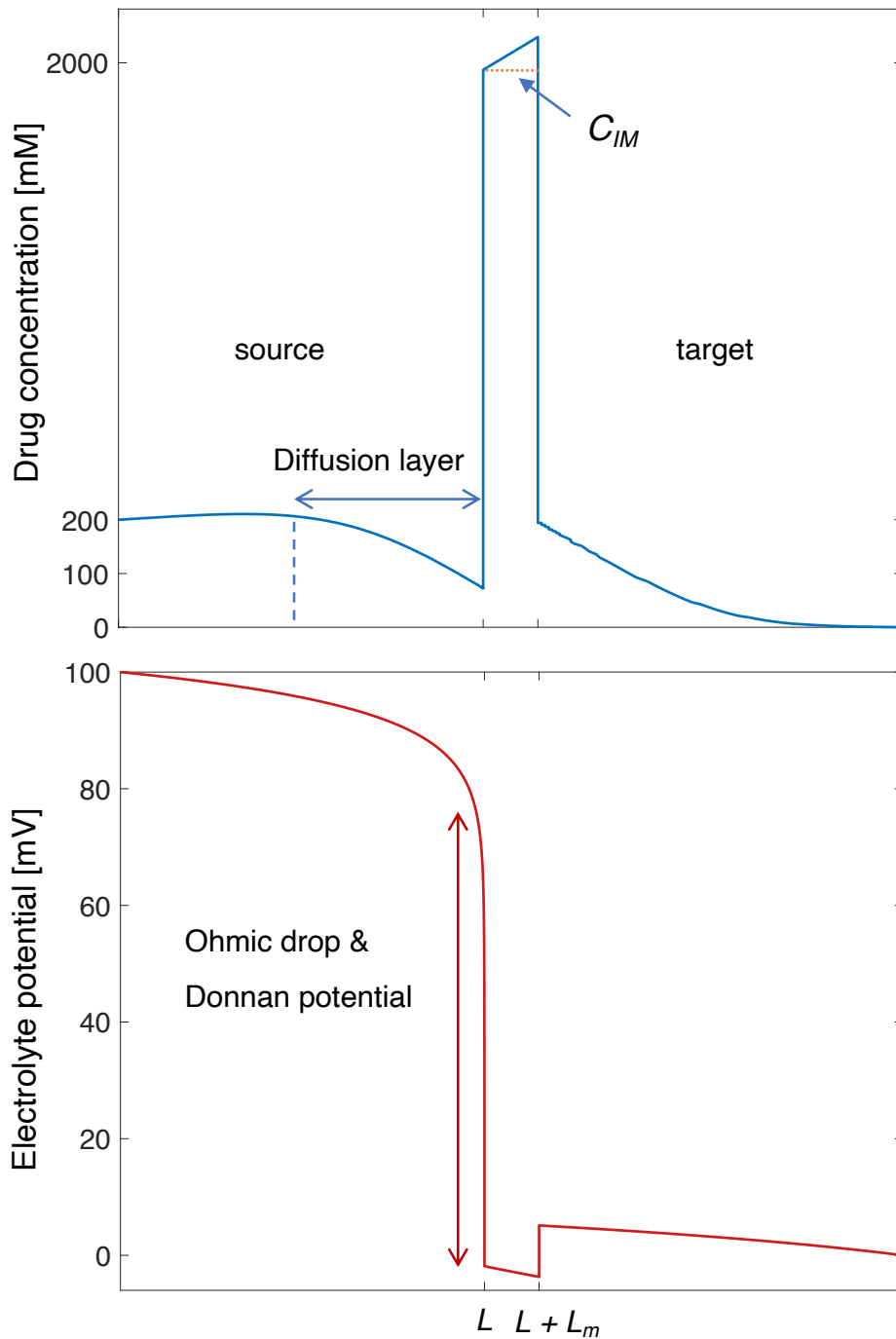


Fig. 2.2 Snapshots of drug concentration (top) and voltage (bottom) profiles at $t = 20$ s. Initial drug concentration C_D is 200 mM, and fixed charge concentration C_{IM} is 2 M. Reservoir length $L = 100 \mu\text{m}$ and membrane thickness $L_m = 10 \mu\text{m}$.

2.4 Performance indices for electrophoretic drug delivery devices

For an electrophoretic drug delivery device, a critical performance index is the total amount of drug the device can deliver upon application of a voltage. One would like to control this quantity as some applications require bursts of high dosage, while other needs low and sustained delivery. The pumping efficiency η , defined as the ratio between drug transport over the total amount of ions transported, is another important quantity. Despite the selectivity of ion exchange membranes, co-ions in the source reservoir and ions in the target may still be driven by the electric field concentration gradient, thus passing through the IEM, so η is not necessarily equal to one [Ji et al. (2018)]. Lastly, the ability to resist passive leakage for electrophoretic drug delivery devices is characterized by the ON/OFF ratio, which is defined as the ratio of amount of transported drug between active pumping (voltage on) and passive diffusion (voltage off). Poor control of passive diffusion can lead to chronic sub-therapeutic levels of drug, which is not desirable.

The capacitive charging in the electrodes will gradually screen out the applied voltage. Therefore, the response time for capacitive charging will determine the active pumping time for an electrophoretic drug delivery device. The amount of drug transported (Q) by an electrophoretic drug delivery device was obtained by integrating the influx to obtain Q as a function of time. To avoid numerical noise caused by discontinuities at the interface between the IEM and target [Verfürth (2013)], we performed numerical integration on influx of drug transported to target at a short distance ($20\ \mu\text{m}$) away from the IEM/target interface to calculate Q .

The temporal response of an electrophoretic drug delivery device is shown in Figure 2.3. The voltage (0.5 V) is applied at $t = 0$, and the electric field is gradually screened out by capacitive charging leading to a saturation in the net transported drug after a few hundred seconds. The total amount of drug transported at steady-state (defined as Q at $t = 1000\text{ s}$) increases with C_D , as the concentration gradient at the source reservoir is steeper for higher C_D . Before the electrodes are fully charged, the instantaneous drug delivery, represented by the slopes of the curve in Figure 2.3, is also higher with higher C_D . Figure 2.4 shows the amount of drug delivered Q as a function of time for different C_{IM} with $C_D = 50\text{ mM}$. When the fixed charge concentration C_{IM} in the membrane is increased, the number of sites in the IEM available to attract the drug increases (i.e. increased ion exchange capacity [Kamcev et al. (2017a)]) leading to an increase in the flux of drug from source to target. This suggests that

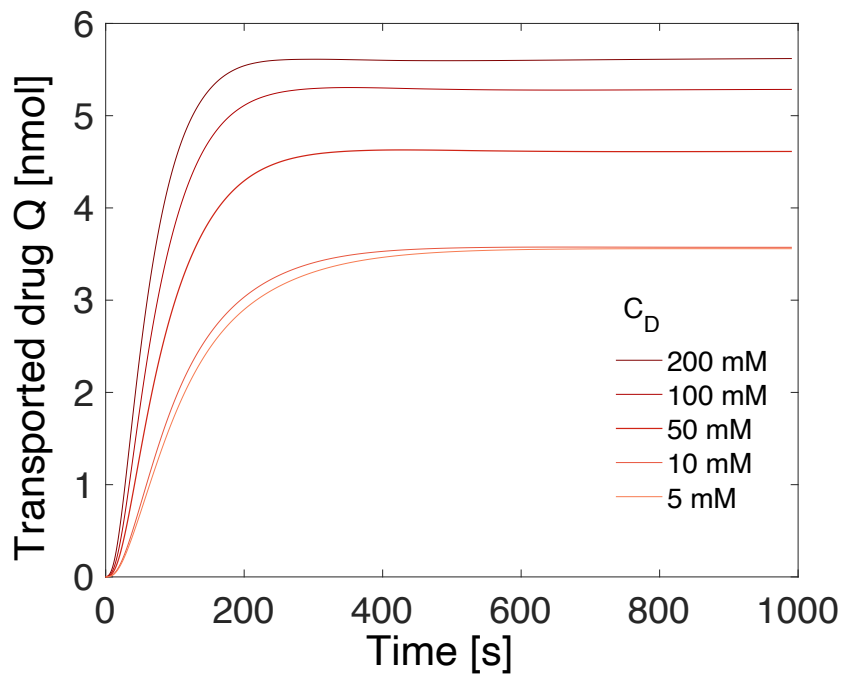


Fig. 2.3 Transported drug Q as a function of time with various initial drug concentration C_D where $C_{IM} = 2M$.

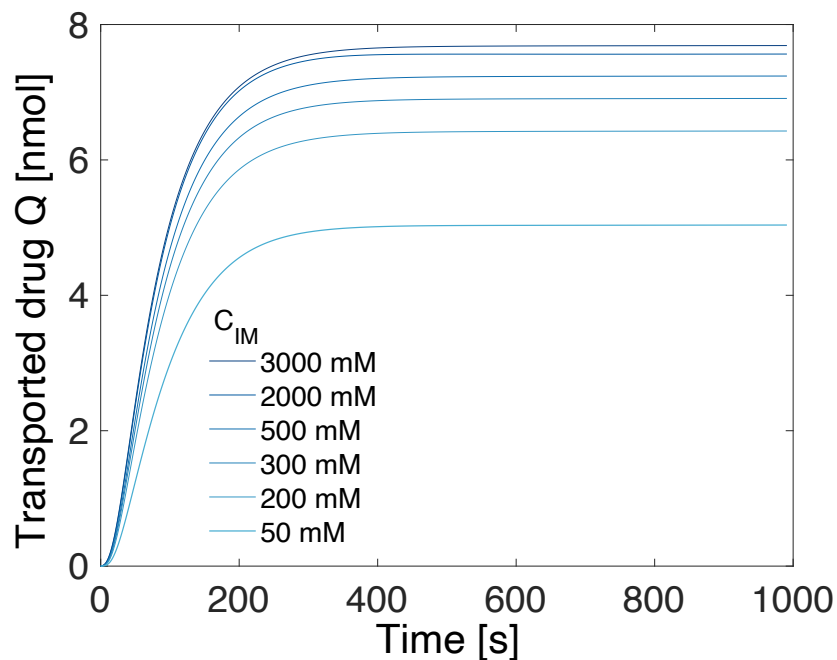


Fig. 2.4 Transported drug Q as a function of time with various fixed charge concentration C_{IM} in the IEM, where $C_D = 50mM$.

developing IEM materials with a higher C_{IM} could be a viable path forward to increasing drug delivery capacity.

In previous studies, the ON/OFF ratio for devices has been reported as a single value at discrete time-points, where ON/OFF ratio is acquired experimentally by comparing the transported drug with and without an applied voltage for a given duration [Uguz et al. (2017), Isaksson et al. (2007), Tybrandt et al. (2009), Jonsson et al. (2016)], or theoretically by performing steady-state calculations with a numerical model [Tybrandt (2017)]. However, the transient response of the ON/OFF ratio in a device with capacitive electrodes has not been explored. By calculating the amount of drug transported between active pumping and passive diffusion, the transient ON/OFF ratio dependence on applied voltage can be captured with the computational model.

For active pumping, the maximum flux of drug occurs at the start upon applying a voltage and gradually decreases thereafter, due to capacitive charging of the electrodes. In contrast, in the OFF state, the driving force is the steep concentration gradient at the IEM/target interface. Since no potential is applied during the OFF state, the concentration in the IEM remains nearly constant during passive diffusion, and the variation of concentration gradient is negligible at the IEM/target interface. As a result, the passive diffusion process when the device is switched off can be treated as ion diffusion with constant permeability through an ion exchange membrane.

Figure 2.5 demonstrates the amount of transported drug Q between when the device is switched ON and OFF, and Figure 2.6 shows the corresponding transient ON/OFF ratio of an electrophoretic drug delivery device. The initial concentrations of C_D and C_{IM} for Figure 2.5 and 2.6 are similar to previously reported values when delivering GABA for seizure control 11 with $C_D = 20$ mM and $C_{IM} = 400$ mM. From 0-100 s, the ON/OFF ratio starts at around 40000 and quickly decreases as the capacitive charging of the electrodes screen out the applied potential. After the applied potential is fully screened out, passive diffusion dominates for both ON and OFF scenarios, and the ON/OFF ratio finally decays to around 120 at $t = 800$ s.

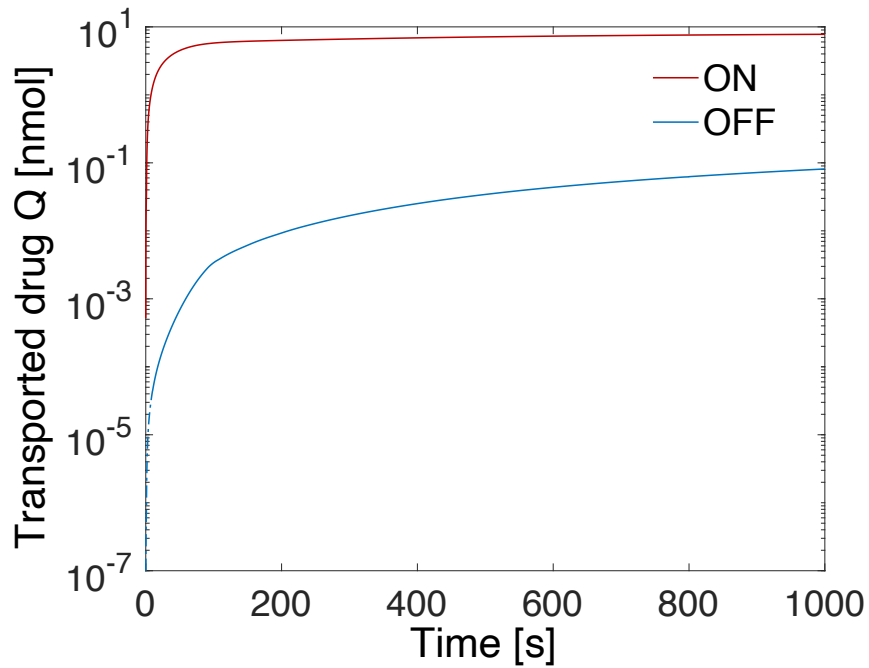


Fig. 2.5 Comparison between amount of drug delivered by active pumping and passive diffusion with $C_D = 20$ mM and $C_{IM} = 400$ mM. Due to numerical noise in the simulation, the first 5 seconds of the passive leakage data are extrapolated with exponential regression.

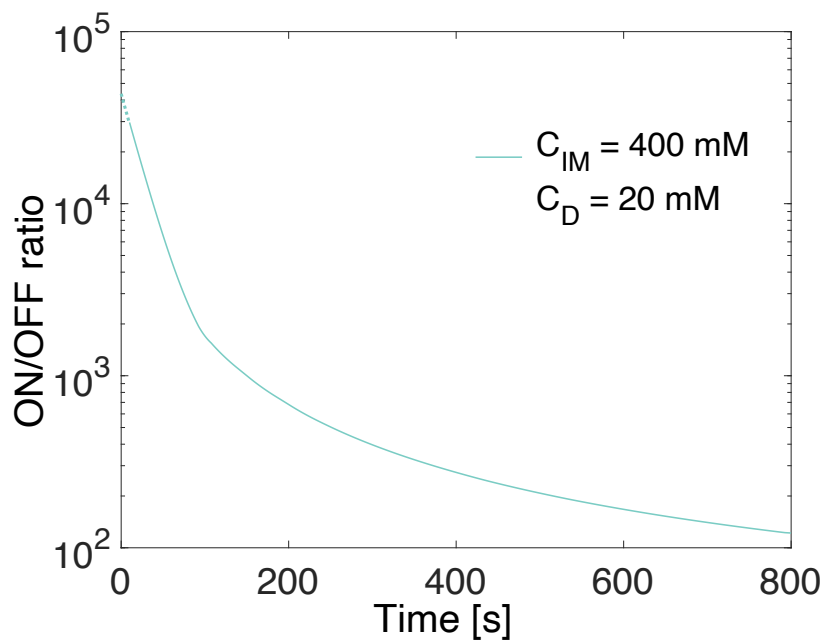


Fig. 2.6 Resulting transient ON/OFF ratio from Fig 2.5 as a function of time for an electrophoretic drug delivery device

The above results demonstrate that capacitive charging of the electrodes dominates the temporal characteristics of electrophoretic drug delivery devices. However, the outcome at the end of the capacitive charging of the electrodes (steady-state) is also of interest, as it can inform applicability to different treatment scenarios.

The steady-state performance index contour plots are shown in Figure 2.7, Figure 2.8 and Figure 2.9. Both the initial drug concentration C_D and the fixed charge concentration in the IEM C_{IM} were varied by three orders of magnitude (with C_D ranging from 1 mM to 1 M, and C_{IM} ranging from 10 mM to 10 M), a parameter space that is larger than in previous studies [Proctor et al. (2018), Peighambaroust et al. (2010), Proctor et al. (2019b)]. The contour plot for Q in Figure 2.7 shows that the maximum is obtained for the highest values of initial drug concentration C_D and fixed charge concentration C_{IM} in the IEM. Increasing these concentrations reduces the ionic resistance of the electrolyte. For weak electrolytes, the ionic resistance can be approximated as inversely proportional to square root of electrolyte concentration [Xing et al. (2013)]. As a result, increasing the concentration C_D or C_{IM} by 2 orders of magnitude should increase the amount of transported drug Q by 10-fold. However, reducing the resistance for the target and ion exchange membrane would also lead to a shorter pumping time for the device before the capacitive electrodes are fully charged [Kohlrausch (2016)]. As a result, increasing C_D and C_{IM} would increase the initial drug transport but reduce the active pumping time for an electrophoretic drug delivery device. Therefore, as depicted in Figure 2.7, by increasing C_D and C_{IM} for a span of 3 orders of magnitude, the amount of transported drug at steady-state can only be increased by 6-fold.

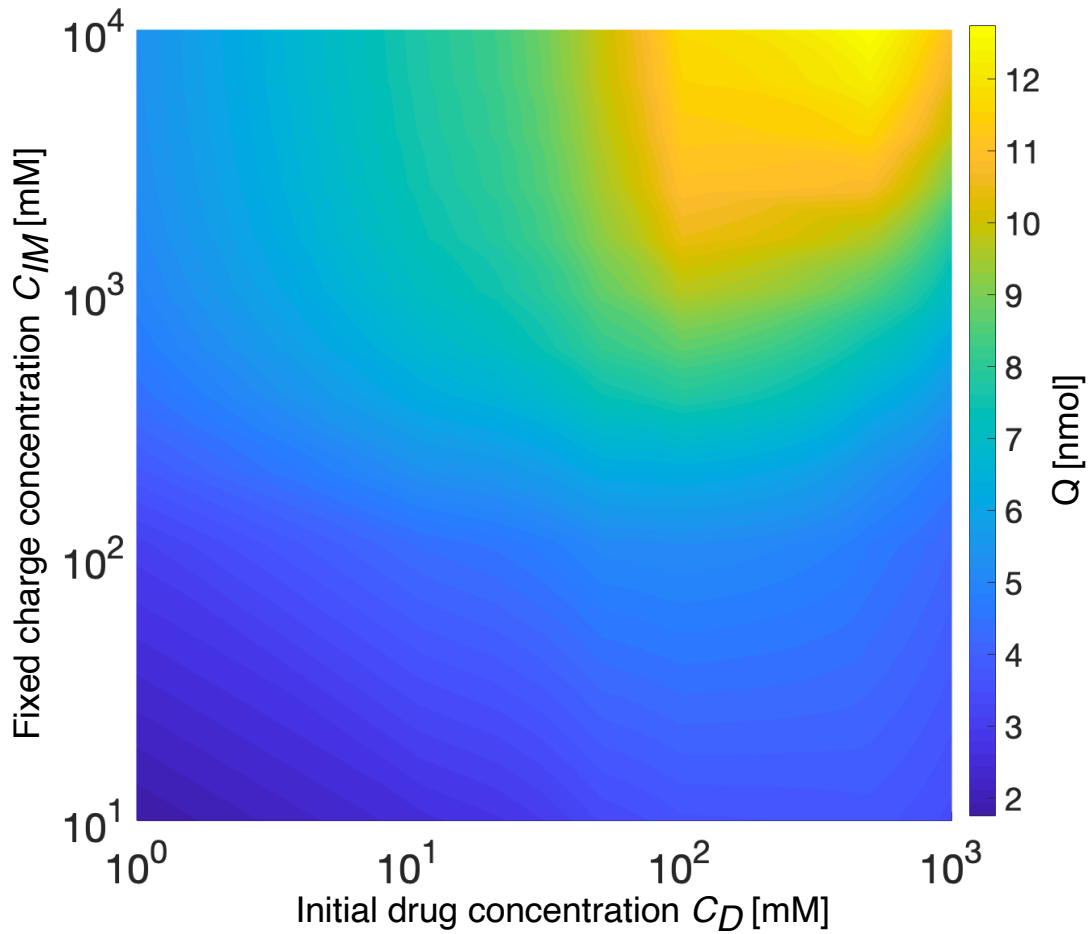


Fig. 2.7 Contour plot of amount of drug transported Q at steady-state as functions of both C_D and C_{IM} , both varying by three orders of magnitude.

Figure 2.8 shows the contour plot for pumping efficiency η as a function of C_D and C_{IM} . For different initial drug concentration C_D , η increases with C_{IM} . When the concentration ratio between C_{IM} to C_D increases, the Donnan potential between the electrolyte and IEM increases. As a result, the increased repulsive force between co-ions and the fixed charged ions in the IEM leads to higher degree of exclusion of co-ions (Donnan exclusion), and also a higher pumping efficiency η for the electrophoretic drug delivery device. Previous research into IEMs has shown that membrane selectivity generally exceeds 0.9 when the fixed ion concentration is at least ten times the electrolyte concentration [Teorell (1935)]. The simulation results here indicate that a similar trend holds true in terms of pumping efficiency η for electrophoretic drug delivery devices in the case that C_D is at least 10 mM (see dashed line). However, Figure 2.8 also shows this rule of thumb starts to break down at lower source concentrations ($C_D < 10$ mM), with nearly 100-fold greater C_{IM} required to approach pumping efficiencies

> 0.9 . This can be understood by considering the comparatively high concentration of Cl^- on the target side (160 mM) is not adequately blocked by the IEM for $C_{IM} < 100 \text{ mM}$, and therefore an increasingly significant portion of the ionic current across the IEM is attributable to Cl^- flowing from target to source when the device is during operation.

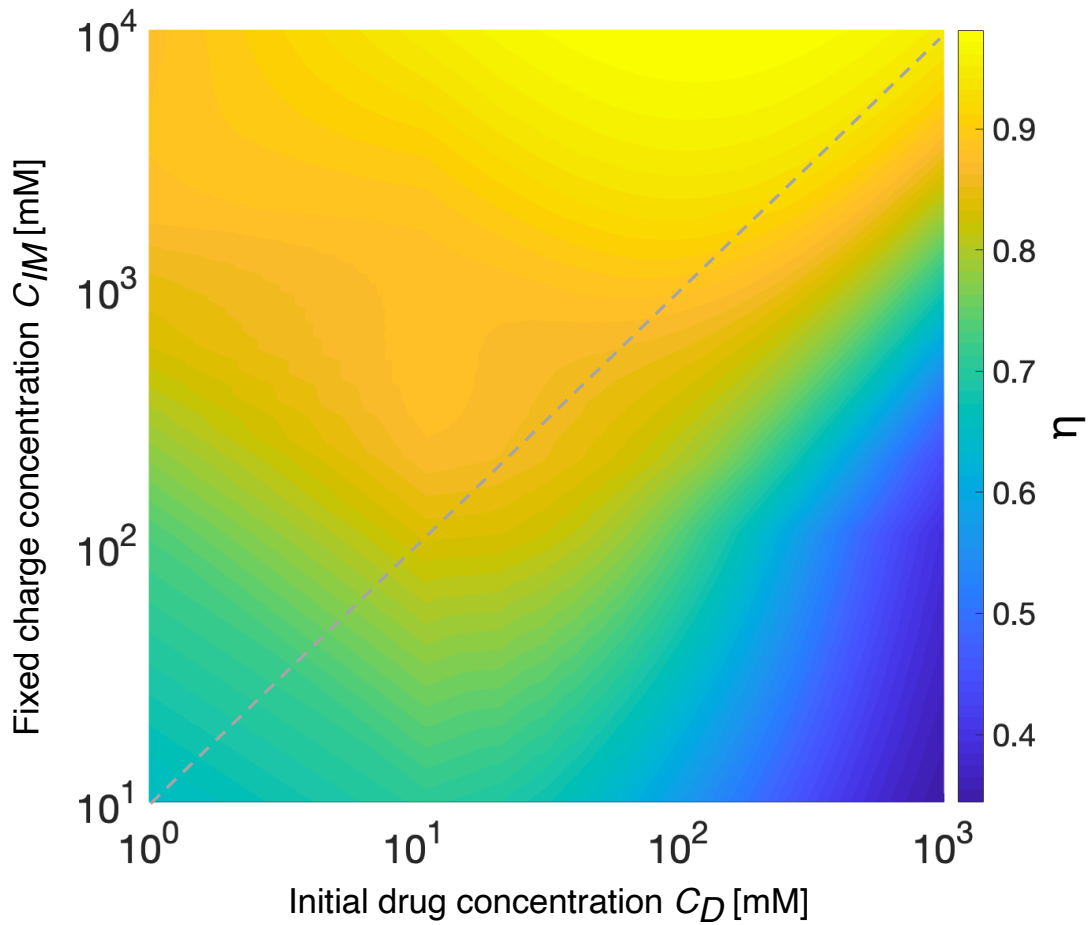


Fig. 2.8 Contour plot of amount of pumping efficiency η at steady-state as functions of both C_D and C_{IM} , both varying by three orders of magnitude.

The ON/OFF ratio contour plot of the device at steady-state is shown in Figure 2.9. It is found that the ON/OFF ratio is very sensitive to changes in initial drug concentration C_D , as the ON/OFF ratio at steady-state is higher than 1000 when C_D is lower than 5 mM. For C_D between 10 – 100 mM, the ON/OFF ratio is around 102, and the ON/OFF ratio decreases to around 10 when we increase C_D to 1 M. The ON/OFF ratio at steady-state ($t = 1000 \text{ s}$) is consistent with previously reported values for devices with IEM of similar thickness [Proctor

et al. (2018), Uguz et al. (2017)]. Devices with thicker ion exchange membranes can achieve higher ON/OFF ratio, at the cost of higher ionic resistance and higher operating voltage [Isaksson et al. (2007)]. We also notice for different C_D , the ON/OFF ratio is less dependent on the fixed charge concentration C_{IM} . This is due to the fact that with higher C_{IM} , more sites in the IEM are available to attract drug ions. As a result, the increased electrostatic attractions between the fixed charge polymers on the IEM and drug ions would increase the amount of drug transported for both active pumping and passive diffusion (amount of transported drugs at steady-state between ON and OFF states can be found in Figure 2.10), and the ON/OFF ratio is therefore much less dependent on C_{IM} compared to C_D .

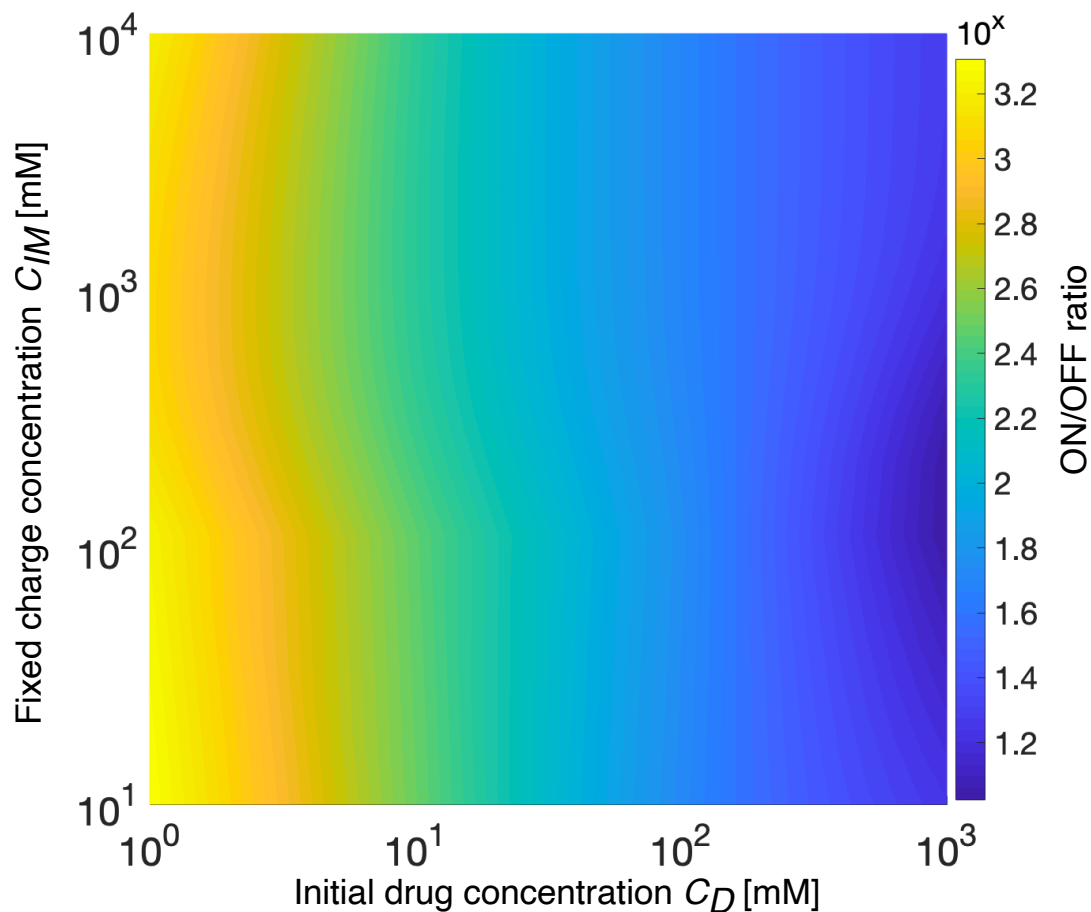


Fig. 2.9 Contour plot of amount of ON/OFF ratio at steady-state as functions of both C_D and C_{IM} , both varying by three orders of magnitude.

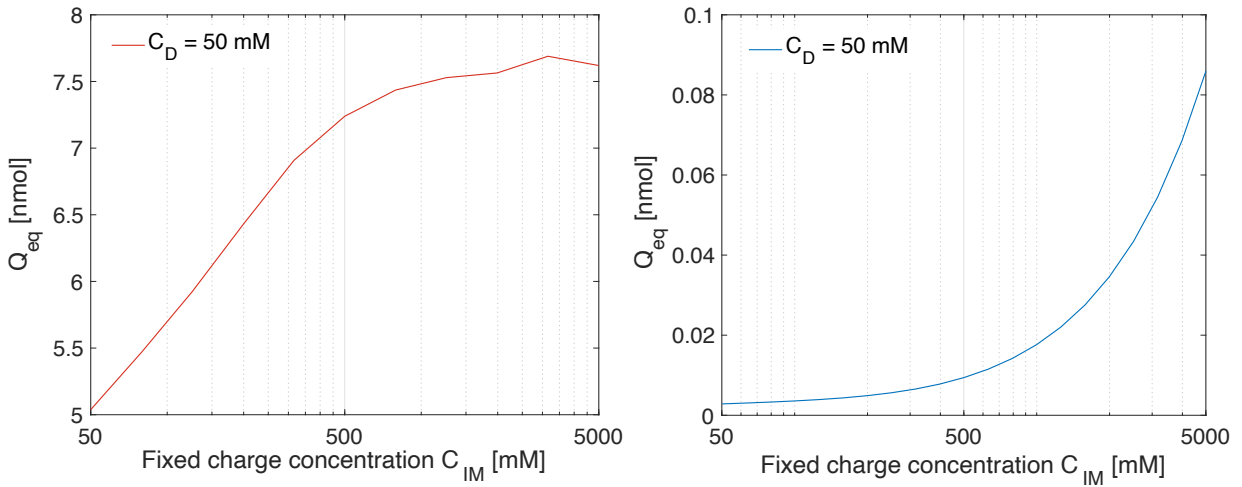


Fig. 2.10 Amount of drug transported at steady-state for different CIM when the device is ON (left) and OFF (right).

2.5 Device performance optimization

Based on the contour plots for each of the performance indices presented in this chapter, the electrophoretic drug delivery device can be optimized for different disease models based on different desired device characteristics. There isn't a way to maximize all three performance indices at once. The amount of transported drug Q can be increased by increasing C_D and C_{IM} , but due to capacitive charging of the electrodes, Q is predominantly limited by the active pumping time, and the effect of increasing C_D and C_{IM} on transporting more drug is limited. The pumping efficiency η is determined by the concentration ratio between C_D and C_{IM} , and the device can reach a high pumping efficiency once the lower concentration ratio limit of 10:1 between C_{IM} to C_D is reached. The ON/OFF ratio is highly dependent on C_D and much less so on C_{IM} . Devices with higher C_D lead to higher amount of passive leakage, which is the dominant factor for a device to have a lower ON/OFF ratio at higher initial drug concentration.

In the context of tailoring the device performance based on different diseases, applications such as delivering chemotherapy for cancer treatment may require a large dosage in a short period of time. Accordingly, the results presented here indicate such devices should be loaded with a high initial drug concentration C_D to maximize Q . Also, considering the short active pumping time due to capacitive charging, it is preferable for the device to have a high pumping efficiency η by having higher C_{IM} , so that the applied potential is pumping predominately the drug. In contrast, for chronic treatments such as seizure control for which minimal passive leakage may be a requisite for safe and long-term implantation, a lower initial drug

concentration C_D is desirable to achieve a high ON/OFF ratio for electrophoretic drug delivery devices.

2.6 Discussion

Much advancement for electrophoretic drug delivery devices relies on membrane materials development and concentration ratio optimization between the drug and the fixed charge groups in the IEM. The capacitive charging in the electrodes and selectivity of IEM dictates the devices characteristics for electrophoretic drug delivery devices.

One might think that having higher initial drug concentration C_D in the electrophoretic drug delivery device is always advantageous, since devices with higher C_D can obtain higher instantaneous drug delivery. Also, the lifetime of the device can be prolonged by having higher C_D in the source reservoir. However, having higher initial drug concentration C_D in the device would lead to worse pumping efficiency η and worse ON/OFF ratio which may not be preferable for chronic treatments. Likewise, even though having higher fixed charge concentration C_{IM} in the IEM can increase the pumping efficiency η and the amount of transported drug Q when actively pumping, it can also lead to drawback such as higher leakage when device is switched off.

Looking ahead, it can be seen that the device parameters in terms of concentration for current electrophoretic drug delivery devices sit in the middle part of the contour plots. (Most commercially available ion exchange membrane materials typically have a fixed charge concentration in the range between 100-1000 mM [Peighamardoust et al. (2010)], whereas drug concentration commonly used in electrophoretic drug delivery devices ranges from 10-100 mM [Proctor et al. (2018), Proctor et al. (2019b)].) One can increase the device performance by either pushing for higher fixed charge concentration, higher drug solubility, or higher concentration ratio between drug and ion exchange membrane with lower initial drug concentration.

2.7 Conclusion

A one-dimensional computational model is developed to illustrate the underlying physics and optimal materials parameters for electrophoretic drug delivery devices incorporating an ion exchange membrane. The capacitive nature of the electrodes is incorporated in the model thereby allowing for a depiction of the temporal dependence of drug delivery under experimentally relevant conditions. The results indicate that the device can be optimized for maximum drug transported by having high C_D and high C_{IM} . For chronic treatment, the device should be optimized for high ON/OFF ratio and high pumping efficiency by having lower initial drug concentration and high fixed charge concentration for the ion exchange membrane to be selective and prevent passive leakage of drugs when the device is switched off. Finally, strategies for future improvements is presented in electrophoretic drug delivery devices and materials development for ion exchange membranes used in the context of different diseases.

Chapter 3

Reducing passive drug diffusion from electrophoretic drug delivery devices through co-ion engineering

Abstract

Implantable electrophoretic drug delivery devices have shown promise for applications ranging from treating pathologies such as epilepsy and cancer to regulating plant physiology. Upon applying a voltage, the devices electrophoretically transport charged drug molecules across an ion conducting membrane out to the local implanted area. This solvent-flow-free “dry” delivery enables controlled drug release with minimal pressure increase at the outlet. However, a major challenge these devices face is limiting drug leakage in their idle state. In this chapter, a method of reducing passive drug leakage through the choice of the drug co-ion is presented. By switching acetylcholine’s associated co-ion from chloride to carboxylate co-ions as well as sulfopropyl acrylate based polyanions, steady-state drug leakage rate was reduced up to 7-fold with minimal effect on the active drug delivery rate. Numerical simulations further illustrate the potential of this method and offer guidance for new material systems to suppress passive drug leakage in electrophoretic drug delivery devices.

3.1 Introduction

Electrophoretic drug delivery devices can be implanted directly into the targeted treatment site, bypassing physiological obstacles such as the blood brain barrier [Pardridge (2005)] and can achieve higher efficacy while delivering lower dosage compared to systemic administrations [Bae and Park (2011)]. In contrast to other implantable drug delivery methods such as convection-enhanced delivery devices [Bobo et al. (1994)], electrophoretic drug delivery does not increase local pressure by injecting solvent, reducing risks of backflow [Casanova et al. (2012)] and issues with long-term device reliability [Boissenot et al. (2016)]. Instead of solvent flow, electrophoretic devices use an applied electric field to push drugs across an ion conducting membrane which in turn allows for precise control of the rate of drug delivery and, ideally, a high ratio of drug flow between active and idle states (i.e. ON/OFF ratio). Electrophoretic drug delivery devices encompass a growing family of devices that include different architectures such as the microfluidic ion pump [Uguz et al. (2017)] and the capillary organic electronic ion pump [Poxson et al. (2019)], which have previously shown promise for addressing a wide range of physiological conditions from epilepsy to stress in plants [Bernacka-Wojcik et al. (2019); Isaksson et al. (2007); Jonsson et al. (2015); Poxson et al. (2017); Proctor et al. (2018); Seitanidou et al. (2019)].

Despite this success, limiting drug leakage when the device is idle remains a hurdle to long-term implantation. The flow of drug from the device when it is intended to be OFF could cause side effects or buildup of drug tolerances; not to mention drug leakage reduces the lifetime of the drug source reservoir thereby requiring more frequent refills. Reducing drug leakage is ever more important considering recent advancements in the field that have relied on ever thinner membranes to reduce power requirements and enhance drug delivery rates [Proctor et al. (2018); Sjöström et al. (2020); Uguz et al. (2017)]. Previous attempts to limit diffusive drug leakage for electrophoretic drug delivery devices include increasing membrane resistance [Williamson et al. (2015)], using a bipolar membrane in a diode configuration rather than a single cation or anion exchange membrane [Tybrandt (2017)], increasing the concentration ratio between fixed charge concentration in the membrane to source reservoir, and applying a reverse “retaining” potential during the idle state [Tybrandt et al. (2009)]. While many of these efforts have proven effective, these solutions increase the energy required to deliver drugs to a therapeutic level thereby reducing the device power efficiency and/or drug delivery rate. Here, a combination of experimental work and computational modeling are carried out to demonstrate a new method of reducing drug leakage in electrophoretic drug delivery devices with minimal impact on other performance metrics: changing the drug co-ion in the source reservoir.

3.2 Mass transport in an electrophoretic drug delivery device

Drug leakage in an electrophoretic drug delivery device can be understood by analyzing the mass transport mechanisms from the drug source reservoir through an ion exchange membrane (IEM) into the target site (e.g. tissue area immediately external to the implant) (Figure 3.1). The IEM is a polymeric membrane containing fixed charge groups [Tanaka (2015)] and in recent years IEMs have been the most commonly reported type of ion conducting membrane used in electrophoretic devices due to their charge selectivity. The IEM separates the drug reservoir, or source, from the target.

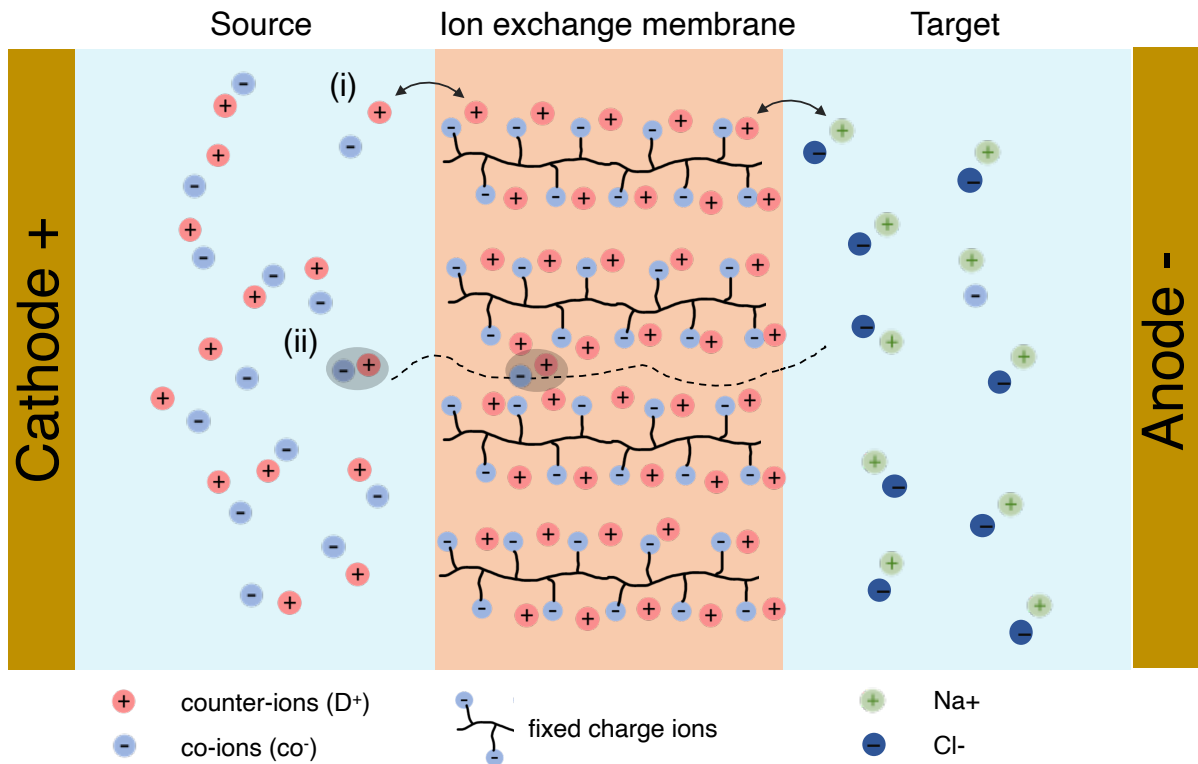


Fig. 3.1 Schematic of mass transport in an electrophoretic drug delivery device. Two drug permeation pathways, (i) Counter-Ion Exchange (IE) and (ii) Associated Ion Diffusion (AID) exist during both active and idle states.

In both active and idle states, the ionic flux J_i for species i through an IEM of an electrophoretic drug delivery device is described by the one dimensional Nernst-Planck equation

along the x-direction as [Strathmann (2004)]:

$$J_i = -D_i \left(\frac{da_i}{dx} + \frac{z_i F C_i}{RT} \frac{d\phi}{dx} \right), \quad (3.1)$$

where D_i is diffusion coefficient, a_i is the activity ($a_i = \gamma_i C_i$), z_i is charge number, F is Faraday's constant, R is the gas constant, T is temperature and ϕ is the applied electric potential. In this study, $\gamma_i = 1$ and so $a_i = C_i$. In a standard electrophoretic drug delivery device, the high drug activity gradient at the IEM-target interface drives drug out of the membrane and into the target where it is typically metabolized or transported away via convection [Cherian et al. (2019); Proctor et al. (2019b)].

The continued loss of drug creates a concentration gradient $\frac{dC}{dx}$ in the membrane, and this concentration gradient is due to irreversible thermodynamic process, regardless of the presence of an external voltage. Reducing this concentration gradient has been the focus of previous reports [Jonsson et al. (2016); Williamson et al. (2015)]. However, these approaches introduce additional power consumption due to increased ionic resistance. Likewise, reducing the drug concentration in the source reservoir simultaneously reduces the reservoir lifetime as well as the drug delivery rate [Chen et al. (2020)].

This chapter focuses on altering the D_i in Equation 3.1 with the aim of reducing drug leakage without a concurrent effect on power consumption or active drug transport. It is hypothesized this may be possible as there are two major pathways for concentration-driven diffusion of charged molecules across an IEM [Kamcev et al. (2016)]: ion exchange [Helfferich (1995)] (IE) and associated ion diffusion [Cussler et al. (1971)] (AID). In IE, a source counter-ion, which is an ion of opposite charge to fixed-ions, exchanges with a counter-ion that was electrostatically coupled to a fixed-ion in the IEM [Cussler et al. (1971)]. After diffusing across the membrane through IE from fixed-ion to fixed-ion, these counter-ions can once again undergo IE with available counter-ions in the target. The second mechanism, AID, is when a counter-ion dissolves into the membrane as part of a "charge neutral pair" with a co-ion. The ions in this pair are considered associated ions and their transport parameters are coupled. In the absence of an applied electric field, AID is understood to be the primary diffusion mechanism at steady-state for an IEM separating electrolytes of different concentration [Kamcev et al. (2017a); Tanaka (2015)].

Assuming non-ideal thermodynamic factors such as the mismatch in activity coefficients between species in source and target are small [Kamcev et al. (2017b)], the overall effective coupled diffusion coefficient D_s of the charge neutral pair has previously been derived

by accounting for electrostatic interactions (counter-ion condensation), tortuosity effect and concentration difference in the IEM [Kamcev et al. (2017c, 2018b)]. The coupled diffusion coefficient is :

$$D_s = \frac{D_{drug}^m D_{co}^m (C_{drug}^m + C_{co}^m)}{D_{drug}^m C_{drug}^m + D_{co}^m C_{co}^m}, \quad (3.2)$$

where $C_{drug}^m, C_{co}^m, D_{drug}^m, D_{co}^m$ with superscript m representing the respective concentration and diffusion coefficient values in the IEM.

Considering Equations 3.1 and 3.2, it is observed that at steady-state the overall mass transfer of drug due to concentration-driven diffusion in the absence of an applied field is dependent on the diffusion coefficient of the associated co-ions. In theory, one could therefore suppress the drug diffusing from the source reservoir into the target by designing a system with a small co-ion diffusion coefficient. Critically, one would not expect that the co-ion diffusion coefficient would affect drug transport in an applied electric field as such transport primarily occurs via IE and is independent of D_{co} [Marcus and Hefter (2006)].

With this theoretical basis in mind, a series of experiments were conducted to measure the effect of co-ions on drug leakage. Acetylcholine (ACh), a drug commonly used in organic electronic ion pumps, was paired with a series of carboxylate co-ions with increasing alkyl chain length, specifically butyrate (But), hexanoate (Hex) and octanoate (Oct) (see Appendix A for synthesis process). These new acetylcholine salts were prepared by using typical protocols for ionic liquid synthesis (see Appendix A for protocol). It is worth remarking that all of salts used in this study are within the family of bioactive ionic liquids based on natural compounds which may have applications in other drug delivery technologies.

3.3 Diffusion experiments of acetylcholine paired with different co-ions

Figure 3.2 shows the ACh concentration measured in the target as a function of time when paired with a series of carboxylate co-ions using a custom-made testing cell with a standard source-IEM-target layout (Figure 3.3), with acetylcholine chloride as comparison. Measurements were conducted using a polystyrene sulfonate (PSS) based IEM with no externally applied field (see Experimental section for detail). For all timepoints the average concentration of diffused ACh was highest for ACh-Cl with a roughly 55% reduction in drug leakage observed for the largest

co-ion pairing (ACh-Oct). However, differences in measured ACh concentration between the carboxylate co-ions were within measurement error (95% confidence interval for at least 3 samples). The results can be understood in terms of D_{co} by employing the modified Stokes-Einstein equation, a power-law relationship between diffusion coefficient D and molecular weight M ($D \propto M^{-\frac{1}{\alpha}}$, $\alpha = 2.56 - 3$) [Augé et al. (2009); Flory (1953)]. Using this analysis as a first approximation of the relative changes in D_{co} , it is estimated a roughly 40% decrease in D_{co} for Oct compared to D_{co} for Cl and a no more than 18% relative reduction in D_{co} when comparing Oct and But co-ions. The results in Figure 3.2 thus suggest that modest changes in D_{co} can lead to modest changes in drug leakage.

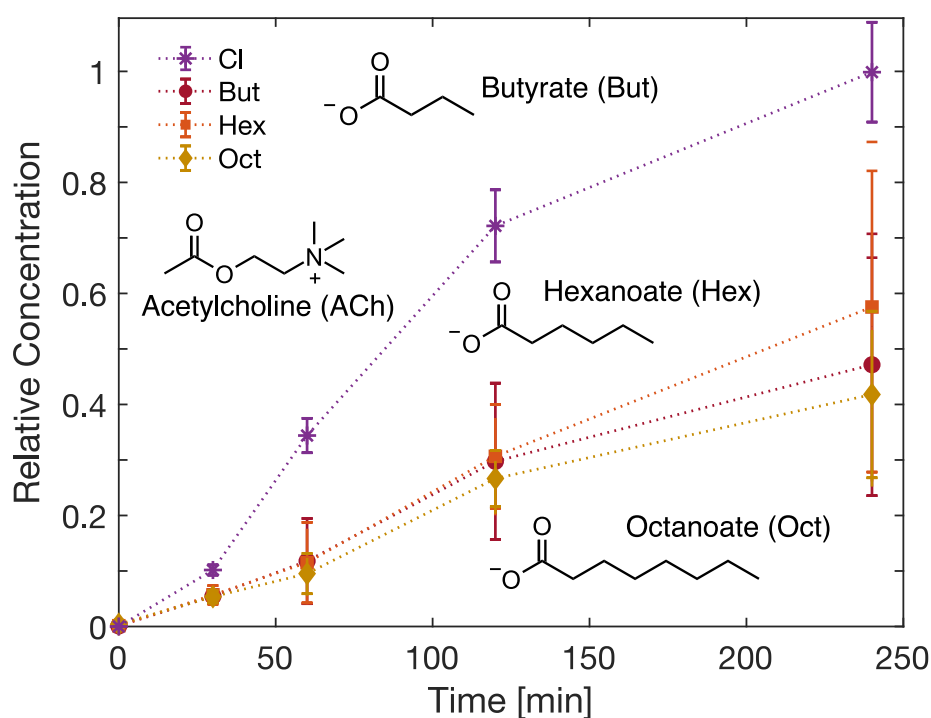


Fig. 3.2 Acetylcholine leakage profile when the source solution was an aqueous electrolyte of Acetylcholine:Carboxylate salt of variable carbon-chain lengths. Inset: molecular structure of Acetylcholine, Butyrate, Hexanoate and Octanoate. Relative concentration is calculated by normalizing against ACh Cl concentration at 240 min.

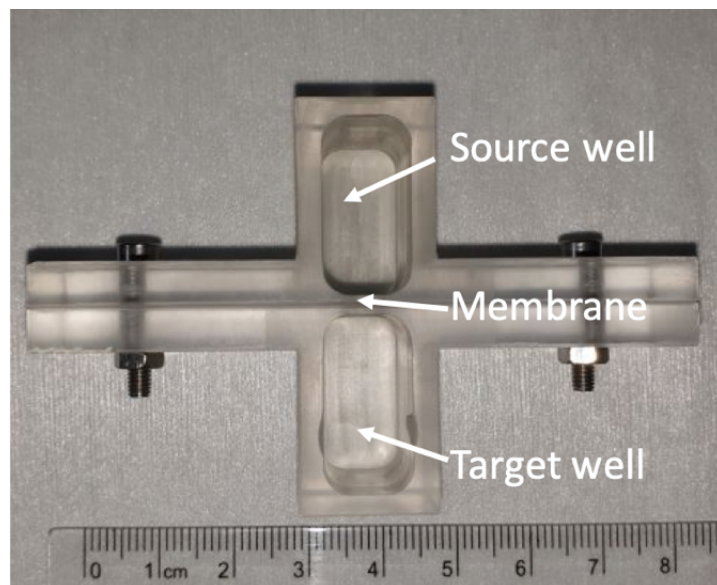


Fig. 3.3 Custom-made test cell for membrane characterization, employed for diffusion experiment in this study.

To further explore the potential effects of D_{co} on drug leakage, ACh was coupled to polymeric co-ions for diffusion experiments. Sulfopropyl acrylate (SPA) was paired with ACh to form the monomer acetylcholine 3-sulfopropyl acrylate (ACh SPA). By synthesizing polyanion forms of the monomer ACh SPA through free radical polymerization and inverse emulsion (see Appendix A for further synthetic procedures), poly(sulfopropyl acrylate) polyanions with ACh were prepared as counter-cations, and molecular weight were on the order of 85,000 g/mol for low MW poly(SPA ACh) and $> 1,000,000$ g/mol for high MW poly(SPA ACh), respectively.

Following the same calculations based on the modified Stokes-Einstein equation, it is estimated the D_{co} for low MW and high MW poly(SPA ACh) to be approximately 10-12% and 4-5% to that of the ACh SPA monomer respectively. It should be noted this estimate is applicable to diffusion in a solvent and, though the IEM is hydrated, it may still significantly underestimate the reduction in diffusion coefficient for polymeric co-ions within the IEM.

Figure 3.4 shows the relative ACh concentration in the target as a function of time when paired with the ACh SPA monomer, low MW poly(SPA ACh), and high MW poly(SPA ACh) with data points normalized to the ACh concentration with the SPA monomer at 240 minutes. Within 60 minutes, all three samples are observed to approach a constant steady-state rate of acetylcholine leakage. Comparing drug solutions with the three different co-ions, a significant reduction in the steady-state drug leakage rates is observed when ACh was paired with the polymers as co-ions. For the low MW SPA polymer, the steady-state leakage rate was reduced

4-fold, while further switching to high MW SPA polymer resulted in nearly 7-fold reduction in drug leakage compared to the monomeric form of SPA. These findings illustrate the powerful role of the drug co-ion in drug leakage across an IEM in an electrophoretic drug delivery device. A 7-fold reduction could lead to an equivalent extension of the time between re-filling drug solutions. Moreover, drugs typically have a strong dose dependence, so even a 2-fold reduction in leakage rate could mark the difference between safe operation and undesirable effects [Holford and Sheiner (1981)].

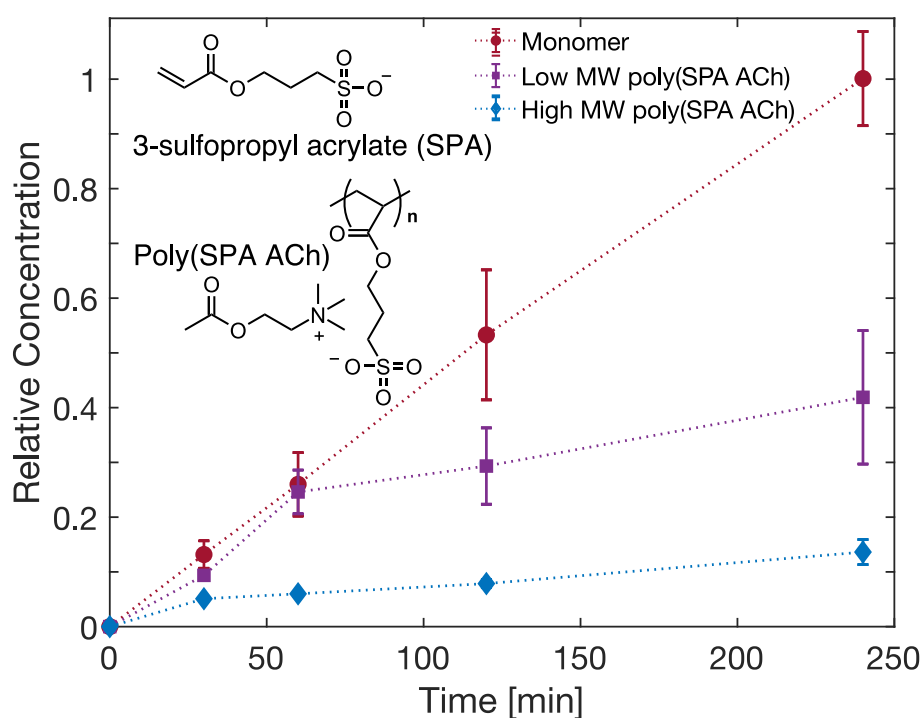


Fig. 3.4 Acetylcholine leakage profile when paired with a series Acetylcholine:poly(sulfopropyl acrylate)s. Inset: molecular structure of sulfopropyl acrylate (SPA) monomer and polymer. Relative concentration is calculated by normalizing against ACh SPA monomer concentration at 240 min.

3.4 Computational modeling of drug diffusion through ion exchange membranes

To better understand the role of D_{co} in particular on drug leakage and to explore whether the change in D_{co} can explain the findings presented in Figure 3.1- 3.4, numerical simulations were conducted using the computational model developed for electrophoretic drug delivery devices in chapter 2 [Chen et al. (2020)]. The one-dimensional model mirrors the geometry of a microfluidic ion pump [Uguz et al. (2017)] with blocking electrode boundary conditions. The temporal behavior of drug leakage was explored with three sets of time-dependent numerical simulations where D_{co} between each run was reduced by an order of magnitude (Figure 3.5) with the D_{drug} and initial D_{co} equivalent to D_{ACh} .

As in the experimental work, the simulated IEM was loaded with drug at the start of each simulation, causing a higher transient leakage rate as a result of the high initial electrochemical potential gradient. The time-dependent drug leakage profiles demonstrate similar characteristics as shown in Figure 3.4, where drug leakage rates approach a constant value after the initial transient phase. The steady-state drug leakage rates were found to be 1.1, 0.32 and 0.13 $\mu\text{M}/\text{min} \cdot \text{cm}^2$ from high to low D_{co} solutions by extracting the slope of these three curves from 150 min onward. These results indicate that the steady state drug leakage rate can be reduced by ca. 3 times and 8 times by reducing D_{co} by one and two orders of magnitude respectively. That these simulation results are on par with the experimental findings in Figure 3.4 supports the notion that the change in D_{co} is the primary reason for the observed reduction in diffusion when comparing ACh with SPA and poly-SPA co-ions.

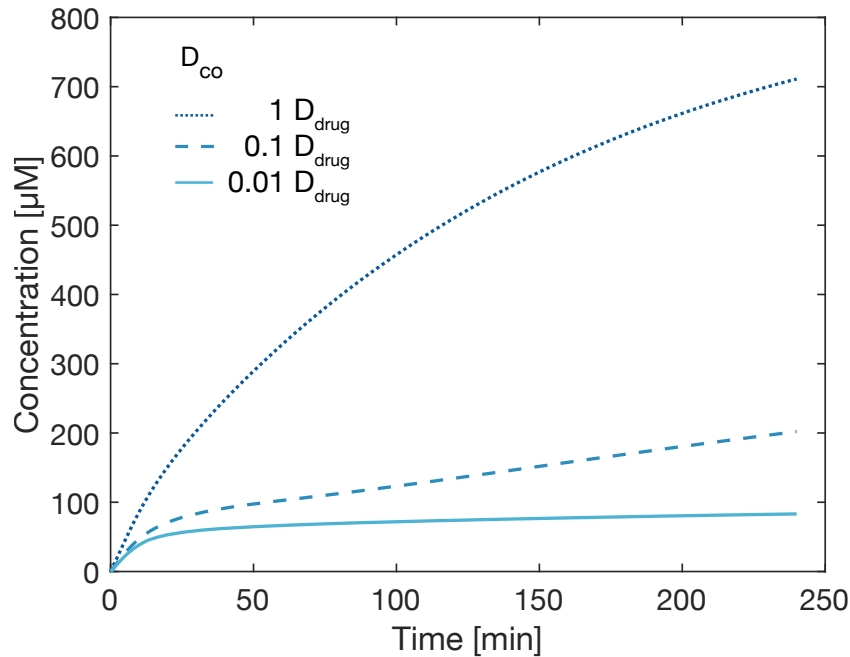


Fig. 3.5 Time-dependent drug leakage profile for different values of co-ion diffusion coefficients D_{co} with D_{drug} equal to D_{ACh} .

Having observed the importance of D_{co} in steady-state drug leakage, numerical simulations were further employed to explore a wider range of diffusion coefficient considering both D_{co} and D_{drug} . Figure 3.6 shows the steady-state drug leakage rate for two systems where D_{co} and D_{drug} are alternatively fixed at D_{ACh} while the other is varied over three orders of magnitude relative to D_{Cl} . The leakage rate is observed to depend strongly on D_{co} (blue line) in the range of roughly 10^{-2} to $10^{-1} D_{Cl}$. A pronounced saturation in drug leakage rate is observed as D_{co} approaches $10^{-3} D_{Cl}$ and likewise as D_{co} increases above D_{ACh} (noted by dotted line).

In contrast, steady-state drug leakage rate is remarkably independent of D_{drug} across nearly two orders of magnitude with a significant decrease starting only when as D_{drug} falls below roughly $10^{-2} D_{co}$ (Figure 3.6, orange line). Extending the simulations to consider simultaneous changes in D_{co} and D_{drug} indicates a similar dependence between D_{co} and steady-state drug leakage for D_{drug} ranging from 1 to $10^{-2} D_{Cl}$ with an even more pronounced reduction in drug leakage as D_{drug} approaches $10^{-3} D_{Cl}$ (Figure 3.7). For reference, dashed lines in Figure 3.7 indicate values for D_{drug} of commonly used compounds GABA, ACh, Dopamine, and Paclitaxel, a notably larger charged drug that may be possible to deliver in the future with further advancements in the development of IEMs for electrophoresis [Poxson et al. (2017); Proctor et al. (2019a); Sjöström et al. (2020)].

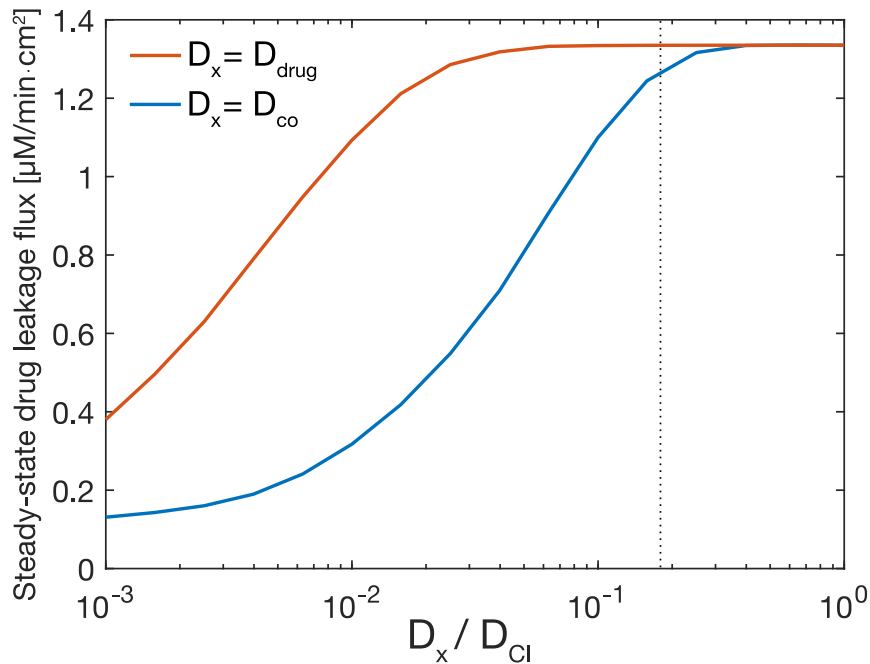


Fig. 3.6 Simulation of steady-state drug leakage rate as a function of co-ion (blue line) and drug (orange line) diffusion coefficients. Dotted line represents diffusion coefficient for ACh.

The contour plot in Figure 3.7 shows the remarkable contrast in the effects of D_{drug} and D_{co} on drug leakage rate persist across the spectrum of relevant diffusion coefficient values; where as a decreasing D_{drug} by a factor of 100 may have a negligible effect on steady-state drug leakage rate, the equivalent reduction in D_{co} could reduce the leakage rate 5-fold. These findings can be understood in terms of Equation 2. Due to Donnan exclusion, $C_{co}^m \gg C_{drug}^m$, and therefore a change in D_{ACh} would be effectively canceled out whereas a reduction in D_{drug} would directly reduce the effective coupled diffusion coefficient. It is only when D_{drug} is reduced to a factor similar to the ratio of C_{co}^m / C_{drug}^m , that the drug leakage rate is noticeably reduced as well.

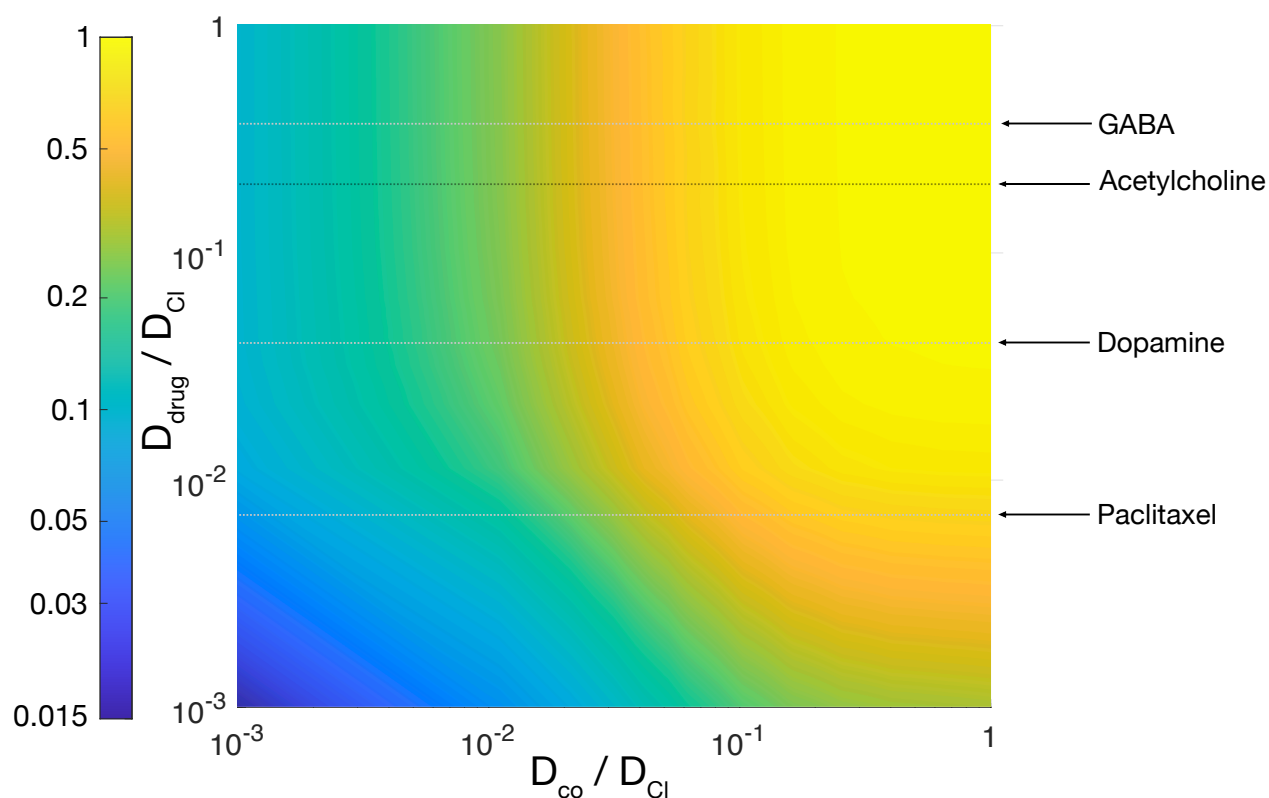


Fig. 3.7 Contour plot of steady-state drug leakage as functions of both drug and co-ion diffusion coefficient. Color bar indicates log scale of normalized drug leak rate. Dotted lines represent diffusion coefficient for GABA, ACh, Dopamine, and Paclitaxel.

3.5 Device active performance when paired with different co-ions

Finally, how the choice of co-ion affects drug transport with an applied voltage is investigated. A microfluidic ion pump device with a PSS based membrane [Uguz et al. (2017)] was prepared with three different 10 mM source solutions of ACh combined with Cl, low MW SPA polymer and high MW SPA polymer co-ions. A 0.5 V potential was applied between source and target electrodes with phosphate buffered saline in the target well. The measured current and transported charge were found to be nearly identical between the three co-ion samples (Figure 3.8). Simulations from our computational model of the microfluidic ion pump further illustrates that active drug transport is largely independent of co-ion diffusion coefficient (Figure 3.9).

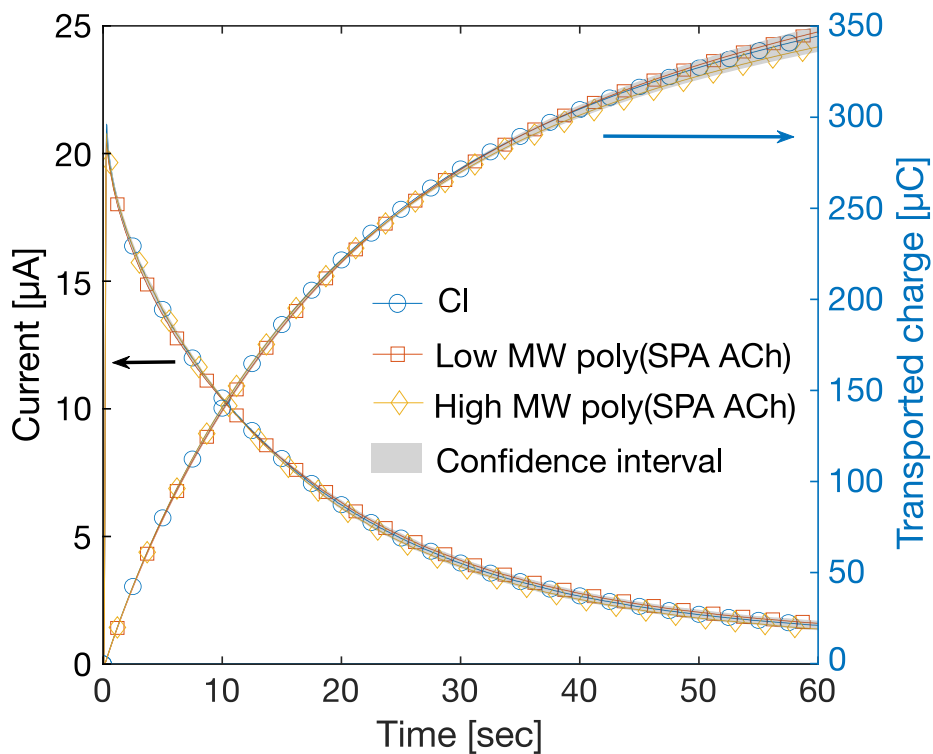


Fig. 3.8 Chronoamperometric measurement for ACh transport by varying co-ions from Chloride to high MW SPA polymer (averaged results where $n = 4$ for each co-ion sample).

Likewise, the simulation shows electrophoretic drug delivery depends strongly on the D_{drug} with an approximately linear correlation consistent with previously reported experiments [Proctor et al. (2019b); Simon et al. (2009); Tybrandt et al. (2009)]. The results in Figure 3.8 and Figure 3.9 follow from established theory of electrophoresis in IEMs – most notably the Nernst-Plank relation and associated expressions for the conductivity of an IEM. Also, according to Marcus Theory for ion pairing [Marcus and Hefter (2006)], with the presence of an external electric field, the charged drug is carried across the membrane faster and so the drug salt in the source will dissociate to compensate this unequal loss of drug counter-ion and associated pairs. As a result, IE would be the dominant transport mechanism (see Theory for drug diffusion mechanisms section).

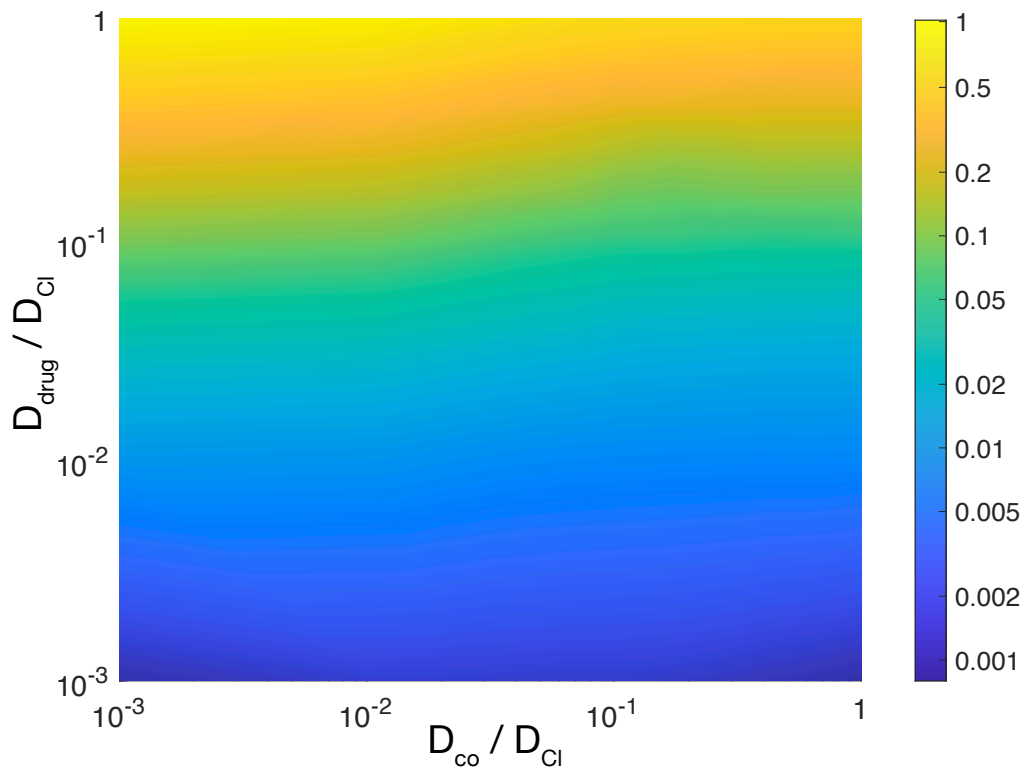


Fig. 3.9 Contour plot of active drug transport as functions of both drug and co-ion diffusion coefficient. Color bar indicates log scale of normalized drug delivery rate.

These results demonstrate that the drug co-ion can be chosen to minimize drug leakage without affecting the active drug delivery rate. The findings also suggest that a change in binding affinity between ACh and poly-SPA polymer compared to ACh and Cl is unlikely to be a significant contributor to the decreased transport in either the on or off state. (A method for estimating the ionic strength for a drug with different co-ions can be found in theory for diffusion mechanisms section). By the same reasoning, Figure 3.8 indicates that the reduction of drug leakage in the poly (ACh poly-SPA ACh) system cannot be explained by the potential entrapment of ACh molecules in the poly-SPA polymer matrix.

3.6 Discussion

All together the results presented here indicate that drug leakage in IEM based electrophoretic delivery devices can be significantly reduced by coupling drugs to slow moving co-ions. Critically, the use of slower co-ions does not come at the cost of active drug delivery rates nor operational power requirements. Though this work focuses on anionic co-ions, the same approach should equally apply to cationic co-ions. As this approach concerns only a change to the drug solution rather than the device geometry, it can be readily integrated into the variety of reported electrophoretic device architectures which to date have relied almost exclusively on the use of drugs with small co-ions such as Cl [Bernacka-Wojcik et al. (2019); Cherian et al. (2019); Isaksson et al. (2007); Jonsson et al. (2015); Poxson et al. (2017); Simon et al. (2009)]. It is posited that that the simulation results in Figure 3.7 may prove particularly useful in guiding future design of new drug co-ion systems with drug leakage rates tailored for the application.

3.7 Conclusion

To summarize, it is demonstrated that drug leakage in IEM based electrophoretic drug delivery devices can be suppressed without affecting the active device performance by changing the associated co-ion in the drug solution. By way of example, it is shown that the steady-state leakage rate of acetylcholine can be reduced up to 7-fold by changing its associated co-ion from chloride or carboxylates of increasing alkyl chain length (C4 to C8) to poly(sulfopropyl acrylate). Active drug delivery experiments show that the choice of co-ions in the drug solution does not affect the amount of drug delivered with an applied voltage. Comparing experimental results with numerical simulations, it is further demonstrated that the strategy presented in this chapter is compatible with a range of drugs commonly used in electrophoretic drug delivery devices. The simulations results can be used to guide the design of future drug co-ion systems for optimal drug leakage reduction. The method presented in this chapter can be readily applied to other electrophoretic drug delivery device architectures thereby extending device lifetime and enabling safe operation for long-term implantations.

3.8 Experimental setup and procedures

The details of the experimental setup and procedures are listed below in this section.

1. Membrane Preparation

The membrane was made of over-oxidized polyethyldioxythiophene doped with polystyrene sulfonate (PEDOT:PSS). The PEDOT:PSS was mixed as dodecylbenzyl sulfonic acid [0.1% w/w], ethylene glycol [5 % w/w], Clevios PH 1000 supplied by Heraeus [94.9 % w/w]. To this, 3-glycidymethoxypropyl silane was added [1 % w/w]. After 3 minutes of sonication, 250 μL of this solution was drop cast on Whatman Cyclopore Polycarbonate, track etched membrane with a nominal pore size of 5 microns. The membrane surface was activated by plasma treatment for 150 seconds prior to drop casting. After drying overnight, films soaked for 25 seconds in 3:1 deionized water:Clorox bleach and then rinsed in deionized water. Films were measured to be about 4.3 microns thick.

2. Electrolyte Preparation

The butyric acid (≥ 99 wt% pure), octanoic acid (≥ 99 %), ACh chloride (≥ 99 %), 3-sulfopropyl acrylate potassium salt (KSPA, 96 %), 2,2'-Azobis(2-methylpropionamide) dihydrochloride (AIBA, 97 %), Isopal L (> 90 %), Span 83 (> 60 %) and sodium metabisulfite (SMB, > 99 %) were purchased from Sigma-Aldrich (Spain). The potassium hydroxide (KOH, ≥ 85 %) was supplied by Fisher Scientific (Spain), while hexanoic acid (≥ 99 %) and Softanol 90 were provided by Acros Organics (Spain) and Quimidroga (Spain), respectively. All these chemicals were used as received. The solvents were of analytical grade and used without further purification.

3. Diffusion Experiments

The test-cell assembly with IEM was placed on a hotplate/stirrer which was set to 25 degrees Celsius and 60 rpm. A stir bar was placed only on the target side reservoir during tests and glass cover slips were used to cover each side to prevent any evaporation. The source side was filled with 2.5 mL of 10 mM ACh electrolyte and the target side was filled with 2.5 mL of phosphate buffered saline solution prepared as suggested. At regular times, the target size cover slip was removed only long enough to collect 200 μL of the target side solution. The level of solution on the target side was always above the port hole in the PDMS gasket for the duration of the experiment so that the mass transfer area of the membrane did not change. Each sample was assumed to be well mixed. Before switching to a new ACh:Anion pair, the membrane was flushed on both sides with deionized water at least five times. A colorimetric

assay of ACh was used to quantify the amount of ACh that had diffused into the target via an ACh assay kit [MBS169077] provided by MyBioSource.

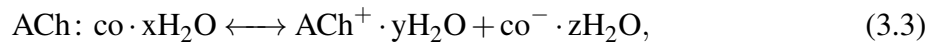
4. Computational Modeling

The governing equations of the one-dimensional model were solved by Finite Element Method using COMSOL 5.4 software. Initial conditions were set where the source reservoir contains both counter-ions and co-ions with concentration of 10 mM, and target reservoir contains 160 mM of NaCl to mimic physiological conditions. Fixed charge concentration in the IEM were set as 0.5M. For boundary conditions, the electrodes of the electrophoretic drug delivery device were assumed to be perfectly polarizable, with no ionic flux entering or leaving from the electrode surface. No restriction of influx and efflux between electrolyte-IEM interface were imposed on any charged particles considered in the study. For both diffusion and active pumping simulations, final drug concentration in target reservoir was obtained by considering both the influx from IEM to target interface and the integral of drug concentration along the entire length of the target reservoir. Adaptive mesh density scheme was used, where the length of the mesh elements in the bulk of reservoirs were set to be 10^{-10} m, and 10^{-12} m at the electrode-reservoir and reservoir-IEM interfaces to ensure convergence. Diffusion coefficients for charged particles considered in the model are as follow: $D_{Na^+} = 1.33 \times 10^{-9} \text{m}^2 \text{s}^{-1}$, $D_{Cl^-} = 2.03 \times 10^{-9} \text{m}^2 \text{s}^{-1}$ with both D_{drug} and D_{co} varying from $2.03 \times 10^{-9} \text{m}^2 \text{s}^{-1}$ to $2.03 \times 10^{-12} \text{m}^2 \text{s}^{-1}$ with a 0.1 reduction factor for the diffusion coefficient of charged species in the IEM [Tanaka (2015); Tybrandt (2017)].

3.9 Theory for drug diffusion mechanisms

Ionic Strength (μ) Consideration

The drug may spontaneously associate or dissociate with the co-ion in the electrolyte. Such reaction, characterized by changes in hydration sphere necessary to accommodate the different forms, can be written for this process:



The left side of the reaction details the associated form of the drug and the right side of the reaction details the dissociated form. The ratio of dissociated to nominal drug concentrations at equilibrium can be described by the ionic strength, μ .

Marcus Theory for ion pairing states that the energy cost to isolate a multivalent anion from cations is higher than isolating a monovalent anion from the cation. Therefore, in an electrophoretic drug delivery device, the portion of associated ion pairs between ACh and a multivalent high MW SPA polyanion is higher than that of a monovalent chloride system. The ionic strength μ between the drug and co-ion in the electrolyte would dictate the portion between IE and AID pathway.

During active drug pumping, IE is the dominant mass transfer mechanism not only because it is faster due to a larger driving force but because the ratio of dissociated drug remains constant, as dictated by μ , while the total concentration of associated drug diminishes. In the absence of an external electric field, the portion of drug diffusion through IE versus AID for a given drug co-ion system may be proportional to the ionic strength μ of that given system. The total amount of drug diffusion F_{total} through the two mechanisms at steady-state can therefore be written as:

$$F_{total} = \left[\mu D_{drug} \frac{\mu S}{l} + (1 - \mu) D_s \frac{(1 - \mu) S}{l} \right], \quad (3.4)$$

where S is the solubility coefficient, D_{drug} and D_s is the drug diffusion coefficient and coupled diffusion coefficient between drug and co-ion in the membrane, and l is the membrane thickness.

Membrane conductivity derivation

The measurement results shown in Figure 3.8 can be understood by relating the measured current to the total ionic flux transported described Nernst-Planck equation.

During drug transport, the total ionic current I with i species is given as:

$$I = F \sum_i z_i J_i, \quad (3.5)$$

Plug Equation 3.5 into the Nernst-Planck equation (Equation 3.1):

$$I = -\frac{F^2}{RT} \sum_i z_i^2 C_i^m D_i^m \frac{d\psi}{dx}. \quad (3.6)$$

The membrane conductivity K for an ion exchange membrane is defined as:

$$K = \frac{-I}{\frac{d\psi}{dx}}, \quad (3.7)$$

plug in Equation 3.7 back to Equation 3.6, the membrane conductivity K can be expressed as a function of the valency, concentration and diffusion coefficient of all the species as:

$$K = \frac{F^2}{RT} \left(z_{drug}^2 D_{drug} C_{drug} + z_{Co}^2 D_{Co} C_{Co} + z_{Na}^2 D_{Na} C_{Na} + z_{Cl}^2 D_{Cl} C_{Cl} \right). \quad (3.8)$$

Under this framework, changing D_{Co} has the least amount of effect on the overall membrane conductivity, since C_{Co} is lowest than the rest of the three ions. As a result, further decreasing D_{Co} it would not contribute to significant change in membrane conductivity and the amount of transported charge with the same applied voltage.

Chapter 4

Enhancing electrophoretic delivery rate via split electrode design and optimal switching scheme

Abstract

Electrophoretic transport of ions is widely used in diverse applications ranging from drug delivery to water desalination. A major limitation in the design of electrophoretic systems arises from electron transfer reactions that occur at the electrodes. These reactions lead to gas formation and changes in pH, which complicate system design and limit *in vivo* applications. Polarizable electrodes can drive electrophoresis whilst avoiding such reactions, but the formation of electrical double layers limits overall ion delivery rate. In this chapter, a split electrode design combined with an optimal switching scheme are developed to improve the ionic delivery rate of electrophoretic delivery devices. The experimental results show that a 2-split electrode setup with optimal switching achieved a 68% increase in delivery rate compared to the single electrode setup with the same overall electrode surface area. Numerical simulations further provide guidelines for using split electrode designs to improve delivery rate of electrophoretic delivery devices used in different applications.

4.1 Introduction

Electrophoresis is described as the migration of charged species under the influence of an electric field. It has been exploited for over 100 years and is still prominent in modern era technology [Gas (2005)], for example, in electro dialysis systems for water purification and treatment [Pérez-González et al. (2012); Strathmann (2010)], in DNA fragment separation for forensics [Houck and Siegel (2015)], in immuno-electrophoresis systems for studies of proteins and antibodies [Laurell (1966); Yagi et al. (1962)], and for testing antibiotics or vaccines [Bottero et al. (2007)]. Electrophoresis is also used for drug delivery in transdermal iontophoresis devices [Byrne et al. (2015); Ita (2016)] and more recently, in implantable organic electronic ion pumps (OEIP's) [Isaksson et al. (2007); Poxson et al. (2017); Simon et al. (2009); Williamson et al. (2015)]. These devices comprise a drug solution reservoir, a semipermeable membrane that separates the drug solution from the target biological tissue, and two electrodes. A “source” electrode is inserted in the drug reservoir, while a “target” electrode is located in the target tissue. When a voltage is applied between the two electrodes, drug ions are transported from the source reservoir, through the membrane, into the target tissue. This delivery method transports the drug without the solvent and as such does not suffer from backflow [Casanova et al. (2012, 2014)] or pressure-induced edemas in the implanted areas [Voges et al. (2003)] associated with convection enhanced delivery methods. Moreover, the use of a voltage as a driving force allows the precise temporal control of the drug delivery process [Jonsson et al. (2016)].

In electrophoretic systems, the choice of electrode materials requires careful consideration. Electrodes can be classified into non-polarizable and polarizable ones [Bard and Faulkner (2000); Berggren and Malliaras (2019)]. Non-polarizable electrodes (e.g., Ag/AgCl electrodes) transfer electrons into species in the electrolyte via Faradaic reactions. Though this mechanism can sustain a constant current, the production of new chemical species, including gases at the electrode/electrolyte interface and undesirable changes in pH [Zeglio et al. (2019)] raise biocompatibility and safety issues [Cogan (2008)]. In biological environments, these Faradaic reactions degrade the electrode material over time and form metal-protein complexes, both of which are particularly detrimental for implantable devices [Cogan (2008); Rivnay et al. (2017); Zeglio et al. (2019)].

On the other hand, polarizable electrodes (e.g., Au or Pt electrodes) are more suitable to be used *in vivo*, as they do not promote charge transfer reactions. Upon the application of a DC voltage, ions accumulate at the surface of the electrodes, creating electrical double layers (EDLs). However, despite having better safety and longevity, one major limitation in using polarizable electrodes is that they do not sustain a steady-state current. Instead, the current decays in time as EDL formation screens out the applied voltage [Ferro and Melosh (2018); Martin and Malliaras (2016)]. In electrophoretic delivery devices, this phenomenon limits drug delivery capacity [Cantrell et al. (2007); Grant and Lowery (2009)]. Increasing the intensity of the applied voltage is not necessarily an option, as this may enable Faradaic processes [Yuk et al. (2019)].

To increase drug delivery capacity, conducting polymers such as poly(3,4-ethylenedioxythiophene) doped with the polyanion poly(styrene sulfonate) (PEDOT:PSS) are often used as coatings on polarizable electrodes [Groenendaal et al. (2000); Heywang and Jonas (1992); Zeglio et al. (2019)]. In these cases, the PEDOT:PSS coatings are used to increase the electrode capacitance by promoting the formation of EDLs throughout the film volume [Proctor et al. (2016)]. While the inclusion of PEDOT:PSS coatings on metal electrodes has shown to greatly increase the electrophoretic delivery capability [Ferro and Melosh (2018)], capacitive charging of electrodes persists as the main limitation in implantable drug delivery devices. As a result, these devices are usually driven with voltage pulses [Proctor et al. (2018, 2019b); Uguz et al. (2017)].

The duration of the voltage pulse is based on the capacitance of the electrodes: the applied voltage is switched off when the electrode is fully charged. Switching off the applied voltage allows the ions in the EDL to diffuse back into the electrolyte before another voltage pulse is applied. The electrophoretic delivery rate by using pulsed stimulation is then limited by the time it takes for the EDL on the electrode to be fully discharged. By increasing the electrode capacitance with a PEDOT:PSS layer, the time for the electrode to be fully discharged increases accordingly. It is therefore hypothesized that optimizing number of source electrodes and using a sequential charging scheme may improve the delivery rate in electrophoretic delivery devices.

4.2 Split electrode design validation with electrophoretic delivery experiment

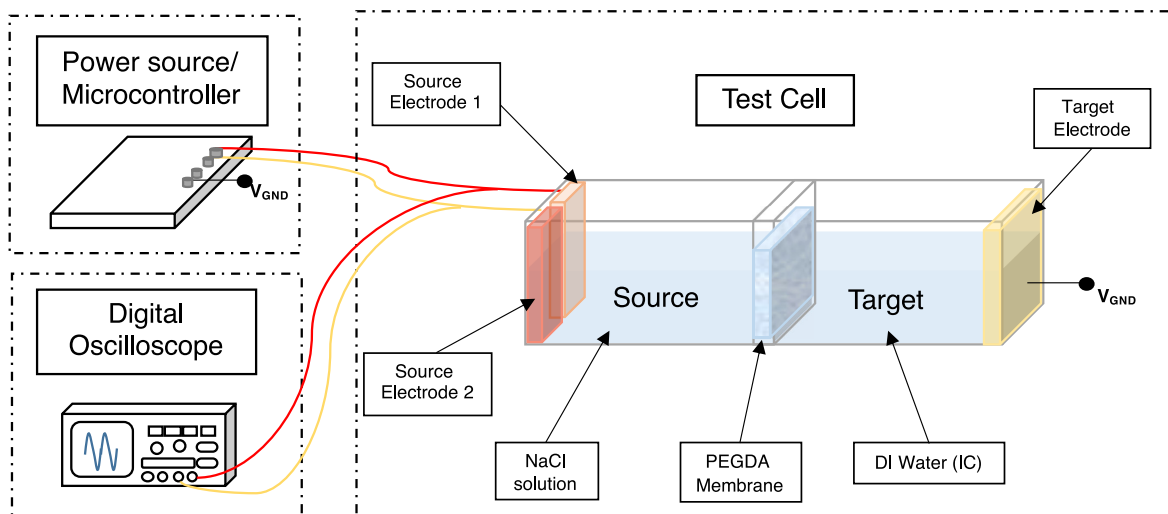


Fig. 4.1 Electrophoretic delivery experiments between using single and split source electrodes, showing the setup for a 2-split electrode system.

To validate the hypothesis of delivery rate improvement with split electrode design, electrophoretic delivery experiments using both the single and 2-split source electrode setups were carried out (Figure 4.1). The custom-made test cell employs a standard source-membrane-target layout (same as seen in Chapter 3). Initially, source reservoir was filled with 6 mL of 10 mM NaCl solution, and target reservoir was filled with DI water of the same volume. Two reservoirs were separated by a permeable PEGDA membrane to limit diffusion and avoid fluid mixing between source and target reservoirs. Source electrodes were made with a 100 nm thick Au layer deposited on a glass slide and spin coated with PEDOT:PSS to increase the electrode capacitance. Electrodes with the same surface area were fabricated, and one electrode was divided in half to be used in the split-electrode setup (See experimental section). The source electrodes were connected to a microcontroller (Arduino Mega 2560), which supplies a 0.5V pulse to each source electrode with specified duration via a driving circuit. Based on the EDL capacitance, the ON and OFF time for the applied voltage were both equal to 2 seconds for the single source electrode setup (See experimental section). Since the capacitance of the electrode is proportional to surface area, the ON and OFF time for the smaller split source electrodes were both set to be 1 second. Each electrophoretic delivery experiment was run for 30 minutes,

afterwards solution in the target reservoir was collected for measurement. Conductivity values for electrolyte in the target reservoir was measured with a conductivity probe (Toledo) and converted to concentrations based on the molar conductivity of NaCl solution.

Figure 4.2 shows the average conductivity and corresponding NaCl concentration in the target reservoir after 30 minutes between diffusion, single electrode and 2-split electrode setups. It should be noted that diffusion has been subtracted for both the single electrode and 2-split electrode measurements to compare the relative delivery rate improvement of the split electrode design. It is observed that with a 0.5 V pulsed stimulation, a single source electrode delivered around twice the amount of NaCl compared to diffusion. The 2-split electrode setup with 0.5 V pulsed stimulation delivered a significantly higher amount of NaCl, with the delivery rate improved by around 68% compared to the single source electrode setup.

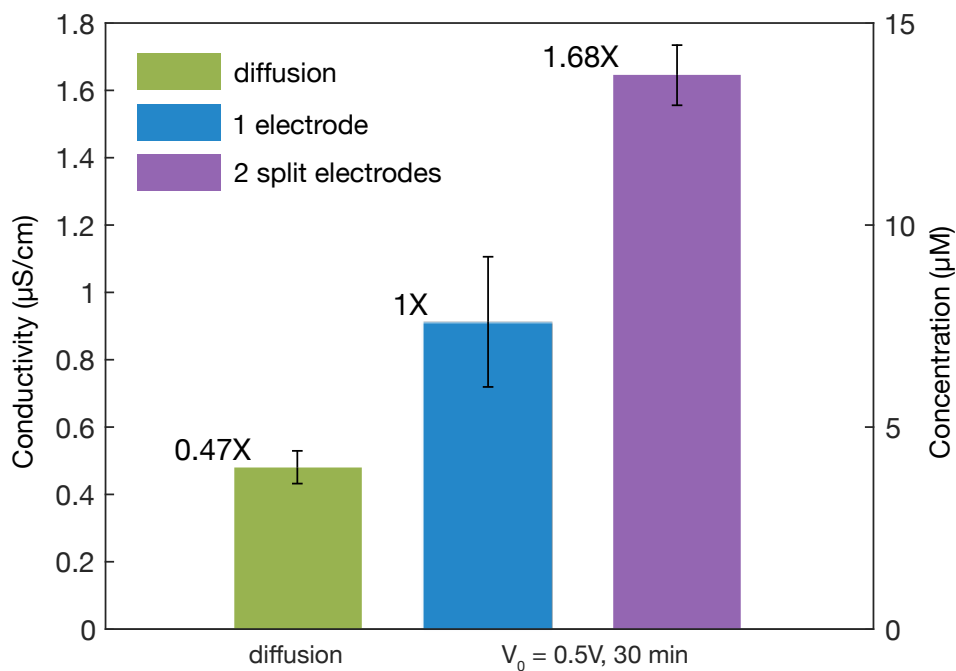


Fig. 4.2 Target reservoir conductivity and concentration measurements between diffusion, single electrode, and 2-split electrode setup (5 repeats for each condition), with relative delivery rate after 30 minutes between three conditions indicated on the plot.

4.3 Equivalent circuit model for split electrode design

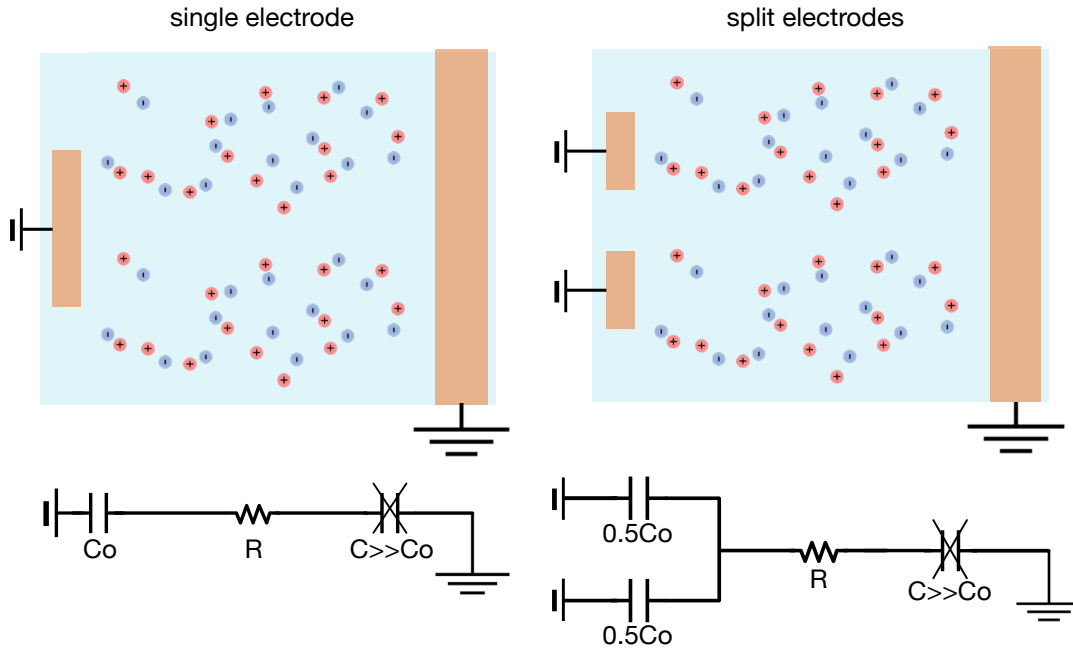


Fig. 4.3 Schematic and equivalent circuit models of electrophoretic delivery devices for a single source electrode and a split source electrode setup.

Having demonstrated the improvement of delivery rate with split-electrode design, an equivalent circuit model is further employed to describe the characteristics of an electrophoretic delivery device and explain the advantages of using the split electrode design. Figure 4.3 demonstrates the concept of splitting the source electrode into two and shows the relevant equivalent circuit elements. The original setup consists of one source electrode and one target electrode (which is grounded) immersed in an electrolyte. The equivalent circuit consists of a capacitor C_o representing the source electrode, a resistor R representing the electrolyte and the membrane, and a capacitor C representing the target electrode [Bard and Faulkner (2000)]. In typical device configurations, the target electrode is considerably larger than the source electrode [Koutsouras et al. (2017)], and hence the equivalent circuit is simplified to C_o in series with R . The current $I(t)$ that flows in the electrolyte upon the application of a voltage V is given by:

$$I(t) = \frac{V}{R} e^{-\frac{t}{\tau}}, \quad (4.1)$$

where τ is the RC time constant of the equivalent circuit, i.e. $\tau = R \times C_o$.

Typical driving voltage in electrophoretic drug delivery devices with polarizable electrodes involve monophasic pulses (positive phase during ON time, zero otherwise) [Proctor et al. (2018, 2019b); Uguz et al. (2017)]. Figure 4.4 shows the optimized monophasic pulsing stimulation, where the duration of the applied voltage is equivalent to the charging time T_{Co} of the EDL capacitor ($T_{Co} = 4\tau$). Here it is evident that the ionic current flowing across the device approaches zero at T_{Co} . In addition, during the discharging phase from $t = T_{Co}$ to $t = 2T_{Co}$, the ionic current in the bulk solution remains negligible until the next charging phase begins. Now, consider a split electrode design where the equivalent surface area is split across two electrodes. The capacitance of each split electrode is now half the original, thus the equivalent charging time is $\frac{1}{2}T_{Co}$ for both smaller electrodes. With the split electrode design, a switching operation can be implemented so that electrode 2 is turned ON when electrode 1 is discharging, and vice versa. Unlike with the single electrode setup where the entire electrode is idle during the discharge phase, the goal of the split electrode design is to have at least one electrode actively delivering current across the device at any given time.

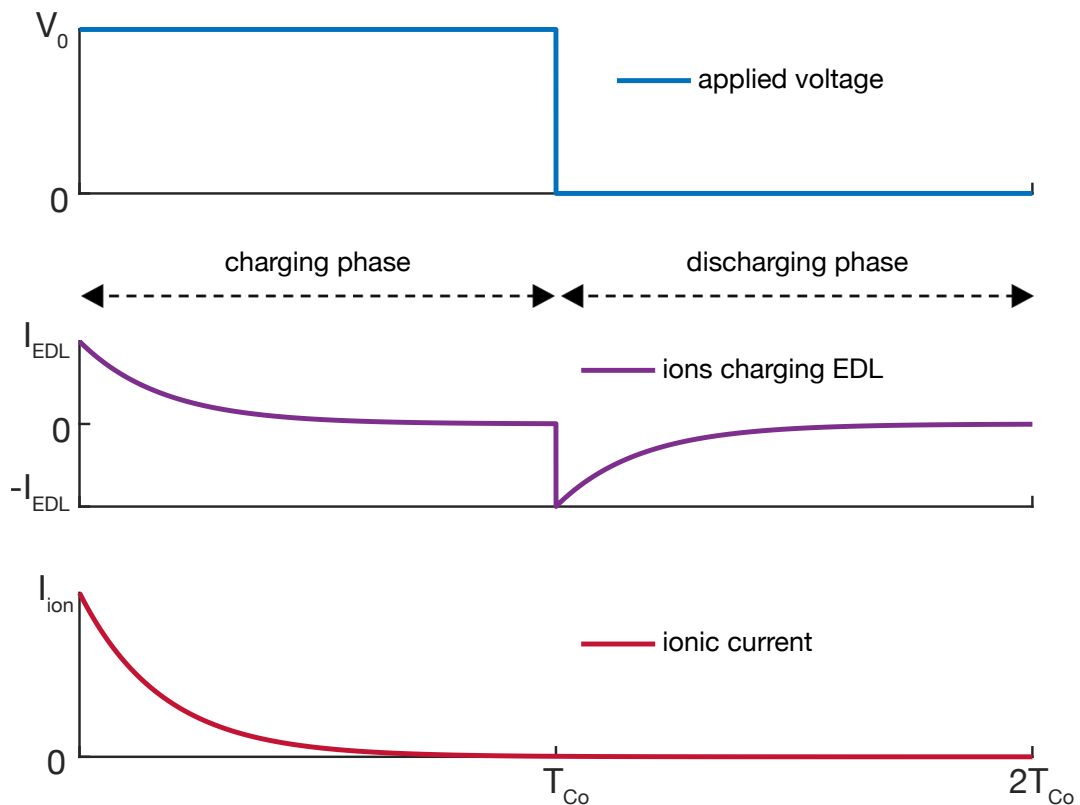


Fig. 4.4 Time dependent relationship between applied voltage, ionic charges forming the EDL, and the ionic current flowing across an electrophoretic delivery device.

However, the split electrode design alone is not sufficient to improve the delivery rate of electrophoretic delivery devices, as the timing of switching ON each electrode also needs to be carefully optimized. Figure 4.5 shows one example of the charge transported between a single source electrode and a n -split electrode setup without optimized switching. During the duration $2T_{Co}$, the amount of charge Q_{Co} transported by the single source electrode can be obtained by integrating Equation 4.1 as:

$$Q_{Co} = \frac{V}{R} \times \int_0^{2T_{Co}} e^{-\frac{t}{\tau}} dt. \quad (4.2)$$

For the split electrode design, each of the n smaller electrode has $(\frac{1}{n})^{\text{th}}$ of the capacitance compared to the single source electrode. The amount of charge each smaller electrode can deliver in a charging cycle $2T_{Cn}$ is therefore $\frac{1}{n} Q_{Co}$. If the electrodes were switched ON one at a time, such as the case in Figure 4.5, the resulting charge transported for a n -split electrode setup in $2T_{Co}$ would be the same as using the single source electrode ($n \times \frac{1}{n} Q_{Co} = Q_{Co}$).

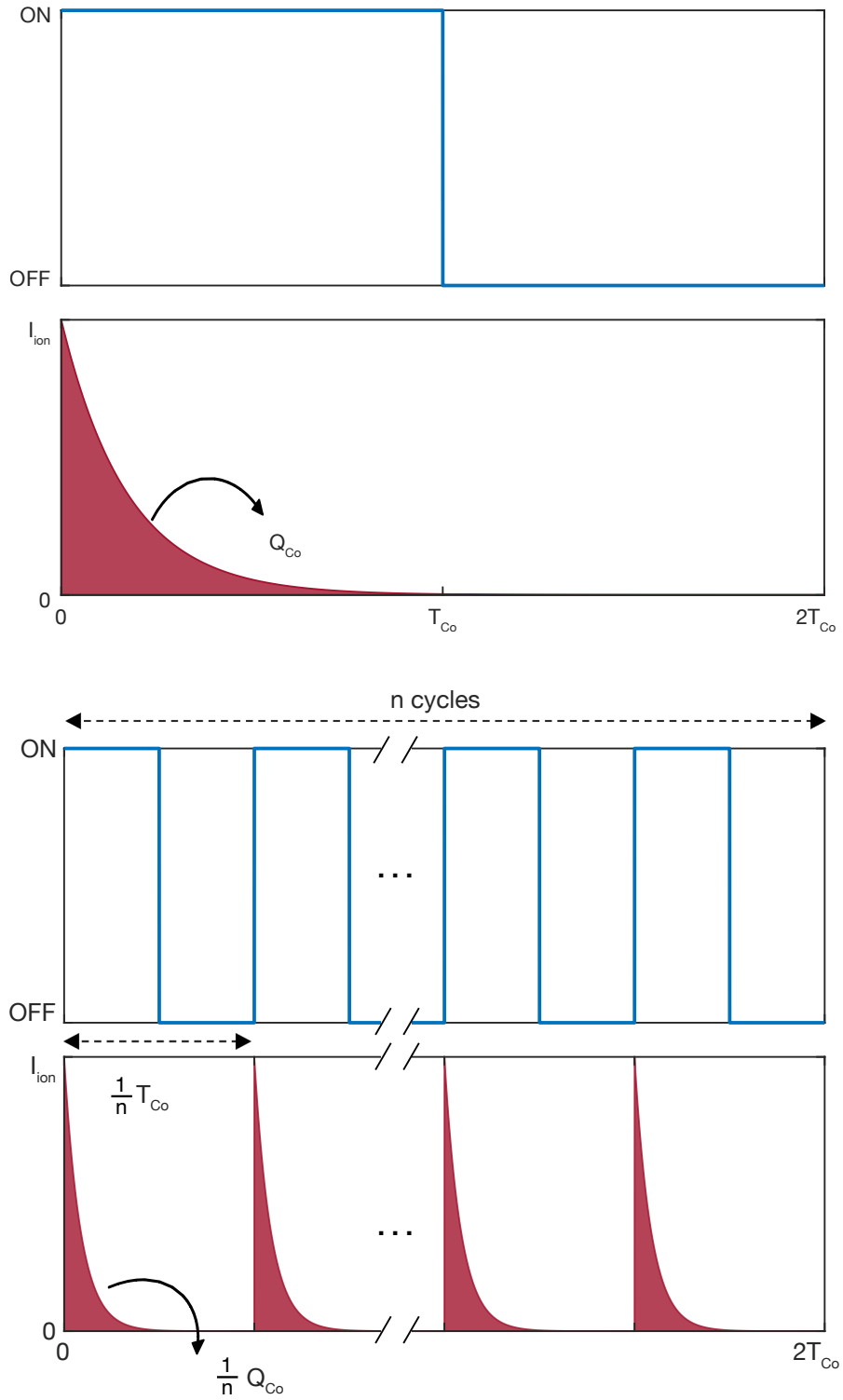


Fig. 4.5 Comparison of applied voltage and transported charges between a single electrode (top) and a n -split electrode (bottom) setup.

4.4 Optimal switching scheme

Having individually addressable smaller electrodes enables us to design switching schemes with overlaps between the charging and discharging cycle of individual electrode. The electrophoretic delivery rate for a n -split electrode setup can therefore be maximized with an optimal switching scheme. Figure 4.6 demonstrates the optimal switching scheme for a system with n electrodes. The entire scheme involves a controller and two timing parameters, T_s and T_{Cn} . The controller switches on the electrodes sequentially from the 1st to the n^{th} with a time delay T_s between each electrode, so the time it takes to switch ON all n electrodes is $n \times T_s$. This process is iterated for the entire duration the device is active. The ON and OFF time for each electrode both are equal to the relative T_{Cn} (thus total operating cycle of a n -split electrode setup is $2T_{Cn}$). This is to ensure the EDL on each electrode can be fully discharged before the it is switched on again. To avoid device being idle and to maximize delivery rate, the optimal switching scheme requires each electrode to start the charging phase once the previous discharging phase is finished. So, it follows that $n \times T_s = 2T_{Cn}$. Substituting the relationship between T_{Co} and T_{Cn} yield the final relationship:

$$T_s = \frac{2}{n^2} T_{Co}. \quad (4.3)$$

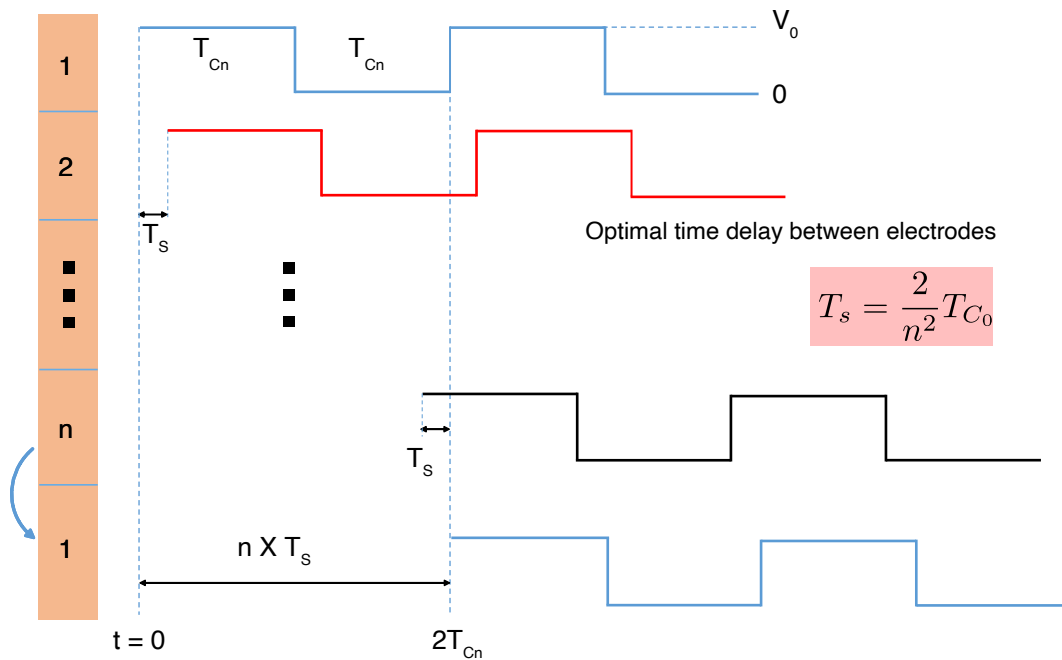


Fig. 4.6 Timing diagram of n -split electrode setup using the optimal switching scheme.

Figure 4.7 shows an example of the ionic current delivered using the optimal switching scheme for a 3-split electrode setup. According to the optimal switching scheme, after switching ON at $t = 0$, electrode 1 should be switched on again at $t = 3T_s$. In this case, $3T_s$ is equal to the time it takes for electrode 1 to complete a complete charging and discharging cycle $2T_{Cn}$. Following Equation 4.3, $T_{Cn} = \frac{1}{3}T_{Co}$, and $T_s = \frac{2}{9}T_{Co}$.

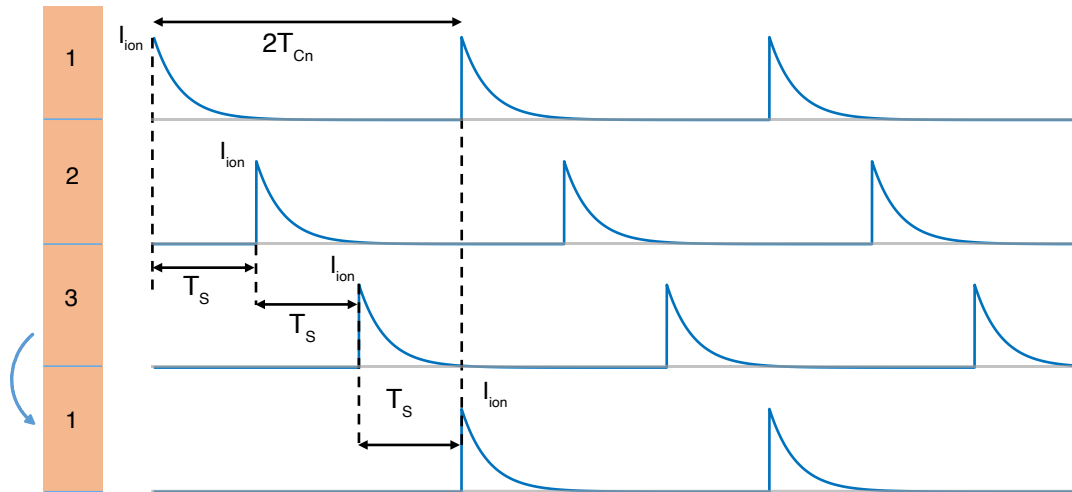


Fig. 4.7 Ionic current from each electrode with optimal switching interval T_s and ON time T_{Cn} for a 3-split electrode setup.

Figure 4.8 shows the relative transported charge between a 3-split electrode with optimal switching and a single electrode setup. In $2T_{Co}$, all 3 electrodes in the split electrode setup can each be switched on 3 times, whereas the single source electrode can be switched on 1 time. With $\frac{1}{3}$ of the capacitance compared to the original source electrode, each smaller electrode can deliver $\frac{1}{3}$ of the charge in a single charging cycle. As a result, the 3-split electrode setup should deliver 3 times the charge compared to the single source electrode setup in the same duration, i.e., $\frac{1}{3}$ (ionic current in 1 charging cycle) $\times 3$ (3 cycles for a split electrode in $2T_{Co}$) $\times 3$ (total of 3 split electrodes) = 3. Table 4.1 provides an overview of the expected charge, optimal charging time, optimal switching time and theoretical delivery rate improvement from $n = 1$ to $n = 5$ using the optimal switching scheme.

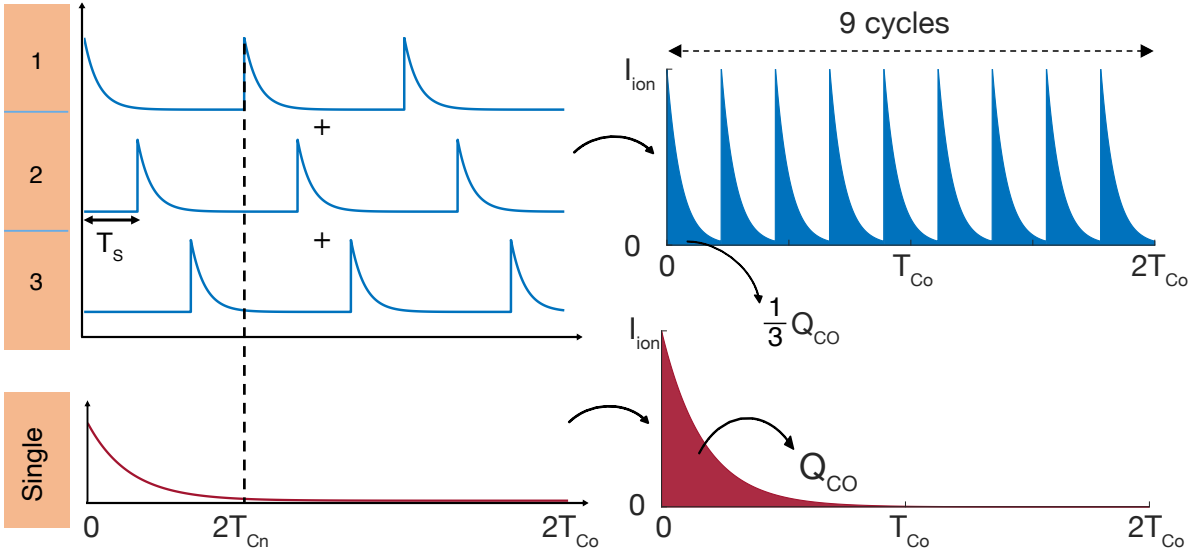


Fig. 4.8 Comparison of time-dependent ionic current (left) and transported charge (right) in $2T_{Co}$ between a 3-split electrode and a single electrode setup. The overall transported charge is equal to the summation of transported charges by all electrodes, represented by the area plots.

Table 4.1 Relative charging time and delivery rate for a n -split electrode setup

n -split electrodes	Charge delivered by one electrode	Charging time for one electrode	Switching time T_s	Relative delivery rate
1	Q_{Co}	T_{Co}	$2T_{Co}$	1
2	$\frac{1}{2}Q_{Co}$	$\frac{1}{2}T_{Co}$	$\frac{1}{2}T_{Co}$	2
3	$\frac{1}{3}Q_{Co}$	$\frac{1}{3}T_{Co}$	$\frac{2}{9}T_{Co}$	3
4	$\frac{1}{4}Q_{Co}$	$\frac{1}{4}T_{Co}$	$\frac{1}{8}T_{Co}$	4
5	$\frac{1}{5}Q_{Co}$	$\frac{1}{5}T_{Co}$	$\frac{2}{25}T_{Co}$	5

As seen from Table 4.1, theoretical calculations using the circuit model predict the delivery rate of a n -split electrode system to be n times to that of the single electrode setup. The discrepancy between theoretical predictions and experimental results from Figure 4.2 can be attributed to crosstalk current between the electrodes. During electrophoretic delivery experiments, an average of 0.13V was measured between the 2 split electrodes. As a result, instead of flowing from source to target reservoir when external voltage is applied, a portion of ions would flow between the two electrodes, thus reducing the delivery rate. As the number of electrodes increases, non-ideal factors such as crosstalk affecting the delivery rate may also increase.

4.5 Extending the applicability of split electrode design to n electrodes

A Finite-Element Method (FEM) based computational model was developed to study how crosstalk current affect device performance [COMSOL (2018)]. Figure 4.9 and Figure 4.10 shows the electric potential distribution and crosstalk current densities $|J_y|$ between a 2- and 4-split electrode device at $t = T_y$. Electrodes are separated by insulating gaps, and the overall electrode surface areas are kept constant across both systems. The arrow lines describe the normalized electric field vectors. Crosstalk current between electrodes can be observed for both setups, as indicated by the inward arrow lines pointing from the electrolyte into the electrodes. However, as seen from Figure 4.9, crosstalk current density $|J_y|$ is much stronger in the 4-split electrode system compared to the 2-split electrode system (Figure 4.10). This can be explained by the larger number of paths for crosstalk current in the 4-split electrode compared to the 2-split electrode setup. Evidently, there is a tradeoff between crosstalk and delivery rate by increasing the number of electrodes.

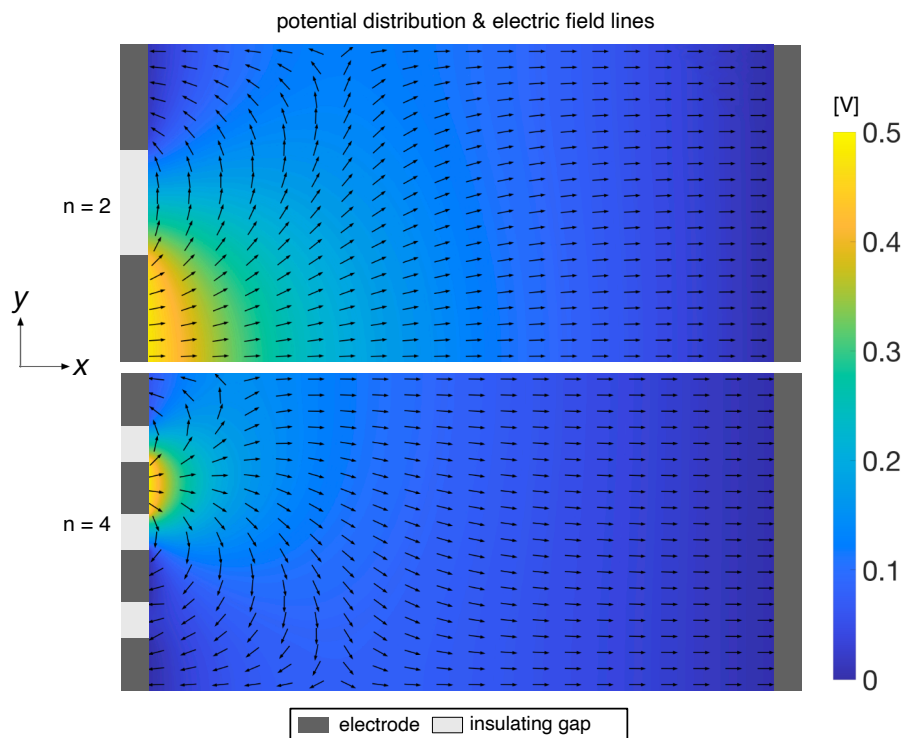


Fig. 4.9 Snapshots of electric potential distribution and electric field lines for a 2-split electrode and 4-split electrode setup.

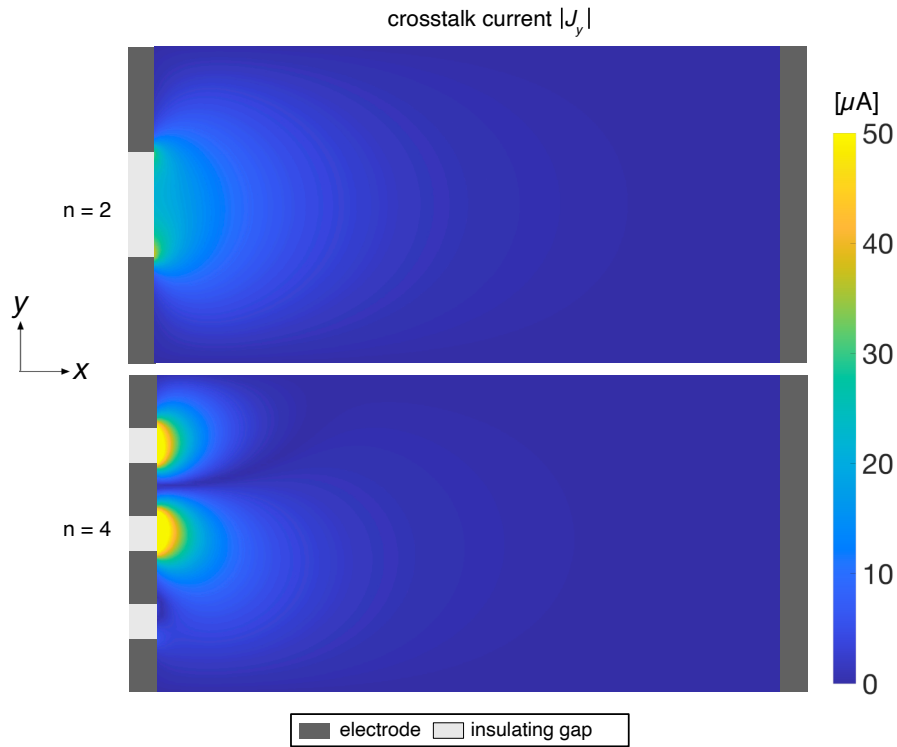


Fig. 4.10 Snapshots of crosstalk current intensity for a 2-split electrode and 4-split electrode setup.

Figure 4.11 shows the delivery rate and relative average power for an n -split electrode setup operating under optimal switching scheme for $n = 1 - 10$. Most significant improvement in delivery rate occurs when increasing n from 1 to 2. The $\approx 75\%$ increase in delivery rate matches well with experimental result from Figure 4.2. As n increases above 4, only marginal increase in delivery rate can be achieved, as crosstalk current eventually dominates when external voltage is applied on a split electrode setup with higher n . The relative average power shown in green is calculated as the ratio between the total ON time of all electrodes in $2T_C$ to an operating cycle $2T_{Co}$. As n increases, more ON time between electrodes overlap, resulting in a higher average power consumption, and it is also observed that further increasing n would lead to diminishing returns as power consumption grows faster than the delivery rate. Figure 4.12 shows the normalized power efficiency and target to source current ratio $|J_x|/|J_{x,y}|$ of an n -split electrode system operating under optimal switching scheme for $n = 1 - 10$. Similarly, as crosstalk current increases with n , power efficiency decreases. As seen from the trend for transverse current $|J_x|/|J_{x,y}|$, when $n > 4$, more than half of the ionic current is traveling between the electrodes in the y direction instead of migrating from the source to target in the x direction. For applications with stringent power consumption requirements such as those in long-term implantable devices,

trade-offs between delivery rate and power efficiency should be a major design consideration when using split electrode design.

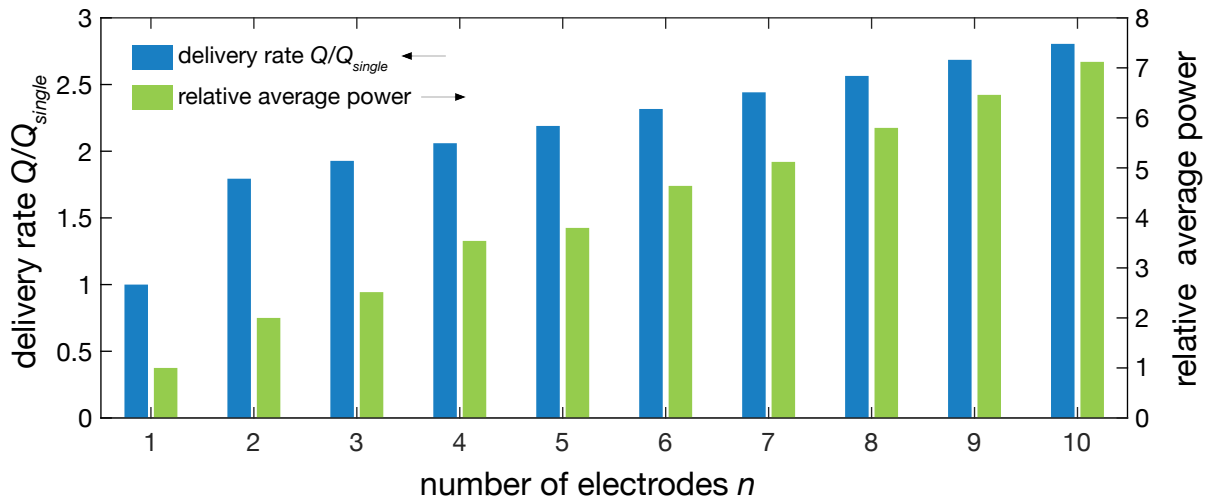


Fig. 4.11 Delivery rate and relative average power for a n -split electrode setup where $n = 1 - 10$.

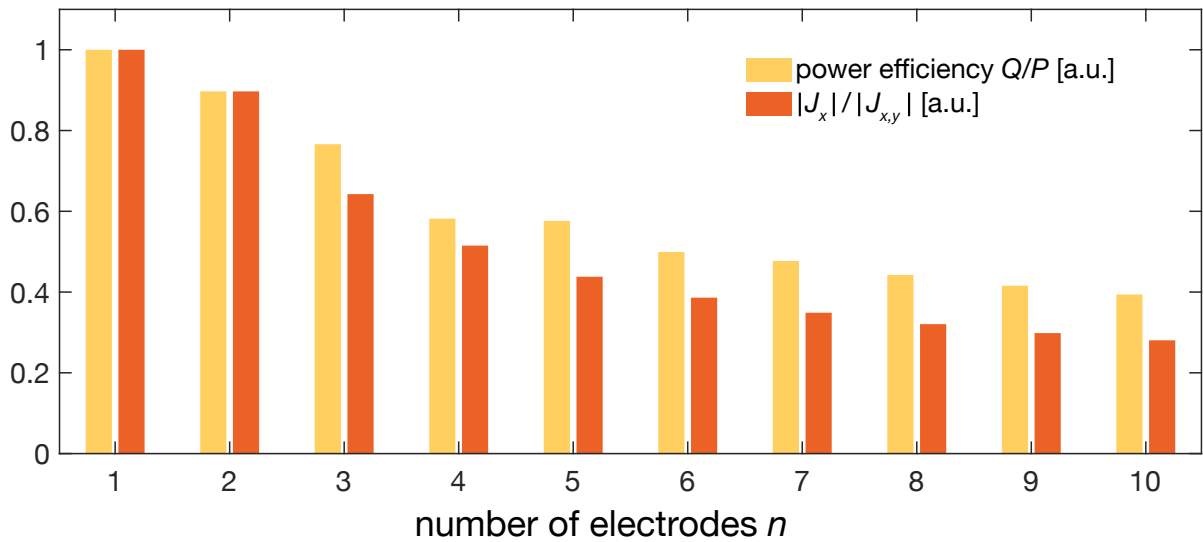


Fig. 4.12 Power efficiency and portion of source-target current for a n -split electrode setup where $n = 1 - 10$.

4.6 Conclusion

Altogether the results presented in this paper suggest that the split electrode design combined with optimal switching scheme is able to increase the delivery rate for electrophoretic delivery devices. The design is extremely simple and requires minimal additional control instructions. The split electrode design allows each electrode to charge and discharge individually. Therefore, instead of requiring long idle time for the EDL to discharge, the split electrode design ensures that at least one electrode is active at any given time. The numerical simulation results further provide guidelines when designing the split electrode setups for electrophoretic delivery devices. Although splitting the source electrodes into smaller electrodes can increase electrophoretic delivery rate, non-ideal factors including crosstalk current and increased power consumption will be the limiting factors in deciding the appropriate number of split electrodes for different applications. The split electrode design presented here is able to be applied to existing electrophoretic delivery devices. Improvements in reducing non-ideal factors, such as geometric designs to minimize crosstalk current can further improve the power efficiency of the split electrode design and improve the delivery rate for electrophoretic delivery devices.

4.7 Experimental section

1. PEGDA Membrane

Permeable membranes were developed with 500 uL of poly-ethylene-glycol(PEG) diacrylate 575 mn (Sigma Aldrich) with 2% photo initiator (2-hydroxy-2-methylpropiopheone) 97% concentration (approximately 10-12 uL). The solution was held in an IKA Vortex 2 for 45 seconds to mix. Two glass slides were washed in ethanol, dried and separated by two pieces of cut parafilm at both edges. Approximately three drops of the combined solution were pipetted in the center of the slide which was sandwiched by the other glass slide. The membrane encapsulated slides were places in a UVP Crosslinker at maximum energy (9999) for 15 minutes to cross-link. Slides were removed and placed in a DI bath for 5 minutes before membranes were removed from glass slides and placed in new bath of DI water in preparation for experiments. Membranes were replaced for each experiment.

2. Electrode fabrication

On glass slides, metal layers of Ti (5 nm) / Au (100 nm) were deposited by an e-beam evaporator (Kurt J Lesker PVD-75) PEDOT:PSS (Clevios PH1000, Heraeus) containing 5% of ethylene glycol, 0.25% of dodecyl benzene sulfonic acid (DBSA, Sigma Aldrich) and 1% of GOPS (Sigma Aldrich) cross linker was spin coated, followed by the annealing at 130 °C for 30 min and immersed into DI water overnight to remove excess compounds.

3. Computational modeling

COMSOL 5.4 software was used to solve the governing equations of the 2-dimensional model of the electrophoretic device using Finite Element Method. Initial concentration is set to 10 mM of NaCl. No flux condition was set on the electrode-electrolyte interface to represent polarizable electrode used in the electrophoretic delivery device. The mesh was applied using adaptive density scheme were in the bulk of the electrolyte the maximum length of each mesh element is be 10^{-10} m, and 10^{-12} m at the electrode-electrolyte interface. Diffusion coefficients for charged particles considered in the model are as follow: $D_{Na^+} = 1.33 \times 10^{-9} \text{m}^2\text{s}^{-1}$ and $D_{Cl^-} = 2.03 \times 10^{-9} \text{m}^2\text{s}^{-1}$.

4. Driving circuit for microcontroller

Experiments were performed according to the cell setup in Figure 4.2. Electrodes were rinsed in DI water between each experiment. The Arduino Mega digital output pins were used to deliver a 5V output that was reduced to 0.5V with a simple voltage diving circuit. The switching scheme was determined by sending a digital high (5V - reduced to $\approx 0.5V$) followed by a delay determined by the optimal T_s and followed by a digital low (0V). The microcontroller ran the instructions on infinite loop and was only altered according to the T_{Cn}/T_s times required. RC times were determined according to the charging time to achieve 95% of 0.5V (1 electrode : $T_{Cn} = 2$ seconds, 2 split electrodes : $T_{Cn} = T_s = 1$ second). In each experiment, the same target electrode was used.

Chapter 5

Steerable and localized neuromodulation via temporal interference field

Abstract

Electrical modulation works by stimulating the nervous tissues with electrical currents to either provide therapeutic benefits or aid impaired sensory-motor functions for patients with neurological deficits or disorders. One of the most common electrical neuromodulation treatments, the spinal cord stimulation, has shown promise for applications ranging from chronic pain management to helping patient regain locomotion functions after suffering severe injuries. However, a major challenge this treatment faces is the lack of specificity and steerability with existing device architecture and stimulation protocol. This can lead to side effects and long-term efficacy issues. In this chapter, a localized and steerable neuromodulation device and stimulation protocol is developed in the context of spinal cord stimulation. The stimulation waveform-temporal interfering fields used here has recently been applied in deep brain stimulations and demonstrated promising results of non-invasive neuromodulations. In this chapter, the working principle of temporal interfering stimulation is introduced, a coupled FEM - Equivalent circuit computational model is developed to reveal the relationship between the intensity of temporal interfering stimulation and resulting axonal response in the spinal cord. Computational and experimental works showed that the system developed here is able to achieve a steerable, sub mm^2 stimulation hotspot in the spinal cord cross-section. Parameter studies provide guidelines in how to further optimize the device for targeting different tracts within the spinal cord.

5.1 Introduction

Spinal cord stimulation for pain control is one of the most common neuromodulation therapies, with an estimation of 50,000 patients receiving implant surgeries annually for drug-refractory neuropathic pain [Sdrulla et al. (2018)]. The goal of spinal cord stimulation is to reduce pain by modulating neural signaling with electric stimulations. The device performing the modulation—the Spinal Cord Stimulator (SCS), consists of three main components: an implantable pulse generator (IPG) providing power and specifying the waveforms of the electrical stimulation, an electrode array sending out the electric currents to the nerve fibers, and a remote control for patients to adjust the device settings [Meadows et al. (2003); North et al. (1991)] (Figure 5.1(a)). Electrode arrays in current SCS devices are arranged in a long and thin manner, usually in a lead or paddle configuration [North et al. (2005)](Figure 5.1(b)). Surgeons can implant the electrodes to the appropriate areas in the epidural space dorsal to the spinal cord column through percutaneous procedures or laminotomy, respectively [Ridder and Vanneste (2016)] (Figure 5.1(c)).

Current common electrical stimulation waveforms for spinal cord stimulation include tonic, burst, and kilohertz-frequency stimulation (Figure 5.2). Figure 5.2(a) shows the waveform for conventional tonic stimulation, which involves a pulse with $\approx 30 \mu\text{s}$ duration operating at a burst rate of 50-60 Hz. The working theory of applying low frequency (i.e., tonic) stimulation to the spinal cord dorsal column for pain control is based on the gate control theory [Melzack and Wall (1965)]. Under this framework, it was suggested that applying low-frequency electrical stimulation can activate larger-diameter nerve fibers and produce a perceptible paresthesia (tingling, pins and needles sensations), thus 'gating' the conduction of pain signal and achieve pain relief [Caylor et al. (2019)]. Since the first implantation of SCS device with paresthesia-based neuromodulation back in 1967 [Shealy et al. (1967)], tonic stimulation has been the standard waveform for SCS stimulation. However, the success rate with tonic stimulation based on patient feedback is sub-optimal, with 51% of patients reported receiving $\geq 50\%$ pain relief in a clinical study [Deer et al. (2018)].

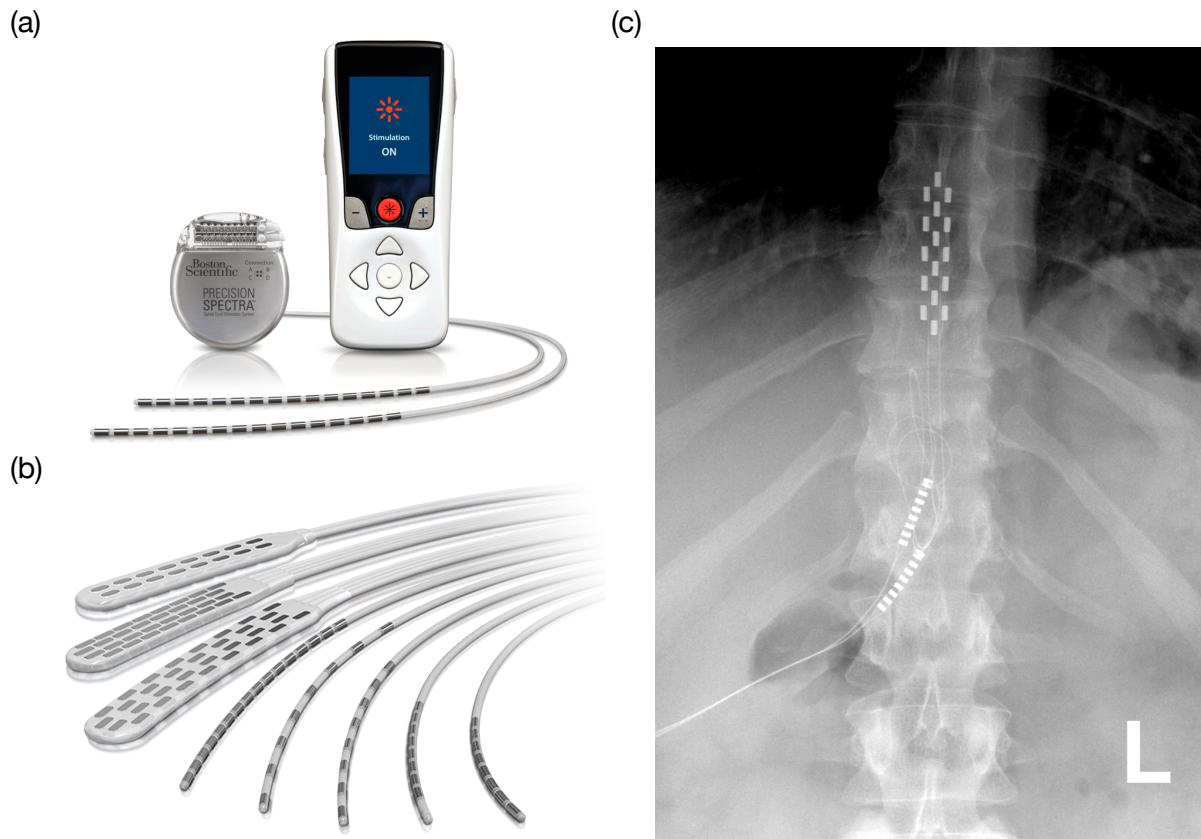


Fig. 5.1 Components and X-ray image of a commercial SCS device. (a) FDA approved SCS device from Boston Scientific, including an IPG (left) connected to the lead, and a hand-held remote control (right) [Adair (2017)]. (b) CAD rendering of paddle and lead shaped electrode arrays in spinal cord stimulation devices, image reproduced from [Whitehurst et al. (2005)]. (c) Anterior view X-ray image of a paddle type SCS implanted in the thoracic level of the spinal cord, image reproduced from [Mconnell (2009)].

To improve clinical efficacy and patient comfort for spinal cord stimulation, several paresthesia-free stimulation waveforms were developed. Bursts stimulation shown in Figure 5.2(b) is one of these paresthesia-free stimulation emerged over the last decade [De Ridder et al. (2010)]. The waveform for burst stimulation typically includes a five-pulse train with 500 Hz of intra-burst frequency with burst rate of 40 Hz. Based on clinical results, it was postulated that unlike tonic stimulation, burst stimulation can modulate both the pain-evoking and pain-inhibitory pathways [De Ridder and Vanneste (2016); Linderoth and Foreman (2017)]. This compound modulation results in moderately higher higher success rate than tonic stimulation (60% compared to the 51% for tonic stimulation [Deer et al. (2018)]), while simultaneously alleviating much discomfort and adverse effects due to paresthesia, thus improving patients' quality of life.

Another novel paresthesia-free stimulation waveform is the kilohertz-frequency stimulation (Figure 5.2(c)). The kilohertz-frequency stimulation, as the name suggests, switches the polarity of the stimulation at frequencies > 1 kHz. To date, no comprehensive theory is able to account for the mechanisms of action for kilohertz-frequency spinal cord stimulation. The working theory for such stimulation waveform was based on nerve conduction block [Kilgore and Bhadra (2014)], where it was postulated that the high frequency electrical stimulation can block the propagation of pain signals along the nerve fibers in the spinal cord. However, recent computational and animal studies have pointed out, considering the stimulation amplitude of kilohertz-frequency stimulation in clinical settings, conduction block is unlikely to be the reason for pain relief using kilohertz-frequency stimulation [Lempka et al. (2015); Song et al. (2014)]. Despite positive clinical results, there are still several technical challenges such as high power consumption, tissue heating, and stimulation parameter optimizations to overcome in order to broaden the applicability of the use of kilohertz-frequency spinal cord stimulation [Vallejo et al. (2017); Zannou et al. (2019)].

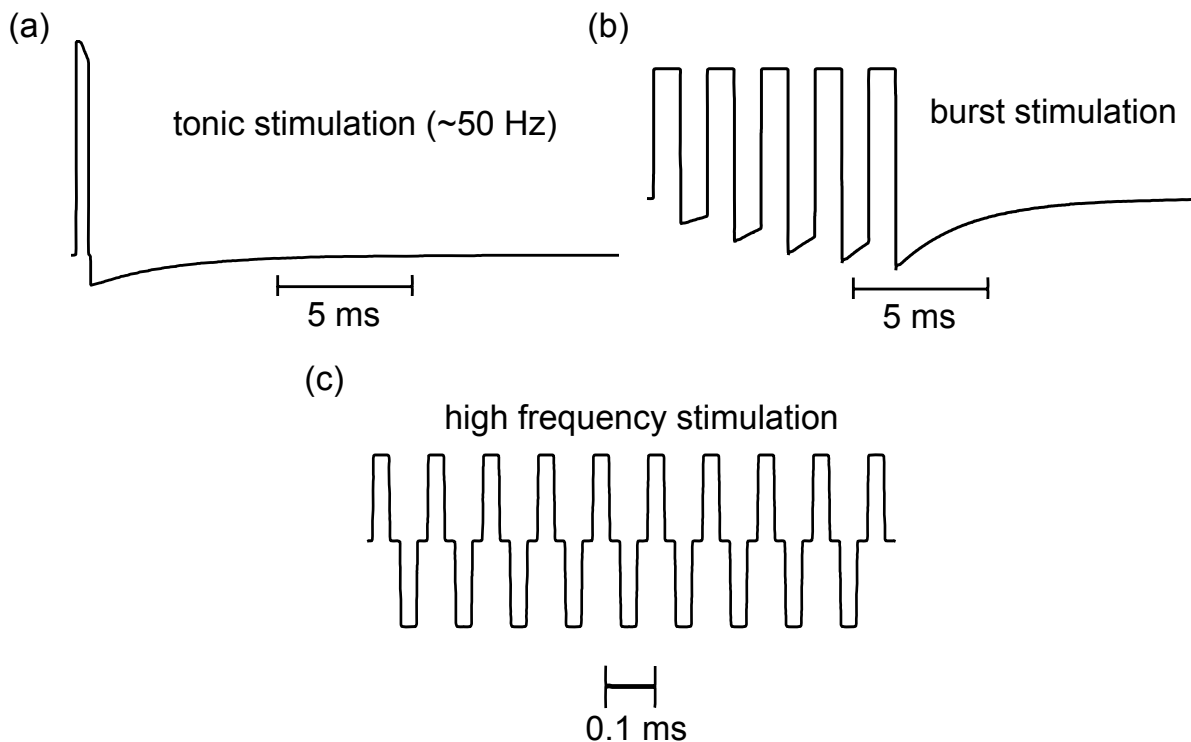


Fig. 5.2 Common stimulation waveforms for spinal cord stimulations. (a) Tonic stimulation, with $\approx 30 \mu\text{s}$ of pulses at a burst rate of 50-60 Hz. (b) Burst stimulation, consisting of five-pulse train with 500 Hz of intra-burst frequency and burst rate of 40 Hz and (c) Kilohertz-frequency stimulation (> 1 kHz). Schematics adapted from [Lempka and Patil (2018)].

Besides pain control, spinal cord stimulation have also been applied to improve motor control capabilities for animals and human subjects with sever spinal cord injuries and paralysis [Moraud et al. (2016); Wagner et al. (2018); Wenger et al. (2014)]. Empirical evidence from these studies have shown that external electrical stimulations can facilitate coordinate movements in rats and primate subjects in the absence of supra-spinal inputs from the brain. Pairs of implants in the brain and in the spinal cord work as recording and stimulating electrodes to establish a neural interface, bypassing the injured part of the spinal cord. The neural interface can in turn transmit signals between the motor cortex and neurons controlling limb motions, enabling subjects with partial or complete loss of motor control to regain voluntary motor functionalities [Ajiboye et al. (2017); Capogrosso et al. (2016)].

Despite success in spinal cord stimulation for both pain relief and motor control, there are still major hurdles preventing such treatment to achieve higher success rate and fewer complications [Eldabe et al. (2016); Kumar et al. (2006)]. From a device design and stimulation protocol point of view, the main challenges for existing spinal cord stimulation technologies are: 1. Non-localized stimulated regions with existing device and stimulation waveforms, and 2. Inability to steer the stimulation hotspot in the case of lead migration.

Previous computational studies have pointed out that with paddle or lead-shaped SCS devices placed in the mid-line of the dorsal column, the axons within the spinal cord cross-section would be activated in a layer-by-layer fashion by either tonic, burst, or kilohertz-frequency stimulation waveforms, without the ability to localize the stimulation hotspot within the spinal cord cross-section [Lempka et al. (2015); Zander et al. (2020)]. Since the neuromodulation research community still lack consensus in the underlying mechanisms of action for spinal cord stimulation [Caylor et al. (2019); Jensen and Brownstone (2019)], the non-localized stimulation waveforms prevent researchers to stimulate specific spinal cord tracts and pinpoint the exact neural circuitry responsible for transmitting/blocking neuropathic pain. Furthermore, in some cases, non-localized spinal cord stimulation can negatively affect the balance and proprioception of patients by accidentally triggering other regions of the spinal cord tracts with higher stimulation intensities [Rijken et al. (2013); Yozu et al. (2016)].

The most common complication for spinal cord stimulation is the long-term reduction in pain relief due to lead migration [Mekhail et al. (2011)]. Variation in intracranial pressure caused by body movement or external impact can push the SCS device away from its original implant site, reducing the electrical stimulation intensity to the intended regions [McGreevy et al. (2012)]. Currently, lead migration often requires surgical intervention, since the SCS device is unable to re-focus its stimulation hotspot once it is displaced, given the device

geometries and stimulation waveforms. Novel approaches such as using penetrating intraspinal electrodes can greatly reduce the risk of lead migration [Holinski et al. (2016); Moritz et al. (2007)], but involves greater risks of infections or dural punctures [Barolat (1993)], and is therefore not being actively pursued for clinical applications.

In light of the challenges existing spinal cord stimulation technologies face, in this chapter, a new flexible stimulating electrode combined with stimulation waveform that is able to localize and steer the stimulation hotspot for spinal cord stimulations is proposed. The temporal interfering stimulation waveform used in this chapter originated from the amplitude modulated signal in telecommunications, and was recently applied to deep brain stimulation to stimulate deeper brain tissues. The potential of localizing and steering the stimulation hotspot with temporal interfering stimulation have attracted broad interests among the neuromodulation research community. Here, the working principle of the temporal interfering stimulation is presented, and a combination of experimental work and computational modeling are carried out to investigate how to optimize the spinal cord stimulation performance with temporal interfering stimulation. Researchers can use the methods developed in this chapter as a tool to stimulate specific spinal cord tracts and investigate the action of mechanisms for neuropathic pain propagation. The insights from the modeling results can also further guide the development for next-generation spinal cord stimulation systems.

5.2 Working principle of temporal interfering stimulation

According to the principle of superposition, when two Alternating Current (AC) electric fields \vec{E}_1, \vec{E}_2 with different frequencies f_1, f_2 interact with each other, the resulting electric field \vec{E}_{net} is the sum of two electric fields, which can be written as [Freegarde (2012)]:

$$\vec{E}_{net} = \vec{E}_1 + \vec{E}_2. \quad (5.1)$$

When the frequency difference between the two interacting electric fields is small, such that $f_2 = f_1 + \Delta f$, the resulting electric field \vec{E}_{net} is a high frequency AC electric field (with frequency being the average of f_1 and f_2) modulated by a low frequency envelope (with frequency being Δf). In acoustics, this kind of envelope pattern is known as ‘beat frequency’, as it creates an audible low frequency humming sound [Jeans (1968)]. In electronics and telecommunications, this kind of wave is called Amplitude Modulated (AM) signal, and is used to transmit audio in radio broadcasting [Noguchi et al. (1986)].

The relative intensity of the amplitude modulated signals are determined by the both the individual amplitude of the interfering signals and their intersecting angle. Figure 5.3 shows some examples of resulting electric fields \vec{E}_{net} due to the interference of two original AC electric fields \vec{E}_1 and \vec{E}_2 . In Figure 5.3(a), two electric fields \vec{E}_1 and \vec{E}_2 are parallel and equal in amplitude. The resulting \vec{E}_{net} is a perfectly modulated electric field \vec{E}_{AM} , where minimum intensity $|\vec{E}_{min}|$ is zero and maximum intensity $|\vec{E}_{max}|$ is twice of $|\vec{E}_1|$ or $|\vec{E}_2|$. The envelope intensity of the amplitude modulated signal is termed the temporal interfering fields intensity, $|\vec{E}_{TI}|$, in [Grossman et al. (2017)]. $|\vec{E}_{TI}|$ is defined as the difference between maximum and minimum of the modulation envelope, and is therefore given as:

$$|\vec{E}_{TI}| = |\vec{E}_{max}| - |\vec{E}_{min}| \quad (5.2)$$

$$= (|\vec{E}_1| + |\vec{E}_2|) - (|\vec{E}_1| - |\vec{E}_2|) \quad (5.3)$$

$$= 2|\vec{E}_2|. \quad (5.4)$$

In Figure 5.3(b), Two electric fields \vec{E}_1 and \vec{E}_2 are parallel, but with different amplitude where $\vec{E}_1 = 2\vec{E}_2$. This results in a partially modulated \vec{E}_{AM} where minimum intensity $|\vec{E}_{min}|$ is $|\vec{E}_1| - |\vec{E}_2|$ and maximum intensity $|\vec{E}_{max}|$ is $|\vec{E}_1| + |\vec{E}_2|$. The envelope intensity $|\vec{E}_{TI}|$ in this case is also $2|\vec{E}_2|$.

The case for Figure 5.3(c) requires more consideration. The two electric fields \vec{E}_1 and \vec{E}_2 have the same amplitude, but are intersecting each other with an angle $\theta = 60^\circ$. In this case,

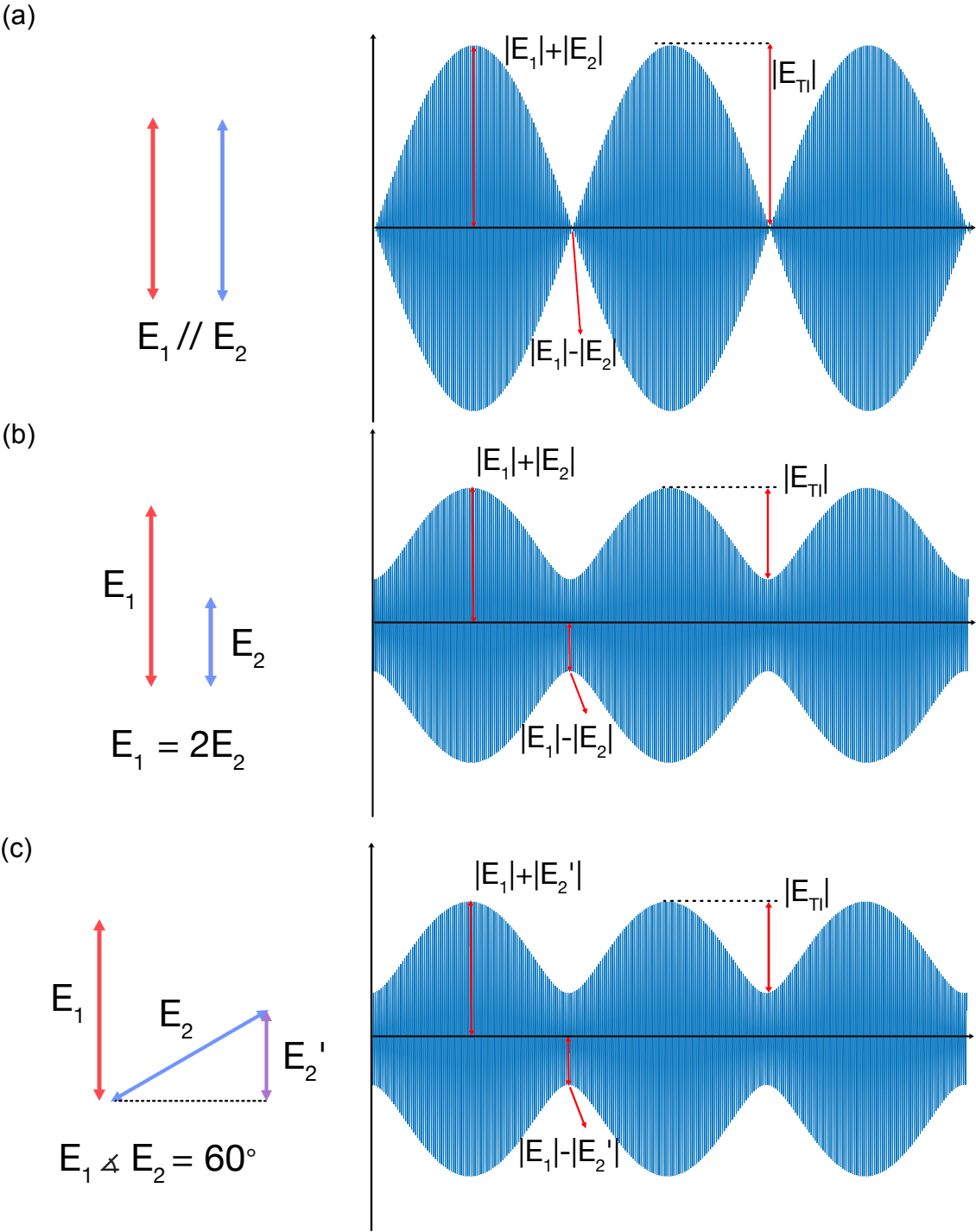


Fig. 5.3 Examples of temporal interfering fields due to two electric fields with different amplitude and direction. (a) Two electric fields \vec{E}_1 and \vec{E}_2 are parallel and equal in amplitude. (b) Two electric fields \vec{E}_1 and \vec{E}_2 are parallel, but $\vec{E}_1 = 2\vec{E}_2$. (c) Two electric fields \vec{E}_1 and \vec{E}_2 have the same amplitude, but are intersecting each other with a 60° angle.

the vectors \vec{E}_1 and \vec{E}_2 need to be projected onto the same direction in order to calculate the relative amplitude of the modulated electric field \vec{E}_s . Along the \vec{E}_1 direction, \vec{E}_2 projection \vec{E}_2' would be:

$$|\vec{E}_2'| = |\vec{E}_2| \times \cos(60^\circ). \quad (5.5)$$

Along a result, the amplitude modulated signal along the \vec{E}_1 in Figure 5.3(c) would have the same relative amplitude as the case in Figure 5.3(b).

Clinical applications of amplitude modulated stimulations

For more than 70 years, physicians and researchers have been using amplitude modulated electrical signals for physical therapies and rehabilitations. Dating back to the 1950s, scientists found that the so-called 'interferential currents' were able to penetrate into deeper tissues compared to pure AC electric currents, and considered these types of waveforms to be great candidates for treating muscle pain and inflammatory diseases [Hans (1952); Leeb (1955)]. Advancements in the following decades have broadened the application of interferential currents to all types of physio-therapies [Ganne (1976); Goats (1990); Nikolova-Troeva (1967)].

Recently, amplitude modulated signals have been used as stimulation waveform for non-invasive deep brain stimulations (DBS) [Grossman et al. (2017)]. The experimental setup involved attaching two working electrodes on the mice's scalp and supplying transcranial AC electric fields with different frequencies. The resulting amplitude modulated signal caused by the two transcranial electrodes were termed '*Temporal Interfering Stimulation*' (TIS). Major findings from this study indicated that with surface electrodes, brain regions experiencing weakly modulated stimulations (surface areas closer to either one of the working electrodes) will not result in neural activities, whereas neural activities were found in deep brain regions experiencing strongly modulated signal. The results from this study also showed that different regions of the motor cortex can be selectively stimulated by adjusting the ratio of intensities between the electric field strengths. This study brought up much excitement among the neuromodulation research community. The ability to selectively stimulate the subsurface areas of the nervous system opens up the possibility to localize the stimulation region. Researchers can therefore use this so-called 'temporal interfering' stimulation waveform to either validate various hypotheses for different neuromodulation techniques, or selectively stimulate specific regions in the tissue for different applications.

In previous works related to applying TIS to deep brain stimulations, instead of minimizing the stimulation hotspot or maximizing the hotspot steerability, focus is mainly put on penetrating as deep into the brain without affecting the tissues adjacent to the electrodes. Moreover, previous works in TIS optimized the electric field distribution based on the stimulation waveforms in order to achieve maximum electric field intensities, whereas the neuron response subjecting to these electrical stimulations were neglected in the modeling process. In this chapter, a comprehensive computational model including the axon response and electric field distribution with external electric stimulation was developed. The coupled computational model is able to capture the nonlinear relationship between electric field intensities and resulting stimulated hotspot with TIS. Parameter studies in stimulation protocols and SCS device geometries is also carried out with the coupled computational model to further optimize the performance for spinal cord stimulation using TIS in different applications.

5.3 Computational models for spinal cord stimulation

This section will cover the development of the computational model used to demonstrate the steerability and spatial resolution of using Temporal Interfering Stimulation (TIS) for spinal cord stimulation. The computational model consists of two parts, which are:

1. Equivalent circuit model to calculate the axon response subjecting to electrical stimulation with given frequency and intensity.
2. FEM model to calculate the electric potential and electric field lines across the cross-section of a spinal cord with an external applied electric potential.

The process of analyzing the steerability and spatial resolution of using TIF for spinal cord stimulation is as follow:

1. For a particular stimulation configuration (i.e., pre-determined frequencies for two electric fields \vec{E}_1 and \vec{E}_2 by two working electrodes with fixed placements), a lookup table (herein referred to as the 'activation map') for axonal response is generated with the equivalent circuit model.
2. For this given stimulation configuration, the two-dimensional electric field intensity and electric potential distribution along the cross-section of the spinal cord is generated with the FEM model.
3. The spatial distribution of axonal responses $f_n(x,y)$ within the cross-section of the spinal cord is obtained by plugging in the spatial distribution of electric field intensities $|\vec{E}_1|$ and $|\vec{E}_2|$ and intersecting angle θ into the activation map obtained from step 1.

The following subsections will introduce the model development process and key insights obtained from the computational model developed in this chapter.

Equivalent circuit model for axon activation

To understand how neural circuits in the spinal cord respond to external applied electrical stimulation, an equivalent electrical circuit models for both the sensory and motor axons were developed using circuit model software Simulink [MathWorks (2018)] (Figure 5.4). First proposed by Alan Hodgkin and Andrew Huxley in their seminal work [Hodgkin and Huxley (1952)], the Hodgkin-Huxley model describes how action potentials are initiated and propagated in neurons upon receiving electrical stimulations. Initially developed to describe the action potentials in a squid giant axon, the Hodgkin-Huxley model treats the components on the excitable cell membranes as a combination of active and passive electrical components. The voltage-gated ion channels on the membrane responsible for initiating action potentials are modeled as nonlinear resistors, governed by a set of nonlinear differential equations. By extending the types of ion channels and adjusting the parameters in the original Hodgkin-Huxley equations, the equivalent circuit approach have been widely applied to study how different types of neurons respond to electrical stimulations [FitzHugh (1961); Hille (1978); Nagumo et al. (1962)].

For both the sensory and motor axon, the types of ion channels shown in Figure 5.4 followed the McIntyre-Richardson-Grill (MRG) model, which is a circuit model developed to describe the mammalian axon response when subjected to electrical stimulations [McIntyre et al. (2002)]. As shown in Figure 5.4, the circuit model include fast sodium channels, persistent sodium channels, fast potassium channels, slow potassium channels, and leakage current channels. It is worth noting that apart from the ion channels (located in nodal regions along the myelinated axon known as the node of Ranvier), the original MRG model also included passive electrical components such as the myelin and paranodal main segments along the longitudinal (i.e., rostral-caudal) direction of the axons.

In the MRG model, these passive components in the internodal regions were modeled as linear resistor-capacitor circuits, with RC time constant less than an order of magnitude smaller than their nodal counterparts [Huxley and Stämpfli (1949); Tasaki (1955)]. The reason to include these passive components mainly was to calculate the action potential propagation speed along the myelinated axons in the longitudinal direction. In this study, instead of investigating the action potential propagation, focus is put on the steerability and localized neuron recruitment of TIF stimulation in the transverse plane. As a result, to reduce computational demands, the linear capacitor-resistor components in the internodal regions were lumped together with the ion channels in the equivalent circuit model developed in this chapter. Figure 5.4 represents

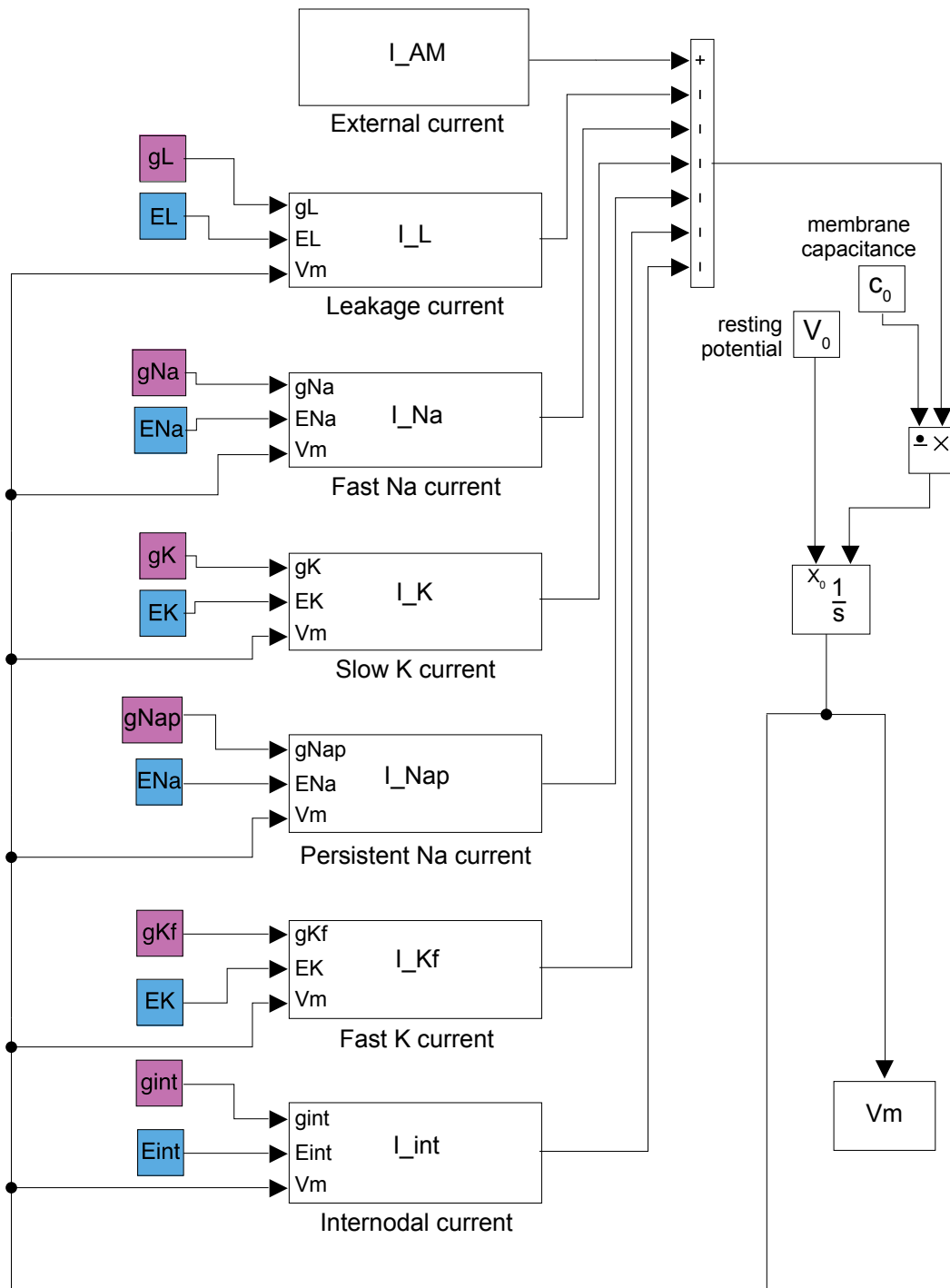


Fig. 5.4 Simulink block diagram showing the equivalent circuit model for sensory and motor axons [MathWorks (2018)]. Ion channels include fast sodium channels, persistent sodium channels, fast potassium channels, slow potassium channels, leakage current channels, and internodal current. Detailed gating variable and rate constant values x, α_x, β_x for both the sensory and motor axons can be found in Appendix B.

the equivalent circuit model with internodal parameters representing an axon with diameter of $11.5 \mu\text{m}$ [Zander et al. (2020)].

For the model shown in Figure 5.4, ionic current flowing through each type of the voltage-gated ion channel i is determined by the nonlinear channel conductance g_i . For both the sensory and motor axons, the nonlinear conductances g_i of each of the ion channels i can be described by specific gating variable x , where $0 \leq x \leq 1$. For example, the current flowing through the fast sodium channel in the sensory axon model, I_{Na} , is governed by two gating variables, m and h , in the form of:

$$I_{Na} = \bar{g}_{Na} \times m^3 h (V_m - E_{Na}), \quad (5.6)$$

where \bar{g}_{Na} is the maximum value of the nonlinear fast sodium channel conductance g_{Na} ($g_{Na} = \bar{g}_{Na} \times m^3 h$), V_m is the membrane voltage, and E_{Na} is the sodium reversal potential. In the original Hodgkin-Huxley model as well as the MRG model, all the gating variables x are further governed by two membrane voltage dependent rate constants, α_x , β_x , such that:

$$\frac{dx}{dt} = \alpha_x(1 - x) - \beta_x. \quad (5.7)$$

For the fast sodium channel, both the m and h gating variables have a pair of rate constants (α_m , β_m) and (α_h , β_h), and the governing differential equations for m and h can be written as:

$$\frac{dm}{dt} = \alpha_m(1 - m) - \beta_m, \quad (5.8)$$

$$\frac{dh}{dt} = \alpha_h(1 - h) - \beta_h. \quad (5.9)$$

The specific values of the rate constants (α_m , β_m) and (α_h , β_h) as functions of membrane voltage V_m can be obtained by fitting the MRG model from Equation 5.6 to voltage-clamp experiments [Clerx et al. (2019); Horn and Vandenberg (1984)]. In this chapter, the values for all the gating variables x and rate constants α_x and β_x follow the previously reported values for human motor and sensory axons in the spinal cord [Capogrosso et al. (2013); Gaines et al. (2018); Howells et al. (2012)]. Detailed values for all the parameters used in the equivalent circuit model in Figure 5.4 can be found in Appendix B.

Axon activation map

As previously shown in Figure 5.3, the list of parameters deciding the relative intensity and characteristics of an amplitude modulation signal $E_{AM}^{\vec{}}$ are:

- f , the base frequency for the AC electric fields,
- Δf , the frequency difference between two AC electric fields (i.e., $f_2 = f + \Delta f$),
- $|\vec{E}_1|$, electric field 1 intensity,
- $|\vec{E}_2|$, electric field 2 intensity,
- θ , the intersecting angle between Electric field 1 and 2.

Expressed in an equation, the functional relationship F between the amplitude modulated signal $E_{AM}^{\vec{}}$ and all the parameters above can be written as:

$$E_{AM}^{\vec{}} = F(f, \Delta f, |\vec{E}_1|, |\vec{E}_2|, \theta). \quad (5.10)$$

The goal of the equivalent circuit model for axon activation is to determine whether a particular electrical stimulation can elicit action potentials. If action potentials were elicited, the circuit model from Figure 5.4 can further calculate the oscillation frequency f_n of the neuron given this electrical stimulation. As a result, the functional relationship G between neural oscillation frequency f_n given a TIS input $E_{AM}^{\vec{}}$ can be written as:

$$f_n = G(E_{AM}^{\vec{}}) = G(F(f, \Delta f, |\vec{E}_1|, |\vec{E}_2|, \theta)). \quad (5.11)$$

Under this framework, both the functions F and G can be highly nonlinear and intractable, so the process of obtaining the spatial distribution of axon activities $f_n(x, y)$ in the cross-section of a spinal cord can be also extremely compute-intensive.

Fortunately, in clinical settings, the frequencies of two electric fields (f_1 and f_2 , corresponding to f and Δf in Equation 5.10) are pre-determined based on specific targeted tissues and applications. In the case for deep brain stimulation, typical values for f and Δf are 2000 Hz and 20 Hz, respectively. Also, as previously shown, for two non-parallel electric fields \vec{E}_1 and \vec{E}_2 , the equivalent temporal interfering field $E_{AM}^{\vec{}}$ along a given direction can be obtained by projecting both \vec{E}_1 and \vec{E}_2 along that direction, i.e., say $\vec{E}_1 > \vec{E}_2$, and \vec{E}_1 and \vec{E}_2 are intersecting

with each other with an angle θ . The equivalent temporal interfering field $E_{AM}^{\vec{}}$ equivalent along the \vec{E}_1 direction would be:

$$E_{AM}^{\vec{}} = \vec{E}_1 + \vec{E}_2 \times \cos \theta, \quad (5.12)$$

$$\text{where } |\vec{E}_{max}| = |\vec{E}_1| + |\vec{E}_2| \times \cos \theta \quad (5.13)$$

$$\text{and } |\vec{E}_{min}| = |\vec{E}_1| - |\vec{E}_2| \times \cos \theta \quad (5.14)$$

given $|\vec{E}_2| \times \cos \theta > |\vec{E}_1|$. The axon response subjected to a given pair of electric field \vec{E}_1 and \vec{E}_2 intersecting with an angle θ , can be therefore obtained by projecting \vec{E}_1 and \vec{E}_2 in the same particular direction such that the resulting $E_{AM}^{\vec{}}$ elicits the highest level of neural activity. A detailed vector projection MATLAB script for calculating the equivalent $E_{AM}^{\vec{}}$ from two electric fields \vec{E}_1 and \vec{E}_2 based on their intersecting angle θ and magnitude can be found in Appendix B.

According to above conditions, it is reasonable to decouple the frequency parameters (f and Δf) and intersecting angle θ from Equation 5.10. The functional relationship K between neural oscillation frequency f_n and relevant parameters can therefore be simplified to:

$$f_n = K(|\vec{E}_1|, |\vec{E}_2|). \quad (5.15)$$

Figure 5.5(a) is the activation map of a sensory axon with a diameter of $11.5 \mu\text{m}$ as functions of AC electric field intensity $|\vec{E}_1|$ and $|\vec{E}_2|$, where $f_1 = 2000 \text{ Hz}$ and $f_2 = 2010 \text{ Hz}$. The activation map represents the relationship of neural oscillation frequency f_n given an amplitude modulated signal input $E_{AM}^{\vec{}}$, where $E_{AM}^{\vec{}}$ in this case can be fully described by two parallel intersecting electric fields \vec{E}_1 and \vec{E}_2 . The activation maps can be used as lookup tables, where it can be later used to construct the spinal distribution of neural oscillation $f_n(x, y)$ in a spinal cord cross-section by plugging in the electric field intensities $\vec{E}_1(x, y)$, $\vec{E}_2(x, y)$ at specific locations (x, y) .

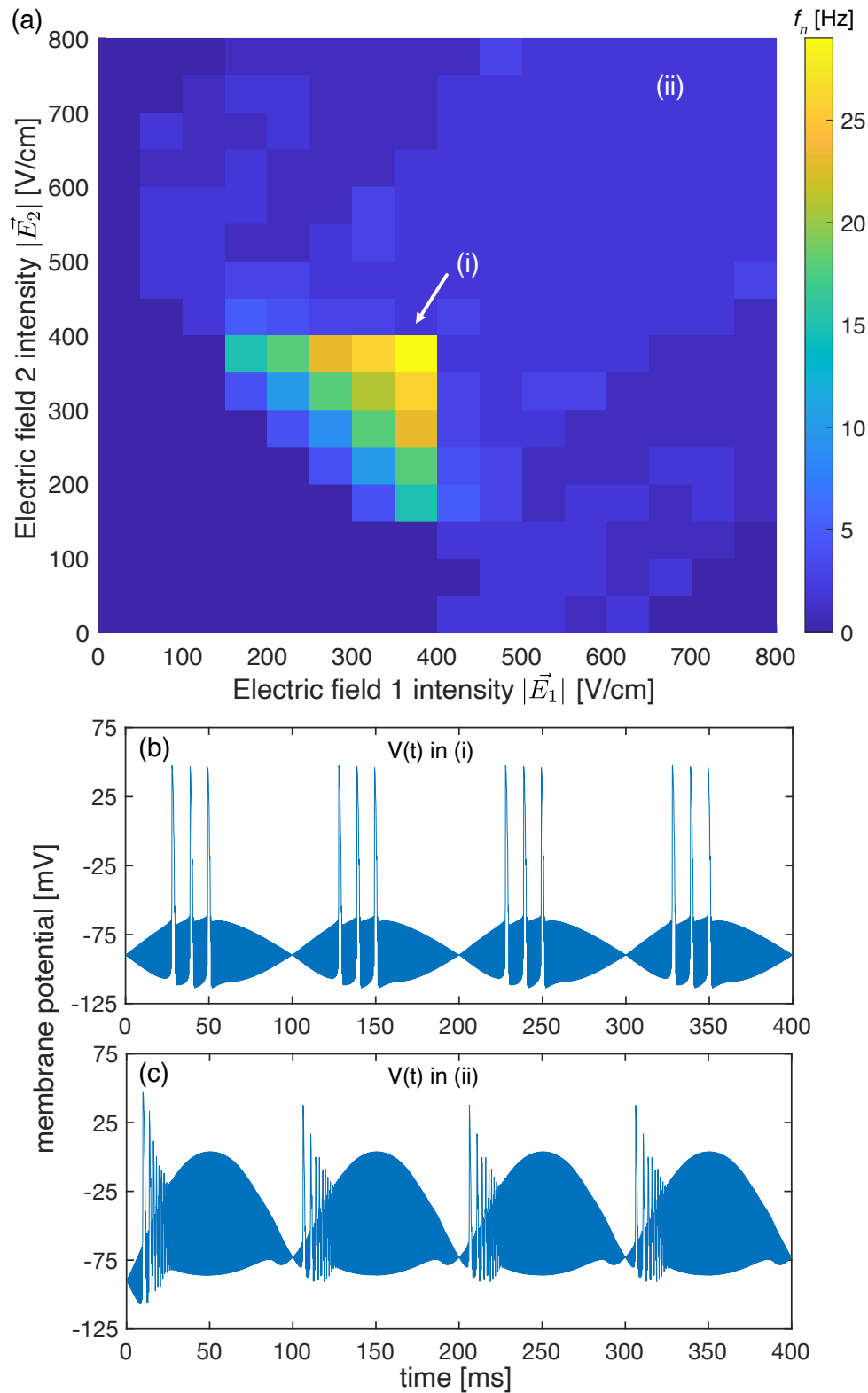


Fig. 5.5 (a) The activation map of a sensory axon with a diameter of $11.5 \mu\text{m}$ as functions of both $|\vec{E}_1|$ and $|\vec{E}_2|$, $f_1 = 2000 \text{ Hz}$ and $f_2 = 2010 \text{ Hz}$. (b) The time-dependent membrane potential in region (i), when E_{AM} is a perfectly modulated signal with $|\vec{E}_1| = |\vec{E}_2| = 400 \text{ V/cm}$. (c) The axonal response in region (ii) when E_{AM} is a perfectly modulated signal with $|\vec{E}_1| = |\vec{E}_2| = 700 \text{ V/cm}$.

Goldilocks zone for using temporal interfering stimulation

As seen from Figure 5.5(a), since the amplitude modulated signal $E_{AM}^{\vec{}}$ is symmetrical about the diagonal line $|\vec{E}_1| = |\vec{E}_2|$, the neural oscillation rate f_n is also symmetric about the diagonal line $|\vec{E}_1| = |\vec{E}_2|$. The diagonal line $|\vec{E}_1| = |\vec{E}_2|$ corresponds to a perfectly modulated signal ($|\vec{E}_1|/|\vec{E}_2| = 1$, corresponding to Figure 5.3(a)), and as the ratio $|\vec{E}_1|/|\vec{E}_2|$ of the stimulation $E_{AM}^{\vec{}}$ deviates from 1, $E_{AM}^{\vec{}}$ becomes less modulated. At lower electric field intensity, ($|\vec{E}_1|$ and $|\vec{E}_2|$ below 200 V/cm), no neural firing events were recorded, as the intensity of the stimulation is equivalent to subthreshold stimulus. At moderately high electric field intensity, which corresponds to region (i) in Figure 5.5(a), axons begin to exhibit high levels of activity, such in the case shown in Figure 5.5(b). As seen from Figure 5.5(b), the neural oscillation rate f_n is 30 Hz when subjected to a perfectly modulated stimulation $E_{AM}^{\vec{}}$ with moderately high intensity ($|\vec{E}_1| = |\vec{E}_2| = 400$ V/cm, so $|\vec{E}_{max}^{\vec{}}| = 800$ V/cm).

Further increasing the electric field intensity from region (i) onward instead led to reduction in neural activity. Figure 5.5(c) shows the axonal response when subjected to a perfectly modulated stimulation $E_{AM}^{\vec{}}$ with high intensity ($|\vec{E}_1| = |\vec{E}_2| = 700$ V/cm, so $|\vec{E}_{max}^{\vec{}}| = 1400$ V/cm, corresponding to region (ii) in Figure 5.5(a)). As seen from the time-dependent membrane voltage in Figure 5.5(c), unlike the case with moderate electric field intensity where neurons are firing three action potentials during the interval of one envelope stimulation (i.e., three firings in every 100 ms as in Figure 5.5(b)), the membrane potential in Figure 5.5(c) exhibits a capacitive behavior, where the external stimulation $E_{AM}^{\vec{}}$ are constantly charging and discharging the membrane capacitor without eliciting action potentials.

The inhibition of neuron activities with high intensity $E_{AM}^{\vec{}}$ can be understood by considering the frequency-dependent properties of the equivalent circuit model [Hutcheon and Yarom (2000)]. Figure 5.6(a) and Figure 5.6(b) illustrate the relative impedance Z as a function of input current frequency between a classical RC-circuit and the simplified equivalent circuit of an axon, respectively. Here the complex-valued impedance Z takes the definition from [Puil et al. (1986)] as:

$$Z = \frac{\text{FFT of voltage response}}{\text{FFT of current input}} \quad (5.16)$$

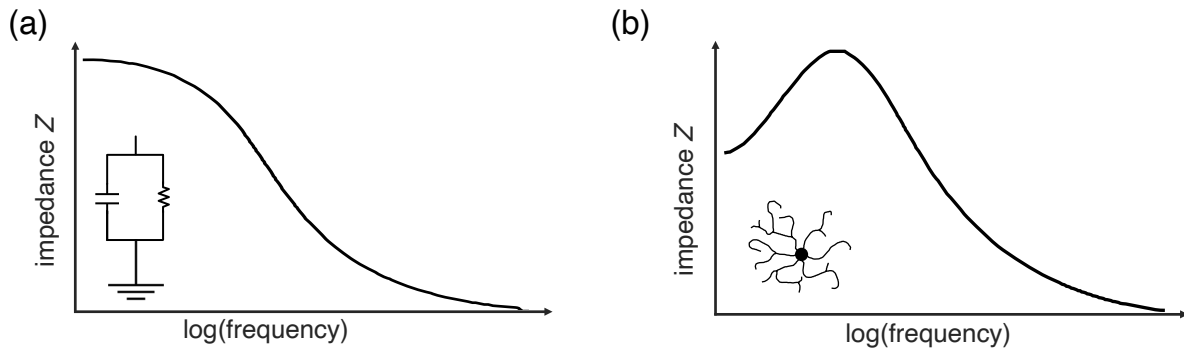


Fig. 5.6 Logarithmic relationship of impedance Z as a function of input current frequency between (a) an RC circuit and (b) a neuron. Schematic adapted from [Hutcheon and Yarom (2000)].

At higher excitation frequencies, the impedance Z between a RC-circuit and an axon are similarly low. This points to the fact that with high frequency stimulation, the neuron behaves similar to a resistor-capacitor system, where the membrane is a capacitor constantly being charged and discharged. The charge stored in the membrane capacitor in a short charging cycle during high frequency stimulation is not sufficient to elicit an action potential, and the following discharging cycle depletes the stored charges in the capacitor. This is the reason why neurons do not fire action potentials when subjected to pure high frequency AC stimulations [Lindén et al. (2010); Pettersen and Einevoll (2008)]. The lack of action potential firing during high frequency excitation also explains why experimentalists first approximated neurons as low-pass filters, according to the frequency-dependent impedance Z of a RC-circuit [Connelly et al. (2016); Tohidi and Nadim (2009)].

For amplitude modulated stimulation such as TIS with $E_{AM}^{\vec{}}$, the waveform involves both high frequency (the 2 kHz AC electric field) and low frequency (the 10 Hz amplitude envelop) components. At relative low stimulation intensity, say $|\vec{E}_1| = |\vec{E}_2| = 200 \text{ V/cm}$, both the low frequency and high frequency components are subthreshold stimulus, thus no action potential was elicited. At higher stimulation intensity (region (i) in Figure 5.5(a)), both the low and high frequency component of $E_{AM}^{\vec{}}$ increased in intensity. Since the impedance Z for neurons are high at lower frequencies, according to Equation 5.16, the low frequency envelop of the input current would elicit high amount of change in membrane voltage. As a result, high level of neurons activity were recorded, as the case shown in Figure 5.5(b). As electric field intensity $|E_{AM}^{\vec{}}|$ continues to increase, eventually the high frequency component dominates the stimulation waveform $E_{AM}^{\vec{}}$, and overall membrane response is dominated by high frequency impedance. This corresponds to region (ii) in Figure 5.5(a), where neuron membrane acts like

a capacitor experiencing fast charging and discharging process subjecting to high frequency AC stimulation without firing action potentials (time-dependent membrane voltage shown in Figure 5.5(c)).

This '*Goldilocks zone*' also presents a substantial difference in calculating the activated regions by TIS from previous works, where the envelop intensity $|\vec{E}_{TI}|$ (i.e., $|\vec{E}_{max}| - |\vec{E}_{min}|$ of a \vec{E}_{AM} stimulation) was the only parameter used to estimate the activated region [Cao and Grover (2020); Grossman et al. (2017); Huang et al. (2020); Huang and Parra (2019); Rampersad et al. (2019)]. As seen from Figure 5.5, higher envelop intensity does not always correlate to higher neural activity. Therefore, using envelop intensity to calculate activation region not only do not provide proper causation, and would also lead to inaccurate estimation for the activated regions. In contrast, axonal response from the circuit model directly link the electric fiend intensity $|\vec{E}_{AM}|$ to neural oscillation frequency f_n , giving a much stronger causal relation between the activated region and the applied temporal interfering stimulation.

To conclude, the activation map shown in Figure 5.5 demonstrates the axon response to temporal interfering stimulations with different degrees of modulation and intensities. The main takeaway information from Figure 5.5 is that even though neuron activity is higher when subjecting to highly modulated electrical stimulation \vec{E}_{AM} , there is a '*Goldilocks zone*' for stimulation intensity in order to achieve maximum neural modulation f_n . This finding can be explained by the frequency-dependent impedance Z of neurons, which were first observed in classical electrophysiology experiments [Adrian and Lucas (1912); Lucas (1907)]. These previous findings showed that action potential initiation are dependent on both the intensity and the frequency of the electrical stimulation, and is consistent with the results shown in this chapter.

FEM model for electric potential distribution

For a given stimulation configuration, the electric potential distribution and electric field lines are calculated with a Finite-Element-Method (FEM) based computational model, consisting of the spinal cord with different tissues and the SCS device. Figure 5.7 and Table 5.1 show the cross-sectional view and corresponding conductivity values of the FEM model in this study. The morphologies of different tissues are based on the spinal cord cross-section of previous cadaveric study at T11 level [Kameyama et al. (1996)] and adapted from [Khadka et al. (2020)]. The computational domains for the spinal cord include the gray matter, white matter, cerebrospinal fluid, and dura mater.

The flexible SCS device used in this study was fabricated following the protocol of NeuroGrid, an ultra-conformable and flexible neural array made of biocompatible materials [Khadagholi et al. (2015)] (Photo shown in Figure 5.7). The soft Parylene C substrate of the SCS device enables the neural array to conform to the surface of the dura mater and allow electrodes to have direct contact with the stimulation site. Furthermore, the PEDOT:PSS coating on the electrodes is able to decrease the electrical impedance mismatch between tissues and electrodes [Owens and Malliaras (2010)], thus allowing larger capacitive charge injection capabilities while avoiding unwanted electrode degradation due to Faradaic effects [Castagnola et al. (2014)].

The electrical conductivity values shown in Table 5.1 were applied to each domain in Figure 5.7. The conductivity for different tissues were assumed to be isotropic, except for the white matter, whereas the myelinated axons in the white matter result in a much higher conductivity value in the longitudinal direction compared to the transverse direction (in this study we use the transverse conductivity for the white matter for calculating the electric potential distribution in the cross-section of the spinal cord). When simulating the flexible SCS in operation, a constant voltage was set as the boundary condition for the working electrode, whereas all the other electrodes are set to be grounded. Finally, the electric potential distribution in the spinal cord tissue was solved in COMSOL software using finite element method [COMSOL (2018)].

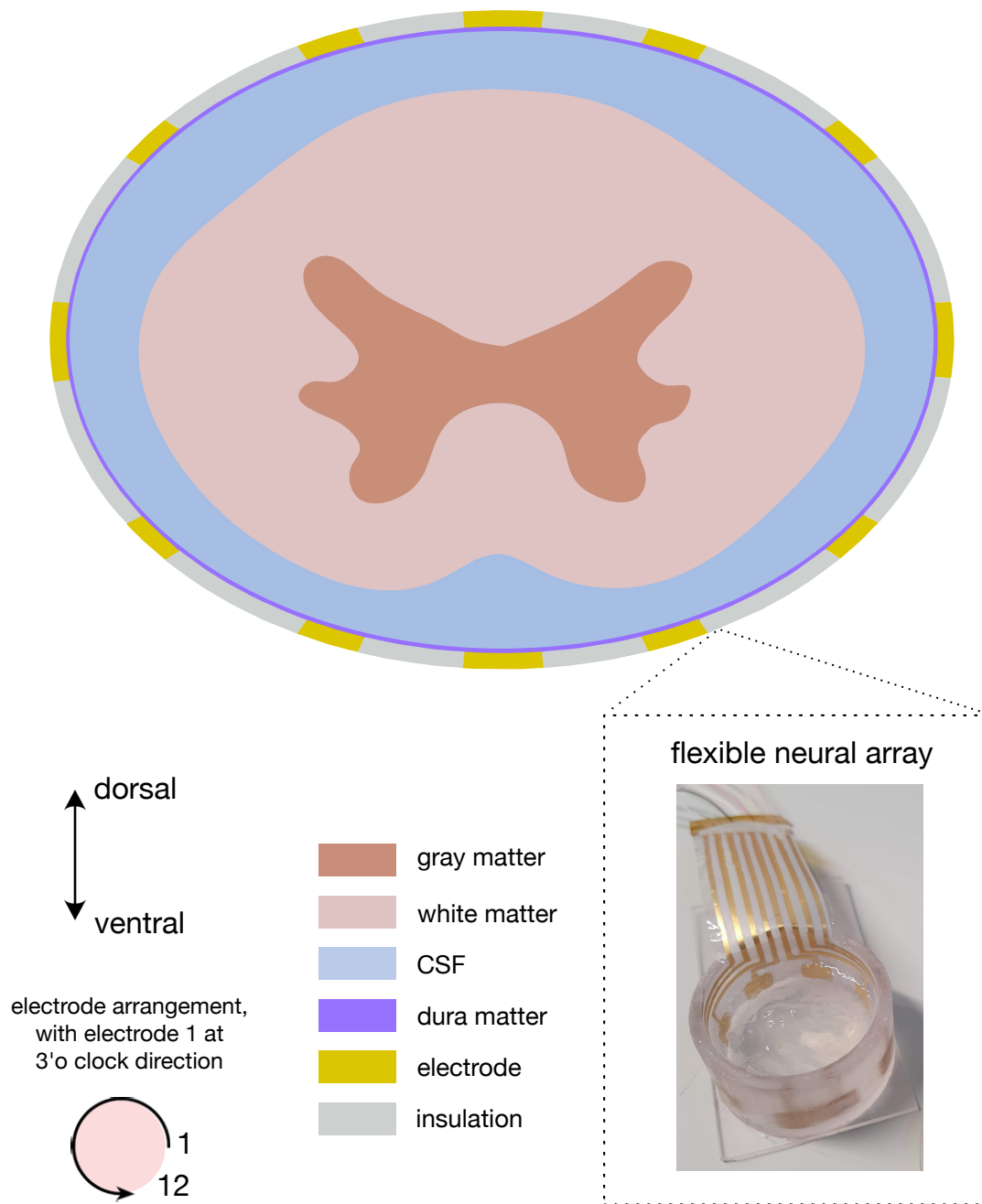


Fig. 5.7 A cross-sectional view of the computational domain consisting of spinal cord with different regions- gray matter, white matter, cerebrospinal fluid, and dura mater. Outer ring is the flexible SCS device made of Parylene C substrate and PEDOT:PSS coated gold electrodes. Electrodes are numbered from 1 to 12 in counterclockwise direction, with electrode 1 located at 3 o'clock direction. The photo of the flexible SCS device surrounding a tissue phantom is shown at the bottom right.

Table 5.1 Tissue conductivity values used in the computational model.

Tissue	Conductivity (S/m)	Reference
Gray matter	0.230	Hernández-Labrado et al. (2011)
White matter (transverse)	0.083	Tuch et al. (2001)
Cerebrospinal fluid	1.700	Baumann et al. (1997)
Dura mater	0.600	Anderson et al. (2019)
Foreign body encapsulation	0.110	Zander et al. (2020)

5.4 Localized spinal cord stimulation via temporal interfering fields

To illustrate the complete workflow of calculating the spatial axon recruitment pattern via temporal interfering stimulation (TIS), a step-by-step process from electrode-configuration, parameter-selection, and data-processing is presented here (Figure 5.8). The targeted localized stimulation region here is the dorsal horn, since it is the initial site for pain processing and plays a critical role in neuropathic pain [Costigan et al. (2009)]. Conventional SCS devices operating in either tonic, burst or kilohertz-frequency stimulation are not able to stimulate the dorsal horn alone without evoking high levels of neural activities in the dorsal column. However, recent studies have suggested targeting the interneurons in the dorsal horn might be the main mechanism for inhibiting neuropathic pain signal transmission [Holinski et al. (2016); Jensen and Brownstone (2019)]. Therefore, the dorsal horn would be an ideal candidate to validate the localization capabilities of TIS waveforms combined with the flexible SCS devices developed in this chapter.

1. For dorsal horn stimulation, electrodes 3 and 11 (numbering convention referred to Figure 5.7) were chosen to be the working electrodes, while all other ten electrodes were grounded. Electrode 3 supplies a 2 V AC current of 2000 Hz and Electrode 11 supplies a 2 V AC current of 2010 Hz. Figure 5.8(a) shows the electric potential profile and respective electric field lines $\vec{E}_1(x,y)$ and $\vec{E}_2(x,y)$ in the spinal cord cross-section with either electrode 3 (left) and electrode 11 (right) is ON.

2. For each location (x, y) within the spinal cord cross-section, the electric field lines $\vec{E}_1(x, y)$ and $\vec{E}_2(x, y)$ from both the working electrodes were obtained from the FEM model, and overall amplitude modulated signal \vec{E}_{AM} were calculated by first projecting $\vec{E}_1(x, y)$ and $\vec{E}_2(x, y)$ onto the same direction using the script shown in Appendix B. The projected field lines are then added together based on the law of superposition ($\vec{E}_{AM}(x, y) = \vec{E}_1(x, y) + \vec{E}_2(x, y)$). Figure 5.7(b) shows the resulting amplitude modulated signal \vec{E}_{AM} from two particular locations in the spinal cord. Case (i) is located near electrode 11, therefore the resulting signal is a \vec{E}_{AM} weakly modulated stimulation, whereas case (ii) located at the dorsal horn experiences a strongly modulated signal \vec{E}_{AM} as a result of the temporal interfering fields by the two working electrodes.
3. The SCS-induced electric fields \vec{E}_{AM} are then interpolated and put into the axon equivalent circuit model from Figure 5.4 to obtain the spatial distribution of axonal responses $f_n(x, y)$ within the spinal cord cross-section. As seen from Figure 5.7(c), weakly modulated stimulation in case (i) would not elicit neural activities, whereas strongly modulated stimulation with intensity within the *Goldilocks zone* of the activation map from Figure 5.5 will result in high levels of neural oscillation f_n . The final spatial axon recruitment pattern in the spinal cord (herein termed **recruitment map**) is shown in Figure 5.7(d).

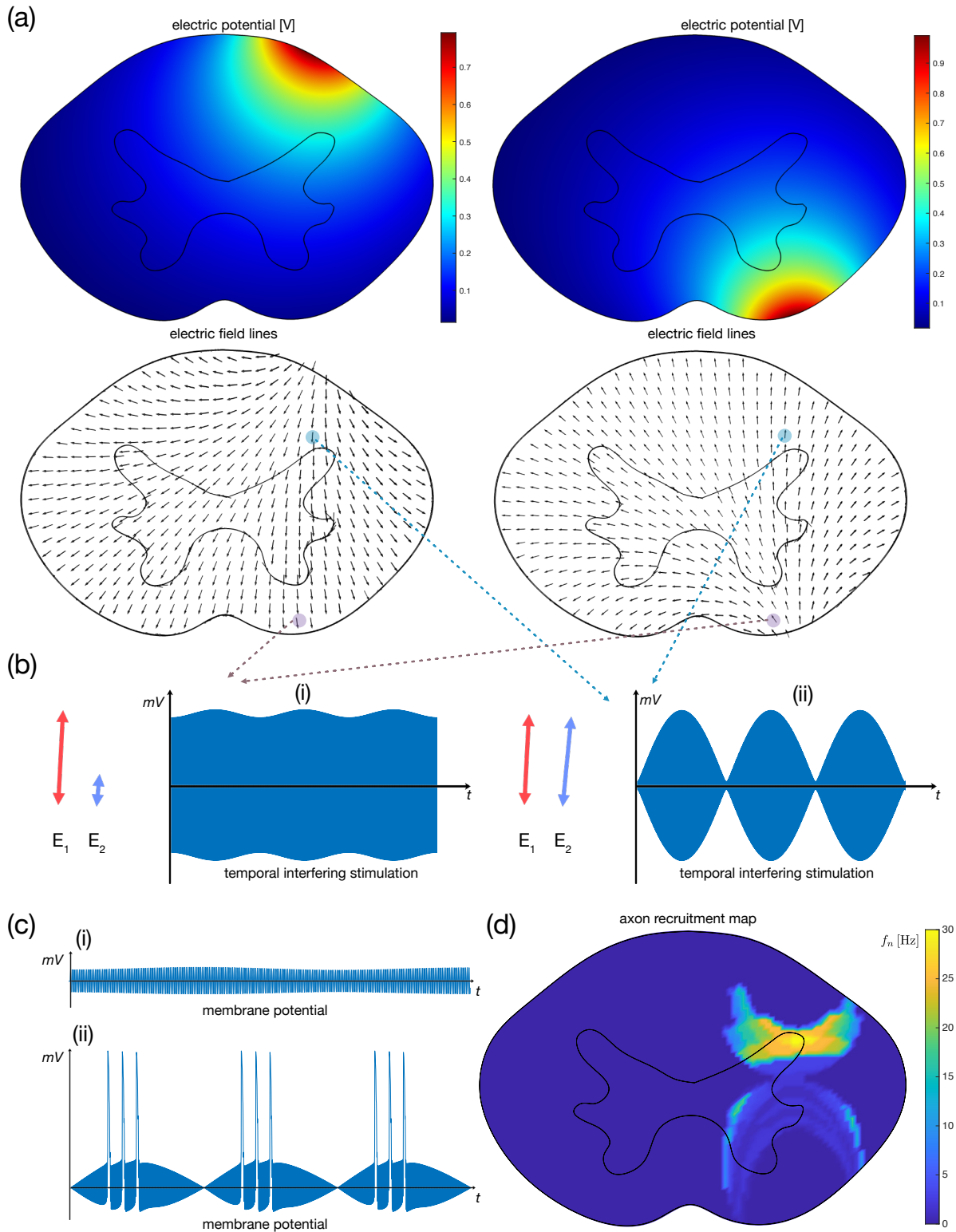


Fig. 5.8 Workflow of obtaining an axon recruitment map from (a) calculating $\vec{E}_1(x,y)$ and $\vec{E}_2(x,y)$ from the FEM model, (b) obtaining resulting $\vec{E}_{AM}(x,y)$ from two working electrodes, and (c) plugging into the equivalent circuit model to construct the (d) axon recruitment map.

***In vitro* validation of temporal interfering stimulation**

To validate the localization capabilities of TIS waveforms *in vitro*, a tissue phantom with electrical conductivity representing the weighted average conductivity value between gray and white matter of 0.12 S/m was used. The tissue phantom was placed in a plastic cylinder, with the flexible SCS device wrapped around the outside of the plastic cylinder. An array of metal pin electrodes was placed on top of the tissue phantom to measure the spatial electric potential $V(x,y)$ within the sample (Figure 5.9 (a) and Figure 5.10 (a)). Figure 5.9 (b) Figure 5.10 (b) illustrate the relative electrode configuration and stimulation parameters, where $f = 2000\text{Hz}$ and $V_1 = V_2 = 500\text{mV}$.

Figure 5.9 (c) and Figure 5.10 (c) show the spatial electric potential $V(x,y)$ sampled from the metal pin array, with the side-by-side comparison with simulation result from the computation model shown in Figure 5.9 (d) and Figure 5.10 (d), showing good level of agreement. The experimental electric potential distribution was constructed from each of the electric potential V measured from the metal pins (Matlab script to process the experimental data included in Appendix B). The spatial electric field profile is then interpolated and put into the equivalent circuit model to construct the spatial axon recruitment for both the *in vitro* and computational model, as shown in Figure 5.9 (e), (f) and Figure 5.10 (e), (f).

As seen from both Figure 5.9 and Figure 5.10, with the working electrode being on the diametrically opposite side of the spinal cord cross-section (electrode 2 and 8 for Figure 5.9 and electrode 4 and 10 for Figure 5.10), the location having the highest level of neural activities would be at the midpoint of the line connecting the two working electrodes together (e.g., midpoint on the white dashed line shown in Figure 5.9 (e) and (f)). The reason is because, the midpoint on this line is the location experiencing the most highly-modulated stimulation with highest intensity $|E_{AM}^{\vec{}}|$ (assuming a quasi-homogeneous conductivity value, such as the case of the tissue phantom used in the *in vitro* model).

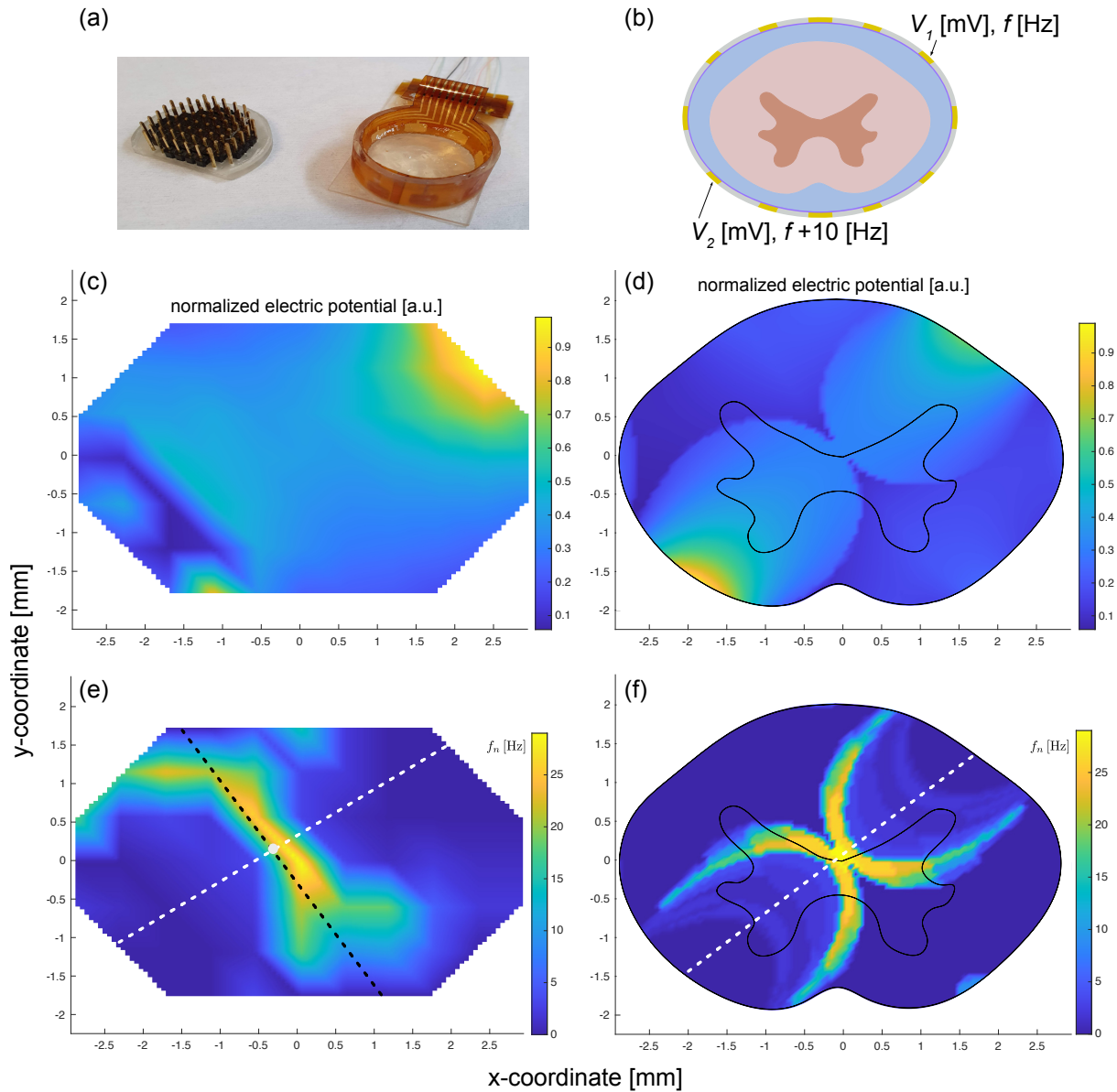


Fig. 5.9 *In vitro* validation with 2-8 working electrode configuration. (a) photo of the *in vitro* model including the tissue phantom and flexible SCS device. (b) working electrode configuration and stimulation parameter. (c) and (d) are the electric potential comparison between *in vitro* measurement, and simulation results. (e) and (f) are the axon recruitment map comparison between *in vitro* measurement, and simulation results.

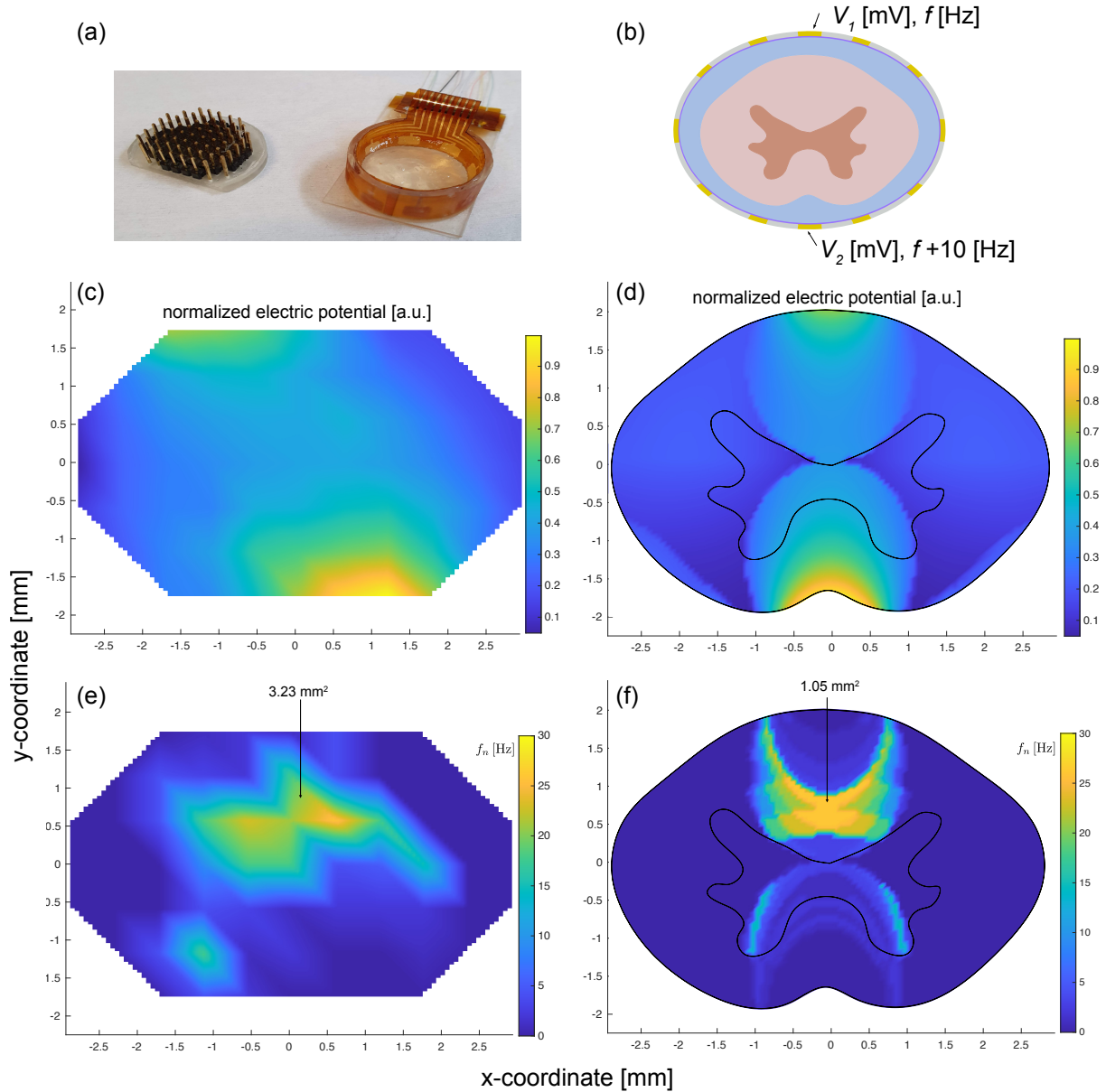


Fig. 5.10 *In vitro* validation with 4-10 working electrode configuration. (a) photo of the *in vitro* model including the tissue phantom and flexible SCS device. (b) working electrode configuration and stimulation parameter. (c) and (d) are the electric potential comparison between *in vitro* measurement, and simulation results. (e) and (f) are the axon recruitment map comparison between *in vitro* measurement, and simulation results.

Subsequent locations equidistant to the two working electrodes connected together would constitute a line passing through the midpoint and while being perpendicular to the line connecting two working electrodes (black dashed line on Figure 5.9 (e)). These locations on the black line will also experience well-modulated stimulation since they are equidistant to the two working electrodes, with weaker stimulation intensity $|E_{AM}^{\vec{}}|$ compared to the midpoint. As a result, the locations with high levels of neural activities would lie on this black dashed line, as shown in Figure 5.9 (e).

The discrepancy in the pattern shown in the simulation model from Figure 5.9 (f) can be largely attributed to the anisotropic conductivities of the tissues used in the FEM model, and also nonlinear electric potential distribution due to capacitive effects on the electrodes considered in the model. Nonetheless, the agreement of relative locations of axon recruitment map between the *in vitro* measurement and computational model still provide valuable insights on the relationship between electrode configuration and location of axon recruitment with TIS waveforms.

Axon recruitment area calculation based on \vec{E}_{TI} versus activation map

As previously mentioned, calculating the axon recruitment area based on the envelop intensity of the stimulation signal $|\vec{E}_{TI}|$ is flawed, mainly because this method assumed a perfectly modulated signal \vec{E}_{AM} would always elicit action potentials, neglecting the Goldilocks zone for stimulation intensity presented in Figure 5.5. To visualize the spatial profile between $|\vec{E}_{TI}(x,y)|$ and $f_n(x,y)$, the difference between using equivalent circuit to calculate neural activity f_n and using envelop intensity $|\vec{E}_{TI}|$ in the spinal cord cross-section subjected to temporal interfering stimulation (TIS) is shown in Figure 5.11 and Figure 5.12 for different targeted axons.

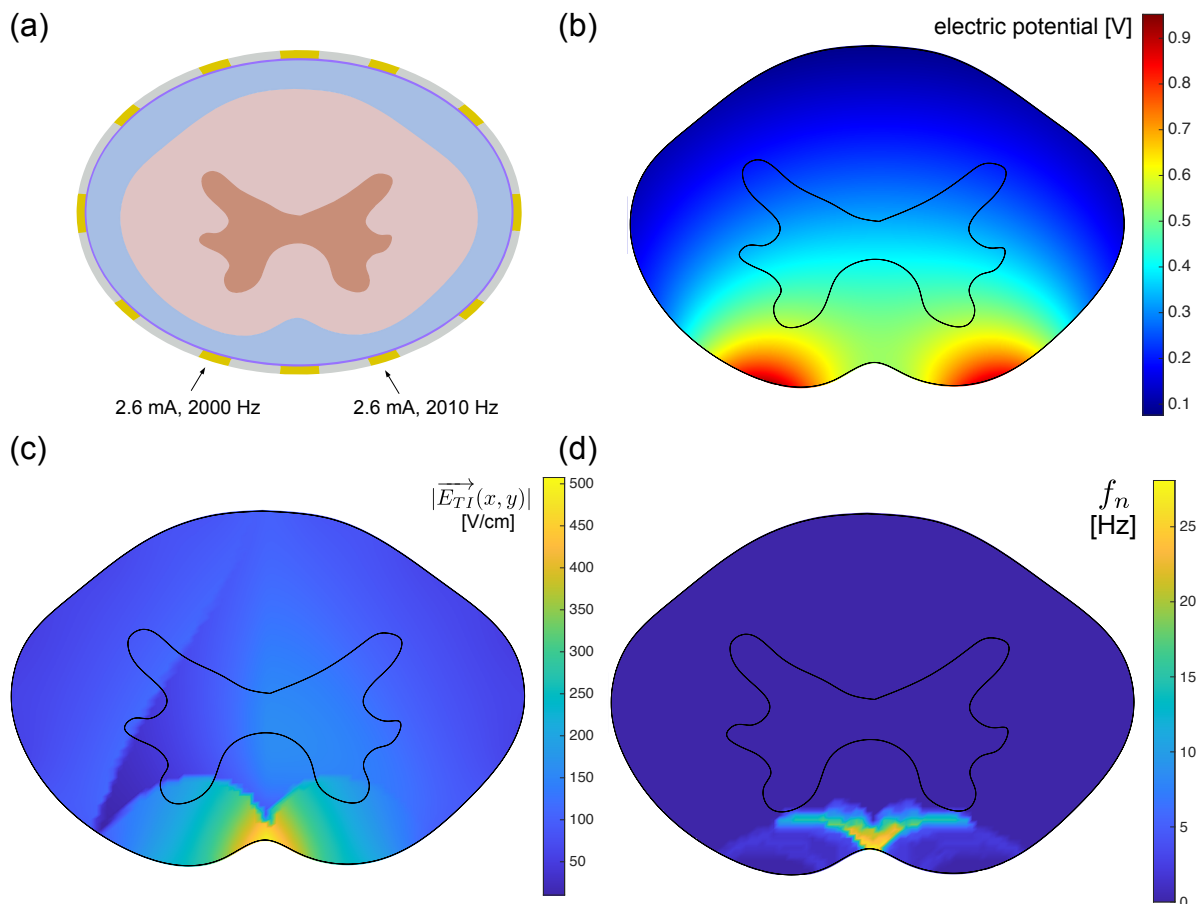


Fig. 5.12 Recruitment area comparison between using $|\vec{E}_{TI}|$ and f_n when the target is the anterior corticospinal tract. (a) shows the electrode configuration and stimulation parameters and (b) shows the resulting potential distribution. (c) is the spatial distribution for $|\vec{E}_{TI}(x,y)|$ and (d) is the spatial axon recruitment map $f_n(x,y)$ using the equivalent circuit model.

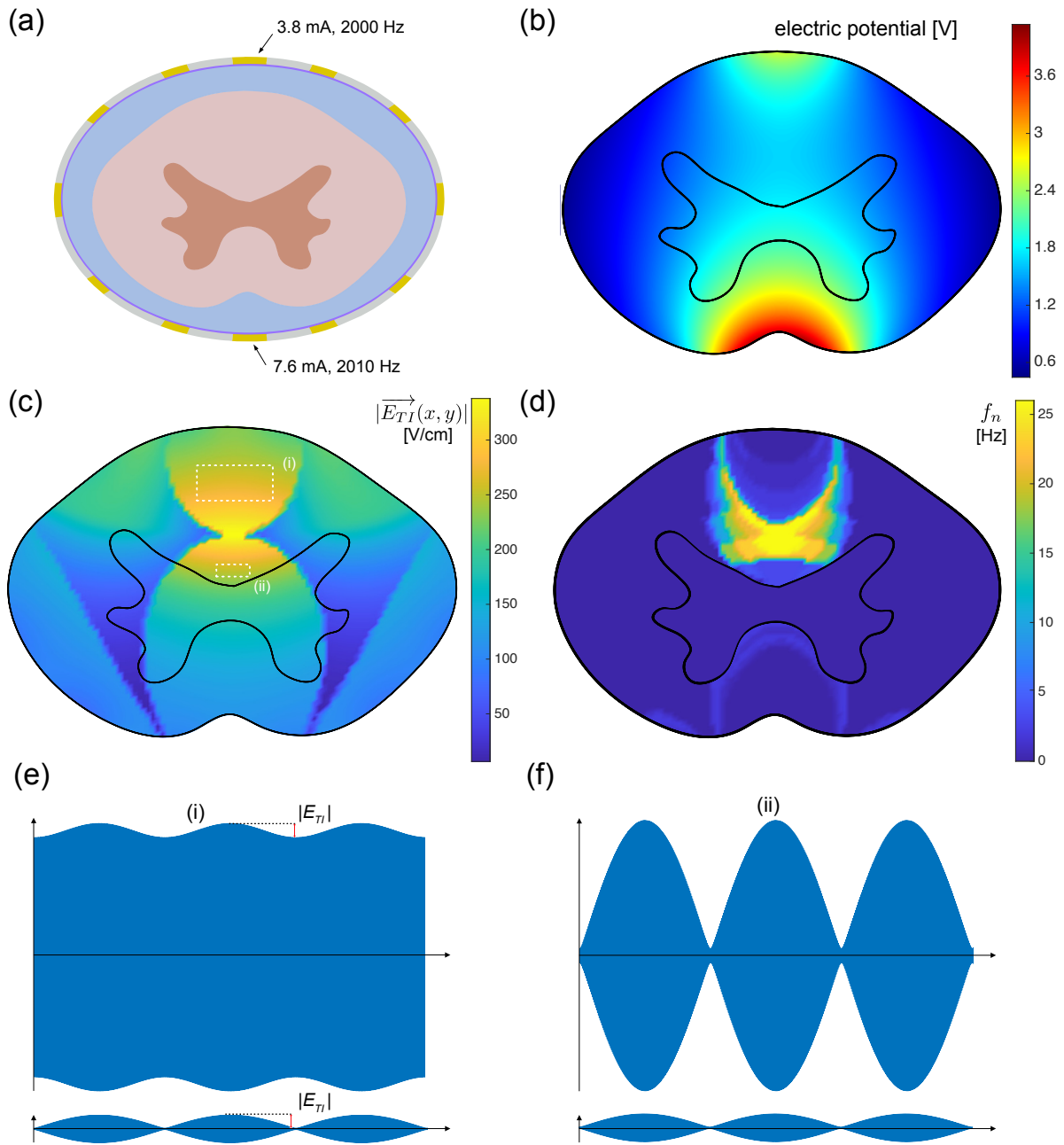


Fig. 5.11 Recruitment area comparison between using $|\vec{E}_{TI}|$ and f_n when the target is the dorsal column. (a) shows the electrode configuration and stimulation parameters and (b) shows the resulting potential distribution. (c) is the spatial distribution for $|\vec{E}_{TI}(x, y)|$ and (d) is the spatial axon recruitment map $f_n(x, y)$ using the equivalent circuit model. (e) and (f) shows the stimulation waveform at two locations in the spinal cord (represented by the white dashed line box) experiencing high envelope intensity without neuron firing.

Figure 5.11 and Figure 5.12 (a), (b) show the working electrode configuration, current intensity, AC frequencies and electric potential distribution in a spinal cord cross-section for dorsal column stimulation. Electrode [4, 10] and [9, 11] are the two working electrodes respectively, whereas all other electrodes are all grounded. The working electrodes supply AC currents with frequencies of [2000 Hz, 2010 Hz], with amplitude ratio of [3.8 mA:7.6 mA] and [2.6 mA:2.6 mA]. The electric potential distribution in Figure 5.11 and Figure 5.12 (b) show higher electric potential at areas closer to the working electrodes. Figure 5.11 and Figure 5.12 (c) show the envelope intensity $|\vec{E}_{TI}(x,y)|$ as a function of position (x,y) along the spinal cord cross-section based on $|\vec{E}_1(x,y)|$ and $|\vec{E}_2(x,y)|$, calculated with Equation 5.3. Figure 5.11 and Figure 5.12 (d) show the neural activity $f_n(x,y)$ as a function of position (x,y) along the spinal cord cross-section, which was calculated using $|\vec{E}_1(x,y)|$ and $|\vec{E}_2(x,y)|$ as input to the activation map in Figure 5.5 (The parameter for sensory and motor axons for targeting the dorsal column and anterior corticospinal tract are both included in Appendix B).

As seen from Figure 5.11, Figure 5.12 (c) and (d), the spatial distribution between $|\vec{E}_{TI}(x,y)|$ and $f_n(x,y)$ are similar, in the sense that the recruited areas with neuron firing experiences high envelop intensity $|\vec{E}_{TI}|$. However, some areas with high envelop intensity did not result in neuron firing, such as area closer to the posterior side of the dorsal column (case (i) highlighted by white dashed line box on top in Figure 5.11(c)), and area on the anterior side of the dorsal column closer to the gray matter (case (ii) highlighted by white dashed line box on the bottom Figure 5.11(c)).

There are two reasons for the discrepancies observed between Figure 5.11, Figure 5.12 (c) and (d). First crucial reason is, higher envelope intensity $|\vec{E}_{TI}|$ does not equate to highly modulated signal $|\vec{E}_{AM}|$. The definition for $|\vec{E}_{TI}|$ used by previous works [Cao and Grover (2020); Grossman et al. (2017); Huang et al. (2020); Huang and Parra (2019); Rampersad et al. (2019)] takes the form of $|\vec{E}_{TI}| = |\vec{E}_{max}| - |\vec{E}_{min}|$. This definition gave the possibility for the modulated stimulation signal \vec{E}_{AM} to have a relatively high envelope intensity $|\vec{E}_{TI}|$ without being well-modulated.

For example, case (i) in Figure 5.11(c), highlighted by white dashed line box on top represented such scenario. Figure 5.11(e) shows the electric field intensity $|\vec{E}_{AM}|$ at case (i). Compared to a perfectly modulated stimulation which can elicit action potentials, shown at the bottom of Figure 5.11(e), stimulation \vec{E}_{AM} at case (i) have the same $|\vec{E}_{TI}|$ but very different waveforms, and this is the reason that weakly-modulated temporal interfering stimulation at this location shown in case (i) will not cause neurons to fire.

Another reason for the discrepancy between Figure 5.11, Figure 5.12 (c) and (d) is because some well-modulated stimulations have intensities above the suitable range (the Goldilocks zone in Figure 5.5) to elicit action potentials. Case (ii) in Figure 5.11(c), highlighted by white dashed line box on bottom represented such scenario. Compared to a perfectly modulated stimulation which can elicit action potentials, shown at the bottom of Figure 5.11(f), the intensity of stimulation E_{AM}^{\rightarrow} at case (ii) falls out of the Goldilocks zone, and this is the reason that temporal interfering stimulation at this location will not cause neurons to fire.

As seen from the above examples, due to the nonlinear relationship between temporal interfering stimulation E_{AM}^{\rightarrow} and neural oscillation frequency f_n , using envelop intensity $|\overrightarrow{E_{TI}}|$ to calculate the recruited areas would lead to inaccurate estimation in terms of number of recruited axons. More importantly, given the clinically relevant stimulation parameters, areas experiencing the highest envelop intensity $|\overrightarrow{E_{TI}}|$ are often not recruited. In contrast, using the equivalent circuit model developed in this chapter directly relate the external electrical stimulation to axon activities. The activation map from Figure 5.5 stores the relationship between neural activity with respect to TIS waveforms with arbitrary degree of modulations and intensities. In terms of computational load, using the activation map as a 'lookup table' is relatively inexpensive, compared to solving the equivalent circuit model in real-time for different stimulation intensities. This makes it possible for future implementations of SCS devices using TIS waveforms to have closed-loop control of the stimulation locations and areas *in vivo*, even under the stringent energy consumption constraints for implantable bioelectronic devices.

Steerability based on stimulation intensity ratio

As previously demonstrated in the *in vitro* validations and simulation results, TIS waveforms are able to localize the stimulation hotspot. The location with the highest level of neural activities would be located in the midpoint on the line connecting two working electrodes, given the current intensities from the two working electrodes are equal, and the electrical conductivity across the spinal cord is fairly uniform. To steer the stimulation hotspot, one obvious method is changing the electrode configuration. However, varying the current intensities between the original working electrodes can also steer the localized hotspot. The ability steer the stimulation region with temporal interference fields (TIF) is demonstrated in this section (Figure 5.13).

As seen from Figure 5.13 (a), if the stimulation current from the two working electrodes are not equal, the stimulation hotspot would be located at regions closer to the weaker working

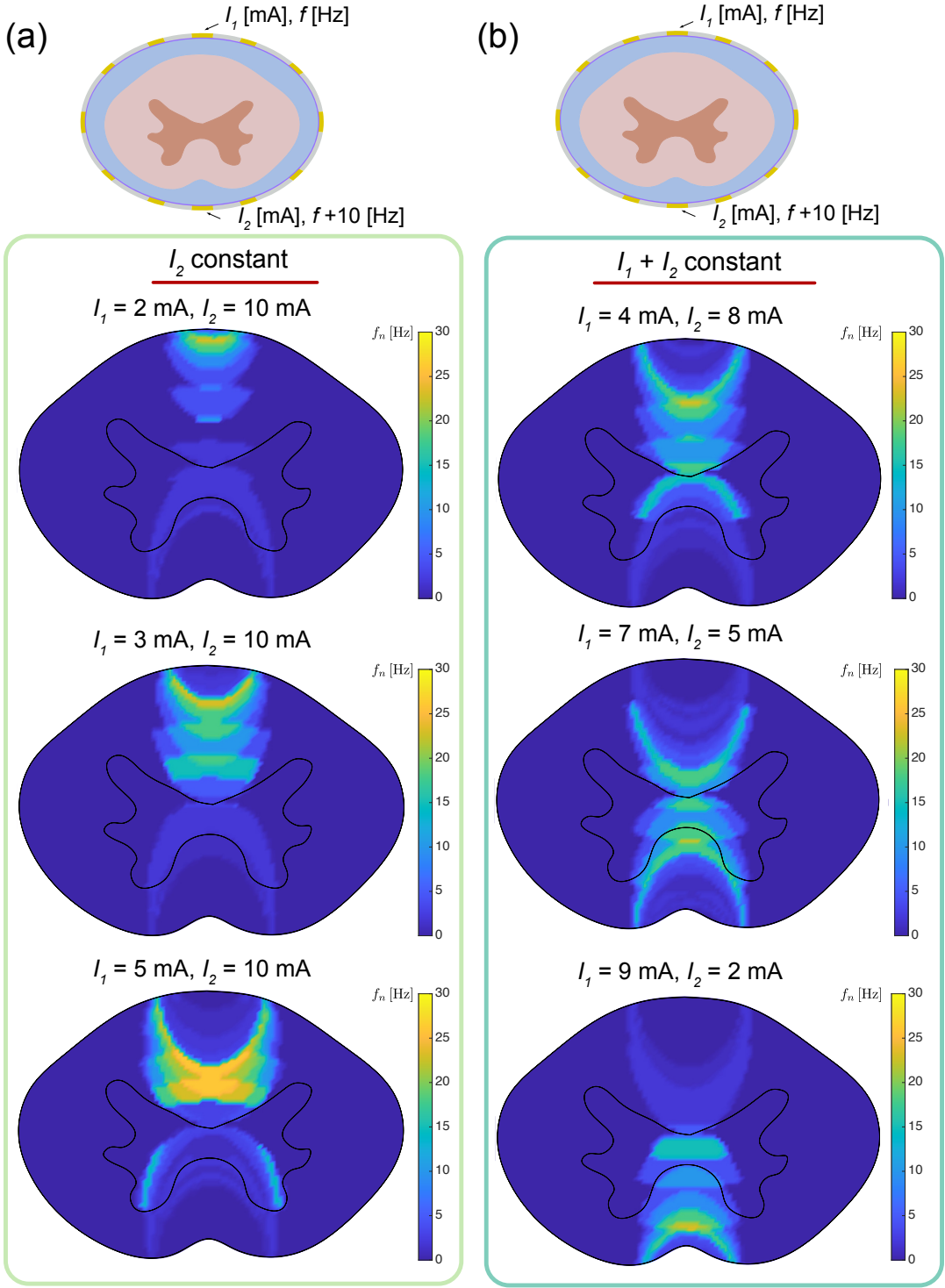


Fig. 5.13 Stimulation hotspot steerability with temporal interfering stimulation. (a) steerability demonstration with I_2 being constant, and (b) steerability demonstration with $I_1 + I_2$ being constant.

electrode. Since the signals from the stronger electrode dominates almost everywhere in the spinal cord cross-section except for locations near the weaker electrode, this is the only region experiencing comparable intensity from two working electrode, i.e., \vec{E}_{AM} with higher envelop intensity $|\vec{E}_{TI}|$.

In Figure 5.13 (a), electrode at the bottom is supplying a AC current with stronger intensity of 10 mA, with the intensity from electrode at the top gradually increasing. As a result, the center of the stimulation hotspot gradually moves down as the intensities from the two working electrodes becomes more comparable. The side effect of holding one working electrode at a constant intensity is, as the overall current intensity increases, the size of the hotspot also increases. This can be understood as more regions are experiencing \vec{E}_{AM} with high enough envelop intensity $|\vec{E}_{TI}|$ to elicit action potentials (refer back to the activation map from Figure 5.5 for the relationship between \vec{E}_{AM} and neural activity f_n).

Alternatively, to avoid the change in size for the stimulation hotspot, Figure 5.13 (b) demonstrates the steerability of TIS waveforms by changing the current intensity ratio between the two working electrodes while keeping the overall stimulation current at a constant. As seen from Figure 5.13 (b), the stimulation hotspot gradually moves down as current from the top electrode increases and current from the bottom electrode decreases. This method can achieve a more localized stimulation hotspot. However, notice when two current intensities are comparable and the hotspot is closer to the middle of the spinal cord (i.e., when $I_1 = 7$ mA and $I_2 = 5$ mA, middle of Figure 5.13 (b)), more current spread along the spinal cord causes more non-parallel electric fields between the two working electrode. This spread creates a more pronounced arc-shaped stimulation pattern, as shown from Figure 5.13 (b). Further optimization in electrode size and grounding configuration can mitigate this arc-shaped stimulation pattern, which will be covered in the following section for parameter optimization.

5.5 Parameters affecting the performance of temporal interfering stimulation

Having measured the envelop intensity of the temporal interfering stimulation $|\overrightarrow{E_{TI}}|$ *in vitro* and demonstrated how TIS waveforms can be used for localized and steerable spinal cord stimulation, this section will discuss how to optimize the TIS performance by varying the device and stimulation parameters. The objective for the parameter optimization is to minimize the stimulation hotspot without exceeding the safety charge injection limit [McCreery et al. (1990)]. The ability to minimize the stimulation hotspot allows the clinicians to selectively stimulate specific spinal cord tracts based on individual subjects' conditions, and make the TIS spinal cord stimulation as a personalized neuromodulation tool.

Base frequency f

In terms of stimulation parameters, the prime candidate for optimization is the base frequency f for the AC electric fields. Figure 5.14 to 5.15 compare the recruited areas with TIS of different base frequencies from 1500 Hz, 2000 Hz to 2500 Hz. From Figure 5.14 (a) to Figure 5.15 (b), the working electrodes are electrode 3 and 11, with stimulating current gradually increases from Figure 5.14 (a) to Figure 5.15 (a) while maintaining the ratio of stimulating current of 1:2 for all cases. When calculating the recruited areas, the electric field distribution profile calculated by the FEM model were plugged into the axon activation maps with different base frequencies f . The activation maps with base frequency $f = 1500\text{Hz}$ and $f = 2500\text{Hz}$ are included in Appendix B.

As seen from Figure 5.14 (a), Figure 5.14 (b) to Figure 5.15 (a), lower base frequency requires lower stimulating current amplitude to elicit action potential for axons in the spinal cord. With I_1 being 2.3 mA (Figure 5.14 (a)), TIS with $f = 1500\text{Hz}$ has already recruited small regions of axons ($\approx 0.08\text{mm}^2$) near electrode 3, while neither TIS with $f = 2000\text{Hz}$ nor TIS with $f = 2500\text{Hz}$ elicit action potentials across the spinal cord cross-section. As the current intensity increases to I_1 being 3.5 mA (Figure 5.14 (b)), much larger area is recruited by TIS with $f = 1500\text{Hz}$ ($\approx 1.01\text{mm}^2$), with TIS with $f = 2000\text{Hz}$ started to recruit spinal cord axons ($\approx 0.35\text{mm}^2$) and small amount of neural activities was activated with TIS with $f = 2500\text{Hz}$. Further increasing the stimulation current to I_1 being 4.4 mA (Figure 5.15 (a)) would instead decrease the recruited area with TIS with $f = 1500\text{Hz}$, since such stimulation intensity have exceeded the Goldilocks zone for the activation map where $f = 1500\text{Hz}$, while

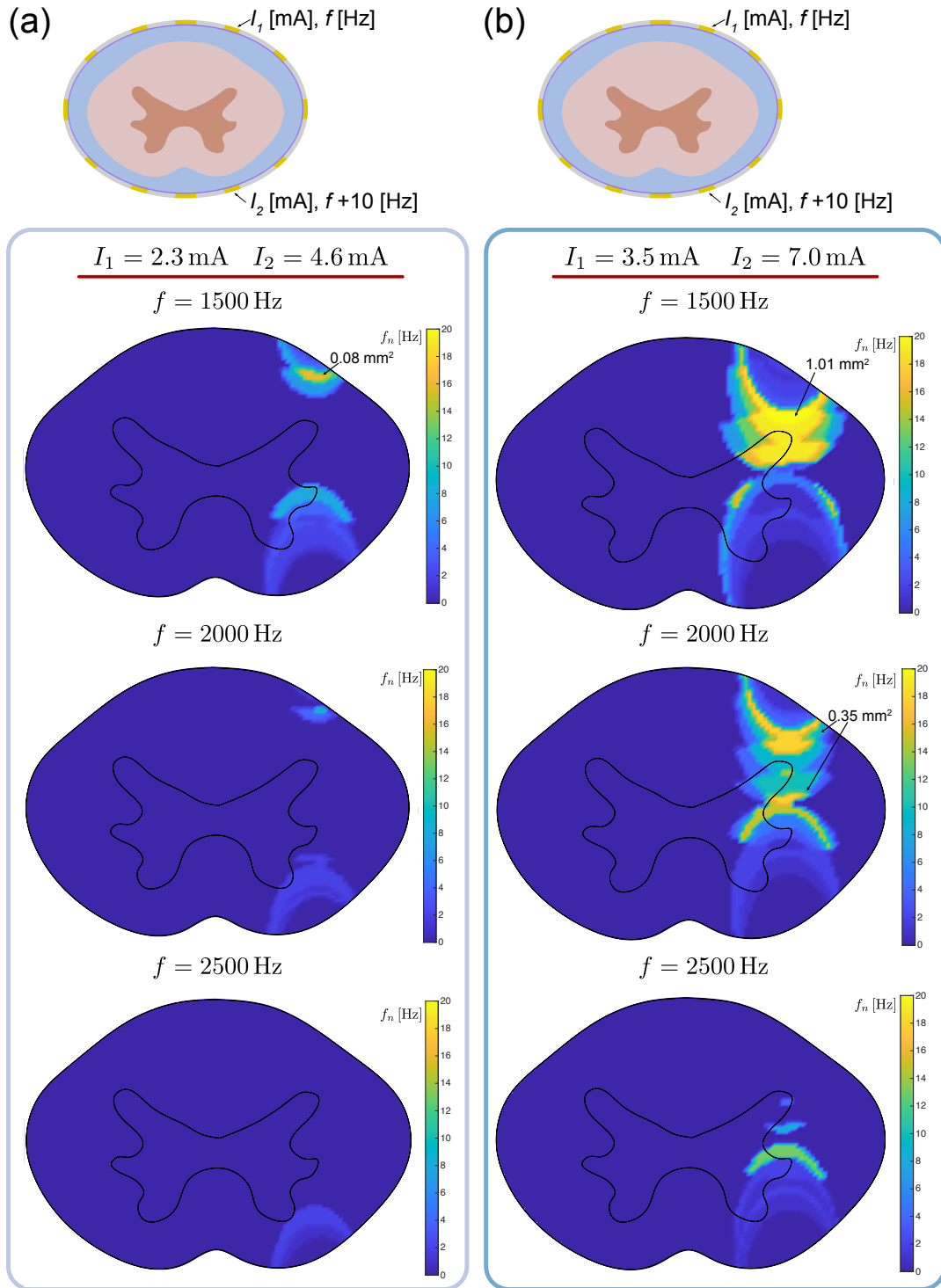


Fig. 5.14 The effect of base frequency f on recruited area with TIS waveform.

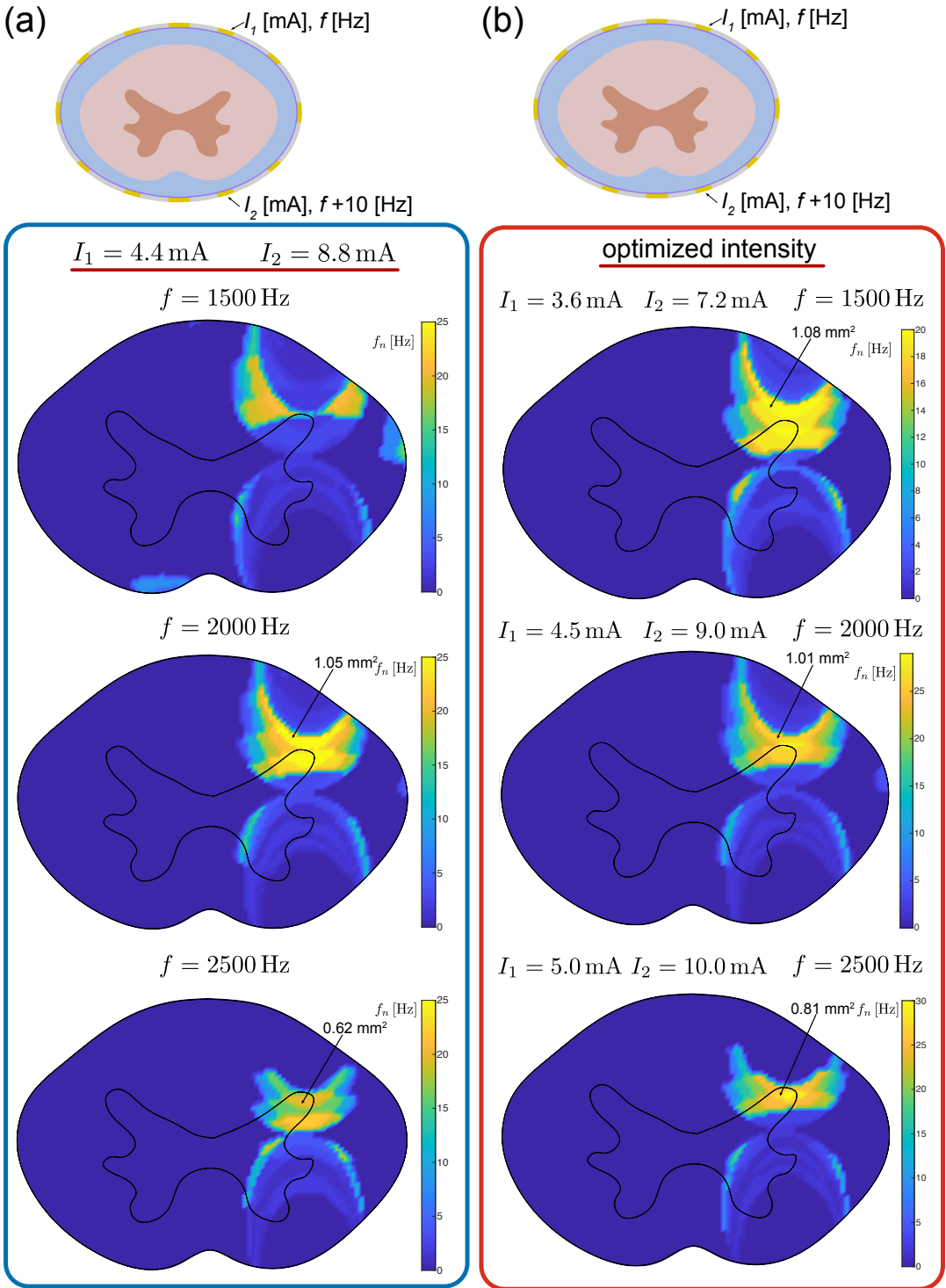


Fig. 5.15 Cont'd from Figure 5.14, the effect of base frequency f on recruited area with TIS waveform.

the area recruited by TIS with both $f = 2000\text{Hz}$ $f = 2500\text{Hz}$ grew in size ($\approx 1.05\text{mm}^2$ and 0.62mm^2 respectively).

Figure 5.15 (b) shows the recruited areas with TIS of different frequencies all under optimized intensity. Here the targeted location is the dorsal horn, and the optimized intensity is defined as the external current eliciting highest amount of activities in the targeted region, (i.e., targeted region experiences TIS stimulation $E_{AM}^{\vec{}}$ in the Goldilocks zone for different base frequencies). As seen from Figure 5.15 (b), the optimized intensity increases with base frequencies of the external AC electric field. With the amplitude modulated stimulation $E_{AM}^{\vec{}}$, locations experiencing weakly modulated signals will not result in action potentials, as a result, all TIS with optimized intensity achieved localized dorsal horn stimulation without activating axons closer to the two working electrodes. More importantly, as base frequency f of the stimulation increases, the stimulation hotspot becomes more localized, and the arc-shaped characteristics of the stimulation pattern also becomes less pronounced. The hotspot size in Figure 5.15 (b) reduced around 20% when base frequency varied from 1500 Hz to 2500 Hz, in exchange for higher charge injection into the spinal cord.

Grounding configuration

Besides the TIS waveform parameters, the dimensions and configurations of the SCS device also can be optimized to further improve the localization capabilities of spinal cord stimulation using TIS waveforms. Based on the observations from the activation map shown in Figure 5.5, the amount of axons recruited with TIS are dependent on how many axons are experiencing high intensity temporal interfering stimulations $E_{AM}^{\vec{}}$, where both $|\vec{E}_1|$ and $|\vec{E}_2|$ falls within the highly active *Goldilocks zone* in the activation map from Figure 5.5. As a result, in order to improve the localization capability of TIS waveforms and minimize the stimulation hotspot, the spread of the temporal interfering stimulation should be minimized, so that highly modulated stimulation $E_{AM}^{\vec{}}$ is restricted only the targeted region. To demonstrate how minimizing current spread can improve localization capabilities of temporal interfering stimulations, Figure 5.16 (a) and (b) compares the recruited area for different grounding configurations. Both working electrodes in Figure 5.16 (a) and (b) are electrode 4 and 10, and the stimulation current are 3.9 mA : 7.8 mA between electrode 4 and 10 for both scenarios.

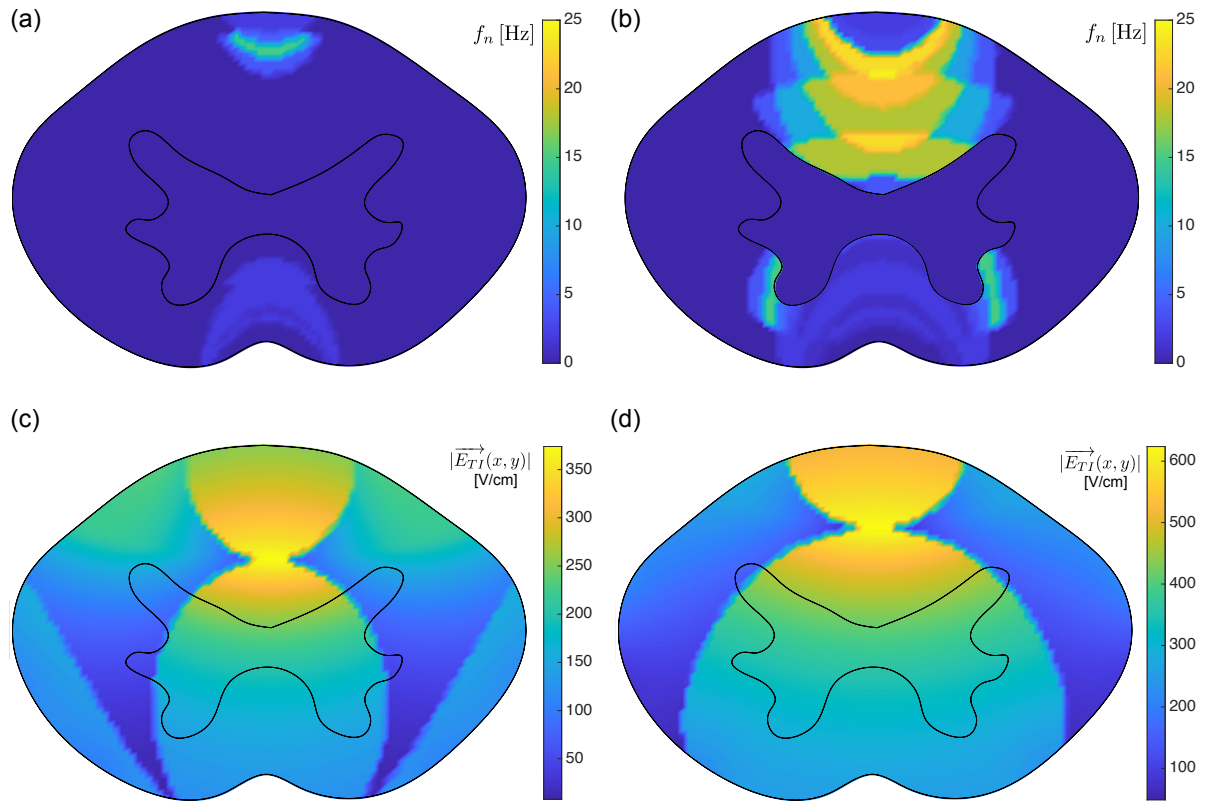


Fig. 5.16 Effect of ground electrode configurations on localization of TIS waveforms. (a) and (b) shows the axon recruitment maps between all the non-working electrodes are grounded and only the top-half of the non-working electrodes are grounded. (c) and (d) show the respective envelop intensity $|\vec{E}_{TI}|$ between two grounding configurations with temporal interfering stimulation.

For Figure 5.16 (a), the ground electrodes are all the non-working electrodes (i.e., electrode 1-12 except for 4 and 10.), whereas in Figure 5.16 (b), only the top-half of the non-working electrodes are grounded (electrode 2, 3, 5, and 6), the rest of the unused electrodes were left to float.

As seen from the axon recruitment comparison, device with more grounded electrodes clearly have a much more localized stimulation hotspot, whereas almost the entire dorsal column is activated in Figure 5.16 (b). The difference in recruited areas can be clearly explained by visualizing the envelop intensity $|\vec{E}_{TI}|$ (Figure 5.16 (c) and (d)). For a well-grounded configuration in Figure 5.16 (a), the current spread is more controlled, and the envelop intensity is both smaller more localized. Without proper grounding, almost the entire spinal cord cross-section experiences a high envelop intensity (Figure 5.16 (d)), and the resulting activated area was much larger.

Electrode size

Figure 5.17 (a) and (b) compares the recruited area for electrode surface area being 12.25 mm^2 ($3.5 \text{ mm} \times 3.5 \text{ mm}$, Figure 5.17 (a)) and half of the size (6.125 mm^2 , Figure 5.17 (b)). Both working electrodes in Figure 5.17 (a) and (b) are electrode 4 and 10, and the stimulation current are $3.9 \text{ mA} : 7.8 \text{ mA}$ between electrode 4 and 10 for both scenarios.

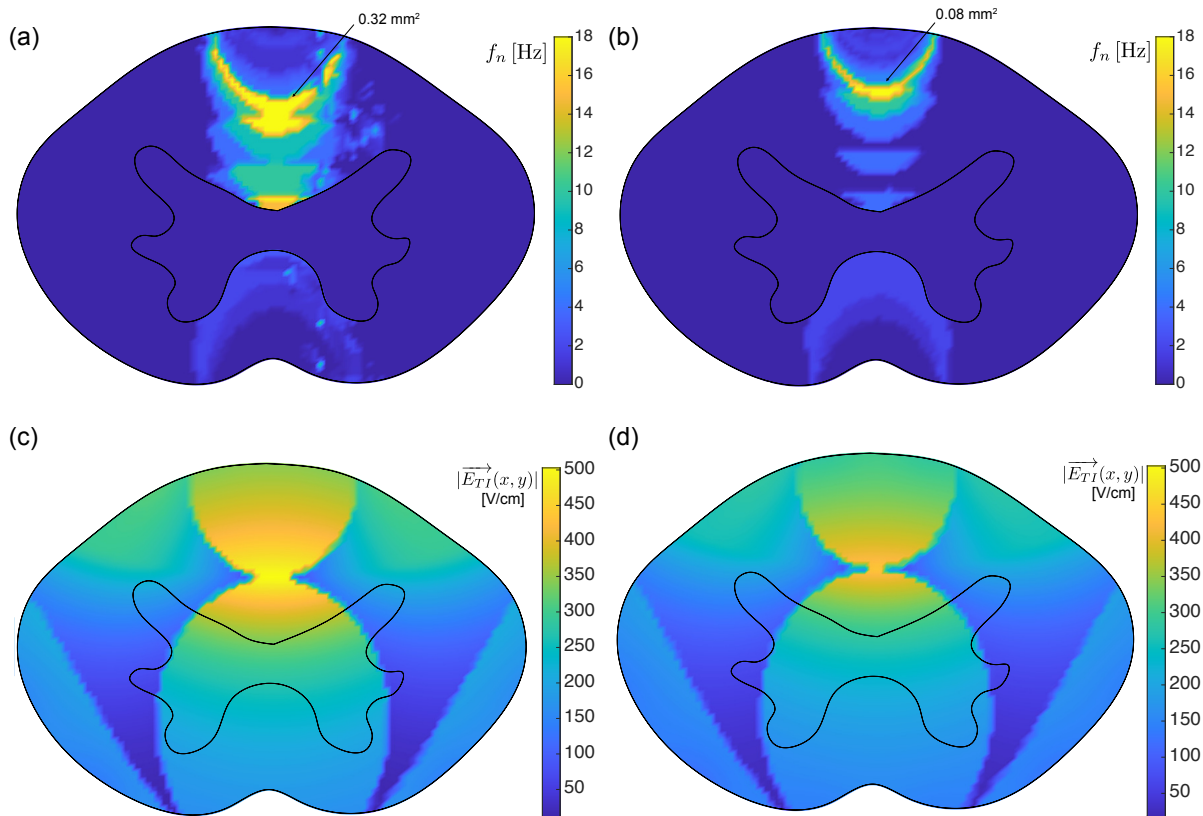


Fig. 5.17 Effect of electrode size on localization of TIS waveforms. (a) and (b) shows the axon recruitment maps between working electrode size of 12.25 mm^2 ($3.5 \text{ mm} \times 3.5 \text{ mm}$) and half of the size (6.125 mm^2). (c) and (d) shows the respective envelop intensity $|\vec{E}_{TI}|$ for a large and small working electrode with temporal interfering stimulation.

As seen from the axon recruitment comparison, device with smaller working electrodes clearly better localize the stimulated region, as the recruited area decreased from 0.32 mm^2 to 0.08 mm^2 between big and small working electrode under the same current intensity. The difference in recruited areas can be explained by visualizing the envelop intensity $|\vec{E}_{TI}|$ (Figure 5.17 (c) and (d)). Envelop intensity profiles show similar patterns between large and small working electrodes, but as the electric current spread will be less pronounced with smaller

electrodes [Bagshaw and Evans (1976)], the envelop intensity is more localized for smaller working electrodes. As a result, the regions experiencing temporal interfering stimulations $E_{AM}^{\vec{}}$ in the range of eliciting action potentials is much smaller with smaller working electrodes.

The above examples show that, to further localize the stimulation hotspot, viable strategies are to increase the base frequency of the AC electric field or decrease the size of the working electrode. However, higher base frequency and smaller working electrode both result in higher injection current. To ensure the applied current do not exceed safety limit, the Shannon criteria for charge injection is used [McCreery et al. (1990); Shannon (1992)], where:

$$\log D = k - \log Q. \quad (5.17)$$

In Equation 5.17, D is the charge density per phase of the stimulation (unit: $\mu C/\text{phase} \cdot \text{cm}^2$), k is a dimensionless safety parameter, and Q is charge per phase (unit: $\mu C/\text{phase}$). For neuromodulation devices such as cochlear implants, deep brain stimulators, or spinal cord stimulators, the empirical law for safe charge injection is to keep $k \leq 1.85$ [Tiede et al. (2013); Wesselink et al. (1998)]. In this chapter, the single electrode is $3.5 \times 3.5 \text{mm}^2$ for the *in vitro* model. With the working electrodes supplying AC current of around 2000 Hz, the safe current injection limit for a single electrode is about 18 mA. Throughout this chapter, the injecting current from a single working electrode is way below this safety charge injection limit of 18 mA, based on the device geometries and stimulation parameters. Furthermore, as seen from Equation 5.17, to maintain the same safety factor k , the relationship between electrode size A and injecting current I is:

$$I \propto \sqrt{A}. \quad (5.18)$$

Therefore, if the electrode size is halved from 12.25mm^2 to 6.125mm^2 , the charge injection limit will be lower to around 12.73 mA. In the context of personalized neuromodulation, for cases requiring more localized stimulation hotspots such as motor axon stimulation for rehabilitation, trade-offs between specificity and charge injection limit should be a major design consideration when for SCS devices using TIS waveforms.

5.6 Discussion

The computational modeling and experimental works presented here indicate that temporal interfering stimulation can achieve localized and steerable neuromodulation. In the context of spinal cord stimulation, the stimulation hotspot size is dependent on the stimulation parameter, electrode configuration, and the device geometry. Critically, the results from the coupled computational model in this work indicates that that the stimulation hotspot does not coincide with regions experiencing the highest envelop intensity, which was an important assumption from previous works [Cao and Grover (2020); Grossman et al. (2017); Huang et al. (2020); Huang and Parra (2019); Rampersad et al. (2019)]. Rather, the so-called *Goldilocks zone* of highly modulated signals with moderate intensity would elicit the highest level of neural activities. Though this work focuses on spinal cord stimulation, the same process of developing computational model, identify axon activation map, to constructing the final axon spatial recruitment profile can be readily applied to other types of neuromodulation devices such as the deep brain stimulator or the cochlear implant. It is posited that the process of decoupling the external stimulations and constructing the lookup table as a function of important parameters (i.e., the activation map in Figure 5.5 as a function of two AC electric field intensities) may prove particularly useful in guiding future design of neuromodulation devices using temporal interfering stimulation, or other types of novel stimulation waveforms for real-time, *in vivo* steering and localizing the targeted regions.

In order to achieve a more accurate estimate of the activation hotspot location and size when subjecting to TI stimulation, one particular area for model refinement is to take into account the axon orientations within the spinal cord. For simplicity, previous computational models in the literature, including the model developed in this chapter, assumed all axons in the spinal cord are perfectly parallel to each other and run along the vertical (i.e., rostral-caudal) direction [Capogrosso et al. (2016); Lempka et al. (2015); McIntyre et al. (2002); Zander et al. (2020)]. However, previous histological studies have shown that in some individuals, the local fiber orientation within the spinal cord can vary up to 28° [Duval et al. (2019); Grussu et al. (2016); Koser et al. (2015)]. This dispersion of axon orientation can lead to an increase in the number of axons activated by TI stimulation.

To a first approximation, the area activated by TI stimulation when the axon orientation deviates the rostral-caudal direction by an angle of α would be $1/\cos \alpha$ times larger compared to when all axons are parallel. Therefore, a 28° axon orientation dispersion angle would increase the activated area by about 15%. As a result, in future *in vitro* validations, the axon

orientation also needs to be taken into account in order to more accurately corresponds the activation area calculated by the computational model. Lastly, in order to maintain the sub mm² stimulation hotspot, the electrode size, grounding configuration, and stimulation parameter all need to accommodate the axon orientation in different testing individuals.

5.7 Conclusion

To summarize, it is demonstrated that the stimulation hotspot of neuromodulation using can be localized by supply two high frequency electric field with slightly different frequencies. The size and the location of the stimulation hotspot depends on both the parameters of the stimulation devices and stimulation waveforms. Steerability of stimulation hotspot can be achieved by changing the ratio of stimulation currents between the working electrodes. Coupled computational modeling combining with *in vitro* measurements demonstrates how to accurately calculate the stimulation hotspot, and the *Goldilocks zone* of stimulation intensity was found, as a result of neural membrane frequency response. Parameter optimization studies further demonstrate how to tailor the device performance for different targeted region and different current injection limit. The simulations results can be used to guide the design of future neuromodulation devices with different architectures thereby improving the stimulation specificity, device safety, and most importantly, the quality of life for the patients.

Chapter 6

Conclusion and future work

6.1 Summary of key findings

This chapter recounts the major findings presented in this work and suggests future research direction to further improve the performances of neuromodulation devices.

Chapter 2

A computational model for an electrophoretic drug delivery devices is developed based on the material properties and geometries of a microfluidic ion pump. Major performance indices for an electrophoretic drug delivery device, namely, the transient drug transport rate, the pumping efficiency, and the ON/OFF ratio were identified and investigated as a function of initial drug concentration and fixed charge concentration in the ion exchange membrane. Computational modeling demonstrated that the capacitive charging behavior of the electrode dominates the transient behavior of the device. Computational modeling also showed that it is not possible to optimize all three performance indices at the same time. For long-term implant applications, device should be loaded with lower drug concentration and high fixed charge concentration in the ion exchange membrane to avoid drug leakage, at the cost of higher power consumption and more constant refills. For applications needing high instantaneous delivery, priority should be put on loading the device with higher drug concentration.

Chapter 3

A critical challenge for electrophoretic drug delivery device- passive leakage due to high drug concentration gradient is identified. The strategy developed here is to pair the drug counter-ion with co-ions of substantially lower diffusion coefficient. A mass transport framework for ions diffusing from the drug reservoir, through the ion exchange membrane, into the target reservoir is established. Theoretical calculations combined with numerical and experimental studies demonstrated the steady-state leakage rate can be lowered 7-fold with the co-ions being high molecular weight SPA polymer developed in this chapter. Due to the high selectivity of the ion exchange membrane, the low diffusivity co-ions would not affect the active performance of the electrophoretic drug delivery device when an external voltage is applied. Due to its simplicity, this method is applicable to all existing electrophoretic drug delivery applications. To conclude, this co-ion engineering method developed in this chapter limits unwanted passive drug leakage without affect the active performance of the electrophoretic drug delivery device.

Chapter 4

Another challenge for electrophoretic drug delivery device- short active pumping time due to electrical double layer formation is identified. The strategy developed here is to split the source electrode into multiple smaller electrodes and activate them asynchronously to maximize the instantaneous electrophoretic delivery rate with polarizable electrodes. Not all asynchronous switching schemes are beneficial, therefore an optimized switching algorithm is developed based on the theoretical calculation of electrical double layer formation dynamics. Experimental results showed that a 2-split electrode device with optimal switching scheme achieved a 68 % increase in electrophoretic delivery rate. Simulation studies further extend the split electrode design into n electrodes, and crosstalk current becomes the bottleneck for further performance improvement. Guidelines for the number of split electrodes in different applications were established based on the trade-off between instantaneous deliver rate the power consumption.

Chapter 5

This chapter developed a new type of localized and steerable electrical neuromodulation device—the spinal cord stimulator with temporal interfering stimulation. One of the main challenges for spinal cord stimulation is the lack of specificity. The temporal interfering stimulation solved this problem by evoking action potentials only in regions experiencing higher envelope intensity. Preliminary work by different groups have suggested the potential of further optimizing this method, but so far previous works all focused on optimizing the electric field distribution alone. The coupled computational model first directly link the stimulation intensity to the neural activity. Instead of optimizing the modulation index of the stimulation, various parameters including stimulation protocols and device geometries can be studied and optimized with the coupled model. *In vitro* measurements with realistic tissue conductivity further demonstrates the validity of the computational model. The localized the steerable stimulation developed here can achieve sub mm^2 resolution, which have huge potential for neuroscientists to apply to different modulation devices.

6.2 Future work

Electrophoretic drug delivery devices

Several exciting directions will be pursued. As mentioned in Chapter 1, a very comprehensive framework for ion diffusion in IEM based on Manning's counter-ion condensation theory is established by Kamcev et al. [Kamcev et al. (2018a, 2015, 2017a,c, 2018b)]. In order to further improve the computational model for electrophoretic drug delivery devices, the electrostatic interaction between mobile ions and fixed charges in the ion exchange membrane must be considered. The electrophoretic drug delivery device also presents a great platform for cancer drug delivery, but as common cancer drugs particles are much larger than a lot of the neurotransmitters used in current studies, the structure of the ion exchange membrane also needs to adapt accordingly. Harvesting the nonlinear behaviors for ion diffusion, such as AC electrophoresis, and developing hybrid structured membrane with mixed conducting properties are also an area of interests.

Spinal cord stimulators

As mentioned in Chapter 5, one of the biggest differences between the coupled computational model developed in this work to previous works by other groups is the discovery of so-called *Goldilocks zone*. Cell culture for electrophysiology work and animal experiments are both being planned. The goal is to replicate this finding, and further applied this localized stimulation method to other domains such as motor control or muscle regenerations. Another important direction is to gain mechanistic understanding of why amplitude modulated signals can elicit action potentials in axons. Preliminary studies indicate the ion channel dynamics and delay between nonlinear channels play an important rule. Further research direction can move toward nonlinear dynamics studies and try to answer this question from a system dynamics/bifurcation theory point of view.

References

- Adair, K. L. (2017). Approval letter from Food and Drug Administration for Boston Scientific Spinal Cord Stimulation System - P030017/S275. Food and Drug Administration, P030017/S275.
- Adrian, E. D. and Lucas, K. (1912). On the summation of propagated disturbances in nerve and muscle. *The Journal of Physiology*, 44(1-2):68–124.
- Ajiboye, A. B., Willett, F. R., Young, D. R., Memberg, W. D., Murphy, B. A., Miller, J. P., Walter, B. L., Sweet, J. A., Hoyen, H. A., Keith, M. W., Peckham, P. H., Simeral, J. D., Donoghue, J. P., Hochberg, L. R., and Kirsch, R. F. (2017). Restoration of reaching and grasping movements through brain-controlled muscle stimulation in a person with tetraplegia: a proof-of-concept demonstration. *The Lancet*, 389(10081):1821–1830.
- Allaire, G. and Allaire, G. (2007). *Numerical Analysis and Optimization: An Introduction to Mathematical Modelling and Numerical Simulation*. OUP Oxford. Google Books ID: HIwSDAAAQBAJ.
- Anderson, D. J., Kipke, D. R., Nagel, S. J., Lempka, S. F., Machado, A. G., Holland, M. T., Gillies, G. T., Howard, M. A. I., and Wilson, S. (2019). Intradural Spinal Cord Stimulation: Performance Modeling of a New Modality. *Frontiers in Neuroscience*, 13.
- Anderson, J. L. and Prieve, D. C. (1984). Diffusiophoresis: Migration of Colloidal Particles in Gradients of Solute Concentration. *Separation and Purification Methods*, 13(1):67–103.
- Augé, S., Schmit, P.-O., Crutchfield, C. A., Islam, M. T., Harris, D. J., Durand, E., Clemancey, M., Quoineaud, A.-A., Lancelin, J.-M., Prigent, Y., Taulelle, F., and Delsuc, M.-A. (2009). NMR Measure of Translational Diffusion and Fractal Dimension. Application to Molecular Mass Measurement. *The Journal of Physical Chemistry B*, 113(7):1914–1918. Publisher: American Chemical Society.
- Bae, Y. H. and Park, K. (2011). Targeted drug delivery to tumors: Myths, reality and possibility. *Journal of Controlled Release*, 153(3):198–205.

- Bagshaw, E. V. and Evans, M. H. (1976). Measurement of current spread from microelectrodes when stimulating within the nervous system. *Experimental Brain Research*, 25(4):391–400.
- Barchini, J., Tchachaghian, S., Shamaa, F., Jabbur, S. J., Meyerson, B. A., Song, Z., Linderoth, B., and Saadé, N. E. (2012). Spinal segmental and supraspinal mechanisms underlying the pain-relieving effects of spinal cord stimulation: An experimental study in a rat model of neuropathy. *Neuroscience*, 215:196–208.
- Bard, A. J. and Faulkner, L. R. (2000). *Electrochemical Methods: Fundamentals and Applications, 2nd Edition*. Wiley Global Education. Google Books ID: hQocAAAAQBAJ.
- Barolat, G. (1993). Experience with 509 plate electrodes implanted epidurally from C1 to L1. *Stereotactic and Functional Neurosurgery*, 61(2):60–79.
- Baumann, S., Wozny, D., Kelly, S., and Meno, F. (1997). The electrical conductivity of human cerebrospinal fluid at body temperature. *IEEE Transactions on Biomedical Engineering*, 44(3):220–223.
- Bazant, M. Z., Thornton, K., and Ajdari, A. (2004). Diffuse-charge dynamics in electrochemical systems. *Physical Review E*, 70(2):021506.
- Berggren, M. and Malliaras, G. G. (2019). How conducting polymer electrodes operate. *Science*, 364(6437):233–234.
- Berggren, M. and Richter-Dahlfors, A. (2007). Organic Bioelectronics. *Advanced Materials*, 19(20):3201–3213.
- Bernacka-Wojcik, I., Huerta, M., Tybrandt, K., Karady, M., Mulla, M. Y., Poxson, D. J., Gabrielsson, E. O., Ljung, K., Simon, D. T., Berggren, M., and Stavriniidou, E. (2019). Implantable Organic Electronic Ion Pump Enables ABA Hormone Delivery for Control of Stomata in an Intact Tobacco Plant. *Small*, 15(43):1902189.
- Biesheuvel, P. M. and Bazant, M. Z. (2010). Nonlinear dynamics of capacitive charging and desalination by porous electrodes. *Physical Review E*, 81(3):031502.
- Bobo, R. H., Laske, D. W., Akbasak, A., Morrison, P. F., Dedrick, R. L., and Oldfield, E. H. (1994). Convection-enhanced delivery of macromolecules in the brain. *Proceedings of the National Academy of Sciences of the United States of America*, 91(6):2076–2080.
- Boissenot, T., Bordat, A., Fattal, E., and Tsapis, N. (2016). Ultrasound-triggered drug delivery for cancer treatment using drug delivery systems: From theoretical considerations to practical applications. *Journal of Controlled Release*, 241:144–163.

- Bottero, D., Gaillard, M. E., Fingermann, M., Weltman, G., Fernández, J., Sisti, F., Graieb, A., Roberts, R., Rico, O., Ríos, G., Regueira, M., Binsztein, N., and Hozbor, D. (2007). Pulsed-Field Gel Electrophoresis, Pertactin, Pertussis Toxin S1 Subunit Polymorphisms, and Surfaceome Analysis of Vaccine and Clinical Bordetella pertussis Strains. *Clinical and Vaccine Immunology*, 14(11):1490–1498. Publisher: American Society for Microbiology Section: Vaccine Research.
- Byrne, J. D., Jajja, M. R. N., O’Neill, A. T., Bickford, L. R., Keeler, A. W., Hyder, N., Wagner, K., Deal, A., Little, R. E., Moffitt, R. A., Stack, C., Nelson, M., Brooks, C. R., Lee, W., Luft, J. C., Napier, M. E., Darr, D., Anders, C. K., Stack, R., Tepper, J. E., Wang, A. Z., Zamboni, W. C., Yeh, J. J., and DeSimone, J. M. (2015). Local iontophoretic administration of cytotoxic therapies to solid tumors. *Science Translational Medicine*, 7(273):273ra14.
- Cajavilca, C., Varon, J., and Sternbach, G. L. (2009). Luigi Galvani and the foundations of electrophysiology. *Resuscitation*, 80(2):159–162.
- Cantrell, D. R., Inayat, S., Taflove, A., Ruoff, R. S., and Troy, J. B. (2007). Incorporation of the electrode–electrolyte interface into finite-element models of metal microelectrodes. *Journal of Neural Engineering*, 5(1):54–67. Publisher: IOP Publishing.
- Cao, J. and Grover, P. (2020). STIMULUS: Noninvasive Dynamic Patterns of Neurostimulation Using Spatio-Temporal Interference. *IEEE Transactions on Biomedical Engineering*, 67(3):726–737.
- Capogrosso, M., Milekovic, T., Borton, D., Wagner, F., Moraud, E. M., Mignardot, J.-B., Buse, N., Gandar, J., Barraud, Q., Xing, D., Rey, E., Duis, S., Jianzhong, Y., Ko, W. K. D., Li, Q., Detemple, P., Denison, T., Micera, S., Bezar, E., Bloch, J., and Courtine, G. (2016). A brain–spine interface alleviating gait deficits after spinal cord injury in primates. *Nature*, 539(7628):284–288. Number: 7628 Publisher: Nature Publishing Group.
- Capogrosso, M., Wenger, N., Raspopovic, S., Musienko, P., Beauparlant, J., Luciani, L. B., Courtine, G., and Micera, S. (2013). A Computational Model for Epidural Electrical Stimulation of Spinal Sensorimotor Circuits. *Journal of Neuroscience*, 33(49):19326–19340. Publisher: Society for Neuroscience Section: Articles.
- Casanova, F., Carney, P. R., and Sarntinoranont, M. (2012). Influence of Needle Insertion Speed on Backflow for Convection-Enhanced Delivery. *Journal of Biomechanical Engineering*, 134(4). Publisher: American Society of Mechanical Engineers Digital Collection.
- Casanova, F., Carney, P. R., and Sarntinoranont, M. (2014). Effect of Needle Insertion Speed on Tissue Injury, Stress, and Backflow Distribution for Convection-Enhanced Delivery in the Rat Brain. *PLOS ONE*, 9(4):e94919. Publisher: Public Library of Science.

- Castagnola, E., Ansaldo, A., Maggiolini, E., Ius, T., Skrap, M., Ricci, D., and Fadiga, L. (2014). Smaller, softer, lower-impedance electrodes for human neuroprosthesis: a pragmatic approach. *Frontiers in Neuroengineering*, 7.
- Caylor, J., Reddy, R., Yin, S., Cui, C., Huang, M., Huang, C., Rao, R., Baker, D. G., Simmons, A., Souza, D., Narouze, S., Vallejo, R., and Lerman, I. (2019). Spinal cord stimulation in chronic pain: evidence and theory for mechanisms of action. *Bioelectronic Medicine*, 5(1):12.
- Chen, S.-T., Proctor, C. M., and Malliaras, G. G. (2020). Materials and Device Considerations in Electrophoretic Drug Delivery Devices. *Scientific Reports*, 10(1):7185. Number: 1 Publisher: Nature Publishing Group.
- Cherian, D., Armgarth, A., Beni, V., Linderhed, U., Tybrandt, K., Nilsson, D., Simon, D. T., and Berggren, M. (2019). Large-area printed organic electronic ion pumps. *Flexible and Printed Electronics*, 4(2):022001.
- Clerx, M., Beattie, K. A., Gavaghan, D. J., and Mirams, G. R. (2019). Four Ways to Fit an Ion Channel Model. *Biophysical Journal*, 117(12):2420–2437.
- Cogan, S. F. (2008). Neural Stimulation and Recording Electrodes. *Annual Review of Biomedical Engineering*, 10(1):275–309.
- Colloca, L., Ludman, T., Bouhassira, D., Baron, R., Dickenson, A. H., Yarnitsky, D., Freeman, R., Truini, A., Attal, N., Finnerup, N. B., Eccleston, C., Kalso, E., Bennett, D. L., Dworkin, R. H., and Raja, S. N. (2017). Neuropathic pain. *Nature Reviews Disease Primers*, 3(1):1–19. Publisher: Nature Publishing Group.
- COMSOL (2018). COMSOL Multiphysics® Modeling Software, Version 5.4.
- Connelly, W. M., Laing, M., Errington, A. C., and Crunelli, V. (2016). The Thalamus as a Low Pass Filter: Filtering at the Cellular Level does Not Equate with Filtering at the Network Level. *Frontiers in Neural Circuits*, 9.
- Cook, B. K. and Jensen, R. P. (2002). *Discrete Element Methods*. American Society of Civil Engineers.
- Costigan, M., Scholz, J., and Woolf, C. J. (2009). Neuropathic Pain: A Maladaptive Response of the Nervous System to Damage. *Annual Review of Neuroscience*, 32(1):1–32. Publisher: Annual Reviews.
- Courtine, G. and Sofroniew, M. V. (2019). Spinal cord repair: advances in biology and technology. *Nature Medicine*, 25(6):898–908. Number: 6 Publisher: Nature Publishing Group.

- Crank, J. and Park, G. (1968). *Diffusion in polymers*. Academic Press Inc, London.
- Crosby, N. D., Weisshaar, C. L., Smith, J. R., Zeeman, M. E., Goodman-Keiser, M. D., and Winkelstein, B. A. (2015). Burst and Tonic Spinal Cord Stimulation Differentially Activate GABAergic Mechanisms to Attenuate Pain in a Rat Model of Cervical Radiculopathy. *IEEE Transactions on Biomedical Engineering*, 62(6):1604–1613. Conference Name: IEEE Transactions on Biomedical Engineering.
- Cussler, E. L., Evans, D. F., and Matesich, S. M. A. (1971). Theoretical and Experimental Basis for a Specific Countertransport System in Membranes. *Science*, 172(3981):377–379. Publisher: American Association for the Advancement of Science Section: Reports.
- De Lima-Pardini, A. C., Coelho, D. B., Souza, C. P., Souza, C. O., Ghilardi, M. G. d. S., Garcia, T., Voos, M., Milosevic, M., Hamani, C., Teixeira, L. A., and Fonoff, E. T. (2018). Effects of spinal cord stimulation on postural control in Parkinson’s disease patients with freezing of gait. *eLife*, 7:e37727. Publisher: eLife Sciences Publications, Ltd.
- De Ridder, D. and Vanneste, S. (2016). Burst and Tonic Spinal Cord Stimulation: Different and Common Brain Mechanisms. *Neuromodulation: Technology at the Neural Interface*, 19(1):47–59.
- De Ridder, D., Vanneste, S., Plazier, M., van der Loo, E., and Menovsky, T. (2010). Burst Spinal Cord Stimulation Toward Paresthesia-Free Pain Suppression. *Neurosurgery*, 66(5):986–990. Publisher: Oxford Academic.
- Deer, T., Slavin, K. V., Amirdelfan, K., North, R. B., Burton, A. W., Yearwood, T. L., Tavel, E., Staats, P., Falowski, S., Pope, J., Justiz, R., Fabi, A. Y., Taghva, A., Paicius, R., Houden, T., and Wilson, D. (2018). Success Using Neuromodulation With BURST (SUNBURST) Study: Results From a Prospective, Randomized Controlled Trial Using a Novel Burst Waveform. *Neuromodulation: Technology at the Neural Interface*, 21(1):56–66.
- Deer, T. R., Levy, R. M., Kramer, J., Poree, L., Amirdelfan, K., Grigsby, E., Staats, P., Burton, A. W., Burgher, A. H., O Bray, J., Scowcroft, J., Golovac, S., Kapural, L., Paicius, R., Kim, C., Pope, J., Yearwood, T., Samuel, S., McRoberts, W. P., Cassim, H., Netherton, M., Miller, N., Schaufele, M., Tavel, E., Davis, T., Davis, K., Johnson, L., and Mekhail, N. (2017). Dorsal root ganglion stimulation yielded higher treatment success rate for complex regional pain syndrome and causalgia at 3 and 12 months: a randomized comparative trial. *Pain*, 158(4):669–681.
- Donnan, F. G. (1924). The Theory of Membrane Equilibria. *Chemical Reviews*, 1(1):73–90.
- Duval, T., Saliiani, A., Nami, H., Nanci, A., Stikov, N., Leblond, H., and Cohen-Adad, J. (2019). Axons morphometry in the human spinal cord. *NeuroImage*, 185:119–128.

- Eldabe, S., Buchser, E., and Duarte, R. V. (2016). Complications of Spinal Cord Stimulation and Peripheral Nerve Stimulation Techniques: A Review of the Literature. *Pain Medicine*, 17(2):325–336. Publisher: Oxford Academic.
- Ferro, M. D. and Melosh, N. A. (2018). Electronic and Ionic Materials for Neurointerfaces. *Advanced Functional Materials*, 28(12):1704335.
- FitzHugh, R. (1961). Impulses and Physiological States in Theoretical Models of Nerve Membrane. *Biophysical Journal*, 1(6):445–466.
- Flory, P. J. (1953). *Principles of Polymer Chemistry*. Cornell University Press. Google Books ID: CQ0EbEKT5R0C.
- Formento, E., Minassian, K., Wagner, F., Mignardot, J. B., Le Goff-Mignardot, C. G., Rowald, A., Bloch, J., Micera, S., Capogrosso, M., and Courtine, G. (2018). Electrical spinal cord stimulation must preserve proprioception to enable locomotion in humans with spinal cord injury. *Nature Neuroscience*, 21(12):1728–1741. Number: 12 Publisher: Nature Publishing Group.
- Freegarde, T. (2012). *Introduction to the Physics of Waves*. Cambridge University Press.
- Gabrielsson, E. O., Tybrandt, K., and Berggren, M. (2012). Ion diode logics for pH control. *Lab on a Chip*, 12(14):2507–2513. Publisher: The Royal Society of Chemistry.
- Gaines, J. L., Finn, K. E., Slopsma, J. P., Heyboer, L. A., and Polasek, K. H. (2018). A model of motor and sensory axon activation in the median nerve using surface electrical stimulation. *Journal of Computational Neuroscience*, 45(1):29–43.
- Ganne, J. M. (1976). Interferential Therapy. *Australian Journal of Physiotherapy*, 22(3):101–110.
- Gas, B. (2005). Electrophoresis Principles. In *Encyclopedia of Analytical Science (Second Edition)*, pages 363–370. Elsevier, Oxford.
- Geise, G. M., Paul, D. R., and Freeman, B. D. (2014). Fundamental water and salt transport properties of polymeric materials. *Progress in Polymer Science*, 39(1):1–42.
- Gkoupidenis, P., Koutsouras, D. A., and Malliaras, G. G. (2017). Neuromorphic device architectures with global connectivity through electrolyte gating. *Nature Communications*, 8(1):15448. Number: 1 Publisher: Nature Publishing Group.
- Goats, G. C. (1990). Interferential current therapy. *British Journal of Sports Medicine*, 24(2):87–92. Publisher: British Association of Sport and Exercise Medicine.

- Grant, P. F. and Lowery, M. M. (2009). Effects of the electrical double layer and dispersive tissue properties in a volume conduction model of deep brain stimulation. In *2009 Annual International Conference of the IEEE Engineering in Medicine and Biology Society*, pages 6497–6500. ISSN: 1558-4615.
- Groenendaal, L., Jonas, F., Freitag, D., Pielartzik, H., and Reynolds, J. R. (2000). Poly(3,4-ethylenedioxythiophene) and Its Derivatives: Past, Present, and Future. *Advanced Materials*, 12(7):481–494.
- Grossman, N., Bono, D., Dedic, N., Kodandaramaiah, S. B., Rudenko, A., Suk, H.-J., Cas-sara, A. M., Neufeld, E., Kuster, N., Tsai, L.-H., Pascual-Leone, A., and Boyden, E. S. (2017). Noninvasive Deep Brain Stimulation via Temporally Interfering Electric Fields. *Cell*, 169(6):1029–1041.e16.
- Grossmann, C., Roos, H.-G., and Stynes, M. M. (2007). *Numerical treatment of partial differential equations*. Berlin ; New York : Springer.
- Grussu, F., Schneider, T., Yates, R. L., Zhang, H., Wheeler-Kingshott, C. A. M. G., DeLuca, G. C., and Alexander, D. C. (2016). A framework for optimal whole-sample histological quantification of neurite orientation dispersion in the human spinal cord. *Journal of Neuroscience Methods*, 273:20–32.
- Gupta, K. K. and Meek, J. L. (1996). A Brief History of the Beginning of the Finite Element Method. *International Journal for Numerical Methods in Engineering*, 39(22):3761–3774.
- Hans, N. (1952). Electric nerve stimulator. US Patent 2,622,601.
- Helferich, F. G. (1995). *Ion Exchange*. Courier Corporation. Google Books ID: F9OQM EA88CAC.
- Hernández-Labrado, G. R., Polo, J. L., López-Dolado, E., and Collazos-Castro, J. E. (2011). Spinal cord direct current stimulation: finite element analysis of the electric field and current density. *Medical & Biological Engineering & Computing*, 49(4):417–429.
- Heywang, G. and Jonas, F. (1992). Poly(alkylenedioxythiophene)s—new, very stable conducting polymers. *Advanced Materials*, 4(2):116–118.
- Hidalgo-Álvarez, R., Martín, A., Fernández, A., Bastos, D., Martínez, F., and de las Nieves, F. J. (1996). Electrokinetic properties, colloidal stability and aggregation kinetics of polymer colloids. *Advances in Colloid and Interface Science*, 67:1–118.
- Hille, B. (1978). Ionic channels in excitable membranes. Current problems and biophysical approaches. *Biophysical Journal*, 22(2):283–294.

- Hodgkin, A. L. and Huxley, A. F. (1952). A quantitative description of membrane current and its application to conduction and excitation in nerve. *The Journal of Physiology*, 117(4):500–544.
- Holford, N. H. G. and Sheiner, L. B. (1981). Understanding the Dose-Effect Relationship. *Clinical Pharmacokinetics*, 6(6):429–453.
- Holinski, B. J., Mazurek, K. A., Everaert, D. G., Toossi, A., Lucas-Osma, A. M., Troyk, P., Etienne-Cummings, R., Stein, R. B., and Mushahwar, V. K. (2016). Intraspinal microstimulation produces over-ground walking in anesthetized cats. *Journal of Neural Engineering*, 13(5):056016. Publisher: IOP Publishing.
- Horn, R. and Vandenberg, C. A. (1984). Statistical properties of single sodium channels. *Journal of General Physiology*, 84(4):505–534. Publisher: The Rockefeller University Press.
- Houck, M. M. and Siegel, J. A. (2015). Chapter 6 - Separation Methods. In Houck, M. M. and Siegel, J. A., editors, *Fundamentals of Forensic Science (Third Edition)*, pages 121–151. Academic Press, San Diego.
- Howells, J., Trevillion, L., Bostock, H., and Burke, D. (2012). The voltage dependence of I_h in human myelinated axons. *The Journal of Physiology*, 590(7):1625–1640.
- Huang, Y., Datta, A., and Parra, L. C. (2020). Optimization of interferential stimulation of the human brain with electrode arrays. *Journal of Neural Engineering*, 17(3):036023.
- Huang, Y. and Parra, L. C. (2019). Can transcranial electric stimulation with multiple electrodes reach deep targets? *Brain Stimulation*, 12(1):30–40.
- Hutcheon, B. and Yarom, Y. (2000). Resonance, oscillation and the intrinsic frequency preferences of neurons. *Trends in Neurosciences*, 23(5):216–222.
- Huxley, A. F. and Stämpfli, R. (1949). Evidence for saltatory conduction in peripheral myelinated nerve fibres. *The Journal of Physiology*, 108(3):315–339.
- Isaksson, J., Kjäll, P., Nilsson, D., Robinson, N., Berggren, M., and Richter-Dahlfors, A. (2007). Electronic control of Ca^{2+} signalling in neuronal cells using an organic electronic ion pump. *Nature Materials*, 6(9):673–679.
- Ita, K. (2016). Transdermal iontophoretic drug delivery: advances and challenges. *Journal of Drug Targeting*, 24(5):386–391.
- Jastrzebska-Perfect, P., Chowdhury, S., Spyropoulos, G. D., Zhao, Z., Cea, C., Gelinis, J. N., and Khodagholy, D. (2020). Translational Neuroelectronics. *Advanced Functional Materials*, 30(29):1909165.

- Jeans, S. J. H. (1968). *Science & Music*. Courier Corporation. Google Books ID: dF7FVc9Tgz4C.
- Jensen, M. P. and Brownstone, R. M. (2019). Mechanisms of spinal cord stimulation for the treatment of pain: Still in the dark after 50 years. *European Journal of Pain*, 23(4):652–659.
- Ji, Y., Luo, H., and Geise, G. M. (2018). Specific co-ion sorption and diffusion properties influence membrane permselectivity. *Journal of Membrane Science*, 563:492–504.
- Jo, S. H., Chang, T., Ebong, I., Bhadviya, B. B., Mazumder, P., and Lu, W. (2010). Nanoscale Memristor Device as Synapse in Neuromorphic Systems. *Nano Letters*, 10(4):1297–1301. Publisher: American Chemical Society.
- Jonsson, A., Sjöström, T. A., Tybrandt, K., Berggren, M., and Simon, D. T. (2016). Chemical delivery array with millisecond neurotransmitter release. *Science Advances*, 2(11):e1601340.
- Jonsson, A., Song, Z., Nilsson, D., Meyerson, B. A., Simon, D. T., Linderöth, B., and Berggren, M. (2015). Therapy using implanted organic bioelectronics. *Science Advances*, 1(4):e1500039.
- Kamcev, J. (2016). *Ion sorption and transport in ion exchange membranes : importance of counter-ion condensation*. Doctoral thesis, University of Texas at Austin.
- Kamcev, J., Doherty, C. M., Lopez, K. P., Hill, A. J., Paul, D. R., and Freeman, B. D. (2018a). Effect of fixed charge group concentration on salt permeability and diffusion coefficients in ion exchange membranes. *Journal of Membrane Science*, 566:307–316.
- Kamcev, J., Galizia, M., Benedetti, F. M., Jang, E.-S., Paul, D. R., Freeman, B. D., and Manning, G. S. (2016). Partitioning of mobile ions between ion exchange polymers and aqueous salt solutions: importance of counter-ion condensation. *Physical Chemistry Chemical Physics*, 18(8):6021–6031. Publisher: The Royal Society of Chemistry.
- Kamcev, J., Paul, D. R., and Freeman, B. D. (2015). Ion Activity Coefficients in Ion Exchange Polymers: Applicability of Manning’s Counterion Condensation Theory. *Macromolecules*, 48(21):8011–8024.
- Kamcev, J., Paul, D. R., and Freeman, B. D. (2017a). Effect of fixed charge group concentration on equilibrium ion sorption in ion exchange membranes. *Journal of Materials Chemistry A*, 5(9):4638–4650.
- Kamcev, J., Paul, D. R., Manning, G. S., and Freeman, B. D. (2017b). Accounting for frame of reference and thermodynamic non-idealities when calculating salt diffusion coefficients in ion exchange membranes. *Journal of Membrane Science*, 537:396–406.

- Kamcev, J., Paul, D. R., Manning, G. S., and Freeman, B. D. (2017c). Predicting Salt Permeability Coefficients in Highly Swollen, Highly Charged Ion Exchange Membranes. *ACS Applied Materials & Interfaces*, 9(4):4044–4056.
- Kamcev, J., Paul, D. R., Manning, G. S., and Freeman, B. D. (2018b). Ion Diffusion Coefficients in Ion Exchange Membranes: Significance of Counterion Condensation. *Macromolecules*, 51(15):5519–5529.
- Kameyama, T., Hashizume, Y., and Sobue, G. (1996). Morphologic Features of the Normal Human Cadaveric Spinal Cord. *Spine*, 21(11):1285–1290.
- Kapural, L., Yu, C., Doust, M. W., Gliner, B. E., Vallejo, R., Sitzman, B. T., Amirdelfan, K., Morgan, D. M., Brown, L. L., Yearwood, T. L., Bundschu, R., Burton, A. W., Yang, T., Benyamin, R., and Burgher, A. H. (2015). Novel 10-kHz High-frequency Therapy (HF10 Therapy) Is Superior to Traditional Low-frequency Spinal Cord Stimulation for the Treatment of Chronic Back and Leg Pain: The SENZA-RCT Randomized Controlled Trial. *Anesthesiology*, 123(4):851–860.
- Kemler, M. A., Barendse, G. A., van Kleef, M., de Vet, H. C., Rijks, C. P., Furnée, C. A., and van den Wildenberg, F. A. (2000). Spinal Cord Stimulation in Patients with Chronic Reflex Sympathetic Dystrophy. *New England Journal of Medicine*, 343(9):618–624. Publisher: Massachusetts Medical Society.
- Khadka, N., Liu, X., Zander, H., Swami, J., Rogers, E., Lempka, S. F., and Bikson, M. (2020). Realistic anatomically detailed open-source spinal cord stimulation (RADO-SCS) model. *Journal of Neural Engineering*, 17(2):026033. Publisher: IOP Publishing.
- Khodagholy, D., Gelinas, J. N., Thesen, T., Doyle, W., Devinsky, O., Malliaras, G. G., and Buzsáki, G. (2015). NeuroGrid: recording action potentials from the surface of the brain. *Nature Neuroscience*, 18(2):310–315. Publisher: Nature Publishing Group.
- Kilgore, K. L. and Bhadra, N. (2014). Reversible Nerve Conduction Block Using Kilohertz Frequency Alternating Current. *Neuromodulation: Technology at the Neural Interface*, 17(3):242–255.
- Kilic, M. S., Bazant, M. Z., and Ajdari, A. (2007). Steric effects in the dynamics of electrolytes at large applied voltages. I. Double-layer charging. *Physical Review. E, Statistical, Nonlinear, and Soft Matter Physics*, 75(2 Pt 1):021502.
- Kohlrausch, F. W. G. . (2016). *An Introduction to Physical Measurement, with Appendices on Absolute Electrical Measurements, Etc. 2D Ed.* WENTWORTH Press. Google Books ID: BR1jvgAACA AJ.

- Koser, D., Moeendarbary, E., Hanne, J., Kuerten, S., and Franze, K. (2015). CNS Cell Distribution and Axon Orientation Determine Local Spinal Cord Mechanical Properties. *Biophysical Journal*, 108(9):2137–2147.
- Koutsouras, D. A., Gkoupidenis, P., Stolz, C., Subramanian, V., Malliaras, G. G., and Martin, D. C. (2017). Impedance Spectroscopy of Spin-Cast and Electrochemically Deposited PEDOT:PSS Films on Microfabricated Electrodes with Various Areas. *ChemElectroChem*, 4(9):2321–2327. Publisher: John Wiley & Sons, Ltd.
- Kozai, T. D. Y., Langhals, N. B., Patel, P. R., Deng, X., Zhang, H., Smith, K. L., Lahann, J., Kotov, N. A., and Kipke, D. R. (2012). Ultrasmall implantable composite microelectrodes with bioactive surfaces for chronic neural interfaces. *Nature Materials*, 11(12):1065–1073. Number: 12 Publisher: Nature Publishing Group.
- Kumar, K., Wilson, J. R., Taylor, R. S., and Gupta, S. (2006). Complications of spinal cord stimulation, suggestions to improve outcome, and financial impact. *Journal of Neurosurgery: Spine*, 5(3):191–203. Publisher: American Association of Neurological Surgeons Section: Journal of Neurosurgery: Spine.
- Lacour, S. P., Courtine, G., and Guck, J. (2016). Materials and technologies for soft implantable neuroprostheses. *Nature Reviews Materials*, 1(10):1–14. Number: 10 Publisher: Nature Publishing Group.
- Laurell, C.-B. (1966). Quantitative estimation of proteins by electrophoresis in agarose gel containing antibodies. *Analytical Biochemistry*, 15(1):45–52.
- Leeb, H. (1955). Initial experiences with the use of interferential alternate currents in inflammatory diseases of the female genitalia. *Wiener medizinische Wochenschrift (1946)*, 105(47):972–975.
- Lempka, S. F., McIntyre, C. C., Kilgore, K. L., and Machado, A. G. (2015). Computational Analysis of Kilohertz Frequency Spinal Cord Stimulation for Chronic Pain Management. *Anesthesiology: The Journal of the American Society of Anesthesiologists*, 122(6):1362–1376. Publisher: The American Society of Anesthesiologists.
- Lempka, S. F. and Patil, P. G. (2018). Innovations in spinal cord stimulation for pain. *Current Opinion in Biomedical Engineering*, 8:51–60.
- Li, H., Gao, Y., Pan, L., Zhang, Y., Chen, Y., and Sun, Z. (2008). Electrosorptive desalination by carbon nanotubes and nanofibres electrodes and ion-exchange membranes. *Water research*, 42(20):4923–4928.
- Li, H. and Zou, L. (2011). Ion-exchange membrane capacitive deionization: A new strategy for brackish water desalination. *Desalination*, 275(1-3):62–66.

- Liao, C., Zhang, M., Yao, M. Y., Hua, T., Li, L., and Yan, F. (2015). Flexible Organic Electronics in Biology: Materials and Devices. *Advanced Materials*, 27(46):7493–7527.
- Linderoth, B. and Foreman, R. D. (2017). Conventional and Novel Spinal Stimulation Algorithms: Hypothetical Mechanisms of Action and Comments on Outcomes. *Neuromodulation: Technology at the Neural Interface*, 20(6):525–533.
- Lindén, H., Pettersen, K. H., and Einevoll, G. T. (2010). Intrinsic dendritic filtering gives low-pass power spectra of local field potentials. *Journal of Computational Neuroscience*, 29(3):423–444.
- Lucas, K. (1907). On the rate of variation of the exciting current as a factor in electric excitation. *The Journal of Physiology*, 36(4-5):253–274.
- Luo, T., Abdu, S., and Wessling, M. (2018). Selectivity of ion exchange membranes: A review. *Journal of Membrane Science*, 555:429–454.
- Löscher, W. and Potschka, H. (2005). Drug resistance in brain diseases and the role of drug efflux transporters. *Nature Reviews. Neuroscience*, 6(8):591–602.
- Mackie, J. S., Meares, P., and Rideal, E. K. (1955). The diffusion of electrolytes in a cation-exchange resin membrane I. Theoretical. *Proceedings of the Royal Society of London. Series A. Mathematical and Physical Sciences*, 232(1191):498–509.
- Manning, G. S. (1969). Limiting Laws and Counterion Condensation in Polyelectrolyte Solutions II. Self-Diffusion of the Small Ions. *The Journal of Chemical Physics*, 51(3):934–938.
- Marcus, Y. and Hefter, G. (2006). Ion Pairing. *Chemical Reviews*, 106(11):4585–4621. Publisher: American Chemical Society.
- Martin, D. C. and Malliaras, G. G. (2016). Interfacing Electronic and Ionic Charge Transport in Bioelectronics. *ChemElectroChem*, 3(5):686–688.
- MathWorks (2018). Simuink, MATLAB-based Modeling Software.
- Mauritz, K. A. and Moore, R. B. (2004). State of understanding of nafion. *Chemical reviews*, 104(10):4535–4586.
- McCreery, D., Agnew, W., Yuen, T., and Bullara, L. (1990). Charge density and charge per phase as cofactors in neural injury induced by electrical stimulation. *IEEE Transactions on Biomedical Engineering*, 37(10):996–1001.
- McGreevy, K., Williams, K. A., and Christo, P. J. (2012). Cephalad lead migration following spinal cord stimulation implantation. *Pain Physician*, 15(1):E79–87.

- McIntyre, C. C., Richardson, A. G., and Grill, W. M. (2002). Modeling the Excitability of Mammalian Nerve Fibers: Influence of Afterpotentials on the Recovery Cycle. *Journal of Neurophysiology*, 87(2):995–1006. Publisher: American Physiological Society.
- Mconnell (2009). Anterior view X-ray image of a paddle type SCS implanted in the thoracic level of the spinal cord. Accessed from Wikipedia under spinal cord stimulator entry.
- Mconnell (2017). Photo of implantation procedure of neurostimulator electrodes. Accessed at: <https://nl.pinterest.com/pin/530017449891538470/>.
- Meadows, P., Mann, C. M., Peterson, D. K.-L., and Chen, J. (2003). Rechargeable spinal cord stimulator system. US Patent 6,516,227.
- Mekhail, N. A., Mathews, M., Nageeb, F., Guirguis, M., Mekhail, M. N., and Cheng, J. (2011). Retrospective Review of 707 Cases of Spinal Cord Stimulation: Indications and Complications. *Pain Practice*, 11(2):148–153.
- Melzack, R. and Wall, P. D. (1965). Pain Mechanisms: A New Theory. *Science*, 150(3699):971–979. Publisher: American Association for the Advancement of Science Section: Articles.
- Moraud, E. M., Capogrosso, M., Formento, E., Wenger, N., DiGiovanna, J., Courtine, G., and Micera, S. (2016). Mechanisms Underlying the Neuromodulation of Spinal Circuits for Correcting Gait and Balance Deficits after Spinal Cord Injury. *Neuron*, 89(4):814–828.
- Moritz, C. T., Lucas, T. H., Perlmutter, S. I., and Fetz, E. E. (2007). Forelimb Movements and Muscle Responses Evoked by Microstimulation of Cervical Spinal Cord in Sedated Monkeys. *Journal of Neurophysiology*, 97(1):110–120. Publisher: American Physiological Society.
- Nagumo, J., Arimoto, S., and Yoshizawa, S. (1962). An Active Pulse Transmission Line Simulating Nerve Axon. *Proceedings of the IRE*, 50(10):2061–2070.
- Nikolova-Troeva, L. (1967). Interferential electrotherapy in distortions, contusions and luxations of joints. *Munchener medizinische Wochenschrift*, 109(11):579–582.
- Noguchi, T., Daido, Y., and Nossek, J. A. (1986). Modulation techniques for microwave digital radio. *IEEE Communications Magazine*, 24:21–30.
- North, R. B., Ewend, M. G., Lawton, M. T., and Piantadosi, S. (1991). Spinal cord stimulation for chronic, intractable pain: Superiority of “multi-channel” devices. *Pain*, 44(2):119–130.
- North, R. B., Kidd, D. H., Petrucci, L., and Dorsi, M. J. (2005). Spinal Cord Stimulation Electrode Design: A Prospective, Randomized, Controlled Trial Comparing Percutaneous with Laminectomy Electrodes: Part II—Clinical Outcomes. *Neurosurgery*, 57(5):990–996. Publisher: Oxford Academic.

- Nucleus (2018). Spinal cord stimulator device and implant location. Stock image, accessed from: <https://www.sciencephoto.com/media/623227/view/a-spinal-cord-stimulator-in-place>.
- Owens, R. M. and Malliaras, G. G. (2010). Organic Electronics at the Interface with Biology. *MRS Bulletin*, 35(6):449–456. Publisher: Cambridge University Press.
- Pardridge, W. M. (2005). The blood-brain barrier: Bottleneck in brain drug development. *NeuroRX*, 2(1):3–14.
- Pardridge, W. M. (2007). Blood–brain barrier delivery. *Drug Discovery Today*, 12(1):54–61.
- Peighambaroust, S. J., Rowshanzamir, S., and Amjadi, M. (2010). Review of the proton exchange membranes for fuel cell applications. *International Journal of Hydrogen Energy*, 35(17):9349–9384.
- Pettersen, K. H. and Einevoll, G. T. (2008). Amplitude Variability and Extracellular Low-Pass Filtering of Neuronal Spikes. *Biophysical Journal*, 94(3):784–802.
- Pollay, M. (1993). Cerebrospinal Fluid in Diseases of the Nervous System. *Neurosurgery*, 32(2).
- Porter, M. C. (1972). Concentration Polarization with Membrane Ultrafiltration. *Product R&D*, 11(3):234–248.
- Poxson, D. J., Gabrielsson, E. O., Bonisoli, A., Linderhed, U., Abrahamsson, T., Matthiesen, I., Tybrandt, K., Berggren, M., and Simon, D. T. (2019). Capillary-Fiber Based Electrophoretic Delivery Device. *ACS Applied Materials & Interfaces*, 11(15):14200–14207. Publisher: American Chemical Society.
- Poxson, D. J., Karady, M., Gabrielsson, R., Alkattan, A. Y., Gustavsson, A., Doyle, S. M., Robert, S., Ljung, K., Grebe, M., Simon, D. T., and Berggren, M. (2017). Regulating plant physiology with organic electronics. *Proceedings of the National Academy of Sciences*, 114(18):4597–4602.
- Prieve, D. C., Anderson, J. L., Ebel, J. P., and Lowell, M. E. (1984). Motion of a particle generated by chemical gradients. Part 2. Electrolytes. *Journal of Fluid Mechanics*, 148:247–269.
- Proctor, C. M., Chan, C. Y., Porcarelli, L., Udabe, E., Sanchez-Sanchez, A., del Agua, I., Mecerreyes, D., and Malliaras, G. G. (2019a). Ionic Hydrogel for Accelerated Dopamine Delivery via Retrodialysis. *Chemistry of Materials*, 31(17):7080–7084. Publisher: American Chemical Society.

- Proctor, C. M., Rivnay, J., and Malliaras, G. G. (2016). Understanding volumetric capacitance in conducting polymers. *Journal of Polymer Science Part B: Polymer Physics*, 54(15):1433–1436.
- Proctor, C. M., Slézia, A., Kaszas, A., Ghestem, A., Agua, I. d., Pappa, A.-M., Bernard, C., Williamson, A., and Malliaras, G. G. (2018). Electrophoretic drug delivery for seizure control. *Science Advances*, 4(8):eaau1291.
- Proctor, C. M., Uguz, I., Slezia, A., Curto, V., Inal, S., Williamson, A., and Malliaras, G. G. (2019b). An ElectroCorticography Device with an Integrated Microfluidic Ion Pump for Simultaneous Neural Recording and Electrophoretic Drug Delivery In Vivo. *Advanced Biosystems*, 3(2):1800270.
- Puil, E., Gimbarzevsky, B., and Miura, R. M. (1986). Quantification of membrane properties of trigeminal root ganglion neurons in guinea pigs. *Journal of Neurophysiology*, 55(5):995–1016. Publisher: American Physiological Society.
- Pérez-González, A., Urtiaga, A. M., Ibáñez, R., and Ortiz, I. (2012). State of the art and review on the treatment technologies of water reverse osmosis concentrates. *Water Research*, 46(2):267–283.
- Rampersad, S., Roig-Solvas, B., Yarossi, M., Kulkarni, P. P., Santarnecchi, E., Dorval, A. D., and Brooks, D. H. (2019). Prospects for transcranial temporal interference stimulation in humans: A computational study. *NeuroImage*, 202:116124.
- Ridder, D. D. and Vanneste, S. (2016). Visions on the future of medical devices in spinal cord stimulation: what medical device is needed? *Expert Review of Medical Devices*, 13(3):233–242. Publisher: Taylor & Francis.
- Rijken, N. H. M., Vonhögen, L. H., Duysens, J., and Keijsers, N. L. W. (2013). The Effect of Spinal Cord Stimulation (SCS) on Static Balance and Gait. *Neuromodulation: Technology at the Neural Interface*, 16(3):244–250.
- Rivnay, J., Leleux, P., Ferro, M., Sessolo, M., Williamson, A., Koutsouras, D. A., Khodagholy, D., Ramuz, M., Strakosas, X., Owens, R. M., Benar, C., Badier, J.-M., Bernard, C., and Malliaras, G. G. (2015). High-performance transistors for bioelectronics through tuning of channel thickness. *Science Advances*, 1(4).
- Rivnay, J., Wang, H., Fenno, L., Deisseroth, K., and Malliaras, G. G. (2017). Next-generation probes, particles, and proteins for neural interfacing. *Science Advances*, 3(6):e1601649. Publisher: American Association for the Advancement of Science Section.

- Samotus, O., Parrent, A., and Jog, M. (2018). Spinal Cord Stimulation Therapy for Gait Dysfunction in Advanced Parkinson's Disease Patients. *Movement Disorders*, 33(5):783–792.
- Sdrulla, A. D., Guan, Y., and Raja, S. N. (2018). Spinal Cord Stimulation: Clinical Efficacy and Potential Mechanisms. *Pain Practice*, 18(8):1048–1067.
- Seitanidou, M., Blomgran, R., Pushpamithran, G., Berggren, M., and Simon, D. T. (2019). Modulating Inflammation in Monocytes Using Capillary Fiber Organic Electronic Ion Pumps. *Advanced Healthcare Materials*, 8(19):1900813.
- Shannon, R. (1992). A model of safe levels for electrical stimulation. *IEEE Transactions on Biomedical Engineering*, 39(4):424–426.
- Shealy, C. N., Mortimer, J. T., and Reswick, J. B. (1967). Electrical Inhibition of Pain by Stimulation of the Dorsal Columns: Preliminary Clinical Report. *Anesthesia & Analgesia*, 46(4):489–491.
- Simon, D. T., Gabrielsson, E. O., Tybrandt, K., and Berggren, M. (2016). Organic Bioelectronics: Bridging the Signaling Gap between Biology and Technology. *Chemical Reviews*, 116(21):13009–13041. Publisher: American Chemical Society.
- Simon, D. T., Kurup, S., Larsson, K. C., Hori, R., Tybrandt, K., Goiny, M., Jager, E. W. H., Berggren, M., Canlon, B., and Richter-Dahlfors, A. (2009). Organic electronics for precise delivery of neurotransmitters to modulate mammalian sensory function. *Nature Materials*, 8(9):742–746.
- Sjöström, T. A., Berggren, M., Gabrielsson, E. O., Janson, P., Poxson, D. J., Seitanidou, M., and Simon, D. T. (2018). A Decade of Iontronic Delivery Devices. *Advanced Materials Technologies*, 3(5):1700360.
- Sjöström, T. A., Jonsson, A., Gabrielsson, E. O., Berggren, M., Simon, D. T., and Tybrandt, K. (2020). Miniaturized Ionic Polarization Diodes for Neurotransmitter Release at Synaptic Speeds. *Advanced Materials Technologies*, 5(3):1900750.
- Someya, T., Bao, Z., and Malliaras, G. G. (2016). The rise of plastic bioelectronics. *Nature*, 540(7633):379–385. Number: 7633 Publisher: Nature Publishing Group.
- Song, Z., Viisanen, H., Meyerson, B. A., Pertovaara, A., and Linderöth, B. (2014). Efficacy of Kilohertz-Frequency and Conventional Spinal Cord Stimulation in Rat Models of Different Pain Conditions. *Neuromodulation: Technology at the Neural Interface*, 17(3):226–235.
- Strathmann, H. (2004). *Ion-Exchange Membrane Separation Processes*. Elsevier. Google Books ID: pcNF7HWbFPIC.

- Strathmann, H. (2010). Electrodialysis, a mature technology with a multitude of new applications. *Desalination*, 264(3):268–288.
- Suzuki, H. and Yoneyama, R. (2003). Integrated microfluidic system with electrochemically actuated on-chip pumps and valves. *Sensors and Actuators B: Chemical*, 96(1):38–45.
- Tanaka, Y. (2015). *Ion Exchange Membranes*. Elsevier, 2nd edition.
- Tanaka, Y., Ehara, R., Itoi, S., and Goto, T. (2003). Ion-exchange membrane electro dialytic salt production using brine discharged from a reverse osmosis seawater desalination plant. *Journal of Membrane Science*, 222(1-2):71–86.
- Tang, R., Martinez, M., Goodman-Keiser, M., Farber, J. P., Qin, C., and Foreman, R. D. (2014). Comparison of burst and tonic spinal cord stimulation on spinal neural processing in an animal model. *Neuromodulation: Journal of the International Neuromodulation Society*, 17(2):143–151.
- Tasaki, I. (1955). New Measurements of the Capacity and the Resistance of the Myelin Sheath and the Nodal Membrane of the Isolated Frog Nerve Fiber. *American Journal of Physiology-Legacy Content*, 181(3):639–650. Publisher: American Physiological Society.
- Teorell, T. (1935). An Attempt to Formulate a Quantitative Theory of Membrane Permeability. *Proceedings of the Society for Experimental Biology and Medicine*, 33(2):282–285.
- Tiede, J., Brown, L., Gekht, G., Vallejo, R., Yearwood, T., and Morgan, D. (2013). Novel Spinal Cord Stimulation Parameters in Patients with Predominant Back Pain. *Neuromodulation: Technology at the Neural Interface*, 16(4):370–375.
- Tohidi, V. and Nadim, F. (2009). Membrane Resonance in Bursting Pacemaker Neurons of an Oscillatory Network Is Correlated with Network Frequency. *Journal of Neuroscience*, 29(20):6427–6435. Publisher: Society for Neuroscience Section: Articles.
- Tuch, D. S., Wedeen, V. J., Dale, A. M., George, J. S., and Belliveau, J. W. (2001). Conductivity tensor mapping of the human brain using diffusion tensor MRI. *Proceedings of the National Academy of Sciences*, 98(20):11697–11701. Publisher: National Academy of Sciences Section: Biological Sciences.
- Tybrandt, K. (2017). Exploring the potential of ionic bipolar diodes for chemical neural interfaces. *Soft Matter*, 13(44):8171–8177.
- Tybrandt, K., Larsson, K. C., Kurup, S., Simon, D. T., Kjäll, P., Isaksson, J., Sandberg, M., Jager, E. W. H., Richter-Dahlfors, A., and Berggren, M. (2009). Translating Electronic Currents to Precise Acetylcholine-Induced Neuronal Signaling Using an Organic Electrophoretic Delivery Device. *Advanced Materials*, 21(44):4442–4446.

- Tybrandt, K., Larsson, K. C., Richter-Dahlfors, A., and Berggren, M. (2010). Ion bipolar junction transistors. *Proceedings of the National Academy of Sciences of the United States of America*, 107(22):9929–9932.
- Tybrandt, K., Zozoulenko, I. V., and Berggren, M. (2017). Chemical potential–electric double layer coupling in conjugated polymer–polyelectrolyte blends. *Science Advances*, 3(12):eaao3659.
- Uguz, I., Proctor, C. M., Curto, V. F., Pappa, A.-M., Donahue, M. J., Ferro, M., Owens, R. M., Khodagholy, D., Inal, S., and Malliaras, G. G. (2017). A Microfluidic Ion Pump for In Vivo Drug Delivery. *Advanced Materials*, 29(27):1701217.
- Vallejo, R., Bradley, K., and Kapural, L. (2017). Spinal Cord Stimulation in Chronic Pain: Mode of Action. *Spine*, 42:S53.
- Verfürth, R. (2013). *A Posteriori Error Estimation Techniques for Finite Element Methods*. OUP Oxford. Google Books ID: SnloAgAAQBAJ.
- Voges, J., Reszka, R., Gossmann, A., Dittmar, C., Richter, R., Garlip, G., Kracht, L., Coenen, H. H., Sturm, V., Wienhard, K., Heiss, W.-D., and Jacobs, A. H. (2003). Imaging-guided convection-enhanced delivery and gene therapy of glioblastoma. *Annals of Neurology*, 54(4):479–487.
- Volkov, A. V., Tybrandt, K., Berggren, M., and Zozoulenko, I. V. (2014). Modeling of Charge Transport in Ion Bipolar Junction Transistors. *Langmuir*, 30(23):6999–7005.
- Volkov, A. V., Wijeratne, K., Mitraga, E., Ail, U., Zhao, D., Tybrandt, K., Andreasen, J. W., Berggren, M., Crispin, X., and Zozoulenko, I. V. (2017). Understanding the Capacitance of PEDOT:PSS. *Advanced Functional Materials*, 27(28):1700329.
- WadmanJun, M. (2017). Electric fields tease buried brain cells into action. Science AAAS, Accessed from: <https://www.sciencemag.org/news/2017/06/electric-fields-tease-buried-brain-cells-action>.
- Wagner, F. B., Mignardot, J.-B., Le Goff-Mignardot, C. G., Demesmaeker, R., Komi, S., Capogrosso, M., Rowald, A., Seáñez, I., Caban, M., Pirondini, E., Vat, M., McCracken, L. A., Heimgartner, R., Fodor, I., Watrin, A., Seguin, P., Paoles, E., Van Den Keybus, K., Eberle, G., Schurch, B., Pralong, E., Becce, F., Prior, J., Buse, N., Buschman, R., Neufeld, E., Kuster, N., Carda, S., von Zitzewitz, J., Delattre, V., Denison, T., Lambert, H., Minassian, K., Bloch, J., and Courtine, G. (2018). Targeted neurotechnology restores walking in humans with spinal cord injury. *Nature*, 563(7729):65–71. Number: 7729 Publisher: Nature Publishing Group.

- Wenger, N., Moraud, E. M., Raspopovic, S., Bonizzato, M., DiGiovanna, J., Musienko, P., Morari, M., Micera, S., and Courtine, G. (2014). Closed-loop neuromodulation of spinal sensorimotor circuits controls refined locomotion after complete spinal cord injury. *Science Translational Medicine*, 6(255):255ra133–255ra133. Publisher: American Association for the Advancement of Science.
- Wesemann, K., Coffey, R. J., Wallace, M. S., Tan, Y., Broste, S., and Buvanendran, A. (2014). Clinical Accuracy and Safety Using the SynchroMed II Intrathecal Drug Infusion Pump. *Regional Anesthesia & Pain Medicine*, 39(4):341–346. Publisher: BMJ Publishing Group Ltd Section: Original Articles.
- Wesselink, W., Holsheimer, J., and Boom, H. (1998). Analysis of current density and related parameters in spinal cord stimulation. *IEEE Transactions on Rehabilitation Engineering*, 6(2):200–207.
- White, H. S., Kittlesen, G. P., and Wrighton, M. S. (1984). Chemical derivatization of an array of three gold microelectrodes with polypyrrole: fabrication of a molecule-based transistor. *Journal of the American Chemical Society*, 106(18):5375–5377.
- Whitehurst, T. K., McGivern, J. P., Mann, C. M., and Kuzma, J. A. (2005). Fully implantable microstimulator for spinal cord stimulation as a therapy for chronic pain. US Patent 6,871,099.
- Wijmans, J. G. and Baker, R. W. (1995). The solution-diffusion model: a review. *Journal of Membrane Science*, 107(1):1–21.
- Williamson, A., Rivnay, J., Kergoat, L., Jonsson, A., Inal, S., Uguz, I., Ferro, M., Ivanov, A., Sjöström, T. A., Simon, D. T., Berggren, M., Malliaras, G. G., and Bernard, C. (2015). Controlling Epileptiform Activity with Organic Electronic Ion Pumps. *Advanced Materials*, 27(20):3138–3144.
- Xing, P., Miled, M. A., and Sawan, M. (2013). Glutamate, gaba and dopamine hydrochloride concentration effects on the conductivity and impedance of cerebrospinal fluid. In *2013 6th International IEEE/EMBS Conference on Neural Engineering (NER)*, pages 1037–1040. IEEE.
- Xu, T. (2005). Ion exchange membranes: State of their development and perspective. *Journal of Membrane Science*, 263(1):1–29.
- Yagi, Y., Maier, P., and Pressman, D. (1962). Immunoelectrophoretic Identification of Guinea Pig Anti-Insulin Antibodies. *The Journal of Immunology*, 89(5):736–744. Publisher: American Association of Immunologists.
- Yanagi, H. and Fukuta, K. (2008). Anion exchange membrane and ionomer for alkaline membrane fuel cells (amfcs). *ECS transactions*, 16(2):257.

- Yasuda, H., Lamaze, C. E., and Ikenberry, L. D. (1968). Permeability of solutes through hydrated polymer membranes. Part I. Diffusion of sodium chloride. *Die Makromolekulare Chemie*, 118(1):19–35.
- Yozu, A., Sumitani, M., Shin, M., Ishi, K., Osumi, M., Katsuhira, J., Chiba, R., and Haga, N. (2016). Effect of Spinal Cord Stimulation on Gait in a Patient with Thalamic Pain. ISSN: 2090-6668 Pages: e8730984 Publisher: Hindawi Volume: 2016.
- Yuk, H., Lu, B., and Zhao, X. (2019). Hydrogel bioelectronics. *Chemical Society Reviews*, 48(6):1642–1667. Publisher: The Royal Society of Chemistry.
- Zander, H. J., Graham, R. D., Anaya, C. J., and Lempka, S. F. (2020). Anatomical and technical factors affecting the neural response to epidural spinal cord stimulation. *Journal of Neural Engineering*, 17(3):036019. Publisher: IOP Publishing.
- Zannou, A. L., Khadka, N., Truong, D. Q., Zhang, T., Esteller, R., Hershey, B., and Bikson, M. (2019). Temperature increases by kilohertz frequency spinal cord stimulation. *Brain Stimulation*, 12(1):62–72.
- Zeglio, E., Rutz, A. L., Winkler, T. E., Malliaras, G. G., and Herland, A. (2019). Conjugated Polymers for Assessing and Controlling Biological Functions. *Advanced Materials*, 31(22).
- Zuo, Y., Cheng, S., and Logan, B. E. (2008). Ion exchange membrane cathodes for scalable microbial fuel cells. *Environmental science & technology*, 42(18):6967–6972.

Appendix A

Synthetic procedure of co-ions used in Chapter 3

Synthesis and analysis provided by Dr. Liliana C. Tomé from University of the Basque Country UPV/EHU.

A.1 Synthetic Procedures

A.1.1 Synthesis of ACh Carboxylate Ionic Liquids

ACh-based ionic liquids combining carboxylate anions with variable carbon-chain lengths, including ACh butyrate (ACh But), ACh hexanoate (ACh Hex) and ACh octanoate (ACh Oct), were synthesized via a two-step ion exchange method at room temperature (Scheme A shown in Figure A.3). In a typical procedure, potassium hydroxide (0.95 mol) was first dissolved in a minimum amount of water and the desired carboxylic acid (1 mol) was added dropwise. After water removal by rotary evaporation, the obtained precipitate was washed with excess of diethyl ether and filtrated. The formed potassium carboxylate salt (1 mol) and ACh chloride (1 mol) were separately dissolved in a minimum amount of ethanol and then mixed by stirring for 1 hour. The mixture was kept in the freezer overnight to complete the precipitation of KCl, which was then filtered off. After solvent removal by rotary evaporation, the obtained ACh carboxylate ionic liquids were dried under high vacuum. The chemical structures were confirmed by NMR analysis.

ACh butyrate: ^1H NMR (400 MHz, D_2O): $\delta/\text{ppm} = 4.01$ (m, 2H, OCH_2); 3.47 (t, 2H, NCH_2); 3.16 (s, 9H, $\text{N}(\text{CH}_3)_3$); 2.23 (t, 2H, CH_2COO); 1.96 (s, 3H, CH_3COO); 1.54 (m, 2H, CH_3CH_2); 0.87 (t, 3H, CH_3CH_2). ^{13}C NMR (101 MHz, D_2O): $\delta/\text{ppm} = 181.42$ (CH_2COO); 179.07 (CH_3COO); 67.66 (t, NCH_2); 55.82 (OCH_2); 54.09 (t, $\text{N}(\text{CH}_3)_3$); 37.61 (CH_2COO); 21.99 (CH_3COO); 18.80 (CH_3CH_2); 13.21 (CH_3CH_2).

ACh hexanoate: ^1H NMR (400 MHz, D_2O): $\delta/\text{ppm} = 4.02$ (t, 2H, OCH_2); 3.48 (t, 2H, NCH_2); 3.16 (s, 9H, $\text{N}(\text{CH}_3)_3$); 2.25 (t, 2H, CH_2COO); 1.97 (s, 3H, CH_3COO); 1.54 (m, 2H, $\text{CH}_2\text{CH}_2\text{COO}$); 1.25 (m, 4H, $\text{CH}_3(\text{CH}_2)_2$); 0.83 (t, 3H, CH_3CH_2). ^{13}C NMR (101 MHz, D_2O): $\delta/\text{ppm} = 181.32$ (CH_2COO); 178.82 (CH_3COO); 67.34 (t, NCH_2); 55.53 (OCH_2); 53.80 (t, $\text{N}(\text{CH}_3)_3$); 35.32 (CH_2COO); 30.66 ($\text{CH}_2\text{CH}_2\text{COO}$); 24.62 ($\text{CH}_3\text{CH}_2\text{CH}_2$); 21.68 (d, CH_3CH_2 , CH_3COO); 13.17 (CH_3CH_2).

ACh octanoate: ^1H NMR (400 MHz, D_2O): $\delta/\text{ppm} = 4.02$ (m, 2H, OCH_2); 3.48 (m, 2H, NCH_2); 3.17 (s, 9H, $\text{N}(\text{CH}_3)_3$); 2.14 (t, 2H, CH_2COO); 1.96 (s, 3H, CH_3COO); 1.54 (m, 2H, $\text{CH}_2\text{CH}_2\text{COO}$); 1.25 (m, 8H, $\text{CH}_3(\text{CH}_2)_4$); 0.82 (t, 3H, CH_3CH_2). ^{13}C NMR (101 MHz, D_2O): $\delta/\text{ppm} = 184.01$ (CH_2COO); 173.19 (CH_3COO); 64.51 (t, NCH_2); 58.29 (OCH_2); 53.72 (t, $\text{N}(\text{CH}_3)_3$); 37.41 (CH_2COO); 31.02 ($\text{CH}_2\text{CH}_2\text{COO}$); 28.66 ($\text{CH}_3(\text{CH}_2)_3\text{CH}_2$); 28.23 ($\text{CH}_3(\text{CH}_2)_2\text{CH}_2$); 25.81 ($\text{CH}_3\text{CH}_2\text{CH}_2$), 21.98 (CH_3CH_2), 20.14 (CH_3COO), 13.37 (CH_3CH_2).

Fig. A.1 NMR data for ACh carboxylate ionic liquids.

A.1.2 Synthesis of poly(sulfopropyl acrylate ACh)

First, the monomer ACh 3-sulfopropyl acrylate (ACh SPA) was prepared (Scheme 1 B). ACh chloride (5 g, 27.5 mmol) and 3-sulfopropyl acrylate potassium salt (6.4 g) were previously dissolved in a minimum amount of methanol and then mixed under vigorous stirring at room temperature for 1 hour. A catalytic amount of 4-methoxyphenol was added as an inhibitor and the methanol was stripped off under reduced pressure at temperature ≤ 40 °C. Afterwards, ethanol was added in order to precipitate the KCl, which is a by-product of the anion exchange reaction. The mixture was kept in the freezer overnight to complete the precipitation of KCl. The precipitate was removed by filtration and the excess of ethanol was gently evaporated. Finally, the resulting white solid monomer was thoroughly dried under high vacuum at room temperature for 2 days.

The polyanion, poly(sulfopropyl acrylate ACh), i.e. poly(SPA ACh), was synthesized by conventional free radical polymerization in water (Scheme B shown in Figure A.3). In a typical procedure, 2 g of the prepared ACh SPA monomer were dissolved in 18 g of MiliQ water to have a 10 wt% solid concentration. The monomer solution was purged with dry nitrogen for 20 min before being putted into an oil bath at 70 °C. The AIBA initiator (1 wt% to the monomer)

ACh 3-sulfopropyl acrylate: ^1H NMR (400 MHz, D_2O): $\delta/\text{ppm} = 6.47\text{--}5.77$ (m, 3H, $\text{CH}_2=\text{CH}$); 4.45 (m, 2H, $\text{OCH}_2\text{CH}_2\text{N}(\text{CH}_3)_3$); 4.20 (m, 2H, $\text{OCH}_2(\text{CH}_2)_2\text{SO}_3$); 3.63 (m, 2H, NCH_2); 3.11 (s, 9H, $\text{N}(\text{CH}_3)_3$); 2.92 (m, 2H, CH_2SO_3); 2.12–1.89 (m, 5H, CH_3COO , $\text{CH}_2\text{CH}_2\text{SO}_3$). ^{13}C NMR (101 MHz, D_2O): $\delta/\text{ppm} = 173.14$ (CH_3COO); 168.58 ($\text{CH}_2=\text{CHCOO}$); 132.22 ($\text{CH}_2=\text{CH}$); 127.50 ($\text{CH}_2=\text{CH}$); 66.44 (t, NCH_2); 63.52 ($\text{OCH}_2(\text{CH}_2)_2\text{SO}_3$); 58.26 ($\text{OCH}_2\text{CH}_2\text{N}(\text{CH}_3)_3$); 53.68 (t, $\text{N}(\text{CH}_3)_3$); 47.66 (CH_2SO_3); 23.60 ($\text{CH}_2\text{CH}_2\text{SO}_3$); 20.12 (CH_3COO).

Fig. A.2 NMR data for ACh 3-sulfopropyl acrylate.

was dissolved in water, purged with nitrogen and added dropwise to the monomer solution at 70 °C. The mixture was then allowed to react for 4 h with constant and vigorous stirring. After polymerization, the excess of water was removed by rotary evaporation. The resulting product was then dried under high vacuum at 60 °C for 24 h to remove traces of water and the polyanion was obtained as a white solid.

In order to obtain a very high molecular weight polyanion, the poly(SPA ACh) was also synthesized by inverse emulsion polymerization (Scheme C shown in Figure A.3). The monomer ACh SPA (1.5 g, 4.31 mmol) was dissolved in 0.6 g of water. Isopal L (1.1 g) was used as organic solvent. Span 83 (0.1 g) and Solftanol 90 (0.15 g) were selected as emulsifiers and sodium metabisulfite (SMB) (0.1 g) as initiator. The polymerization reaction was performed at 70 °C for 2 h, under argon atmosphere. The resulting polymer was then precipitated with cold diethyl ether and thoroughly dried under high vacuum at 60 °C for 24 h.

The chemical structures of the synthesized polymers were confirmed by ^1H NMR. The success of the polymerization reaction can be easily seen from the ^1H NMR spectra shown in Figure A.4. The signals associated with the acrylic protons between 5.8 and 6.4 ppm of the ACh SPA monomer disappeared after both polymerization reactions, revealing that complete conversion of the monomer was achieved. In addition, the characteristic chemical shifts arising from the 3-sulfopropyl acrylate polyanion backbone can be clearly observed together with the proton signals associated with the ACh counter-cation. The molar mass of the synthesized polymers was analyzed by SEC/MALS/RI. The equipment was composed by a LC20 pump (Shimadzu) coupled to a miniDawn Treos multiangle (3 angles) light scattering laser and an OptilabT-Rex differential refractometer (all from Wyatt Technology Corp., USA). Separation was carried out using three columns in series (Ultrahydrogel 120, 250, and 2000 with pore sizes of 120, 250, and 2000 Å, respectively, Waters, Barcelona, Spain). The analyses were carried out at 35 °C, using a 0.1M LiCl/ 1.5×10^{-5} M NaN_3 solution in a mixture of water/acetonitrile (4:1 v/v) at a flow rate of 0.6 mL/min. The refractive index increment was $\text{dn}/\text{dc} = 0.1$ mL/g.

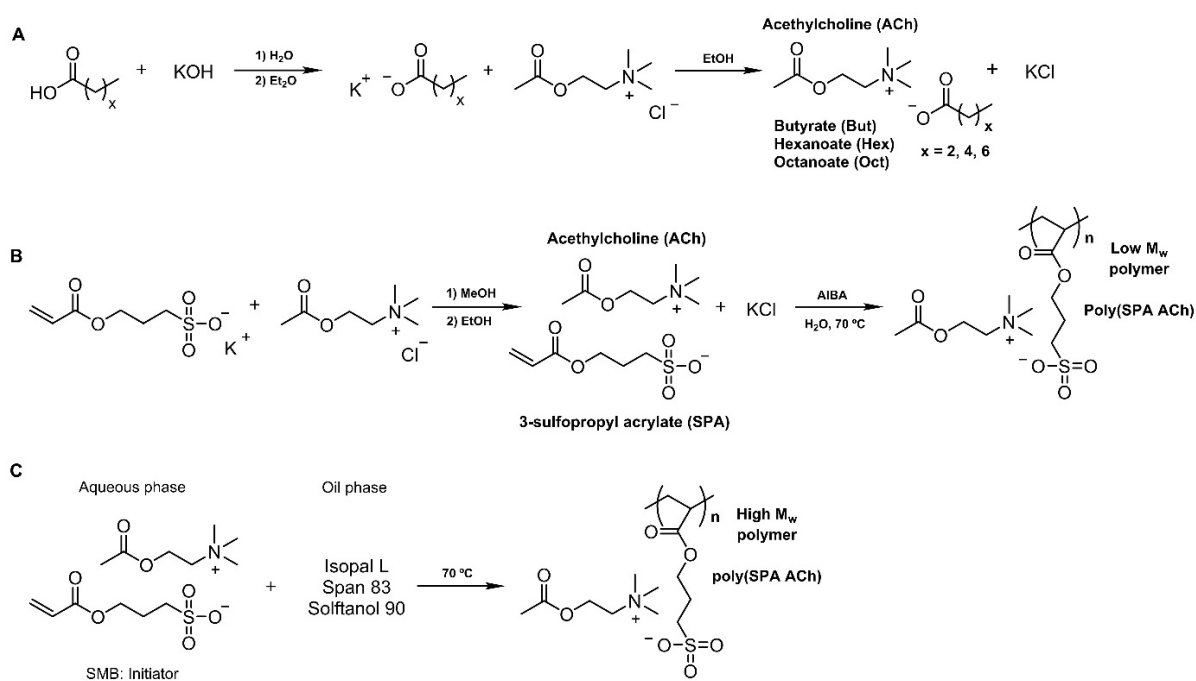


Fig. A.3 Synthetic pathways for (A) ACh-based ionic liquids combining carboxylate anions, (B) ACh SPA monomer and respective free radical polymerization and (C) inverse emulsion polymerization to form poly(SPA ACh).

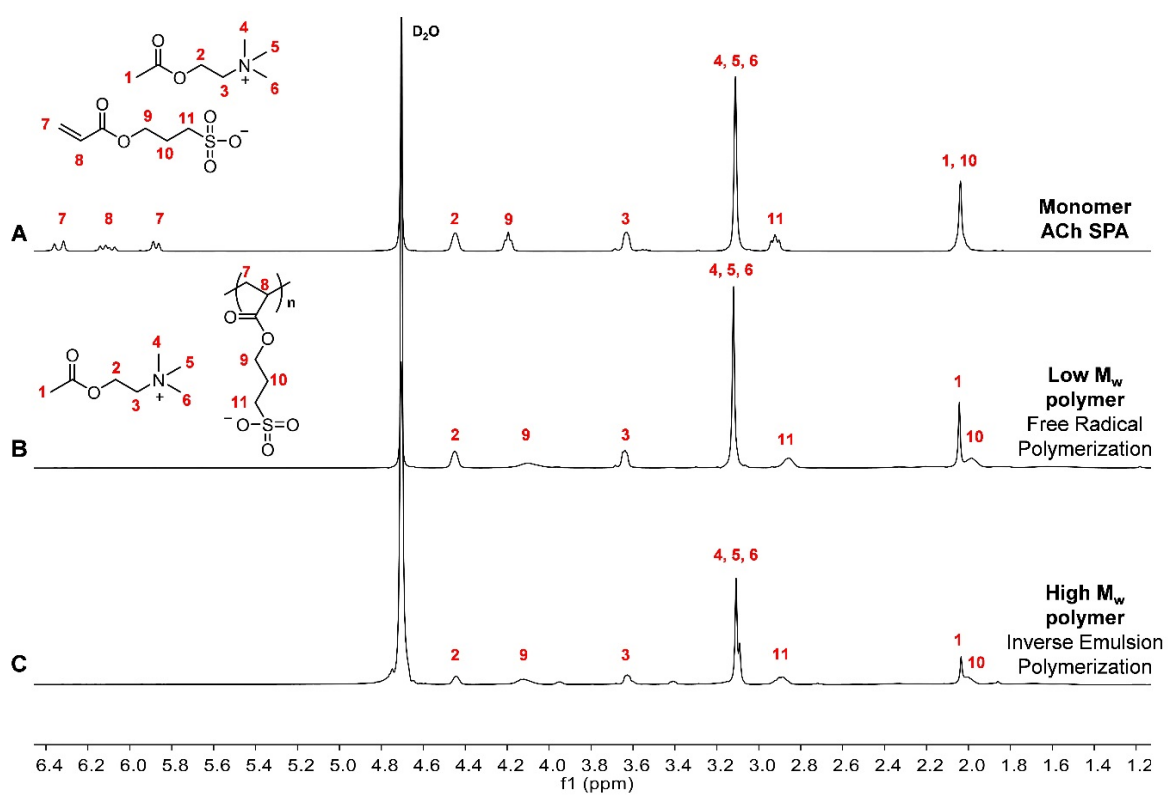


Fig. A.4 $^1\text{H-NMR}$ spectra of (A) ACh 3-sulfopropyl acrylate monomer, and respective polyanions obtained by (B) free radical polymerization and (C) inverse emulsion polymerization.

Appendix B

Axon model parameters and circuit models for Chapter 5

B.1 Axon parameters and equivalent circuits

The membrane voltage dependent parameters for the axon models are based on previous work in [Capogrosso et al. (2013); Gaines et al. (2018); Howells et al. (2012)], consisting of fast sodium channels, persistent sodium channels, fast potassium channels, slow potassium channels, leakage current channels, and internodal passive component.

B.1.1 Sensory axon parameters

Fast sodium current:

$$I_{Na_f} = \bar{g}_{Na_f} \times m^3 h (V_m - E_{Na}) \quad (\text{B.1})$$

$$\alpha_m = \frac{1.77753(V_m + 20.1795)}{1 - e^{-\frac{V_m + 20.1795}{10.3}}} \quad (\text{B.2})$$

$$\beta_m = \frac{0.0823[-(V_m + 25.4746)]}{1 - e^{-\frac{V_m + 25.4746}{9.16}}} \quad (\text{B.3})$$

$$\alpha_h = \frac{0.075286[-(V_m + 112.7124)]}{1 - e^{-\frac{V_m + 112.7124}{8.391}}} \quad (\text{B.4})$$

$$\beta_h = \frac{2.8083}{1 + e^{-\frac{V_m + 30.5435}{10.2263}}} \quad (\text{B.5})$$

Persistent sodium current:

$$I_{Nap} = \bar{g}_{Nap} \times p^3 (V_m - E_{Na}) \quad (\text{B.6})$$

$$\alpha_p = \frac{0.00957(V_m + 26.852)}{1 - e^{-\frac{V_m + 26.852}{10.2}}} \quad (\text{B.7})$$

$$\beta_p = \frac{0.00024[-(V_m + 33.8333)]}{1 - e^{-\frac{V_m + 33.8333}{10}}} \quad (\text{B.8})$$

Fast potassium current:

$$I_{Kf} = \bar{g}_{Kf} \times n^4 (V_m - E_K) \quad (\text{B.9})$$

$$\alpha_n = \frac{0.0462(V_m + 83.2)}{1 - e^{-\frac{V_m - 83.2}{1.1}}} \quad (\text{B.10})$$

$$\beta_n = \frac{0.0824(-V_m - 66)}{1 - e^{-\frac{V_m + 66}{10.5}}} \quad (\text{B.11})$$

Slow potassium current:

$$I_{Ks} = \bar{g}_{Ks} \times s (V_m - E_K) \quad (\text{B.12})$$

$$\alpha_s = \frac{0.3}{1 + e^{-\frac{V_m + 53}{-5}}} \quad (\text{B.13})$$

$$\beta_s = \frac{0.03}{1 + e^{-\frac{V_m + 10}{-1}}} \quad (\text{B.14})$$

B.1.2 Motor axon parameters

Fast sodium current:

$$I_{Naf} = \bar{g}_{Naf} \times m^3 h (V_m - E_{Na}) \quad (\text{B.15})$$

$$\alpha_m = \frac{1.86(V_m + 20.4)}{1 - e^{-\frac{V_m + 20.4}{10.3}}} \quad (\text{B.16})$$

$$\beta_m = \frac{0.086[-(V_m + 25.7)]}{1 - e^{-\frac{V_m + 25.7}{9.16}}} \quad (\text{B.17})$$

$$\alpha_h = \frac{0.062[-(V_m + 114.0)]}{1 - e^{-\frac{V_m + 114.0}{11.0}}} \quad (\text{B.18})$$

$$\beta_h = \frac{2.3}{1 + e^{-\frac{V_m + 31.8}{13.4}}} \quad (\text{B.19})$$

Persistent sodium current:

$$I_{Nap} = \bar{g}_{Nap} \times p^3 (V_m - E_{Na}) \quad (\text{B.20})$$

$$\alpha_p = \frac{0.01(V_m + 27)}{1 - e^{-\frac{V_m + 27}{10.2}}} \quad (\text{B.21})$$

$$\beta_p = \frac{0.00025[-(V_m + 34)]}{1 - e^{-\frac{V_m + 34}{10}}} \quad (\text{B.22})$$

Fast potassium current:

$$I_{Kf} = \bar{g}_{Kf} \times n^4 (V_m - E_K) \quad (\text{B.23})$$

$$\alpha_n = \frac{0.0462(V_m + 83.2)}{1 - e^{-\frac{V_m - 83.2}{1.1}}} \quad (\text{B.24})$$

$$\beta_n = \frac{0.0824(-V_m - 66)}{1 - e^{-\frac{V_m + 66}{10.5}}} \quad (\text{B.25})$$

Slow potassium current:

$$I_{Ks} = \bar{g}_{Ks} \times s (V_m - E_K) \quad (\text{B.26})$$

$$\alpha_s = \frac{0.3}{1 + e^{-\frac{V_m + 53}{-5}}} \quad (\text{B.27})$$

$$\beta_s = \frac{0.03}{1 + e^{-\frac{V_m + 10}{-1}}} \quad (\text{B.28})$$

B.1.3 Simulink model for sensory and motor axon based on MRG model

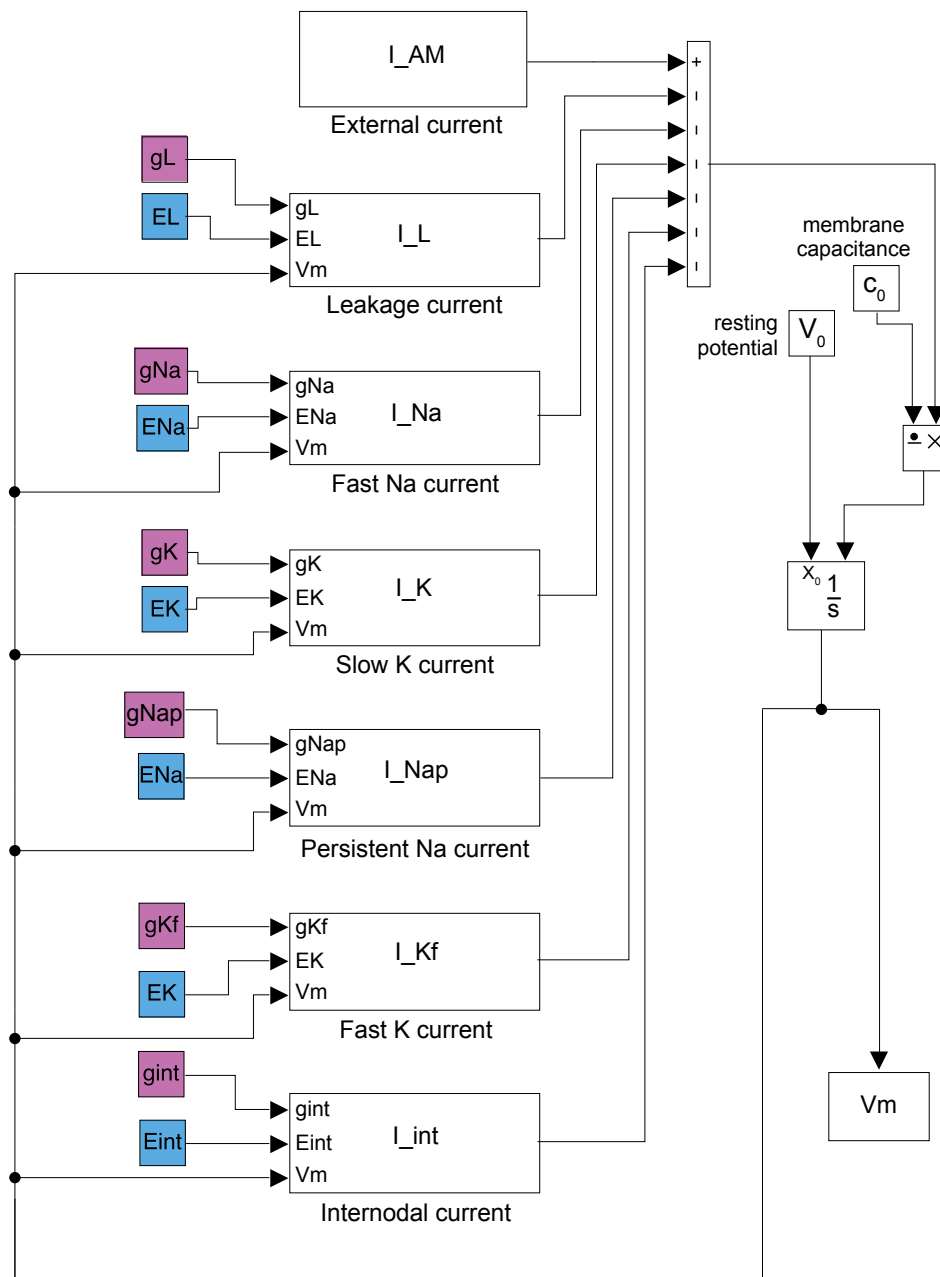


Fig. B.1 Equivalent circuit model representing a sensory axon with diameter of $11.5 \mu\text{m}$.

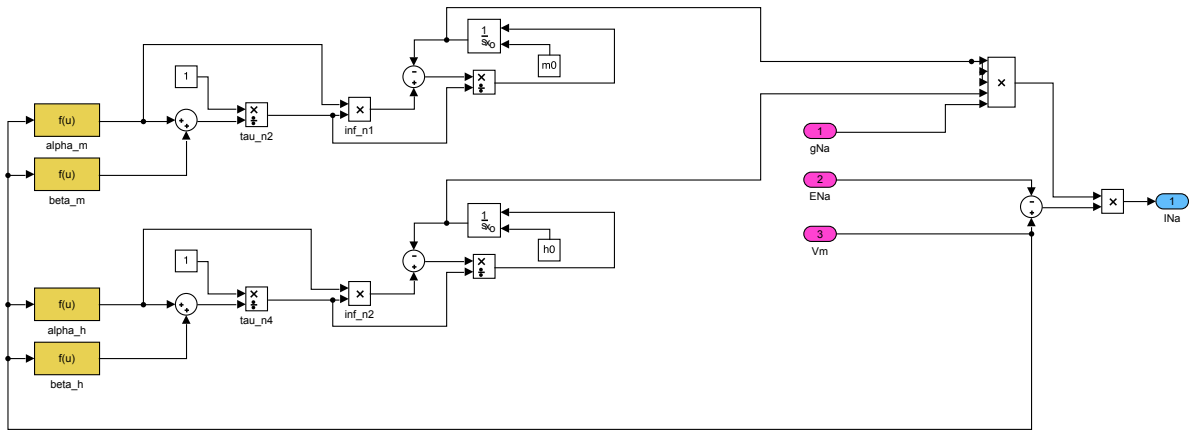


Fig. B.2 Equivalent circuit for the fast sodium ion channel.

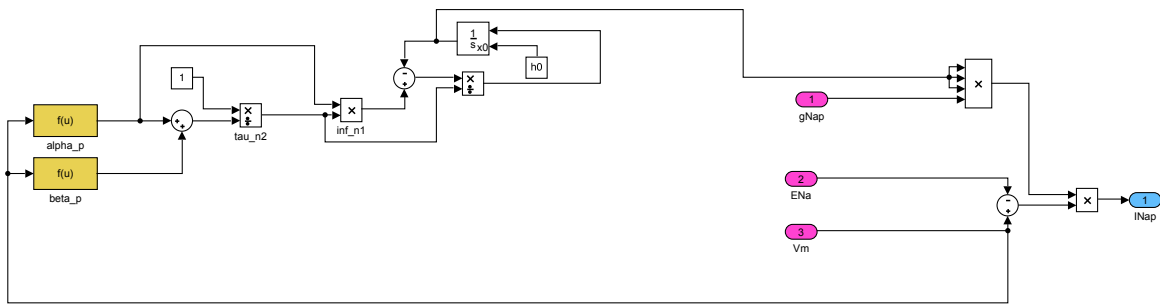


Fig. B.3 Equivalent circuit for the persistent sodium ion channel.

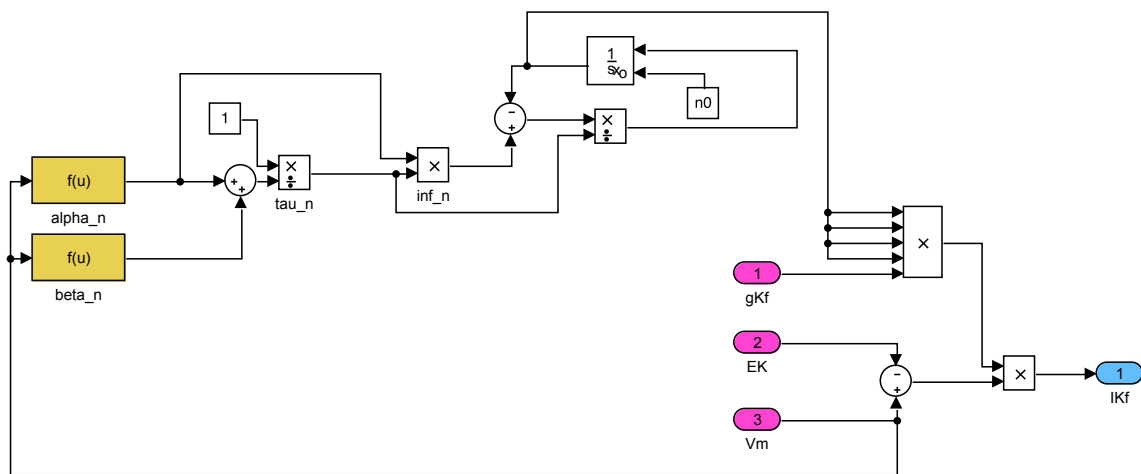


Fig. B.4 Equivalent circuit for the fast potassium ion channel.

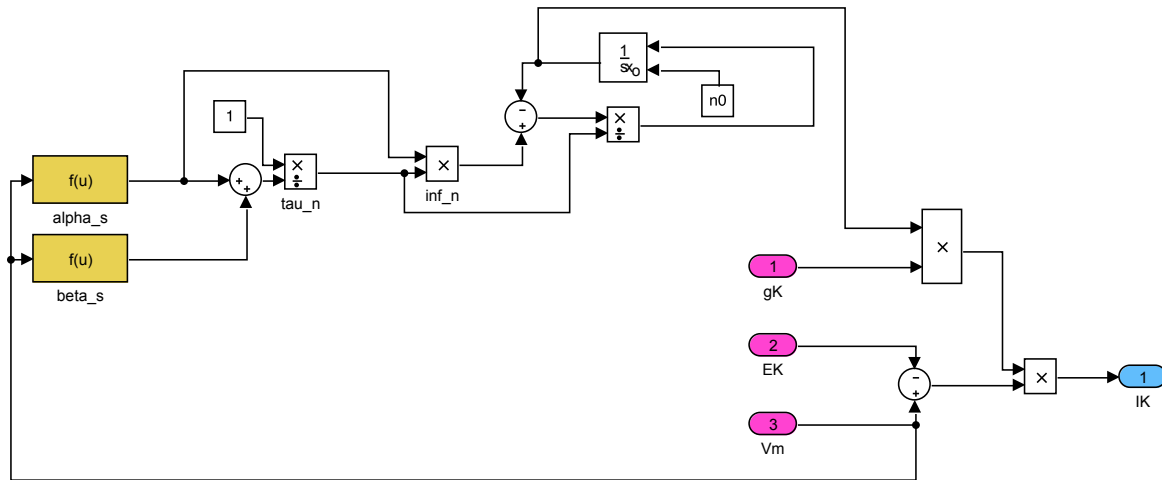


Fig. B.5 Equivalent circuit for the slow potassium ion channel.

B.2 Matlab scripts for temporal interfering stimulation

B.2.1 Calculate the angle between two electric field

```

1 CosAlpha = zeros(length(E1),1); % unprocessed angle data between two E-fields
2 FieldAngle = zeros(length(E1),1); % 0-90 degree angle between two E-fields.
3
4 % The first batch of electric fields are created by 5V in both electrodes.
5 CosTheta = zeros(length(E1),1); % unprocessed angle data between E2 and (E1-E2)
6 DifferenceAngle = zeros(length(E1),1); % 90-180 degree angle between E2 and (E1
  -E2)
7 len_E1 = zeros(length(E1),1); %E1 length
8 len_E2 = zeros(length(E1),1); %E2 length
9 input_E1 = zeros(length(E1),1);
10 input_E2 = zeros(length(E1),1);
11 E3 = E1-E2; % or this can be E2-E1, depends on who is larger.
12 E_ti = zeros(length(E1),1);
13 for i = 1:length(E1)
14     CosAlpha(i) = max(min(dot(E1(i,:),E2(i,:))/(norm(E1(i,:))*norm(E2(i,:))),1
      ,-1));
15     FieldAngle(i) = real(acosd(abs(CosAlpha(i))));
16     CosTheta(i) = max(min(dot(E3(i,:),E2(i,:))/(norm(E3(i,:))*norm(E2(i,:))),1
      ,-1));
17     DifferenceAngle(i) = real(acosd(-abs(CosTheta(i))));
18 end
19
20 for i = 1:length(E1)
21     len_E1(i) = sqrt(E1(i,1)^2+E1(i,2)^2);
22     len_E2(i) = sqrt(E2(i,1)^2+E2(i,2)^2);
23     if len_E1(i)>=len_E2(i)
24         if len_E1(i)* cosd(FieldAngle(i)) > len_E2(i)
25             input_E1(i) = len_E1(i)* cosd(FieldAngle(i));
26             input_E2(i) = len_E2(i);
27         else

```

```

28         input_E1(i) = abs(len_E2(i).*sind(DifferenceAngle(i)));
29         input_E2(i) = abs(len_E2(i).*sind(DifferenceAngle(i)));
30     end
31 end
32
33     if len_E1(i)<len_E2(i)
34         if len_E2(i)* cosd(FieldAngle(i)) > len_E1(i)
35             input_E2(i) = len_E2(i)* cosd(FieldAngle(i));
36             input_E1(i) = len_E1(i);
37         else
38             input_E1(i) = abs(len_E1(i).*sind(DifferenceAngle(i)));
39             input_E2(i) = abs(len_E1(i).*sind(DifferenceAngle(i)));
40         end
41     end
42     E_ti(i) = abs(input_E1(i)+input_E2(i)) -abs(input_E1(i)-input_E2(i));
43 end

```

B.2.2 Extract amplitude modulated stimulation from experimental data

```

1 [filename,filedir] = uigetfile('*.csv','Multiselect','on');%extract all csv
   files
2 path = fullfile(filedir,filename);
3 path = path';
4 file = struct('name',path);
5
6 V1_exp = zeros(length(filename),1);%V1 and V2 are experimentally measured
   potential
7 V2_exp = zeros(length(filename),1);
8
9 for i = 1: length(filename)
10     data = csvread(file(i).name,2,1,'B3..B2002');
11     shift = data(:)-mean(data(:));
12     [yupper,ylower] = envelope(shift);
13     V1_exp(i) = 0.5*(max(yupper)+min(yupper));
14     V2_exp(i) = 0.5*(max(yupper)-min(yupper));
15 end

```

B.2.3 Extract modulation index from experimental data

```

1 % a non-dimensional model for envelope index on a spinal cord
2 % cross-section, with 2 working electrodes each work in monopolar
3 r=1;
4 x0=0;
5 y0=0;
6 syms x y
7 fimplicit((x-x0).^2 + (y-y0).^2 -r^2)
8 axis equal% plot a unit circle first
9 hold on
10 xstart = -1; %unit circle x and y from -1 to 1
11 ystart = -1;
12 xend = 1;

```

```

13 yend = 1;
14 Nx = 100; % divide -1 to 1 into 100 parts
15 Ny = 100;
16 Npts = Nx*Ny;
17 dist = zeros(Npts); %creates empty output matrix to be updated
18 xrange = linspace(xstart,xend,Nx);
19 yrange = linspace(ystart,yend,Ny);
20 [x, y] = meshgrid(xrange, yrange);
21
22 theta_i = 0;
23 theta_ii = 60;
24
25 electrode_1 = [cosd(theta_i) sind(theta_i)];
26 electrode_2 = [cosd(theta_ii) sind(theta_ii)];
27
28 pts = [x(:), y(:)]; %vector form of all points in the x-y grid
29 distances_i = pdist2(pts, electrode_1); %distance to electrode 1
30 distances_ii = pdist2(pts, electrode_2); %distance to electrode 2
31
32 ratio = distances_i./distances_ii; % distance ratio R is the envelope index
33
34 for i = 1: length(ratio) % normalized R so it's less than 1
35     if ratio(i) >1
36         ratio(i) = 1./ratio(i);
37     end
38 end
39
40 Rmatrix = reshape(ratio, 100, 100);
41 contourf(x,y,Rmatrix,500)
42 hold off

```

B.2.4 Animations of recruitment areas with varying stimulation intensities

```

1 x = [0:1*50:29*50];
2 y = [0:1*50:29*50]; % factor for converting from MRG to V/cm.
3 [X,Y] = meshgrid(x,y);
4
5 x_scale = reshape(X,900,1);
6 y_scale = reshape(Y,900,1);
7 v = reshape(Act,900,1); % Act is the activation map, unit in V/cm
8
9 F = scatteredInterpolant(x_scale,y_scale,v,'nearest'); % Activation map
10 vq = zeros(length(input_E1),1); % Interpolated recruitment area
11
12 for i = 1:50 % Vapp from 2 to 7mA in both E1 and E2.
13     vq(:,i) = F(input_E1.*(0.1*i),input_E2*(0.1*i));
14 end
15
16 %creating GIF with a loop
17 h = figure;
18 axis tight equal % this ensures that getframe() returns a consistent size
19 filename = 'simcomp_0804.gif'; % the GIF file name

```

```
20 for i = 1:50
21     pointsToSurf(coord(:,1),coord(:,2),vq(:,i))
22     view(2)
23     axis equal
24     colorbar
25     caxis([0 30]);
26     shading interp
27     drawnow
28     % Capture the plot as an image
29     frame = getframe(h);
30     im = frame2im(frame);
31     [imind,cm] = rgb2ind(im,256);
32     % Write to the GIF File
33     if i == 1
34         imwrite(imind,cm,filename,'gif', 'Loopcount',inf);
35     else
36         imwrite(imind,cm,filename,'gif','WriteMode','append');
37     end
38 end
```

B.3 Axon activation maps for different base frequencies f

B.3.1 $f = 1500$ Hz

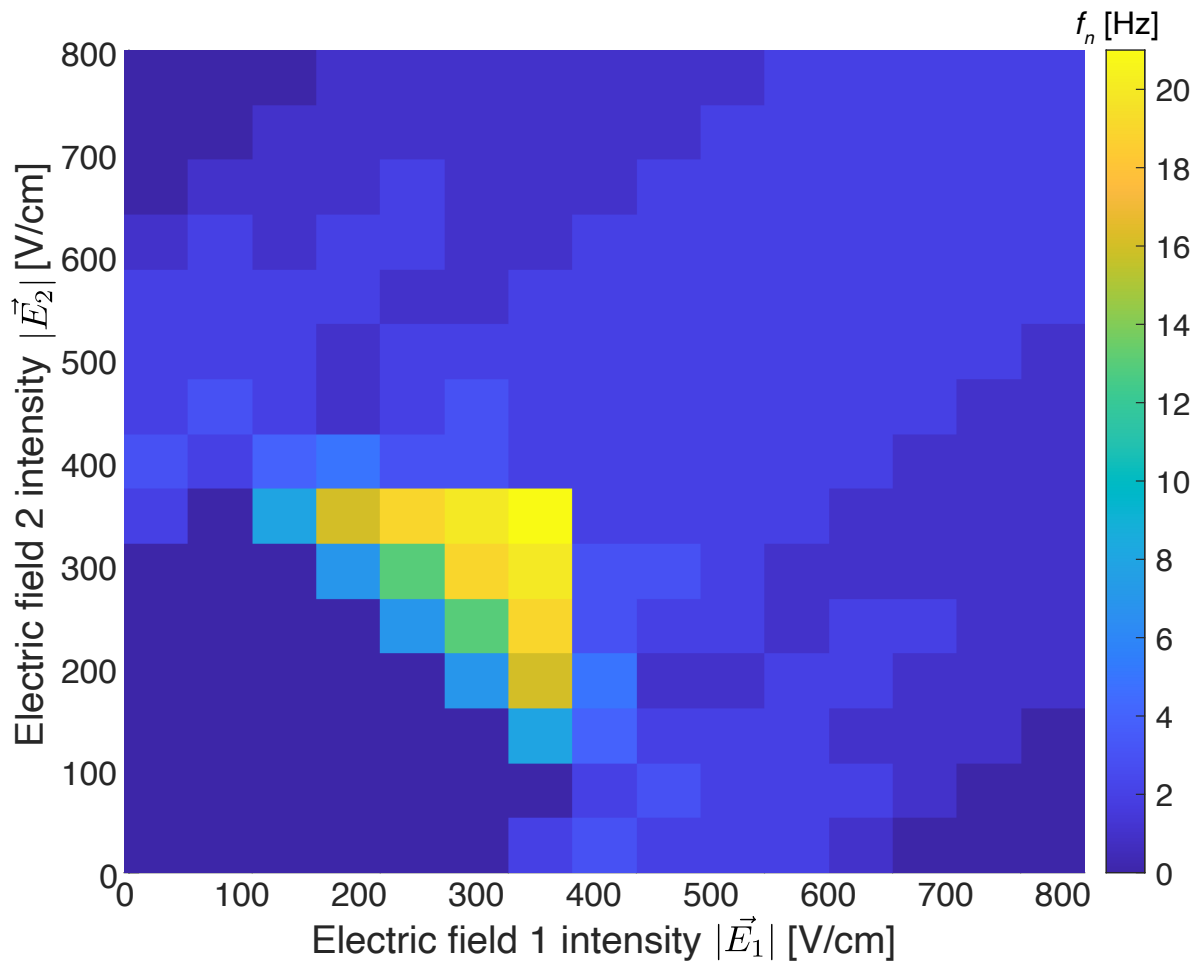


Fig. B.6 Axon activation map for a sensory axon with a diameter of $11.5 \mu\text{m}$ as functions of both $|\vec{E}_1|$ and $|\vec{E}_2|$, $f_1 = 1500$ Hz and $f_2 = 1510$ Hz.

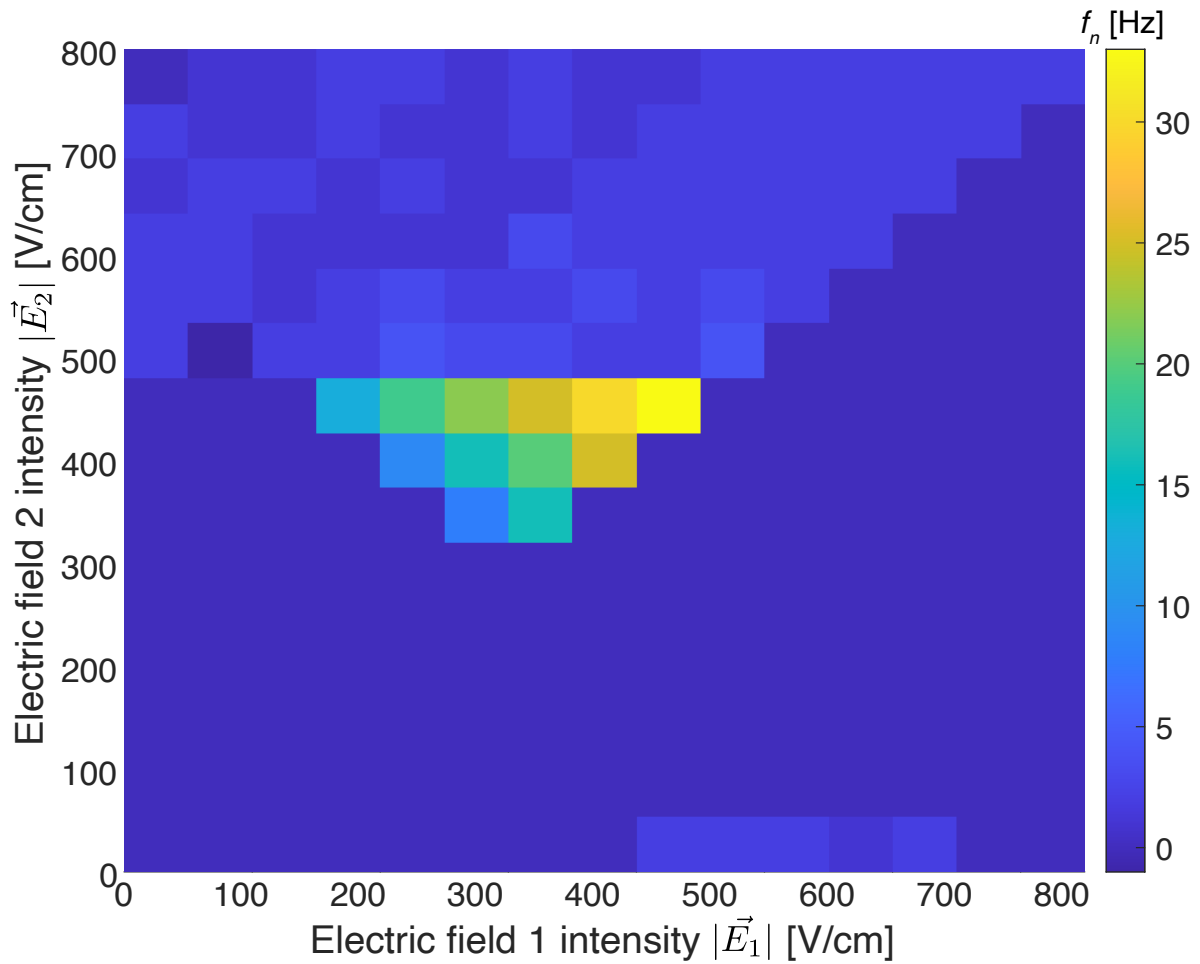
B.3.2 $f = 2500$ Hz

Fig. B.7 Axon activation map for a sensory axon with a diameter of $11.5 \mu\text{m}$ as functions of both $|\vec{E}_1|$ and $|\vec{E}_2|$, $f_1 = 2500$ Hz and $f_2 = 2510$ Hz.

Appendix C

Publication list

This thesis is based on the following publications:

- Shao-Tuan Chen, Christopher M. Proctor, and George G. Malliaras. "Materials and Device Considerations in Electrophoretic Drug Delivery Devices." *Scientific Reports* 10.1 (2020): 1-7. (Chapter 2)
- Shao-Tuan Chen, Megan N. Renny, Liliana C. Tomé, Jorge L. Olmedo-Martínez, Esther Udabe, Elise P.W. Jenkins, David Mecerreyes, George G. Malliaras, Robert R. McLeod* and Christopher M. Proctor. "Reducing Passive Drug Diffusion from Electrophoretic Drug Delivery Devices through Co-ion Engineering." *Under review*. (Chapter 3)
- Shao-Tuan Chen, Elise P. W. Jenkins, Shunsuke Yamamoto and George G. Malliaras. "Enhancing Electrophoretic Delivery rate via Split Electrode Design and Optimal Switching Scheme." *In preparation*. (Chapter 4)
- Shao-Tuan Chen, Ben Woodington, Damiano G. Barone and George G. Malliaras. "Steerable and Localized Spinal Cord Stimulation via Temporal Interference Fields." *In preparation*. (Chapter 5)

Lead-author publications not included in the thesis:

- Shao-Tuan Chen, Sijun Du, Emmanuelle Arroyo, Yu Jia, and Ashwin Seshia. "Shock Reliability Enhancement for MEMS Vibration Energy Harvesters with Nonlinear Air Damping as Soft Stopper." *Journal of Micromechanics and Microengineering* 27.10 (2017): 104003. (Invited Article).
- Shao-Tuan Chen, Sijun Du, Emmanuelle Arroyo, Yu Jia and Ashwin Seshia. " Utilising Nonlinear Air Damping as a Soft Mechanical Stopper for MEMS Vibration Energy Harvesting" *Journal of Physics Conference Series* 773.1 (2016).
- Shao-Tuan Chen, and Chen-li Sun. "Out-of-focus effects on microscale schlieren measurements of mass transport in a microfluidic device." *Measurement Science and Technology* 27.8 (2016): 085203.